Relationship Between Microstructure and Corrosion of Pressure Vessel Cladding Materials

by

Juan Manuel Ranalli

A thesis submitted to the University of Birmingham for the degree of DOCTOR OF PHILOSOPHY

School of Metallurgy and Materials

College of Engineering and Physical Sciences

University of Birmingham

August 2017

Abstract

Type 347L and Type 309L stainless steels used as weld cladding materials of nuclear reactor pressure vessels were investigated under realistic conditions of fabrication and service. Electron backscatter diffraction and metallographic observations were used in combination with double loop electrochemical potentiokinetic reactivation (DLEPR) test and ASTM-262-A test to determine the precipitation behaviour and its influence on intergranular corrosion (IGC) resistance as a function of post welding heat treatment (PWHT) time at 600 °C and after simulated service ageing at 425 °C.

It was shown that during the first stage of PWHT, $M_{23}C_6$ carbides precipitate in both alloys as a result of δ ferrite decomposition. This increased sensitization of the materials is due to the creation of a chromium-depleted zone, which was found to be replenished after 40 h of treatment, recovering the resistance of the materials to IGC. After combined treatment of PWHT + simulated service, 309L was shown to be re-sensitized whereas 347L remained resistant. Sigma phase was found to precipitate during the last stages of PWHT with a higher tendency on 309L.

Two characteristic reactivation potentials were found for both materials. A specific split-cycle DLEPR was applied to show that this technique can be further developed to identify deleterious phases in austenitic stainless steel welds.

Micro hardness and Charpy impact tests showed an increase in hardness and a decrease in absorbed energy of materials without PWHT after ageing at 425 °C.

Dedicated to

My parents in heaven who would have been glad to share this moment with me

My partner, daughter, family and friends who I am glad to share my life with

…..and to those who work for the integration of science, technology, and production for the benefit of the whole society, especially in developing countries.

Acknowledgment

First of all, I would like to express my sincere gratitude to my supervisors Dr Alison J. Davenport and Dr. Martin Strangwood for their patience, support and encouragement during this long adventure of pursuing my PhD while holding a high-responsibility position in a technical support organization in my country. It would not have been possible without their permanent help and patient guidance.

I wish to thank my mentor in Argentina, Dr. Ricardo Carranza for his invaluable contributions to my work and my manager Oscar Beuter for his trust and understanding during these years. Valuable suggestions from Dr. Ariel Danon are also acknowledge

I gratefully acknowledge the assistance I have received from Dr. Martina Avalos and her team from Universidad Nacional de Rosario, and Dr. Silvina Limandri and her team from Universidad Nacional de Córdoba with EBSD measurements, as well as from Luciano de Barberis and Federico Rodriguez with experiments in CNEA. The use of facilities at Instituto Nacional de Tecnología Industrial is also acknowledged to Alejandro Burgueño.

Financial support to this research was provided by Roberto Rocca Education Program, The University of Birmingham and Comisión Nacional de Energía Atómica (CNEA). The use of industrial facilities and provision of samples by IMPSA Argentina S.A. are also greatly appreciated.

Last but not least, I would like to thank my partner in life Paula and my daughter Rocío for the support, patience, and love that in many different ways I receive from them every day.

Table of Contents

1 Introduction 1

2 Literature review 4

2.1 Nuclear reactor pressure vessel claddings 4

2.2 Materials used in RPV claddings 6

2.2.1 Introduction to stainless steel 6

2.2.2 Microstructure of Austenitic Stainless Steel Welds 6

2.2.3 Role of delta ferrite in ASSWs 7

2.2.4 Measurement of delta ferrite 8

2.3 Microstructural changes on ASSWs due to high temperature exposure 8

2.3.1 Spinodal decomposition / precipitation and growth of α and α´ 8

2.3.2 Carbide precipitation 11

2.3.3 Low Temperature Sensitization (LTS) 14

2.3.4 Precipitation of Sigma Phase 16

2.4 Mechanical properties of ASSWs and changes due to high temperature exposure 23

2.4.1 Effects of spinodal decomposition / precipitation and growth of α and α´ 23

2.4.2 Sensitization and low temperature sensitization 24

2.4.3 Effects of sigma phase precipitation 26

2.5 Corrosion properties of ASSWs and changes due to high temperature exposure 26

2.5.1 Introduction to corrosion of stainless steel 26

2.5.2 Corrosion properties of phases existing in duplex SS and ASSWs 28

2.5.3 Effects of spinodal decomposition / precipitation and growth of α and α´.....29

2.5.4 Sensitization and low temperature sensitization 30

2.5.5 Effects of sigma phase precipitation 32

2.6 Tests used for evaluation of sensitization in stainless steel 33

2.6.1 ASTM A262 standard tests 33

2.6.2 Single Loop Electrochemical Potentiokinetic Reactivation test (EPR) ...34

2.6.3 Double Loop Electrochemical Potentiokinetic Reactivation test (DLEPR).....35

2.7 Potential use of DLEPR as a detection tool for deleterious phases 37

2.8 Summary 39

3 Experimental Method 41

3.1 Materials.....41

3.1.1 Fabrication of weld overlays and supply of samples 42

3.1.2 Ageing Treatments 43

3.1.3 Summary of samples and treatments 44

3.2 Microstructural Characterization 47
3.2.1 Chemical Analysis 47
3.2.2 Delta ferrite measurement 47
3.2.3 Microscopic examination 48
3.2.3.1 Mounting and polishing 48
3.2.3.2 Etching with Murakami´s reagent 49
3.2.4 Electron backscatter diffraction (EBSD) 49
3.3 Mechanical Properties Determination 50
3.3.1 Micro hardness 50
3.3.2 Charpy impact test 50
3.4 Corrosion Properties Determination 51
3.4.1 ASTM A262 - Practice A 51
3.4.2 DLEPR test 53
4 Microstructural Evolution of Stainless Steel Cladding Materials following Post-Weld Heat Treatment and Accelerated Ageing 56
4.1 Introduction 56
4.2 Supply of samples and definition of the region to be studied in the present work 57
4.3 Determination of composition profiles using Optical Emission Spectroscopy (OES) 66
4.3.1 Type 347L Stainless Steel 66

4.3.2 Type 309L Stainless Steel 72

4.4 Phase prediction using Thermo-Calc and analytical modelling of sensitization during PWHT 76

4.4.1 Thermo-Calc results using compositions obtained at the working plane 76

4.4.2 Analytical modelling of sensitization during PWHT at 600°C 80

4.5 Measurement of delta ferrite using ferritescope 84

4.5.1 Type 347L Stainless Steel 84

4.5.2 Type 309L Stainless Steel 87

4.6 Microstructural analysis 90

4.6.1 Type 347L SS 91

4.6.2 Type 309L SS 97

4.7 Analysis of phases by means of electron backscatter diffraction (EBSD) and energy dispersive X-ray spectroscopy (EDS) mapping 104

4.7.1 EBSD of Type 347L SS 107

4.7.2 EBSD of Type 309L SS 110

4.8 Discussion on microstructure evolution 115

4.8.1 Graphical Summary 115

4.8.2 Test sample location, microstructural characterization and composition profiles in the as-welded condition 115

4.8.3 Phase prediction 116

4.8.4 As-welded microstructure 119

4.8.5 Microstructural evolution during PWHT at 600°C 121

4.8.6 Microstructural evolution during simulated service conditions 123

4.9 Conclusions 125

5 Mechanical Properties of Stainless Steel Cladding Materials following Accelerated Ageing 128

5.1 Introduction 128

5.2 Determination of Vickers micro-hardness profiles through the weld overlay 128

5.2.1 Type 347L Stainless Steel 129

5.2.2 Type 309L Stainless Steel 133

5.3 Charpy impact testing of weld overlay 137

5.3.1 Type 347L Stainless Steel 138

5.3.2 Type 309L Stainless Steel 139

5.4 Fractographic analysis of Charpy samples 141

5.4.1 Type 347L Stainless Steel 141

5.4.2 Type 309L Stainless Steel 146

5.5 Discussion on Mechanical Properties Evolution 150

5.5.1 Graphical summary 150

5.5.2 Vickers micro-hardness profiles 150

5.5.3 Charpy impact tests 153

5.6 Conclusions 158

6 Corrosion Properties of Stainless Steel Cladding Materials following Post-Weld Heat Treatment and Accelerated Ageing 160

6.1 Introduction 160

6.2 Determination of susceptibility to intergranular corrosion through ASTM 262-practice A method 162

6.2.1 Type 347L SS 162

6.2.2 Type 309L SS 168

6.3 Determination of the Degree of Sensitization (DoS) using Double Loop Electrochemical Potentiokinetic Reactivation test (DLEPR) 173

6.3.1 Type 347L SS 176

6.3.2 Type 309L SS 186

6.4 Potential of DLEPR test for phase identification 194

6.4.1 Reactivation peak splitting in 309L 194

6.5 Discussion on corrosion properties evolution 202

6.5.1 Graphical Summary 202

6.5.2 Reactivation peaks 203

6.5.3 Evolution during simulated service conditions 211

6.5.4 Industrial relevance of the studied parameters 215

6.6 Conclusions 216

7 Summary and conclusions 220

7.1 Summary 220

7.1.1 Relevance of the work 220

7.1.2 Performance of RPV cladding materials analyzed in the present study……..222

7.1.3 Contribution to the development of DLEPR as a detection tool for deleterious phases in stainless steels. 224

7.2 Conclusions.....225

8 Future Work 227

8.1 Consider the effects of neutron irradiation.....227

8.2 Study the existence of a quantitative relationship between DoS_1, DoS_2 and precipitated phases.....227

8.3 Perform potentiostatic etching at the characteristic reactivation potentials found……..228

9 References.....229

1 Introduction

Interior surfaces of modern reactor pressure vessels (RPVs) are weld clad with a relatively thin layer of austenitic stainless steel (SS) which provides protection against corrosion of the load-bearing base material. Low-carbon and Nb-stabilized SS are both used in the industry due to their resistance to sensitization [1].

As a final stage in fabrication the whole RPV is subjected to a post welding heat treatment (PWHT) in order to relieve stresses built in the base material during welding [2]. This PWHT can be detrimental to the corrosion properties of the SS cladding due to the microstructural modifications it can produce. Once in service, the cladding is exposed to temperatures in the range of 280°C – 300°C [1] for very long periods of time for at least 30 to 40 years according to original design specifications [1] and up to 60 and 80 years in plant undergoing licence renewal [3] and subsequent license renewal [4] processes. Service exposure can also produce modifications in the microstructure and potentially affect corrosion and mechanical properties.

The degradation of mechanical and corrosion properties of austenitic stainless steel welds (ASSWs) has largely been studied for both the PWHT temperature range [5-9] and the cladding in-service temperature range [10-13]. However, relatively little work has been published considering the subsequent interaction of both processes. Studies performed so far have pointed out the beneficial effect of Nb additions in reducing the susceptibility of Type 308 SS to intergranular corrosion (IGC) [14] and intergranular stress corrosion cracking (IGSCC) [15]. The reduction of the free carbon required for $M_{23}C_6$ precipitation and the consequent formation of a Cr-

depleted zone (CDZ) was pointed out as the main reason for this improvement. However, detailed information is lacking about the precipitation sequence of weld cladding materials as a function of PWHT time at 600°C, its evolution during further low temperature ageing and how it correlates with the degree of sensitization (DoS) of the material.

Precipitation of σ phase has been observed to occur during short time ageing of austenitic stainless steel weld overlays in the range of 600 ºC to 800 ºC [14, 16-19]. Detection of this phase is generally carried out by metallographic examination, transmission electron microscopy, or by in-situ synchrotron X-ray diffraction [14, 16, 18, 20]. However, some authors indicated the possibility of linking the precipitation of this phase with the presence of multiple peaks in single-loop and double loop electrochemical potentiokinetic reactivation tests (DLEPR) [21-30] but no agreement has been reached yet about the significance of each peak or the optimal experimental conditions. Establishing a good correlation between the DoS determined by a non destructive technique such as DLEPR and the precipitation of deleterious phases in ASSWs would be of great benefit since new detection techniques and instruments could be developed in the future.

The present work will study, under realistic conditions, the evolution of microstructure of Type 347L and Type 309L cladding materials during PWHT and further simulated service ageing and how it correlates to mechanical and IGC resistance properties. DLEPR is used to determine DoS and a correlation between multiple reactivation

peaks and precipitation of $M_{23}C_6$ and σ phase is evaluated by a specifically designed split-cycle test.

2 Literature review

2.1 Nuclear reactor pressure vessel claddings

Modern reactor pressure vessels (RPVs) are composed by forged rings made of low alloy steel which are welded one on top of the other shaping the vessel, as schematically shown in Figure 2-1. Before welding, each ring is internally clad with a relatively thin layer of stainless steel (SS) deposited by welding which provides corrosion protection to the load-bearing base material. Corrosion rate in the clean water conditions of a nuclear reactor is not very high and unclad vessels can operate without severe damage. However, even small amounts of corrosion products are not desirable because they can pass to the water that circulates through the reactor and be activated (i.e. became radioactive) when passing through the reactor core [2]. This effect increases the total radioactive dose of nuclear power plants (NPPs) and for this reason a lot of effort is carried out in order to minimize the generation of corrosion products [31].

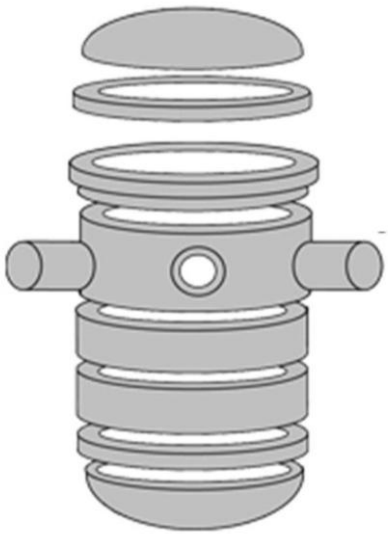

Figure 2-1: Schematic description of a RPV made of forged rings. After [32]

The main corrosion products responsible for radioactivity at Nuclear Power Plants (NPPs) are ^{60}Co and ^{58}Co followed by ^{51}Cr, ^{54}Mn, and ^{59}Fe. For example, ^{59}Co comes from Co-base alloys or as an impurity in structural materials and is activated as ^{60}Co, which is an important source of radioactivity [31].

In this context, the good corrosion properties of the SS weld cladding are highly desirable and all the stages from fabrication to service conditions are to be controlled to ensure its performance. As a final stage in fabrication the whole RPV is subjected to a post welding heat treatment (PWHT) at 600 °C for ~40 h in order to relieve stresses built in the base material during welding [2]. As further described in this chapter, this PWHT can be detrimental to the corrosion properties of the SS cladding due to the microstructural modifications it can produce.

Once in service, the cladding is exposed to neutron irradiation fluxes in the range of 1 x 10^{10} to 1 x 10^{11} $\frac{n}{cm^2\,S}$ and temperatures in the range of 280°C – 300°C [1] for very long periods of time which range from 30 to 40 years according to original design specifications [1] and up to 60 and 80 years in plant undergoing licence renewal [3] and subsequent license renewal [4] processes. This service exposure can also produce modifications in the microstructure of the cladding. In addition to high temperature changes, neutron irradiation is known to affect SS microstructure [33-37]. However, the present study will focus on modifications in SS cladding materials due to high temperature exposure during fabrication and service. Effects of neutron irradiation are considered for future research.

2.2 Materials used in RPV claddings

2.2.1 Introduction to stainless steel

Stainless steels are iron-based alloys which have at least 11% chromium. This element provides the characteristic corrosion resistance of the alloy by forming a passive oxide layer. However, as further discussed in this chapter if some regions of the passive layer became unstable or the local concentration of Cr falls below the lower limit, the material can be exposed to localized corrosion [38, 39].

There are many varieties of stainless steels which achieve a wide range of properties. These materials are classified based on the predominant metallurgical phases in their structure defining the following five different groups: martensitic, ferritic, austenitic, duplex (ferrite + austenite), and precipitation hardened (PH) [40].

Austenitic stainless steels are the widest used material in weld cladding of RPVs. Resulting microstructure of austenitic stainless steel welds (ASSWs) is different from that of the wrought material and is described in the following paragraphs.

2.2.2 Microstructure of Austenitic Stainless Steel Welds

The microstructure of ASSWs used in RPV claddings is in fact not a fully austenitic structure; but a mixture of a predominant austenitic phase with a small percentage of ferrite, typically between 5 and 10 % [8]. Therefore, ASSWs can generally be treated as low-ferrite duplex SSs. Since it is formed at high temperature during solidification; the BCC ferritic phase found in the weld structure is called “delta (δ) ferrite” in order

to distinguish it from the “alpha (α) ferrite” formed by lower temperature transformation from austenite [41].

Chemical composition has a large influence on the amount of δ ferrite in ASSWs, mainly in the balance of austenite stabilizers (Ni, C, N, Mn) and ferrite stabilizer elements (Cr, Mo, Nb). Constitutional diagrams were developed in the past to predict microstructure and solidification mode as a function of composition [41-43]. These diagrams were superseded by thermodynamic calculation software such as Thermo-Calc. Variations of the weld metal solidification rates found within the most common industrial processes do not significantly affect the resulting amount of ferrite in the weld. However, solidification rate can be relevant for very high cooling rate processes, such as electron beam welding and high power laser welding [41, 44].

2.2.3 Role of delta ferrite in ASSWs

Delta ferrite plays a major role in preventing solidification cracking in ASSWs. This phenomenon (also known as “hot cracking”) results from the formation of low-melting point P- and S-containing liquid films along grain boundaries during the last stages of solidification [41].

The higher solubility of P and S in ferrite than in austenite plays a role in the beneficial effect of δ ferrite because these elements are retained in solution and became unavailable for liquid film formation [8]. However, Brooks et al. reported that the complex crack path formed along the γ-δ boundaries and the low wetting of these interfaces by the liquid films were the most important reasons for solidification cracking prevention [45].

2.2.4 Measurement of delta ferrite

Several techniques have been developed for the determination of ferrite content in a given alloy. Metallographic point counting is an accurate technique that gives a direct reading of the volume fraction of ferrite. This technique has been improved by automatic image analysis software but it is still destructive in nature and requires extensive preparation time to be applied. Therefore, efforts have been made to develop several instruments which use the ferromagnetic nature of ferrite to allow for its quantification. Magna-gage and Feritscope are the most widely used instruments [42]. Both instruments can be calibrated to give direct readings of the percent content of ferrite in the alloy or the alloy Ferrite Number (FN), which is an arbitrary standardised value related to the ferrite content of an equivalent magnetic weld metal [46].

2.3 Microstructural changes on ASSWs due to high temperature exposure

2.3.1 Spinodal decomposition / precipitation and growth of α and α´

It is generally accepted that ferritic and duplex SSs are susceptible to thermal ageing embrittlement during service at temperatures in the range of about 250 - 550 ºC [10, 11]. This phenomenon, also known as 475 ºC embrittlement, consists in the decomposition of the ferritic phase into Fe-rich and Cr-rich domains [15,16] called α and α´ respectively . Both domains have BCC structures [47].

Separation of ferrite into α and α´ can occur either by spinodal decomposition or nucleation and growth [48, 49]. In spinodal decomposition the composition of the original alloy lies between inflection points in the free energy curve (see Figure 2-2).

In this case, small variations in composition will produce a reduction in the total free energy of the system. Therefore, there is no thermodynamic barrier for the formation of the nanometric-sized compositional waves that give rise to α and α´ regions. For other compositions within the two phase region (also called miscibility gap), a thermodynamic barrier exists for the transformation giving place to a nucleation and growth process [48, 49]. Chung and Chopra observed that α' spinodal precipitates can develop into much larger plate-like α' precipitates after long term ageing of cast duplex SS indicating that both processes can also be sequential [50]. Composition fluctuations of Cr resulting from spinodal decomposition are reported to produce mottled contrast under TEM observations [51-55].

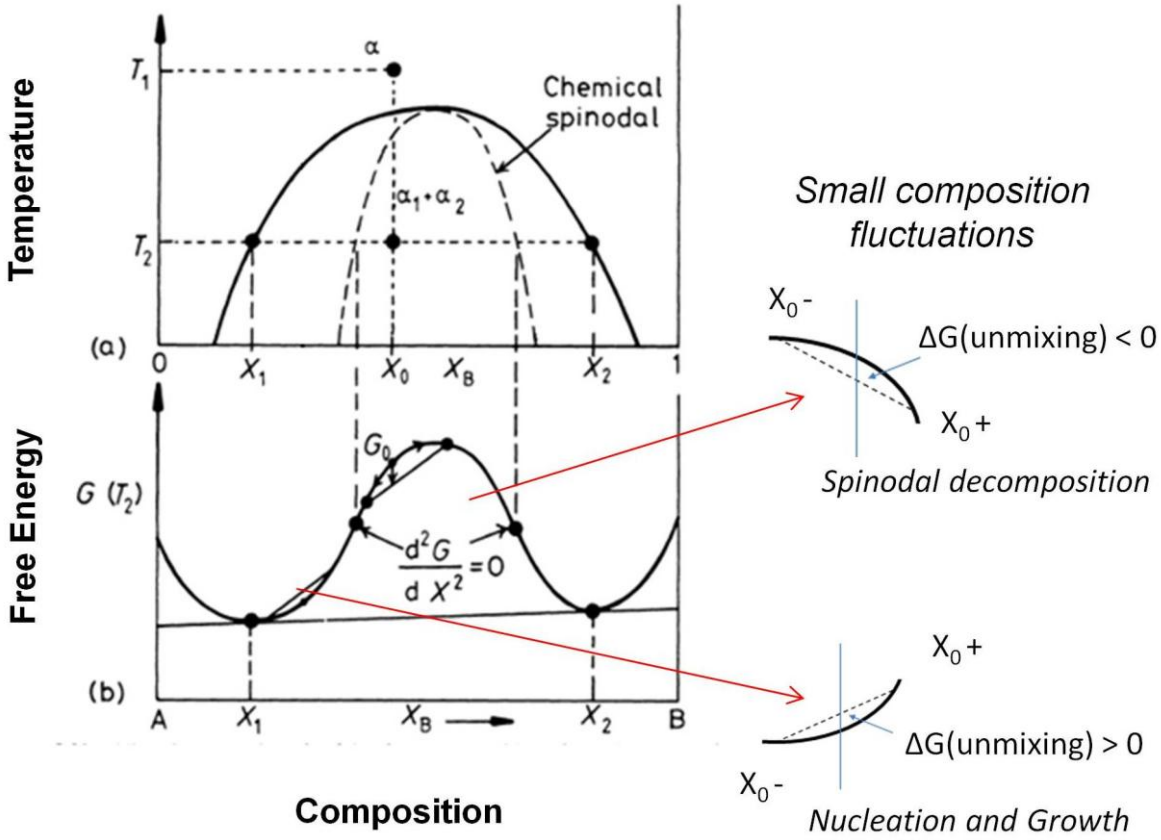

Figure 2-2: Description of spinodal decomposition and nucleation and growth within a miscibility gap (after [48] and [49])

The ageing mechanism is considered as a thermally activated process for which the kinetics can be expressed by an Arrhenius-type equation [10, 11]:

$$t_2 / t_1 = \exp [Q/R(1/T_2 - 1/T_1)]$$

Equation 2-1

Where t_2 and t_1 are the ageing times to reach equivalent material condition at absolute ageing temperatures of T_2 and T_1, respectively. Q is the ageing activation energy, and R is the gas constant. This modelling is of great importance because it allows prediction of the behaviour of in-service components by performing accelerated ageing treatments at higher temperatures for shorter periods of time. Nevertheless, increase in temperature should be limited within the margins where the same ageing mechanism occurs [10].

Single and multiple activation energy models have been proposed by several authors for duplex SS. A single activation energy model implies that a single ageing mechanism is taking place in the whole temperature range. Better agreement between predicted and observed ageing effects on duplex SS has been reported using different activation energies for two temperature sub-ranges [11, 56]. Bonnet et al. [56] reported higher activation energies for the lower temperature range (300-325 ºC) than those for the higher temperature range (350-400 °C).

Activation energies of cast duplex SS reported in literature vary over a wide range of values (from 60 to over 300 kJ/mol) [10, 11] and are said to be influenced by chemical composition (especially of ferrite), sample thermal history, and

experimental method used for its calculation. No activation energy values have been found for the ASSWs of the present study. Strangwood [57] has suggested an activation energy of 200 kJ/mol as a good approximation.

2.3.2 Carbide precipitation

$M_{23}C_6$

The term $M_{23}C_6$ is a more general notation for $Cr_{23}C_6$, since often Ni, Mo and Fe partially substitute for Cr in these carbides [58]. These Cr-rich carbides have an FCC lattice and are formed during exposure to a temperature range of approximately 500 ºC – 800 ºC [41]. The main problem associated with precipitation of $M_{23}C_6$ in stainless steels is the formation of a Cr-depleted zone (CDZ) in the vicinity of the carbides precipitated along grain boundaries, leading to an enhanced susceptibility of the alloy to intergranular corrosion. This metallurgical process is known as "sensitization" [39]. The widely accepted CDZ theory was first formulated by Bain et Al. [59] in the 30s and has now robust experimental support provided by direct observations of Cr-depleted regions by means of scanning transmission electron microscopy (STEM) [60-62].

Precipitation of $M_{23}C_6$ is favoured in ASSWs due to the presence of δ-ferrite. The lower solubility of carbon and the higher diffusivity of Cr in this phase in comparison to the austenite shifts precipitation of $M_{23}C_6$ to shorter times [8]. Figure 2-3 shows Time-Temperature-Precipitation (TTP) diagrams of a ferritic AISI 430 SS and an austenitic AISI 304 SS with similar contents of Cr and C. Intergranular corrosion

region (indicated as IC in the figure) also starts sooner in the ferritic than in the austenitic SS.

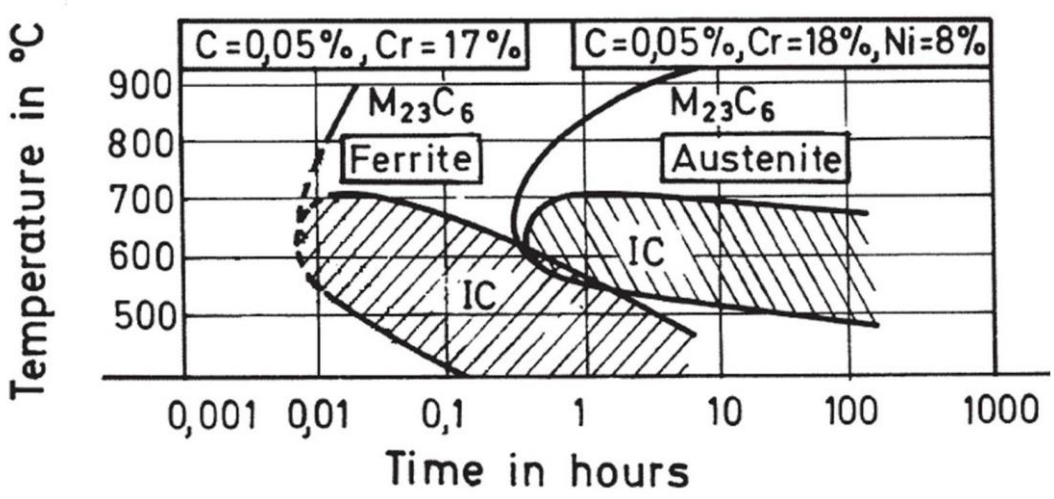

Figure 2-3: TTP diagrams for a ferritic (AISI 430) and austenitic (AISI 304) stainless steel with similar contents of Cr and C. IC indicates intergranular corrosion regions. (After [8])

In austenitic SS $M_{23}C_6$ are reported to precipitate preferably at grain boundaries, twin boundaries and less frequently at intragranular sites [58]. In duplex and ASSWs these carbides are reported to precipitate at the γ-δ interphase at the expense of δ ferrite according to the following equation [5-9]

$$\delta \rightarrow M_{23}C_6 + \gamma_2$$

Equation 2-2

The reduction of Cr concentration in δ ferrite due to the precipitation of Cr-rich $M_{23}C_6$ has been indicated to produce the transformation of δ into secondary austenite (γ_2) [8].

It is widely agreed that the creation of a Cr-depleted zone due to precipitation of $M_{23}C_6$ occurs simultaneously with diffusion of Cr from the bulk material that tends to replenish the CDZ around carbides. This process (known as self-healing or desensitization) was first theoretically demonstrated by Strawstrom and Hillert [63] and experimentally observed by many authors [60, 64-67]. Devine [64] has shown that treatment times longer than ~10 h at 600°C are enough to de-sensitize type 308L duplex SS with 10% of δ ferrite.

Different analytical models have been developed in order to predict sensitization and analyze the influence of alloying elements. According to Tedmon et al. [68] the most important parameter to determine sensitization is the Cr concentration in equilibrium at the matrix-carbide interphase. They predicted this concentration by thermodynamic theory based on alloy composition and sensitization temperature, explaining then the influence of these parameters. Strawstrom and Hillert postulated that sensitization is reached when the width of the CDZ around carbides with is larger than 20 nm and derived an equation to estimate time to sensitization [63]. These models rely upon parameters (mainly activity coefficients of Cr, C, and Cr concentration in the gamma-carbide interface) for which a big spread exists in literature about values and calculation methodologies [68, 69]. No specific values of

activity coefficients could be found in the open literature for the materials used in the present work.

MC

MC carbides can precipitate due to the content of strong carbide formers (Ti, Nb, V, Zr and Ta) in stabilised stainless steels. MC carbides have an FCC structure and precipitate in preference to $M_{23}C_6$ when a stabilisation treatment is performed in the temperature range of 840 – 900 ºC [58]. In this treatment, carbon is "tied-up" by MC carbides at high temperature leaving less C available for $M_{23}C_6$ precipitation at lower temperature, thus improving resistance to intergranular corrosion [40]. MC carbides can also precipitate during cooling of stabilized ASSWs providing an enhanced resistance to sensitization [70]. A minimum amount of stabiliser in respect to C content of the alloy should be specified in order to guarantee the full stabilisation of the alloy; in the case of Nb-stabilised stainless steels, the minimum content of Nb (wt %) should be at least 10 times the wt % C [39].

2.3.3 Low Temperature Sensitization (LTS)

It has been shown that sensitization can occur at temperatures lower than 500°C if the material has carbides already precipitated in the structure. At these low temperatures, the precipitation of $M_{23}C_6$ is inhibited and sensitization occurs by growing of the previously deposited carbides (during welding or high temperature thermal treatment). This growth occurs with the consequent creation of a CDZ that cannot be replenished with bulk-diffused Cr due to the low diffusivity of this element

at low temperature. This phenomenon is known as low temperature sensitization [71, 72].

Given that diffusion is very slow at low temperatures, the microstructure of the material plays an important role in the kinetics of the process. Nishimoto et al. [12] showed that LTS in ASSWs take place in much shorter times than in a single phase austenitic SS due to the sites provided by the δ-γ interface for carbide nucleation during welding. The importance of the higher diffusivity of Cr in δ ferrite present in the weld was also pointed out when comparing the higher susceptibility of the weld pool of AISI 304LN against the single phase base metal [13]. Cold working also increases susceptibility to LTS due to the increase in dislocation density [71] and formation of deformation-induced martensite, which favours Cr diffusion [66, 67, 73, 74].

For very long ageing times it was reported that LTS can be found concomitantly with spinodal decomposition affecting both corrosion and mechanical properties of duplex SS and ASSWs [10, 75]. Given that δ ferrite cannot be avoided in ASSWs, efforts to reduce LTS are concentrated at reducing the amount of carbides precipitated during welding that will be available to continue growing. This could be achieved either by using stabilized or low-carbon grades [14]. According to Lippold [76], LTS has been observed in L-grade alloys but does not seem to be a problem for stabilized grades such as Type 347. Another option is applying very high cooling rates to avoid precipitation. However, cooling rate during welding is limited by the thermal stresses imposed to the components. Therefore, laser surface re-melting has been shown to

be successful in achieving a layer of material with little or no $M_{23}C_6$ without affecting the bulk material properties [12, 77, 78]

2.3.4 Precipitation of Sigma Phase

σ phase is a hard and brittle intermetallic phase composed of Cr and Fe. It has a complex tetragonal unit cell formed by 30 atoms and a nominal composition of 48 wt % Cr [79]. Precipitation of σ phase has been observed to occur during short time ageing of austenitic stainless steel weld overlays in the range of 600 ºC to 800 ºC [14, 16-19]. This temperature range coincides with the one of the PWHTs used during reactor pressure vessel fabrication. Treatment times reported for precipitation of σ phase in wrought austenitic stainless steel are well beyond the 40 hours used in RPV PWHT [80, 81]. However, σ phase can precipitate in duplex SS and ASSWS in shorter times because, as shown by Barcik [82], the precipitation of σ is favoured by the presence of δ ferrite due to the higher diffusivity (~100 times higher) of alloying elements in this phase than in the austenite. Vitek and David observed this effect after comparing the kinetics of σ precipitation in Type 308 ASSWs in the as-welded condition (with 7-8 % of δ) [19] and following an homogenization treatment to reduce the amount of ferrite [83]. It was also shown that crystallographic misorientation between the ferritic and austenitic phase promotes precipitation of σ in duplex SS [84].

Apart from the accelerating effect of δ ferrite in σ precipitation, effects of different alloying elements on the tendency to form σ have been studied. Hull [85] proposed the formulation of the “equivalent Cr” parameter to quantify in a relative way the

influence of different alloying elements on the embrittlement produced by σ precipitation according to Equation 2-3 [85]. Elements with positive signs promote σ formation whereas those which have negative signs tend to delay precipitation.

$$\text{Equiv. Cr} = \text{Cr} + 0.31\,\text{Mn} + 1.76\,\text{Mo} + 0.97\,\text{W} + 2.02\,\text{V} + 1.58\,\text{Si} + 2.44\,\text{Ti} + 1.7\,\text{Nb} + 1.22\,\text{Ta} - 0.226\,\text{Ni} - 0.177\,\text{Co}$$

Equation 2-3

Depletion of carbon in solid solution in the matrix is required for σ precipitation. The CDZ produced during $M_{23}C_6$ precipitation provides this condition explaining why σ is generally observed after carbide precipitation [82]. Therefore, a higher content of C (which is not considered in Equation 2-3) implies longer times for sigma precipitation. For this reason, low-carbon and stabilized SS show a greater tendency to form sigma. Hamada and Yamauchi found that additions of Nb higher than 0.65% on Type 308L weld overlays produced embrittlement due to σ precipitation following PWHT at 610°C for 40 - 50 h [14].

The effect of nitrogen is similar to that of carbon in the sense that its content in solid solution has to be lowered before σ can precipitate. For this reason an increase of the content of N in the alloy shifts σ precipitation to longer times [8].

Figure 2-4 shows time-temperature-precipitation (TTP) diagrams for σ phase precipitation on different stainless steels where the above-discussed influences of composition and microstructure can be appreciated. It is seen that all alloys containing δ ferrite have a higher tendency to form σ than the fully austenitic Type

304 SS. Precipitation is seen to occur ~100 times faster from δ than from γ as indicated by Barcik [82]. The effect of N can be appreciated in the different precipitation behaviour showed by Type 316 SS with different N content [8].

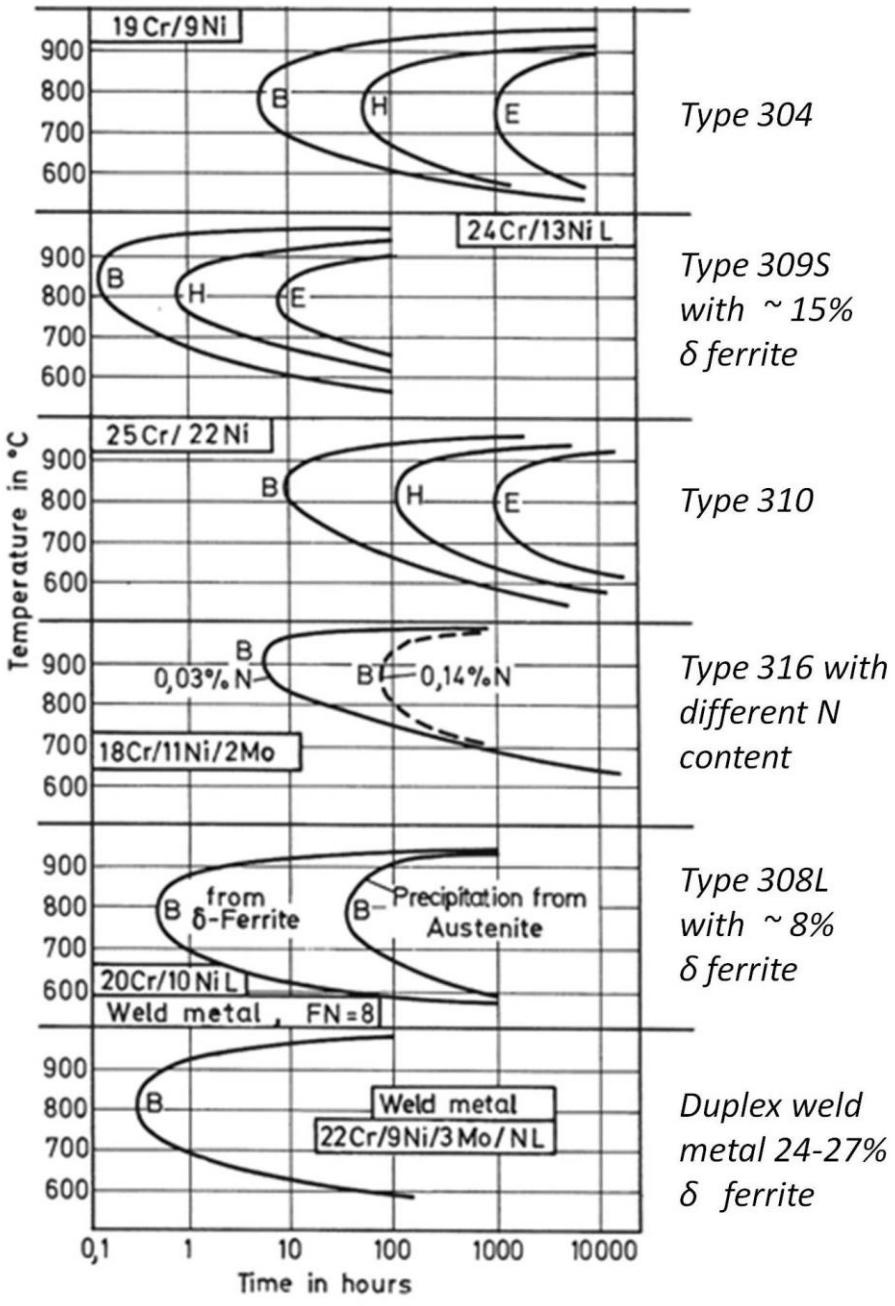

Figure 2-4: TTP diagrams for different austenitic stainless steels showing the effect of δ ferrite and alloy composition in the time required for σ precipitation. B, H, and E represent beginning, half and end of transformation (After [8]).

In duplex SS and ASSWs sigma phase was observed to be formed as a result of δ ferrite transformation according Equation 2-4, where γ_2 represents secondary austenite [8, 86-88]

$$\delta \rightarrow \sigma + \gamma_2$$

Equation 2-4

The ferrite-austenite interface and the interior of δ ferrite grains are reported as the preferential nucleation sites for this transformation [19, 41, 89-92]. For increasing ageing times δ ferrite can be completely consumed leaving σ and γ_2 in its place with a characteristic “coral-like” morphology as shown in Figure 2-5

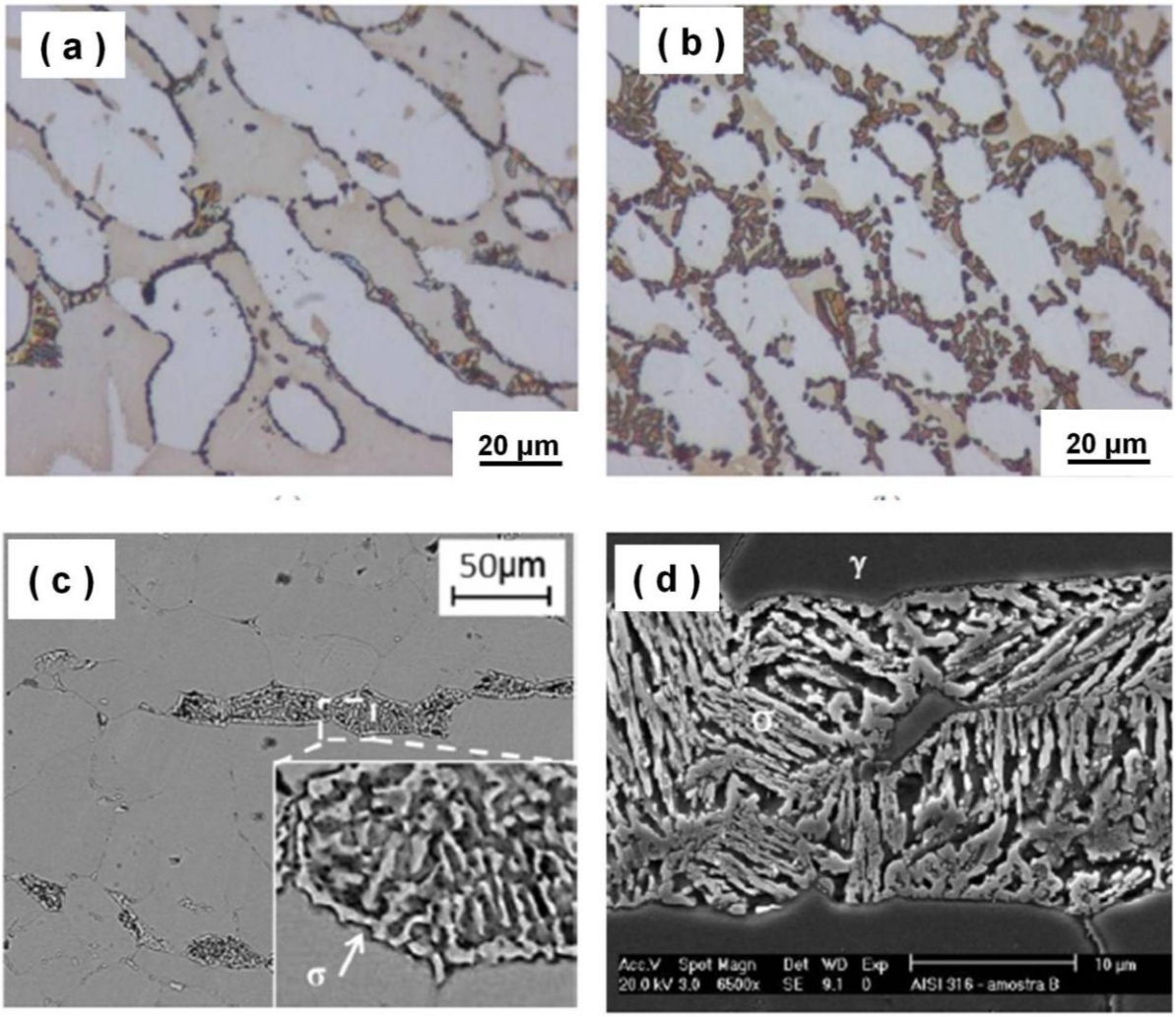

Figure 2-5: Coral-like morphology of sigma phase precipitated in the interior of δ ferrite in UNS 31803 Type Duplex Stainless (a) and (b) [93], Ti-modified Super 304H austenitic SS (c) [65] and in 316L austenitic SS [91].

Pohl et al. [94] observed that morphology of σ phase in duplex SS depends on ageing temperature. These authors indicated that the coral-like morphology (Figure 2-5) corresponds to the lower temperature range (750°C) whereas massive precipitation (Figure 2-6) is observed for the higher ageing temperatures (850°C and 950°C).

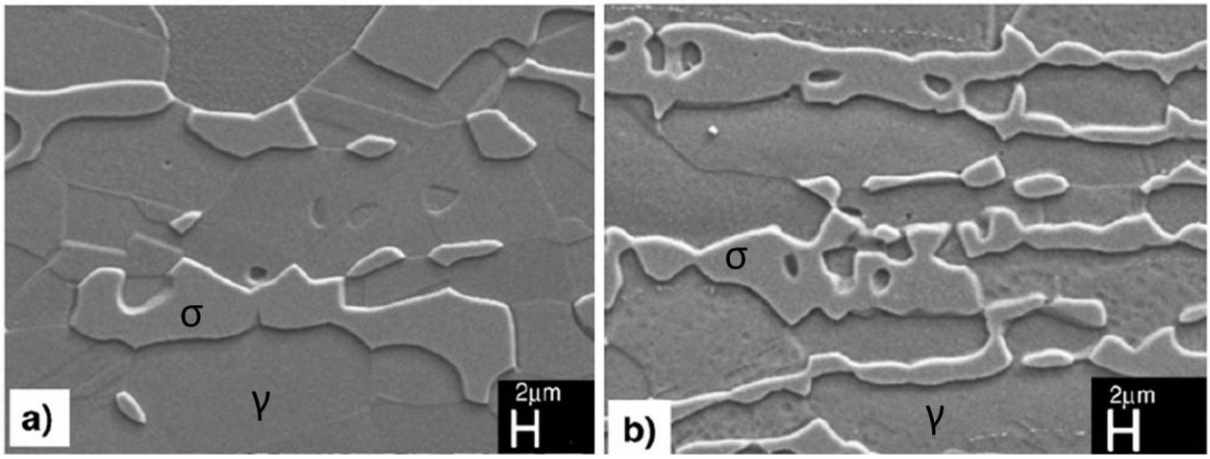

Figure 2-6: Massive morphology of sigma phase precipitated in the interior of δ ferrite in UNS 31803 Type Duplex Stainless aged at 950°C (a) and 850°C (b). [94]

Vitek and David [95] have concluded that precipitation of σ phase is a nucleation-controlled process based on the lack of differences in Cr concentration they found between σ and the surrounding residual δ ferrite after long ageing times. However, much research supports the idea that precipitation of σ is governed by the substitutional diffusion of alloying elements (mainly Cr, Mo, and Si) required for enrichment of δ prior to σ precipitation [96-100].

According to several authors the fraction of σ formed after an isothermal ageing can be described by a Johnson-Mel-Avrami (JMA) expression [20, 96, 101]

$$f(\sigma) = 1 - e^{(-k\,t^n)}$$

Equation 2-5

Where:

$f(\sigma)$ = extent of transformation measured as a fraction of the total equilibrium content of σ

n = JMA exponent

k = rate constant given by $k = k_0 . e^{-(\frac{Q}{RT})}$ with k_0 pre-exponential constant, Q the activation energy of the transformation, R the gas constant and T the absolute temperature

The value of the exponent n is related to the growth mode of the involved transformation. Values from 1 to more than 4 imply discontinuous precipitation or interface controlled growth whereas values of n between 0.5 and 2.5 represent different conditions of diffusion controlled growth [102]

In several studies [20, 96, 98, 103, 104] the fraction of σ phase during isothermal ageing was experimentally determined in order to obtain k and n parameters by plotting Equation 2-6, which is a linearization of Equation 2-5.

$$\ln\left(-\ln\left(1 - f(\sigma)\right)\right) = n.\ln(t) + \ln(k)$$

Equation 2-6

Ferro and Bonollo [103] and Magnabosco [96] found single slopes on the plots for duplex SS with n values between 0.8 and 1.05 concluding that precipitation of sigma is a diffusion controlled process. However, dos Santos and Magnabosco [104] and Elmer et al. [20] found a change in the slope during isothermal ageing suggesting a

change in the growing mode of the phase. For the first stages of ageing the highest values of n were reported (1.5 - 7) indicating a preponderant interphase-controlled growth during the nucleation stage whereas for longer ageing times lower values of n (0.22 – 0.75) were reported indicating the prevalence of the diffusion-controlled growing of the already nucleated σ.

2.4 Mechanical properties of ASSWs and changes due to high temperature exposure

2.4.1 Effects of spinodal decomposition / precipitation and growth of α and α´

Spinodal decomposition has largely been studied in ferritic SS and in the ferritic phase of wrought and cast duplex SS [10, 51, 53, 54, 56, 105-110] showing a reduction of fracture toughness and an increase in hardness with ageing time. Actual reactor cast duplex SS aged during operation was analyzed by Chung and Leax [107] showing good correlation with spinodal decomposition as a primary ageing mechanism. Fewer studies are available on ASSWs [52, 111]. Vitek et al. showed that the microstructural behaviour of a Type 308 ASSW aged at 475 ºC is quite similar to that found for SS castings and that the effects of ageing are also comparable [52].

The increase in hardness observed in duplex and ASSWs is due to transformations undergone by the ferritic phase with little or no changes in the austenite [11, 51, 52, 110]. Changes in hardness due to spinodal decomposition occur more rapidly than modifications on the electrochemical behaviour of the material [53, 110].

Impact properties are impaired in both cast duplex and ASSWs as a result of spinodal decomposition. Vitek et al. [52] have shown that the Charpy impact properties of a type 308 ASSW aged at 475 ºC are significantly degraded, both in terms of the Ductile-Brittle Transition Temperature (DBTT) and Upper Shelf Energy (USE). They showed a two-stage degradation process with a shift in the DBTT for the first stages of ageing (100 hours) followed by a decrease in the USE for 1000 h or more. This particular behaviour led them to conclude that considering only room temperature results could be misleading, since impact energy at 20 ºC does not show a further decrease after more than 100 hours, and yet a substantial decrease in the USE was observed for longer ageing times. However, other authors [110, 112] have characterised the degree of thermal embrittlement of cast stainless steels in terms of room-temperature Charpy-impact energy.

2.4.2 Sensitization and low temperature sensitization

Sensitization of stainless steels has been found to be linked to the development of intergranular stress corrosion cracking (IGSCC) [113-116]. Stress corrosion cracking is defined as the cracking produced by the simultaneous presence of tensile stress and specific corrosive environments. As a result of SCC ductile materials exposed to certain corrosive environments have a pseudo-brittle behaviour. Fine cracks propagate under stress levels even below the yield limit whereas the rest of the material remains ductile [38, 117]. Apart from specific environment-alloy combinations, several other factors such as stress level, temperature, metallurgical condition of the material (cold work, sensitization, etc.), pH, oxygen concentration and electrode potential play influence SCC susceptibility [118].

Stress corrosion cracking of austenitic stainless steels in nuclear industry has a different impact depending on the type of reactor considered mainly due to the water chemistry of the reactor coolant. Boiling water reactors (BWRs, 78 out of 449 operating reactors worldwide [119]) operate with a higher level of oxygen in comparison to pressurized water reactors (290 reactors worldwide) where oxygen is controlled by hydrogen additions [120]. In BWRs, several failures due to IGSCC have been observed in reactor internals made of not only standard grade stainless steels, but also low-carbon and stabilized SS showing the relevance of the problem for this kind of reactors [121-123].

On the other hand, as indicated by Raquet et al. [124], the electrochemical potential measured for austenitic stainless steels exposed to the hydrogenated conditions of PWR reactor coolant is well below the critical potential recognized for SSC initiation and too low to promote susceptibility to SCC on these materials in absence of a significant amount of specific impurities. Therefore instances of SCC of austenitic stainless steel in PWR are not frequently reported and those found were attributed to a combination of an accidental presence of oxygen trapped in stagnant regions and cold work [124, 125]. The most frequently reported SCC failures under PWR reactor coolant conditions are associated with Alloy 600, its associated weld metals, and other Ni-based alloys [125-128]. This phenomenon is commonly known as primary water stress corrosion cracking (PWSCC).

2.4.3 Effects of sigma phase precipitation

The transformation of δ ferrite into σ phase during PWHT has a deleterious effect in mechanical properties of duplex SS and ASSWs. The reduction of ductility and toughness associated with σ phase precipitation has been studied to great detail [6, 80, 101, 129], and is usually referred in literature as “σ phase embrittlement” [41].

Pohl et al. observed different degree of reduction of toughness depending on the morphology of precipitated sigma indicating the higher reduction for the “coral-like” morphology (Figure 2-5) in comparison to the massive precipitation observed at higher temperatures (Figure 2-6).

Sigma phase precipitation has been associated with deleterious effects on creep properties of duplex SS and ASSWs [18, 58, 130]. However, some authors found that, when finely dispersed, σ phase can increase creep resistance [131, 132] due to the effect of extensive σ/γ interphase in hindering dislocation movements.

2.5 Corrosion properties of ASSWs and changes due to high temperature exposure

2.5.1 Introduction to corrosion of stainless steel

Corrosion can be defined as the deterioration of the properties of a material due to its interaction with the environment [38]. In general a metal or alloy can be resistant to corrosion in a given environment for the following two cases [133, 134]:

a) The corrosion of the alloy is thermodynamically not possible (noble metals)

b) The alloy forms a thin and protective surface film, known as the passive film, which is self healing when damaged (passive metals)

The price of noble metals excludes them from consideration in engineering applications and all corrosion resistant alloys rely on passivity to perform their functions [135]. Stainless steels belong to this family of alloys and show a very good resistance to general corrosion due to the formation of a very thin and protective Cr-rich oxide layer. However, SS are susceptible to other forms of corrosion such as pitting corrosion and intergranular corrosion, which are due to local instabilities of the passive layer (localized corrosion) [134]. For this reason, selection of SS must be considered carefully based on service environment and metallurgical transformations that might affect the stability of the passive film [40, 41]

Pitting corrosion is a form of localized corrosion observed as a very strong attack in small areas whereas the rest of the material remains passive. It is an autocatalytic process which requires the presence of an aggressive ion, such as Cl^- or Br^- for stainless steel. In this process acidified conditions within the pit are produced due to hydrolysis of metal cations that are being dissolved. Chloride ions are drawn into the pit to balance the charge and the environment created within the pit promotes further metal dissolution and growing of the pit. The cathodic reaction (oxygen reduction) occurs in the area out of the pit which remains protected by the passive layer [136, 137]. Although this form of corrosion is possible in the coolant circuit of nuclear power reactors, the concentration of aggressive anions is kept at a very low level and strictly monitored as a part of normal plant operation and maintenance procedures [138] .

Intergranular corrosion refers to a localized attack at grain boundaries and the adjacent region with relatively little attack to the grains [38, 39]. Under these circumstances loss of material can occur by detachment of the grains and / or the alloy can lose its strength [38]. It should be noted that large reductions in mechanical properties can occur with relatively little amount of material removed [39]. Depending on the system, intergranular corrosion can be caused by impurities at the grain boundaries, or variation in the concentration at the grain boundary area (enrichment or depletion) of one of the alloying elements [38]. In stainless steels, intergranular corrosion occurs due to the formation of a Cr-depleted zone resulting from precipitation of Cr carbides in a metallurgical process called sensitization, as described in Section 2.3.2. This form of corrosion can be a serious problem in Boiling Water Reactors (BWRs) and is frequently observed in the heat affected zone (HAZ) of non stabilised ASSWs [139]. If not properly managed, the heat cycle produced by the welding process can expose the HAZ to the temperature-time cycle required for sensitization.

2.5.2 Corrosion properties of phases existing in duplex SS and ASSWs

The individual electrochemical behaviour of the austenitic phase, ferritic phase and precipitates in duplex SS has been studied by means of micro-electrochemical techniques [87, 140, 141]. A good correlation was found between the corrosion resistance of each phase and the empirical pitting resistance equivalent with nitrogen (PRE_N) [141]. There is no agreement about the individual behaviour of the phases. Perren et al. [141] showed that in strong acids where general corrosion is predominant, the austenitic phase seems to be more susceptible to corrosion.

However, other authors have identified the ferritic phase as the more susceptible. [140, 142]. Nevertheless, wide agreement exists that the worst corrosion behaviour is found in the region were σ and γ_2 coexist after ageing of duplex SS [87, 140]. It is worth noting that σ phase could not be tested isolated due to its small size.

2.5.3 Effects of spinodal decomposition / precipitation and growth of α and α´

Several studies have been carried out showing a reduction in the localised corrosion resistance of duplex SS associated with Cr composition fluctuations due to spinodal decomposition and α´ phase precipitation. Anodic polarisation curves and Double Loop Electrochemical Potentiokinetic Reactivation (DL-EPR) tests have been used to study this effect. These electrochemical methods have also been suggested as suitable techniques for non-destructive evaluation of spinodal decomposition on SS components [47, 143]

Several authors [53, 54, 110, 144] have linked an electrochemical reactivation peak in the cathodic sweep of DL-EPR to the presence of iron-rich (Cr-depleted) regions. Jiang et al. [53] showed that this peak does not appear in the first stages of ageing (composition fluctuation at the nanometre scale), but rather during long term ageing of duplex SS, when α´ phase precipitates. Deleterious effects on corrosion properties due to spinodal decomposition are always linked to very long ageing times (several thousand hours) and appear later than deterioration of mechanical properties [53, 110].

2.5.4 Sensitization and low temperature sensitization

The main effect of sensitization and low temperature sensitization is the higher susceptibility of the material to intergranular corrosion (IGC). IGC is the localized attack at or adjacent to grain boundaries with little or no attack to the grain interiors [76]. One of the main problems associated with IGC is that a relatively small amount of material removed along grain boundaries can produce major damage to the component, even leading to grains falling out under severe conditions [38].

As explained in Section 2.3.2 sensitization in SS occurs due to the formation of a Cr-depleted zone around $M_{23}C_6$ which precipitate under specific Temperature-Time conditions. Improper thermal treatments or welding procedures are frequently the reason behind the several IGC failures reported for stainless steel [39].

During welding of austenitic SS sensitization can occur due to the metallurgical transformations undergone in different regions of the material produced by the time-temperature cycles it is exposed to (Figure 2-7) [38, 39].

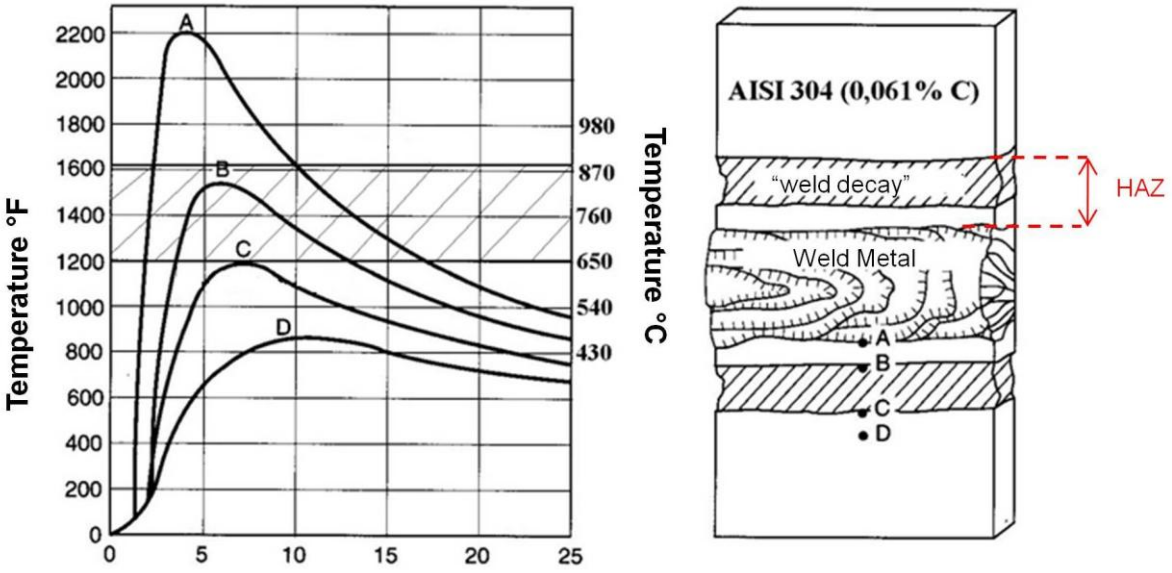

Figure 2-7: Regions and temperature-time cycles in an austenitic stainless steel weld. After [38].

In the region of the heat affected zone (HAZ) closest to the weld metal the increase in temperature is enough as to get into the region where Cr carbides are dissolved (curve A in Figure 2-7). The fast cooling rate can keep carbides in solution thus avoiding sensitization. Between points B and C the thermal cycle produces greater amounts of $M_{23}C_6$ precipitation, leading to the higher sensitization. This phenomenon is known as "weld decay" and can lead to serious IGC if the material is later exposed to a corrosive environment. For longer distances from the deposited weld metal the increase in temperature is not enough as to enter into the $M_{23}C_6$ precipitation region [38, 39, 76, 145].

Low carbon and stabilized SS can be used in order to avoid IGC [14]. The first group of materials bases its better resistance in the fact that they have lower carbon

available for $M_{23}C_6$ precipitation, whereas the stabilized steels have additions of stronger carbide formers such as Nb or Ti that form carbides at higher temperatures without taking Cr out of solution [76].

2.5.5 Effects of sigma phase precipitation

Sigma phase is known to affect corrosion properties of duplex SS and ASSWs. The main corrosion property of ASSWs that was found to be affected by transformation of δ ferrite into σ phase is the pitting corrosion resistance. This effect was observed in Nb-stabilised type 347 SS weld overlays [16] and Type 316LN welds [17].

Considering the high content of Cr in σ, several studies have linked the loss of pitting corrosion resistance to a weakening of the passive layer around sigma due the creation of a CDZ [65, 78, 146, 147]. This mechanism is similar to that of sensitization due to $M_{23}C_6$ precipitation. However, some authors found an increase in susceptibility to pitting corrosion without detecting a higher trend to intergranular corrosion (IGC) [17, 148]. A possible explanation was based on the fact that replenishment of the CDZ with bulk-diffused Cr can occur during ageing, and that the pitting susceptibility could be due to the increase of initiation sites provided by σ-γ and σ-δ interphases [148].

The reduction of stress corrosion cracking resistance of duplex stainless steel as a consequence of σ precipitation was observed by Lopez et al. [129] and more recently by Saithala et al. [149] who have reported a marked effects for levels higher than 2% σ.

2.6 Tests used for evaluation of sensitization in stainless steel

2.6.1 ASTM A262 standard tests

The ASTM A262 standard is one of the most commonly used in stainless steels for detecting susceptibility to intergranular corrosion. It is composed of a set of 5 practices with different characteristics as described in the following paragraphs. All these tests can detect susceptibility to IGC due to $M_{23}C_6$ and some of them also due to sigma phase precipitation. However, none of these practices is able to separate the contribution of each process [150].

Practice A: Oxalic acid test

In this test a sample is polished to a determined finish and over-etched electrolytically with oxalic acid. The resulting microstructures are compared to standard images and classified as “acceptable” or “suspect”. This test is quite fast and simple and can be used to screen out material which is found acceptable. If a sample is classified as “suspect” it cannot be considered failed and should be further tested by one of the other practises.

Practice B: Ferric sulphate-sulphuric acid test (Streicher test)

The sample is immersed in a boiling solution of ferric sulphate and sulphuric acid for 120 h. The loss of weight of the specimens is measured and converted into a corrosion rate using the total area of the sample. The result of the test is expressed in mm of penetration per month.

Practice C: Nitric acid test (Huey test)

In this practice the sample is boiled in a nitric acid solution for five periods of 48 hours each and similarly to what is done in practice B, the loss of weight is measured and converted to a corrosion rate that is reported for each boiling period.

Practice E: Copper-copper sulphate- 16% sulphuric acid test (Strauss test)

The sample is embedded in copper shot or grindings and exposed to boiling acidified copper solution for 15 hours. Metallic copper is put in excess and galvanic contact provided to ensure the conditions of the test. After boiling samples are bent 180°C over a proper radius and examined for intergranular cracks. Cracks detected under a magnification of 5 to 50 X indicate the presence of intergranular attack

Practice F: Copper-copper sulphate-50% sulphuric acid test

In this practice the sample is immersed for 120 hours in a boiling solution of copper sulphate and sulphuric acid with a piece of metallic copper used to maintain a constant corrosion potential. The loss of weight is measured and converted into a corrosion rate using the total area of the sample.

2.6.2 Single Loop Electrochemical Potentiokinetic Reactivation test (EPR)

The EPR test is a quantitative technique used to evaluate sensitization [151]. It was originally developed for austenitic stainless steel and is standardized under the ASTM G-108 for Type 304 and 304L SS [152].

In the first step of the test, samples are potentiostatically passivated before a sweep back into active potentials is initiated and finalized at the corrosion potential (E_{Corr}). The area under the reactivation peak (reactivation charge) is calculated and normalized considering the sample area and the grain boundary area giving as a result the Normalized Charge P_a. This test requires fine surface polishing and grain boundary count according to ASTM E-112 [153].

2.6.3 Double Loop Electrochemical Potentiokinetic Reactivation test (DLEPR)

The DLEPR was developed after the EPR test and is used for obtaining a quantitative evaluation of sensitization on stainless steels and nickel-based alloys.

The whole DLEPR cycle (Figure 2-8) is formed by a forward sweep and a reverse sweep. The forward sweep goes from the open circuit potential (OCP) towards higher potentials passing through active dissolution and getting into the passive region until the reverse potential is achieved. The reverse sweep starts at the reverse potential and brings the potential back to the OCP.

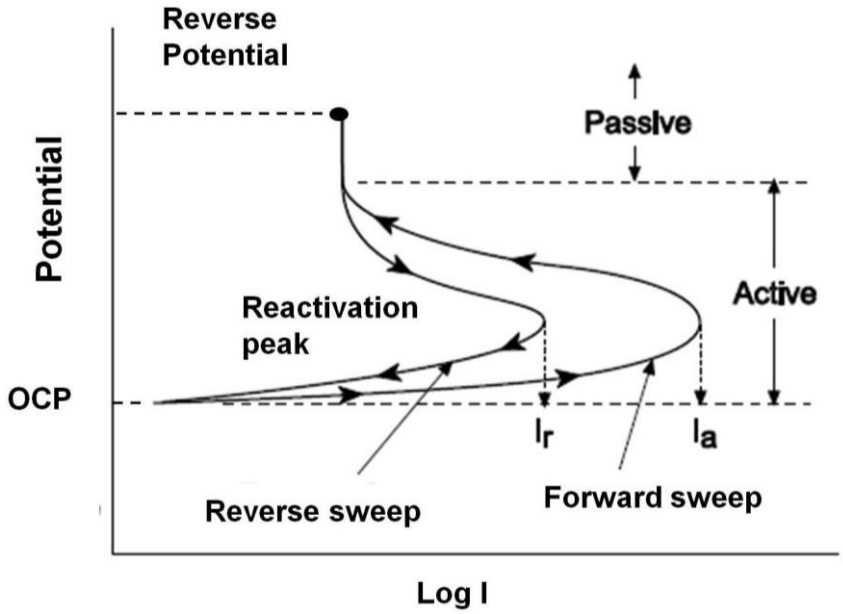

Figure 2-8: Schematic description of the DLEPR. After [154]

If the material is sensitized a clear reactivation peak will be developed during the reverse sweep. The degree of sensitization (DoS) is obtained as the ratio of the reactivation peak current to the active current, which is the maximum current achieved during the forward sweep.

$$DoS\ (\%) = \frac{\mathrm{Ir}}{\mathrm{I}a}\ \mathrm{x}\ 100$$

Where:

Ir = Reactivation peak current

Ia = Active peak current

This technique is currently standardized for stainless steel and nickel-based alloys under the BS-EN-ISO 12.732:2008 standard [155] which also gives as a reference the following guidance for interpretation of results.

Ir/Ia (%)	General Interpretation of the degree of sensitization
< 1	Unsenistized
1 to 5	Slightly sensitized (might pass Streicher, Strauss and Huey test)
> 5	Sensitized (could fail Streicher, Strauss and Huey test)

The use of DLEPR has been increasing since it was developed and the American Society for Testing and Materials (ASTM) is conducting a round-robin series of tests as a part of the process to develop its own standard for the technique [156].

The main advantages of DLEPR are its non-destructive nature and the greater simplicity of the test given that the results are not affected by sample geometry or surface finishing and grain count is not required to obtain the DoS. These characteristics make the test a candidate for industrial applications [21, 157].

2.7 Potential use of DLEPR as a detection tool for deleterious phases

In recent years many EPR and DLEPR studies were performed not only to obtain the DoS of different materials but also aimed at exploring the potential of the technique to identify certain deleterious phases [21-30]. In these studies characteristics of the obtained DLEPR curves such as composed active peaks or multiple reactivation peaks are tried to be linked with the observed phases. This application of DLPR is of particular interest because should it be successful a new generation of instruments for on-site application could be developed [21].

The earlier works found in literature are referred to single-loop EPR. Gill et al. [22] identified three different reactivation peaks in aged 316L ASSW and suggested that they could be linked to the reactivation of Cr- and Mo-depleted regions at the interfaces with the different secondary phases present (δ, carbides, sigma and chi). During the reactivation sweep of Alloy 800H Edgemon et al. [23] found a first reactivation peak corresponding directly to the degree of sensitization of the material (i.e. sole contribution of the sensitized grain boundaries to the reactivation peak), and a second peak they associated with the general activation of the sample surface. Similar results were obtained for Alloy 600 but the authors formulated also the possibility of pitting corrosion as an additional contributor to the first reactivation peak. However they agreed in indicating general surface depassivation as responsible for the second reactivation peak [24].

Most recent works are based on DLEPR tests. The presence of two peaks in the forward sweep of DLEPR as well as in the active-to-passive transition region of polarization curves was reported by several authors for different kinds of duplex SS [21, 25-29]. It is generally agreed that a two step active dissolution process of the austenitic and ferritic phases can explain the double peak given the different electrochemical behaviour of the phases discussed in Section 2.5.1.

In the reverse sweep of DLEPR, deAssis et al. [25] were able to link the first (more anodic) peak to sigma phase by cycling potential around the peak and studying the attacked surface, whereas the second peak was attributed to austenite attack. Leal et al. [30] pointed out that the results obtained in terms of charge ratio $Q_{reactivation}$ /

Q_{active} can be affected not only be the presence of deleterious phases but also by the balance of austenite and ferrite in duplex SS leading to the need for prior studies of the alloy before trying to use DLEPR as a detection tool in the field.

There is still debate about which is the best parameter to be used for phase identification. An integrated charge ratio of $Q_{reactivation}$ / Q_{active} was shown to follow sigma phase in superduplex stainless steel [25]. However, area integration parameters were pointed out to be not appropriated to separate contributions in double peak processes due to the partial overlap of the peaks [23].

It should be also noted that the variety of materials and different test conditions (electrolytes, scan rates, etc.) used make difficult the comparison of the numeric values of peak potentials obtained by different authors.

2.8 Summary

Reactor pressure vessels of nuclear power plants are clad with a weld deposit of austenitic stainless steel in order to protect the vessel from corrosion and reduce the release of corrosion products to the rest of the plant. The microstructure of the weld deposit is not fully austenitic and contains 5-10% of δ-ferrite. This phase can undergo different metallurgical transformations during fabrication (precipitation of $M_{23}C_6$ and σ phase) and service (spinodal decomposition and low temperature sensitization). Low-carbon and Nb-stabilized SS are both used in the industry due to their resistance to sensitization. Although the study of corrosion and mechanical properties of these materials is a well-researched topic, less has been published

about their behaviour on the specific ageing sequences that RPV claddings are subjected to under expected operating conditions.

ASTM A262 standard tests are widely used for the determination of intergranular corrosion resistance. However, the use of DLEPR has gained increasing attention due to its simplicity and quantitative nature. Attempts to link the presence of more than one reactivation peak in the reverse sweep of some materials with the content of specific deleterious phases and/or different corrosion mechanisms have recently been published. Nevertheless, more research is needed in this area since no unequivocal relationships have yet been established.

In the present work, Type 309L (low-carbon) and Type 347L (Nb stabilized) materials are studied in a comparative way. Samples of weld overlays manufactured under industrial procedures are subjected to PWHT and simulated service conditions in order to determine the precipitation sequence during the whole life cycle of the RPV cladding and how it affects mechanical and intergranular corrosion properties. The evolution of microstructure is followed by means of ferritescope, optical and electronic microscopy, EDS and EBSD. Mechanical properties are studied by Vickers micro-hardness, Charpy impact tests, and fractography analysis. Intergranular corrosion resistance is studied using ASTM 262 practice A and DLEPR tests. In addition, a procedure is developed to study the links between the two reactivation peaks found for both materials and the presence of $M_{23}C_6$ and σ phase as a result of PWHT.

3 Experimental Method

3.1 Materials

Two slabs of ASTM A516 Gr 70 carbon steel (1000 mm x 500 mm x 72 mm) were used as base material where strip cladding weld overlays were built. The strip electrodes used were 30 mm wide x 0.5 mm thick. Table 3-1 shows nominal composition of the materials. Soudokay (currently Voestalpine Bohler Welding) Record INT 109 neutral flux was used for all the samples. Type 347L cladding comprised a first layer made with a CN 24/13 Nb R 800 – BS electrode and a second layer made with a CN 21/10 Nb R 800 – BS electrode. Type 309L cladding comprised two layers made with an EQ 309L electrode. All materials have been provided by IMPSA Argentina except for the welding flux which has been supplied by Aceros Boheler Argentina S.A.

Table 3-1: Nominal composition of materials

SA-516 Gr.70 [158]											
C		Mn		P		S		Si		Fe	
0.30 max		0.79-1.30		0.035 max		0.035 max		0.13 – 0.45		Bal.	
CN 24/13 Nb R 800– BS [159]											
C	Si	Mn	P	S	Cr	Ni	Co	Nb	N	Ta	Fe
< 0.02	0.2	2	< 0.02	< 0.02	24	12	<0.08	0.9	<0.05	<0.08	Bal.
CN 21/10 Nb R 800– BS [159]											
C	Si	Mn	P	S	Cr	Ni	Co	Nb	N	Ta	Fe
< 0.02	0.2	1.8	< 0.02	< 0.02	20.5	11	<0.08	0.8	<0.05	<0.08	Bal.
EQ 309L [158]											
C		Si	Mn	P	S	Cr	Ni	Mo	Cu	Fe	
< 0.03		0.30 -0.65	1.0-2.5	<0.03	<0.03	23-25	12-14	<0.75	< 0.75	Bal.	

3.1.1 Fabrication of weld overlays and supply of samples

Weld overlays of Type 347L and Type 309L SS were fabricated by submerged arc welding (SAW) using strip electrodes in a two layer process. The welding machine used was an ESAB LAE 1600 located at IMPSA Argentina S.A. (Figure 3-1). Process parameters were taken from a previous CNEA specification [160] and are summarized in Table 3-2 along with the actual values obtained. Once the deposits were finished the first and last 10 cm of the slab were discarded in order to exclude from the study the regions of the beginning and ending of the welding arc.

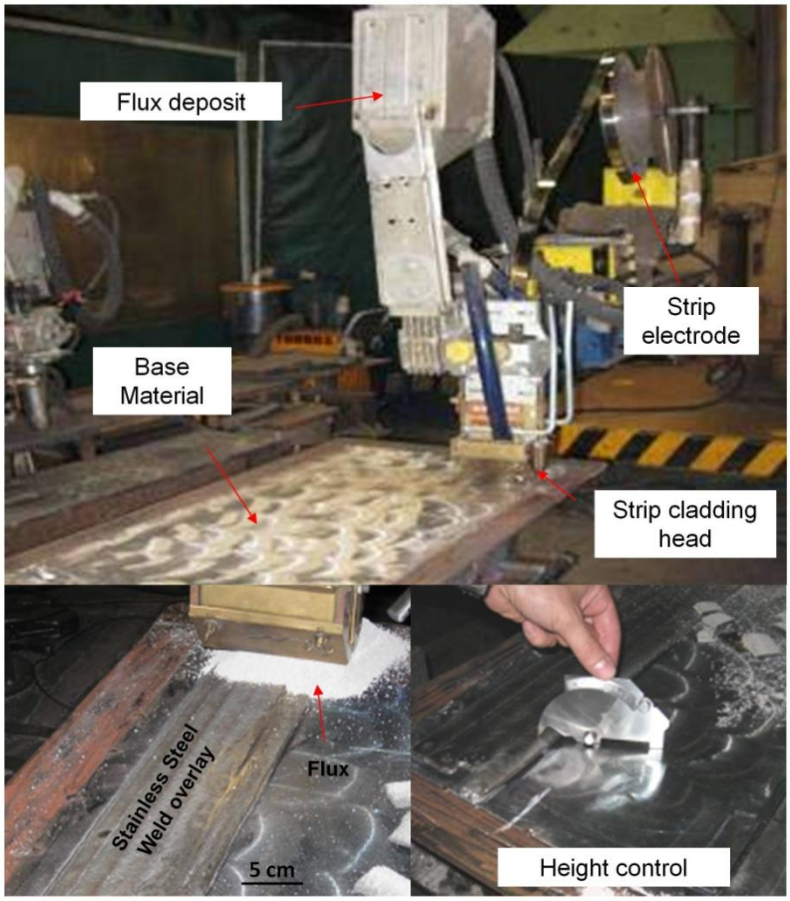

Figure 3-1: Fabrication of weld overlays by SAW process with strip electrodes

Table 3-2: Specified and measured welding parameters

Parameter	First layer		Second layer	
	Specified value	**Measured value**	**Specified value**	**Measured value**
Preheating temperature	150 ºC min.	130-152 ºC	150 ºC min	130-152 ºC
Inter pass keeping temperature	200 ºC max.	185 ºC	200 ºC max	185 ºC
Current	270 – 300 A	300 A	360-440 A	350 - 360 A
Voltage	26-28 V	28 V	28-30 V	28 V
Overlap (bead to bead)	3-7 mm	5 mm	8-14 mm	11 mm
Welding speed	140 -160 mm/min	150 mm/min	200-240 mm/min	200 mm/min
Layer height obtained	2 mm	2-3 mm	4 mm	4-6 mm

3.1.2 Ageing Treatments

Ageing of samples was performed in air atmosphere using a Termoquar laboratory tubular furnace supplied with a Honeywell UDC 2000 controller. Ageing was finished by water quenching. Three ageing procedures were designed to reproduce fabrication and service conditions of RPVs.

1) Simulated service ageing at 425 °C without PWHT

This treatment simulates 60 years of service at 300 °C in an accelerated way by ageing as-received samples for 284.4 h at 425 °C. Temperature was selected to accelerate the in-service ageing process which occurs at ~300 °C but without changing the ageing mechanism. Ageing time was calculated according to the following Arrhenius equation considering an activation energy of 200 kJ/mol.

$$t_{ageing} = t_{service} * e^{\frac{Q}{R}\left(\frac{1}{T_{ageing}} - \frac{1}{T_{service}}\right)}$$

Where t_{ageing} and $t_{service}$ are the accelerated ageing and service times at corresponding absolute temperatures of T_{ageing} and $T_{service}$. Q is the ageing activation energy, and R is the gas constant. In addition, a set of samples aged for 142.2 h at the same temperature were also tested to provide more information about the evolution of the process.

2) PWHT – ageing 600 °C up to 100 h

This treatment is the same as that applied to the whole pressure vessel after welding the forged rings, which are clad individually. In most RPV specifications, PWHT time at 600 °C is around 40 h. In the present study PWHT time was extended up to 100 h in order to have a better understanding of the microstructural changes produced by the treatment.

3) Further ageing for 284.4 h at 425 °C of samples that had been given a PWHT for 40 h at 600 °C

This treatment represents the real conditions to which RPV clad surfaces are subjected during fabrication and service. As a first step, samples were PWHT at 600 °C for 40 h representing the fabrication conditions as previously described. Later, these treated samples were subjected to accelerated ageing at 425 °C for 284.4 h in order to simulate 60 years of service at 300 °C.

3.1.3 Summary of samples and treatments

Table 3-3 shows the nomenclature of samples for all thermal treatments and Table 3-4 summarizes the experiments performed for each ageing condition.

Table 3-3: Sample nomenclature

	As-welded	Ageing at 425 °C		PWHT 600 °C					PWHT 600 °C 40 h + Ageing 425 °C 284.4 h
		142.2 h	284.4 h	1 h	10 h	25 h	40 h	100 h	
347L	347 AW	347 1/2A	347 A	347 PWHT 1H	347 PWHT 10H	347 PWHT 25H	347 PWHT 40H	347 PWHT 100H	347 PWHT+A
309L	309 AW	309 1/2A	309 A	309 PWHT 1H	309 PWHT 10H	309 PWHT 25H	309 PWHT 40H	309 PWHT 100H	309 PWHT+A

Table 3-4: Experimental matrix

	Metallographic characterisation	OES	Delta ferrite	EBSD	Vickers hardness	Charpy impact test & Fractography	ASTM 262	DLEPR	Split Cycle DLEPR
347 AW	X	X	X	X	X	X	X	X	
347 1/2A	X		X		X	X	X	X	
347 A	X		X		X	X	X	X	
347 PWHT 1H	X		X				X	X	
347 PWHT 10H	X		X				X	X	
347 PWHT 25H	X		X				X	X	
347 PWHT 40H	X		X				X	X	
347 PWHT 100H	X		X	X			X	X	
347 PWHT+A	X		X				X	X	
309 AW	X	X	X	X	X	X	X	X	X
309 1/2A	X		X		X	X	X	X	
309 A	X		X		X	X	X	X	
309 PWHT 1H	X		X				X	X	
309 PWHT 10H	X		X	X			X	X	X
309 PWHT 25H	X		X				X	X	
309 PWHT 40H	X		X	X			X	X	
309 PWHT 100H	X		X	X			X	X	X
309 PWHT+A	X		X				X	X	

3.2 Microstructural Characterization

3.2.1 Chemical Analysis

Optical emission spectroscopy (OES) was performed in a Spectro - SPECTROLAB LAVWA18A equipment. A 9 cm x 3 cm block of base material containing both welding layers was cut from each weld coupon in the as-welded condition to perform the chemical analysis.

In order to obtain compositional profiles, 1 mm of each sample was milled out and 10 tests were performed evenly distributed on this surface. The procedure was repeated 3 more times giving as a result compositional information at 1, 2, 3, and 4 mm from the overlay surface for 347L and 309L. Material sampled by each OES spot is between 8 and 10 mm in diameter and less than 1 mm in depth.

3.2.2 Delta ferrite measurement

The equipment used was a Fisher FERITSCOPE FMP30 instrument with a FGAB1.3-Fe probe able to measure in the range of 0.1-80 % ferrite. Calibration was performed before each measurement.

Samples were obtained from the middle of the second weld layer of each material and measurements were taken on the “working planes” defined in Chapter 4. For 347L material, samples were 10 cm x 7 mm x 1.5 mm and for 309L material, samples were 10 cm x 7 mm x 2.5 mm due to the higher thickness of the weld overlay obtained for this material.

Data were collected from the centre line of the samples in order to avoid extra contributions of the edge effects to the total error of the instrument. According to manufacturer indications [161] a correction factor of 1.05 was required for 347L samples due to their low thickness (1.5 mm).

3.2.3 Microscopic examination

An Olympus GX51 optical microscope with a CCD camera and image acquisition software was used for metallographic observations. A scanning electron microscope (SEM) FEI- Quanta 200-MK2 with tungsten filament supplied with an EDAX EDS detector was used for fractographic analysis and microstructure characterization in secondary electron and backscattered electron mode. All the samples used for microscopic examination were obtained from the middle of the second weld layer of each material and measurements were taken on the “working planes” defined in Chapter 4

3.2.3.1 Mounting and polishing

Samples for SEM observation were hot mounted in conductive Poly-Fast resin (Struers) using a Struers CitoPress-1 mounting press with a cycle of 3.5 minutes at 180 °C and 250 bar followed by water cooling of the chamber for 1.5 min. For the rest of the samples cold mounting with Subiton acrylic resin provided by Laboratorios SL S.A. was used.

Samples were ground using SiC papers from grit size 220 to grit size 1000. Polishing started with 6 μm DiaDuo-2 suspension on a poliNat-1 polishing cloth, then 3 μm

DiaDuo-2 suspension on a DP-Floc polishing cloth and finished with 0.04 µm OP-S on a OP-Chem cloth. All consumables from Struers.

3.2.3.2 Etching with Murakami´s reagent

Etching solution was prepared mixing 5 g of reagent grade sodium hydroxide (NaOH) and 5 g of reagent grade of potassium ferrocyanide (K_4 [$Fe(CN)_6$]) with 50ml of deionised water (Milipore 18 Megahom.cm). Solution was heated under fume hood up to 80 °C and each sample was submerged for 60 seconds. After that the sample was rinsed in a beaker with deionised water first to keep the waste solution and finally in running tap water. A maximum of 3 samples were etched with the same batch of solution.

3.2.4 Electron backscatter diffraction (EBSD)

Two different pieces of equipment were used for EBSD. Measurements on 347L were performed in a Sigma-Zeiss field-emission SEM with an Oxford Nordlys Nano EBSD camera. The software used for phase index was the AZtec 3.1.

Type 309L samples were measured in a field emission SEM FEI QUANTA 200F with a Digiview EDAX/TSL EBSD camera. The software used for image process and acquisition was TSL OIM Data Collection 5.31

The SEM parameters used were: 20 keV beam energy, 8.5 - 11 mm working distance, and 70° tilt angle. Steps of 100 nm and 200 nm were used for the low magnification maps and were switched to 70 nm and 50 nm for high magnification maps.

3.3 Mechanical Properties Determination

3.3.1 Micro hardness

A Leitz Durimet Vickers hardness tester was used with a 200 g load. Cross sections (~1 cm wide) of the weld coupons containing base material and both weld layers were obtained as shown in Figure 3-2. Samples were ground with SiC papers and polished to 1 μm diamond paste before the experiments.

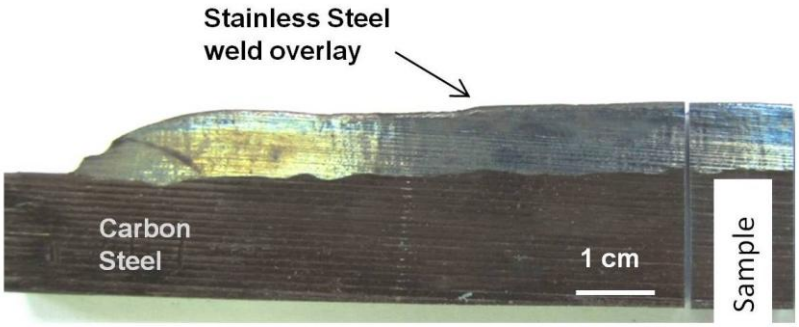

Figure 3-2: Orientation of samples for hardness measurements

Four hardness profiles were obtained for each sample. A minimum distance of 2 mm was allowed from line to line and with the borders of the sample in order to avoid overlaps effects. Measurements started at the fusion line and were shifted towards the surface with a pitch of 0.6 mm.

3.3.2 Charpy impact test

The equipment used was a Riehle Charpy impact testing machine with a capacity of 30 lb ft (40.7 Joules).

Sub-size Charpy samples (5 mm x 5 mm x 55 mm) according to ASTM E-23 standard [162] were machined from weld overlays of 347L and 309L in the as-

welded condition and after ageing at 425 °C for 142.2 h and 284.4 h. The tip of the notch of each sample was located to coincide with the middle of the second weld layer, as shown in Figure 3-3 and described in detail in Chapter 4.

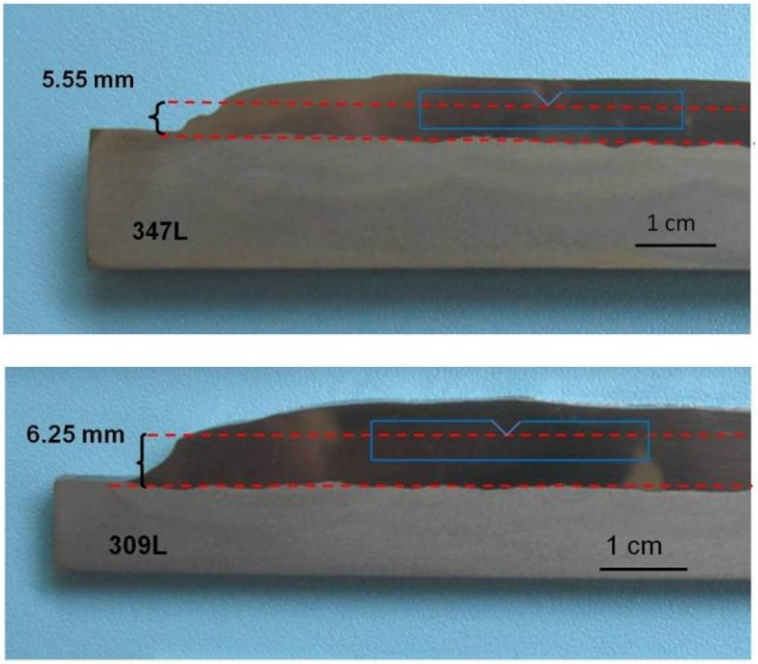

Figure 3-3: Orientation of samples for Charpy impact tests

Tests were performed at room temperature (24 ± 1 °C) and a minimum of 3 samples were tested for each condition.

3.4 Corrosion Properties Determination

3.4.1 ASTM A262 - Practice A

The ASTM 262 [150] is a standard comprising 5 practices widely used in the industry to detect susceptibility of stainless steel to intergranular corrosion in different environments. Practice A (also known as “Oxalic acid test”) is a fast screening test based on the comparison of obtained etching structures against standard patterns.

Samples were obtained from the middle of the second weld layer of each material and experiments were performed on the “working planes” defined in Chapter 4. Exposed area of the samples was 2 cm x 7 mm. Samples were ground with SiC papers to 600 grit size and then polished to 3 microns diamond paste.

Etching solution (10% (m/v) oxalic acid) was prepares using 20 g of reagent grade oxalic acid and adding deionised water to complete 200 cm^3 of solution. Polished specimens were electrochemically etched at 1 A/cm^2 for 1.5 minute at room temperature (24 ± 1 °C). After etching, resulting microstructures were classified as “acceptable” or “suspect” as shown in Figure 3-4.

.

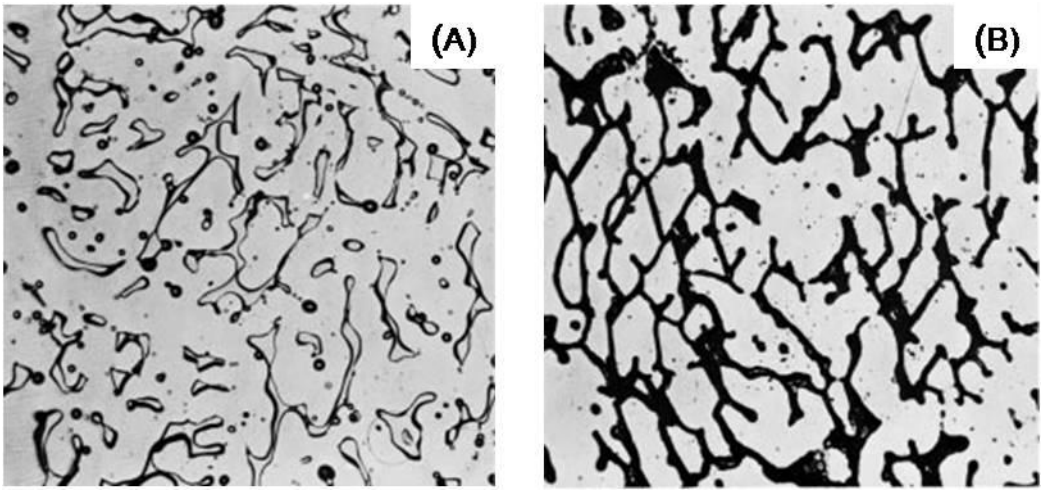

Figure 3-4: Classification of etching microstructures in ASTM 262-practice A. Isolated Ferrite Islands (A) are considered “acceptable”. Inter-phase ditches (B), referred as interdendritic ditches in the standard, are considered “suspect”. Figure after [150].

In addition to ferrite islands and/or inter-phase ditches, etched specimens can show other features such as different heights between phases, shallow etch pits and end grain pits. Except for the end grain pits, whose excessive presence can lead to the specimen being classified as “suspect”, other variations are not considered as relevant in the practice and the classification of the structures is performed only considering the presence of ditches. Dual microstructures (i.e. those showing isolated ferrite islands as well as some Interphase ditches but with no single grain completely surrounded by ditches) are also considered “acceptable” in the standard

3.4.2 DLEPR test

DLEPR tests were performed using a three-electrode electrochemical cell with a platinum wire counter electrode and a Hg / Hg_2SO_4 reference electrode (V Hg / Hg_2SO_4 = 0.654 V vs NHE). Deaeration was provided by bubbling nitrogen into the solution and the potentiostat used was a Gamry Reference 600. Before each test, the reference electrode was compared to a calibrated reference electrode. The general arrangement of the cell and a detail of the sample are shown in Figure 3-5.

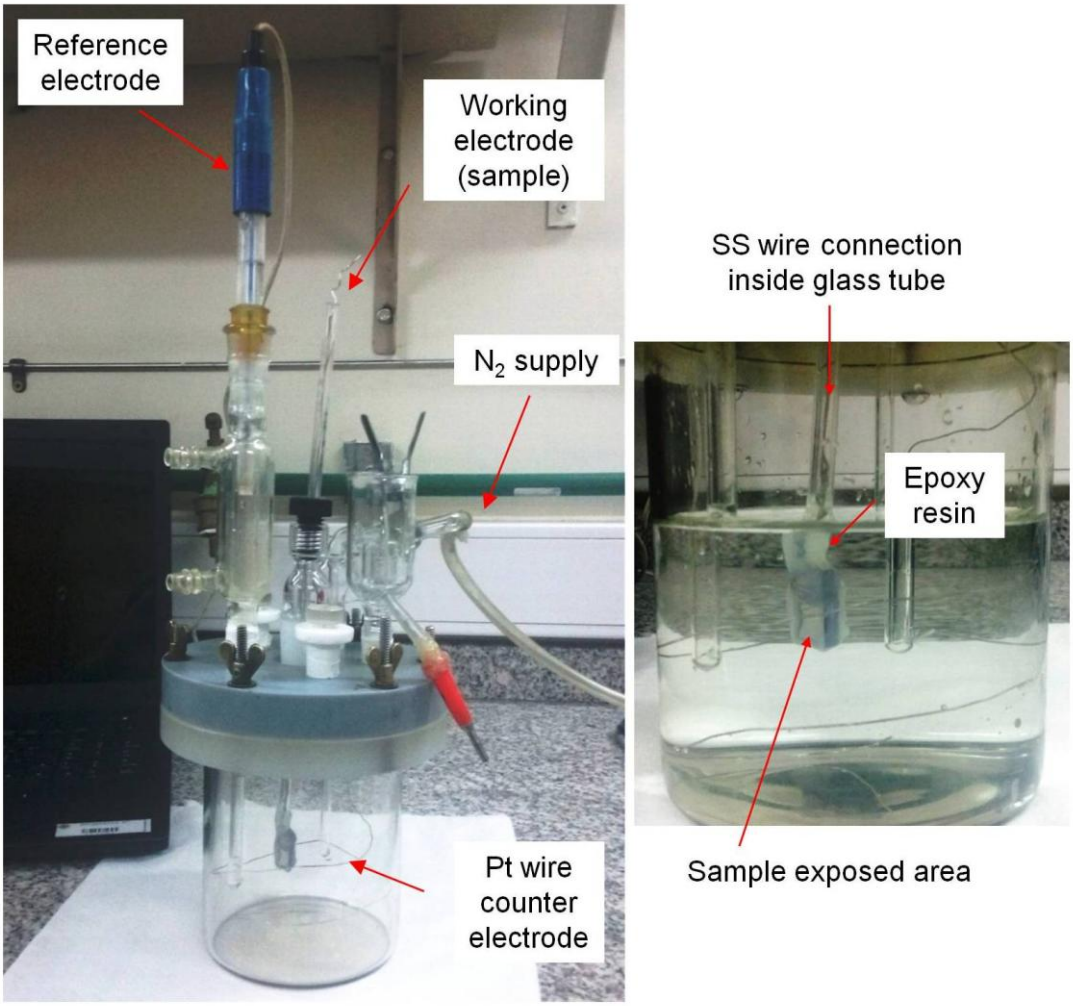

Figure 3-5: Electrochemical cell used for DLEPR experiments and detail of samples

Samples were obtained from the middle of the second weld layer of each material and experiments were performed on the “working planes” defined in Chapter 4. Samples of 2 cm x 7 mm were cut and drilled with a 3 mm bit in a region close to one end of the sample. The hole was used to fix a stainless steel wire to the sample with a bolt and a nut of the same material. Before fixing the wire, samples were ground using SiC papers to 600 grit size. This wire was placed within a 5 mm diameter glass tube, providing electrical conductivity to the sample. The arrangement was covered with epoxy resin (provided by Akapol S.A.) leaving an exposed area of ~0.4 cm^2

which was individually measured after each experiment using a digital camera and an image processing software.

The test solution used was 0.5 M H_2SO_4 + 0.01 M KSCN at room temperature (24 ±1 °C). Fresh solution was used for each sample. After filling the cell with ~300 cm^3 of solution deareation started for 75 minutes. At that time the sample was introduced into the solution and a cathodic cleaning run at -1.5 V for 60 seconds. During this time hydrogen bubbles formed on the sample surface were removed by gently shaking the sample glass tube. The open circuit potential (OCP) was then measured and allowed to stabilize for 900 seconds and after that the cyclic test started. Test parameters are summarized in Table 3-5.

Table 3-5: DLEPR test parameters

Test Solution	0.5 M H_2SO_4 + 0.01 M KSCN
Deaeration time	75 min
Cathodic cleaning	-1.5 V – 1 min.
OCP determination time	15 min.
Forward sweep / scan rate	From OCP to -0.1 V / 100 mV / min.
Reverse sweep /scan rate	From -0.1 V to OCP / 100 mV / min.

4 Microstructural Evolution of Stainless Steel Cladding Materials following Post-Weld Heat Treatment and Accelerated Ageing

4.1 Introduction

The aim of the present work is to follow the evolution of the microstructure of weld cladding materials used in reactor pressure vessels (RPV) under conditions that simulate all stages of fabrication and service conditions they can be exposed to during their operational life.

Given the variability in the microstructure of large scale structures such as those used in the current work, a procedure for identifying a region suitable for tests was developed (Section 4.2) based on the characterization of cross-section samples.

Chemical composition profiles of 347L and 309L in the as-welded condition were obtained with optical emission spectroscopy (OES) and resulting compositions were used as an input for thermodynamic prediction of phases using Thermo-Calc to evaluate the risk of sensitization. In addition to the as-welded material, samples subjected to the following thermal treatments were characterized by means of optical microscopy, SEM, EDS, EBSD and δ ferrite measurements with ferritescope. Treatments considered are:

1) *Simulated service ageing at 425°C without PWHT*

   This treatment simulates 60 years of service at 300°C in an accelerated way by ageing as-received samples for 284.4 h at 425°C, according to the Arrhenius equation described in Chapter 3. In addition, a set of samples aged

for 142.2 h at the same temperature were also tested to provide more information about the evolution of the process.

2) *PWHT – ageing 600°C up to 100 h*

   This treatment is the same as that applied to the whole pressure vessel after welding the forged rings, which are clad individually. In most RPV specifications, PWHT time at 600°C is around 40 h. In the present study PWHT time was extended up to 100 h in order to have a better understanding of the microstructural changes produced by the treatment.

3) *Further ageing for 284.4 h at 425°C of samples that had been given a PWHT for 40 h at 600°*

   This treatment represents the real conditions to which RPV clad surfaces are subjected during fabrication and service. As a first step, samples were PWHT at 600°C for 40 h representing the fabrication conditions as previously described. Later, these treated samples were subjected to accelerated ageing at 425°C for 284.4 h in order to simulate 60 years of service at 300°C.

4.2 Supply of samples and definition of the region to be studied in the present work

Weld coupons were obtained at IMPSA S.A in Mendoza, Argentina by Submerged Arc Welding (SAW) using strip electrodes and following detailed industrial specifications used for RPV claddings [160]. Material compositions and welding parameters are described in Chapter 3. As shown in Figure 4-1, the final stainless steel deposit is formed of two layers. Each layer is composed by several welding

beads in the shape of strips which are partially overlapped. The shape and size of the strips is the result of the molten strip electrode used in the SAW process.

The base material used for the deposit of both 347L and 309L was a 7 cm thick slab of SA-516 Gr-70 carbon steel. Once the deposits were finished the first and last 10 cm of the slab were discarded in order to exclude from the study the regions of the beginning and ending of the welding arc. The resulting slab was then cut into 7 mm thick slices, which became the samples for the different tests of the present study.

The use of an actual industrial process for obtaining the material used in the study implies a big variability. The sample selection sequence described in this section was designed in an attempt to address these variations.

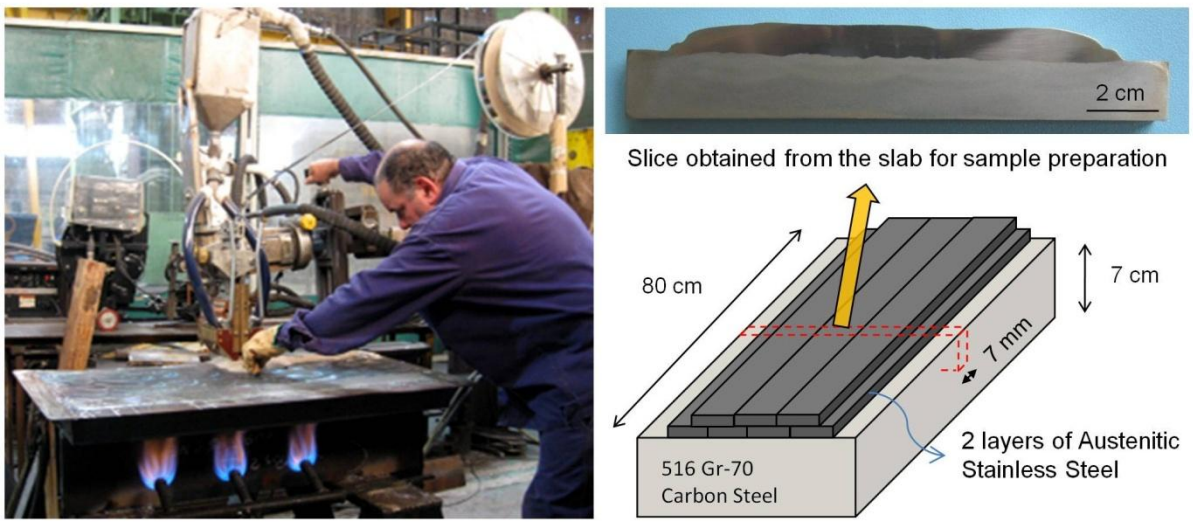

Figure 4-1: Fabrication of welding coupons by submerged arc welding showing location of the slices used for sample preparation

A general view of the slices obtained for sample preparation of 347L and 309L is shown in Figure 4-2. Two clearly defined regions are observed for both materials: the stainless steel deposit on top, and the base carbon steel material underneath. The intersection of both regions, called the “fusion line” in this study, presents an irregular serrated shape and only an average straight line can be drawn to define its position. It is worth noting that the stainless steel deposit was macroscopically uniform and free of voids and cracks. Furthermore, it was not possible to distinguish the first and second welding layer by direct visual observation.

The depth of the heat affected zone (HAZ) in the base material was found to be in the range of 5-10 mm and follows the overlapped strip shape of the stainless steel welding beads. The metallurgical transformations in the base materials are out of the scope of the present work, which is focused on the study of the stainless steel weld deposit.

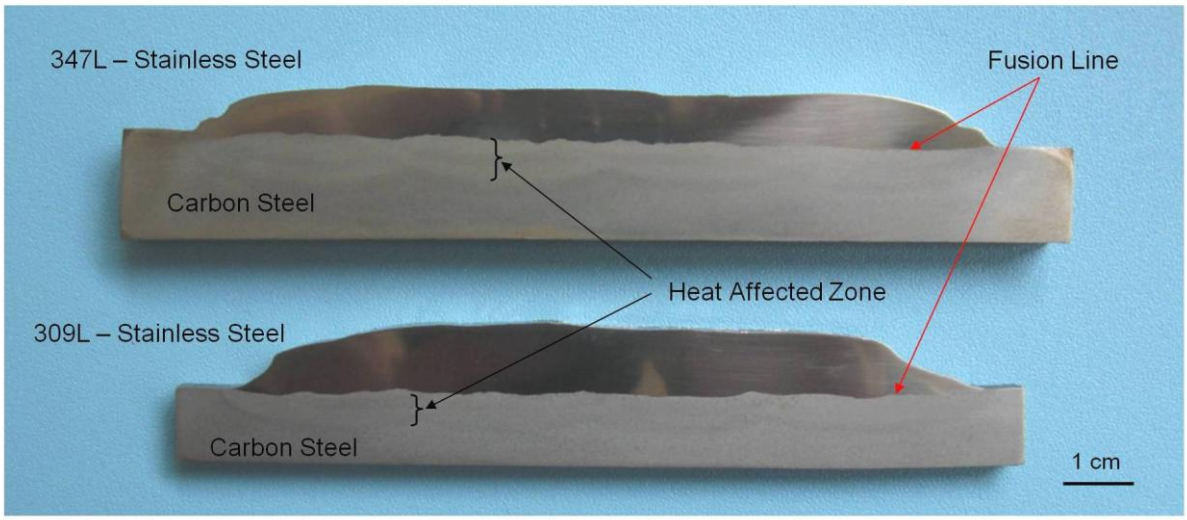

Figure 4-2: Heat affected zone (HAZ) observed in slices of 347L and 309L used for sample preparation

The microstructural analysis of the deposit from the fusion line towards the surface showed three different regions in both samples (Figure 4-3 and Figure 4-4). The fusion line itself is followed by a region where both materials are mixed since part of the carbon steel is also molten when the stainless steel is deposited. The first weld layer was found to be formed by an austenitic matrix (γ) and aligned stringers of delta ferrite (δ). The second weld layer showed the same microstructure but with more closely spaced δ ferrite stringers.

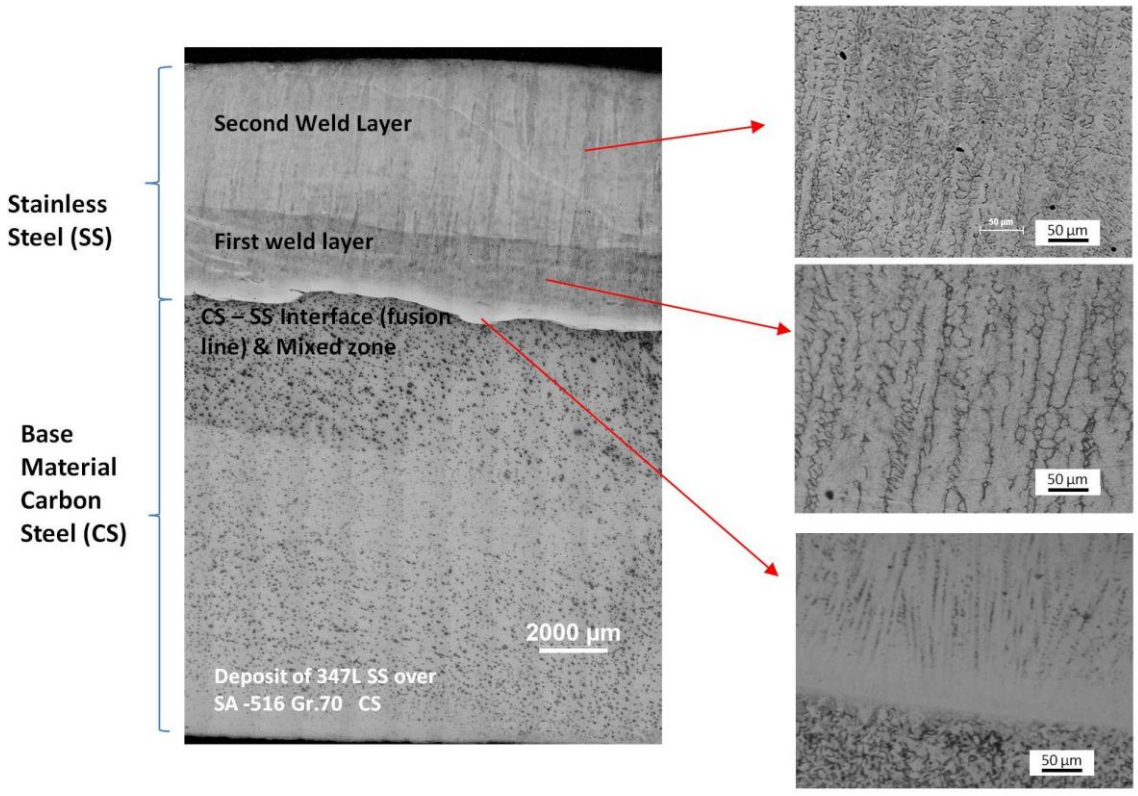

Figure 4-3: Microstructural regions identified in weld deposit of 347L stainless steel

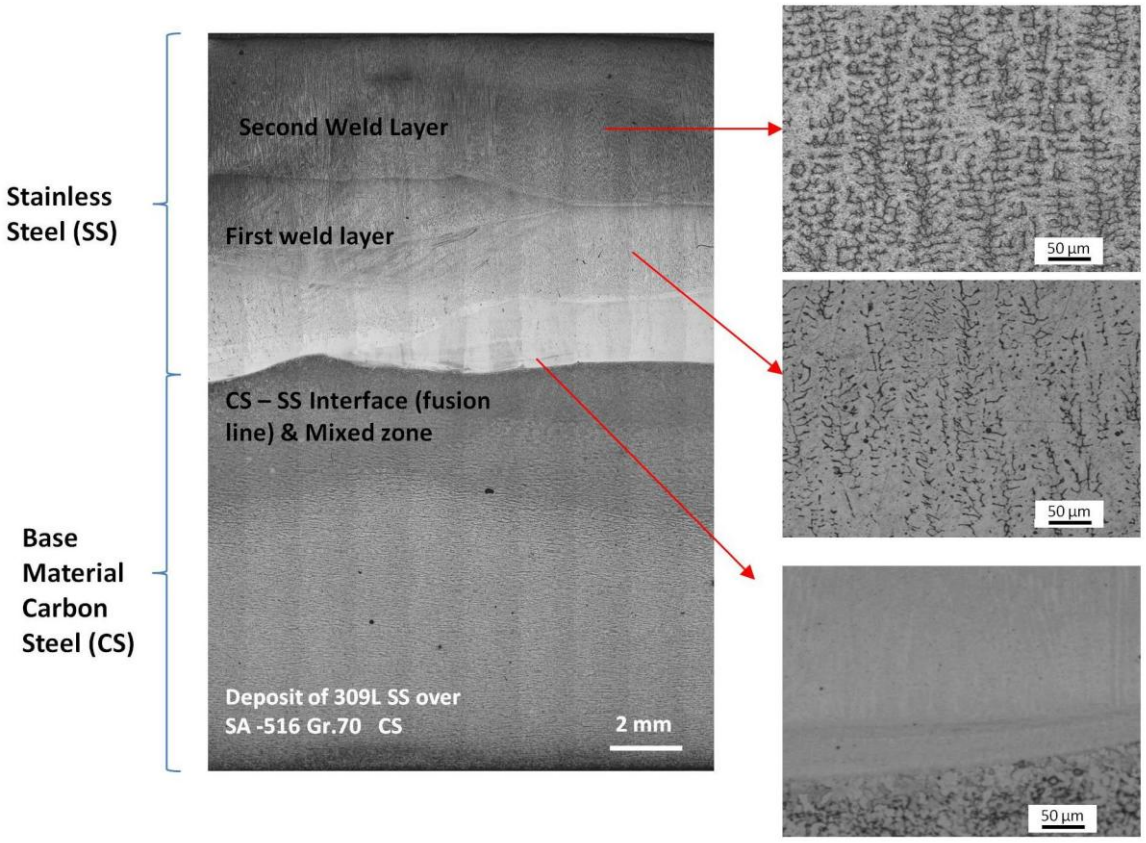

Figure 4-4: Microstructural regions identified in weld deposit of 309L stainless steel

Figure 4-5 shows a comparison of the morphology of the δ ferrite found in this characterization with the “vermicular δ ferrite” reported by David [44] for multi-pass stainless steel welds.

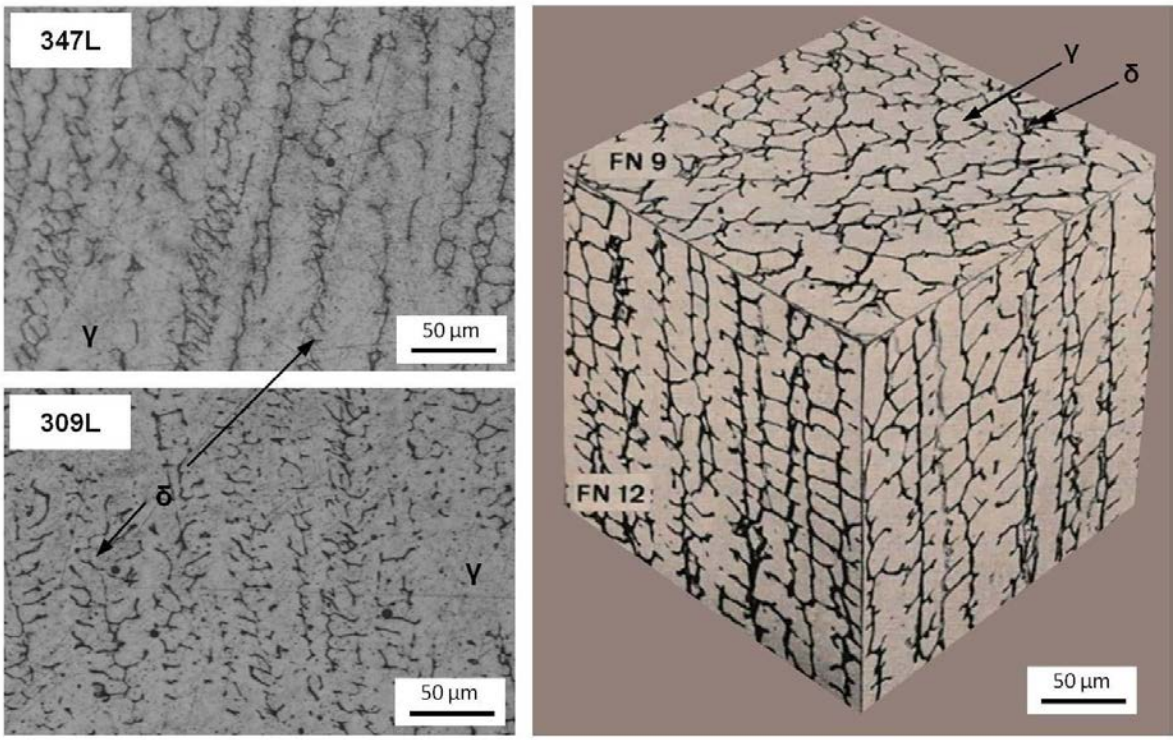

Figure 4-5: vermicular δ ferrite found in weld deposits of the present study and three-dimensional composite micrograph of this morphology in a 308L multi-pass weld [44]

Owing to the microstructural variations found from the fusion line towards the surface (Figure 4-3, Figure 4-4) it was necessary to define a region suitable for performing the microstructural, mechanical and corrosion tests required to evaluate the behaviour of the materials in the different thermal treatment conditions defined in Section 4.1. A “working plane” was defined in the middle of the second weld layer of each material (347L and 309L). These planes were used for obtaining the samples and performing all the tests of the present work. The average distance from fusion line to this plane was found to be 5.55 mm for 347L and 6.25 mm for 309L.

The identification of the working plane and the location of the samples used for microstructural characterisation and corrosion test are shown in Figure 4-6 for 347L and in Figure 4-7 for 309L.

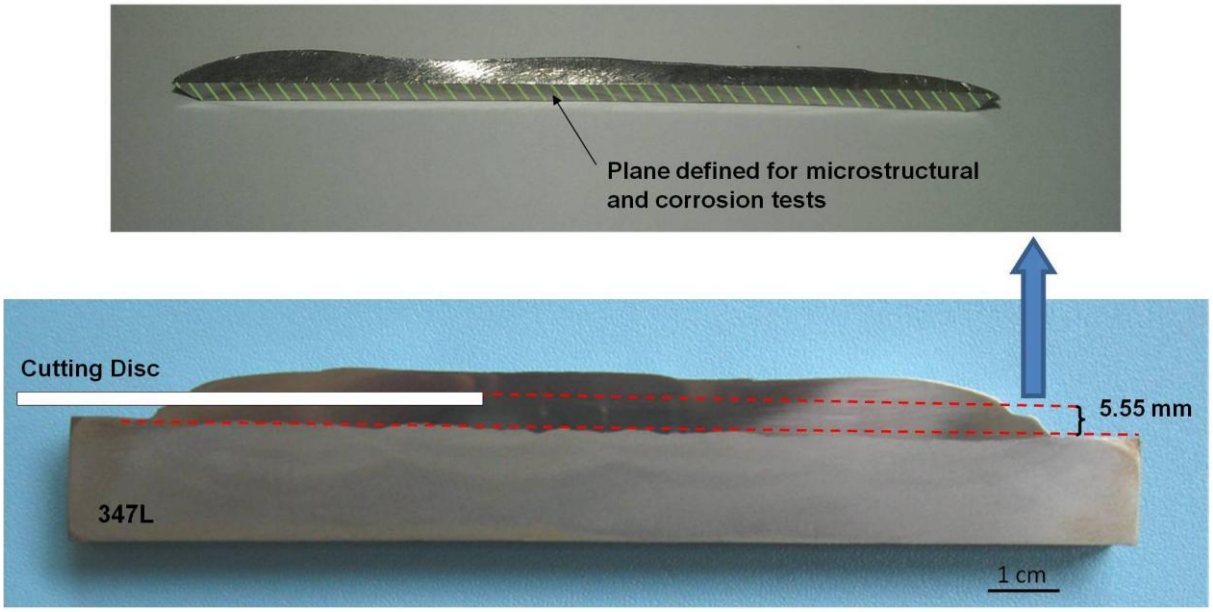

Figure 4-6: Identification of working plane and location of samples used for microstructural characterization and corrosion tests in 347L material

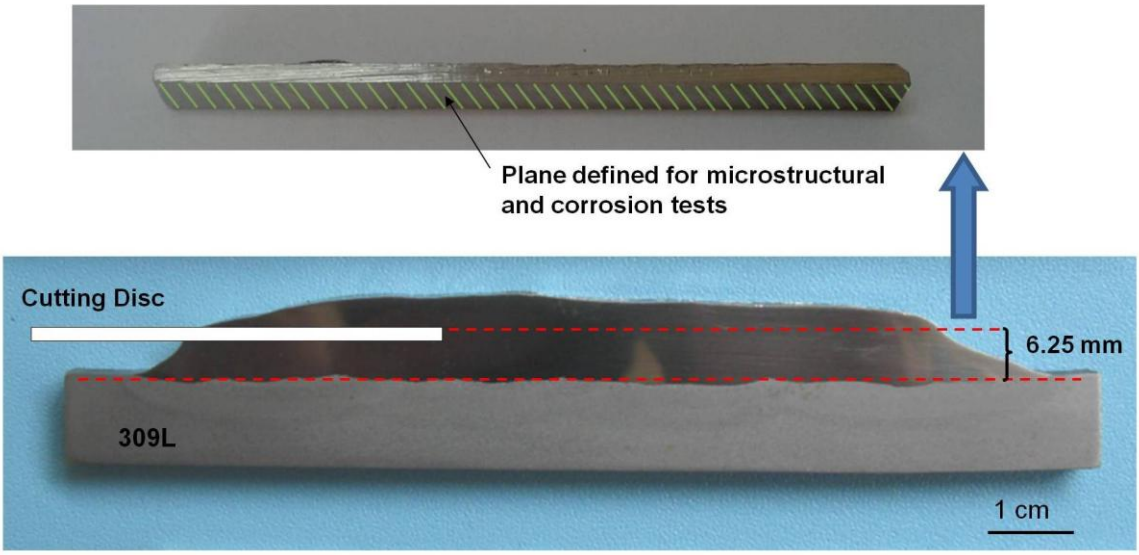

Figure 4-7: Identification of working plane and location of samples used for microstructural characterization and corrosion tests in 347L material

The same approach was used to define the region of the weld deposit used to obtain the sub-size Charpy samples used in Chapter 5. The tip of the notch of each sample was located to coincide with the plane defined for microstructural and corrosion tests, as shown in Figure 4-8 and Figure 4-9.

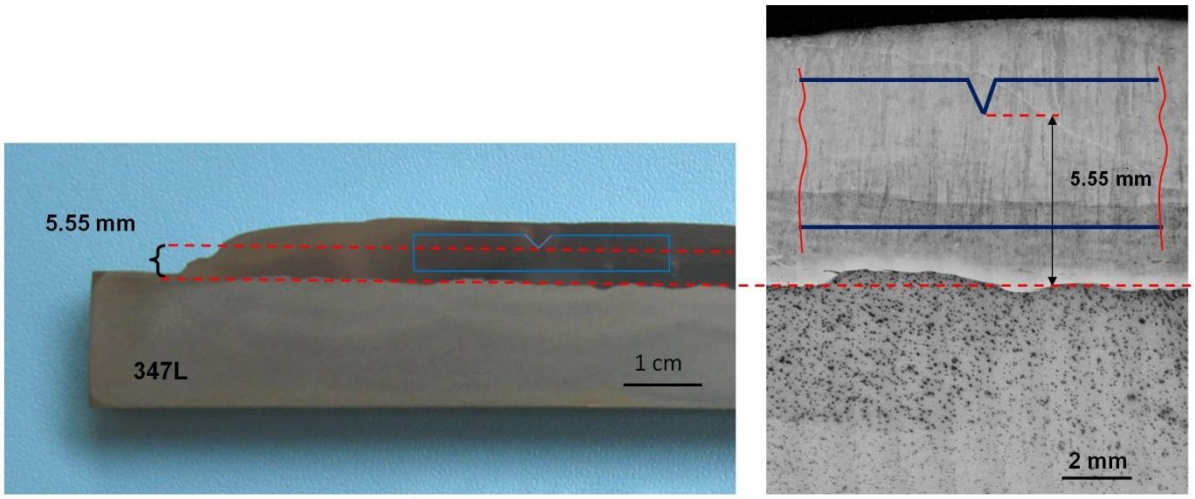

Figure 4-8: Location of Charpy samples in 347L stainless steel weld deposit

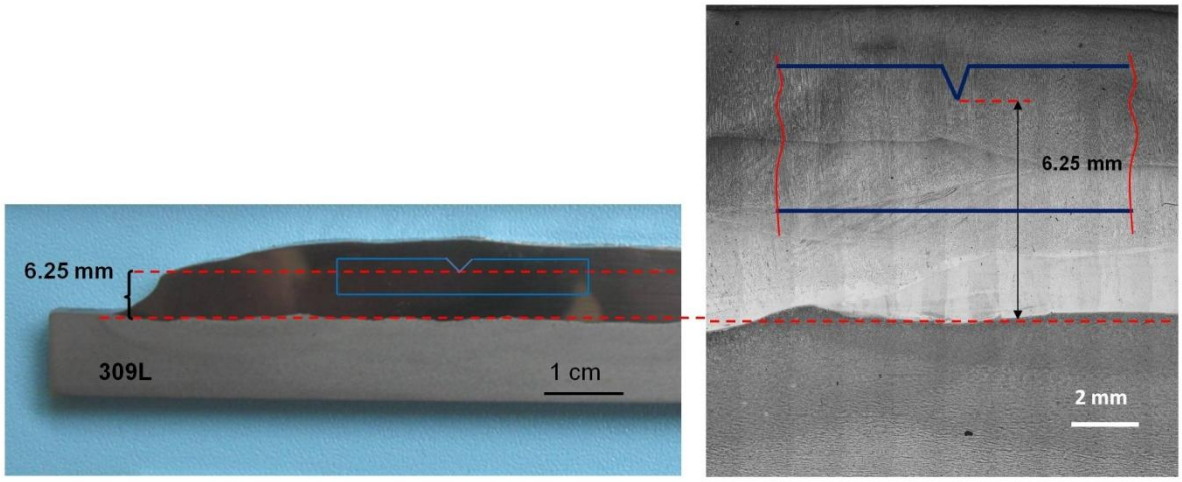

Figure 4-9: Location of Charpy samples in 309L stainless steel weld deposit

4.3 Determination of composition profiles using Optical Emission Spectroscopy (OES)

Chemical analysis with Optical Emission Spectroscopy (OES) was performed on the as-welded samples of both 347L and 309L materials. The objective of the analysis was to study not only the composition of the material, but also its uniformity along the surface; as well as across the depth.

Composition analysis at four different depths from the surface was performed and the chemical composition of the "working plane" (defined in Figure 4-6 for 347L and Figure 4-7 for 309L) was established by comparing the results of the tests immediately above and below these planes. The composition of the working planes will be taken as a reference and considered as an input for phase prediction in Section 4.4.

4.3.1 Type 347L Stainless Steel

A 9 cm x 3 cm coupon containing base material and the two weld layers of 347L SS deposit was obtained from the slab. A 1 mm layer was milled out defining "Plane A" in Figure 4-10. Ten OES spot tests evenly distributed over the surface were performed covering the whole area of the coupon obtaining local content of C, Mn, P, S, Si, Cr, Ni, Mo, Cu, Al, Ti, Nb, V, Co, and N. After that, another 1 mm layer of material was removed defining "Plane B" in Figure 4-10 and the spot measurements over the surface were repeated. The procedure was repeated twice finishing in "Plane D" at approximately 3 mm from the fusion line. Material sampled by each OES spot is between 8 and 10 mm in diameter and less than 1 mm in depth, therefore

compositions obtained for each plane are the average between that plane and the following.

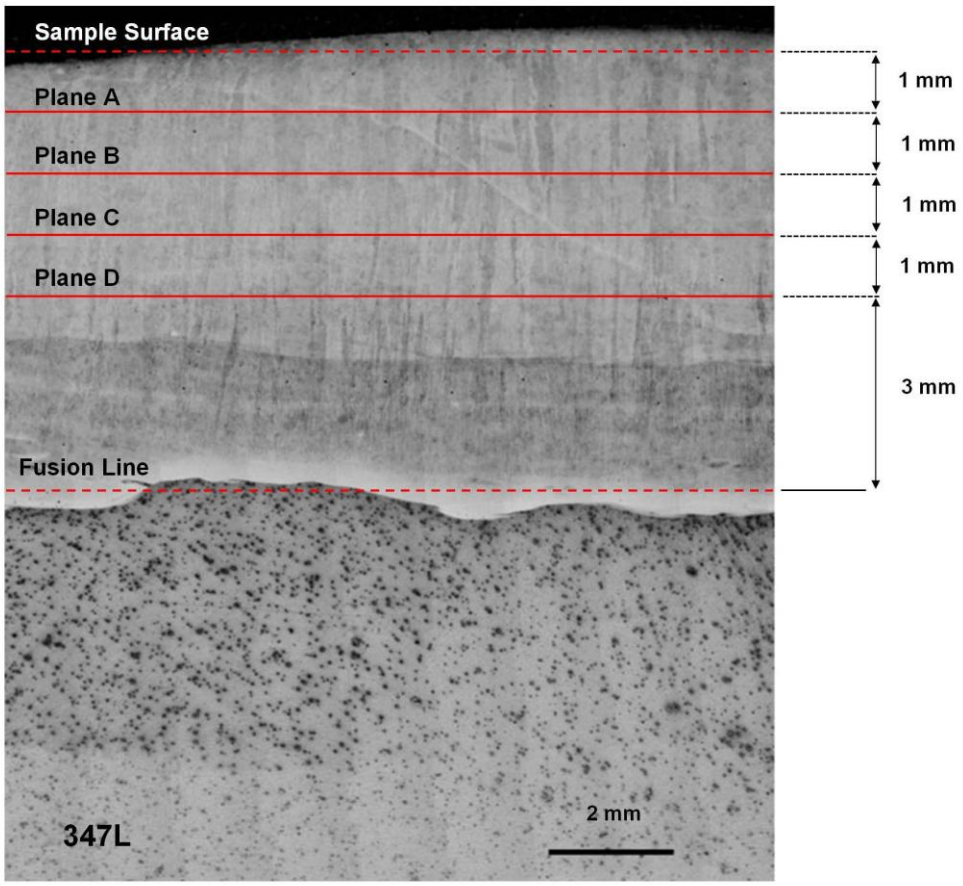

Figure 4-10: Location of surfaces used for chemical composition analysis in 347L cladding

As shown in Figure 4-6, the working plane for 347L was defined at 5.55 mm from fusion line towards the surface. This plane is in between Plane A and Plane B in Figure 4-10. The variation in composition on both sides of the working plane is shown by the compositional profiles of Fe and C (Figure 4-11) and main alloying elements (Cr, Ni, and Nb - Figure 4-12) obtained for this material.

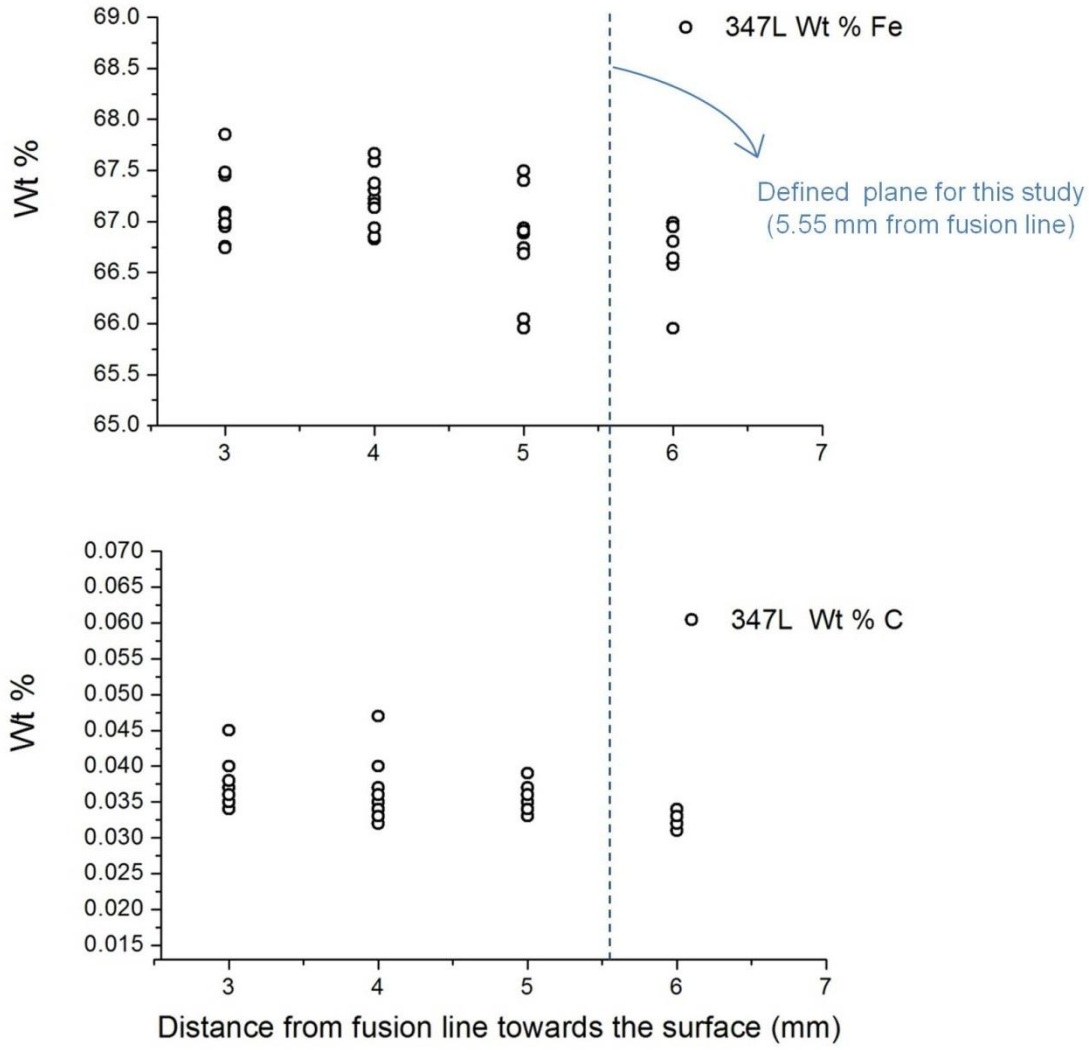

Figure 4-11: Compositional profiles of Fe and C obtained for 347L SS

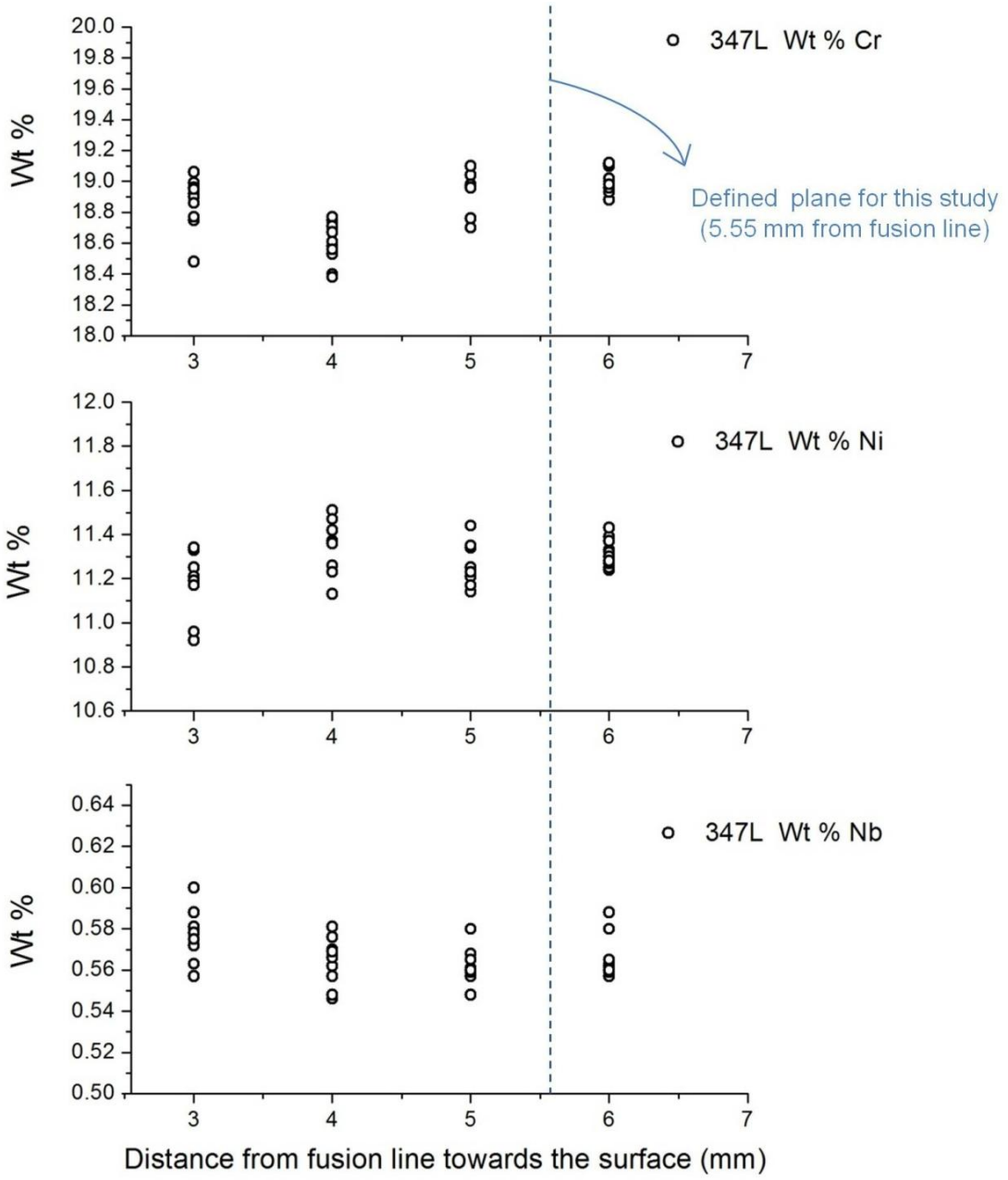

Figure 4-12: Compositional profiles of main alloying elements obtained for 347L SS

A comparison of the complete composition of Plane A and Plane B of Figure 4-10 is shown in Table 4-1. Each reported value corresponds to the mean of the ten tests performed on the plane. A small trend in C composition can be seen in Figure 4-11 across the working plane. However, taking into account the scatter and the small

change in the mean C content (0.035 in Plane B and 0.033 in Plane A) this variation is considered not relevant for the rest of the study. Finally, the composition of the working plane for 347L samples was obtained as the average of compositions in Plane A and Plane B and is reported in Table 4-2.

Table 4-1: OES compositional analysis of Type 347L weld overlay

347L (wt %)	**C**	**Mn**	**P**	**S**	**Si**	**Cr**	**Ni**	**Mo**	**Cu**	**Al**	**Ti**	**Nb**	**V**	**Co**	**N**	**Fe (Bal.)**
	1 mm from surface - Plane A															
Mean	0.033	0.973	0.017	0.006	0.941	19.11	11.32	0.051	0.109	0.004	0.012	0.566	0.032	0.033	0.023	66.78
SD	0.001	0.04	0.0003	0.0004	0.03	0.3	0.06	0.0007	0.001	0.001	0.002	0.01	0.0003	0.001	0.008	0.3
	2 mm from surface – Plane B															
Mean	0.035	0.997	0.017	0.006	0.948	19.14	11.12	0.05	0.113	0.004	0.012	0.563	0.033	0.032	0.022	66.91
SD	0.002	0.04	0.001	0.0005	0.04	0.4	0.4	0.00	0.003	0.0003	0.001	0.01	0.001	0.001	0.003	0.6

Table 4-2: Chemical composition of Type 347L weld overlay at the working plane estimated from measurements of Table 4-1

347L (wt %)	**C**	**Mn**	**P**	**S**	**Si**	**Cr**	**Ni**	**Mo**	**Cu**	**Al**	**Ti**	**Nb**	**V**	**Co**	**N**	**Fe (Bal.)**
	Working Plane – 5.55 mm from fusion line															
	0.034	0.985	0.017	0.006	0.945	19.13	11.22	0.051	0.111	0.004	0.012	0.565	0.033	0.033	0.023	66.83

4.3.2 Type 309L Stainless Steel

The same procedure as that described in Section 4.3.1 for 347L was used to obtain the composition profiles of 309L. Since a thicker deposit was obtained for this material, the planes where the OES tests were performed are located in different positions, as shown in Figure 4-13.

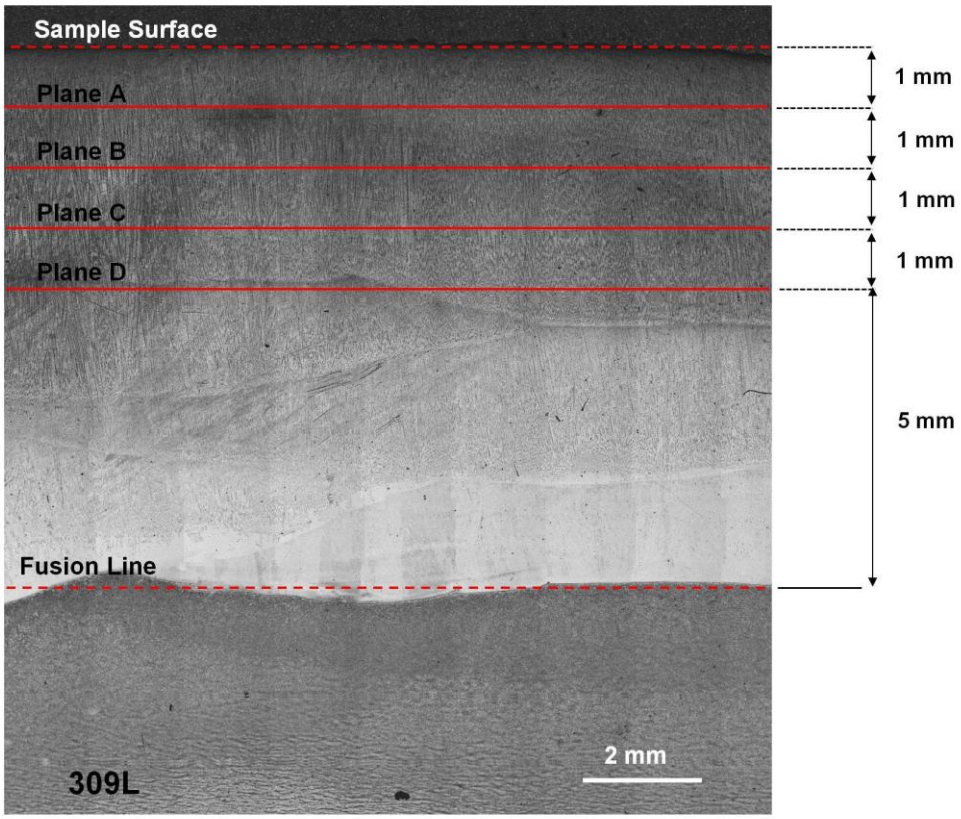

Figure 4-13: Location of surfaces used for chemical composition analysis in 309L cladding

The working plane defined for 309L was defined at 6.25 mm from the fusion line (Figure 4-7). This position is located between planes B and C in Figure 4-13. The variation in composition on both sides of the working plane is shown by the

compositional profiles of Fe and C (Figure 4-14) and main alloying elements (Cr and Ni - Figure 4-15) obtained for the material.

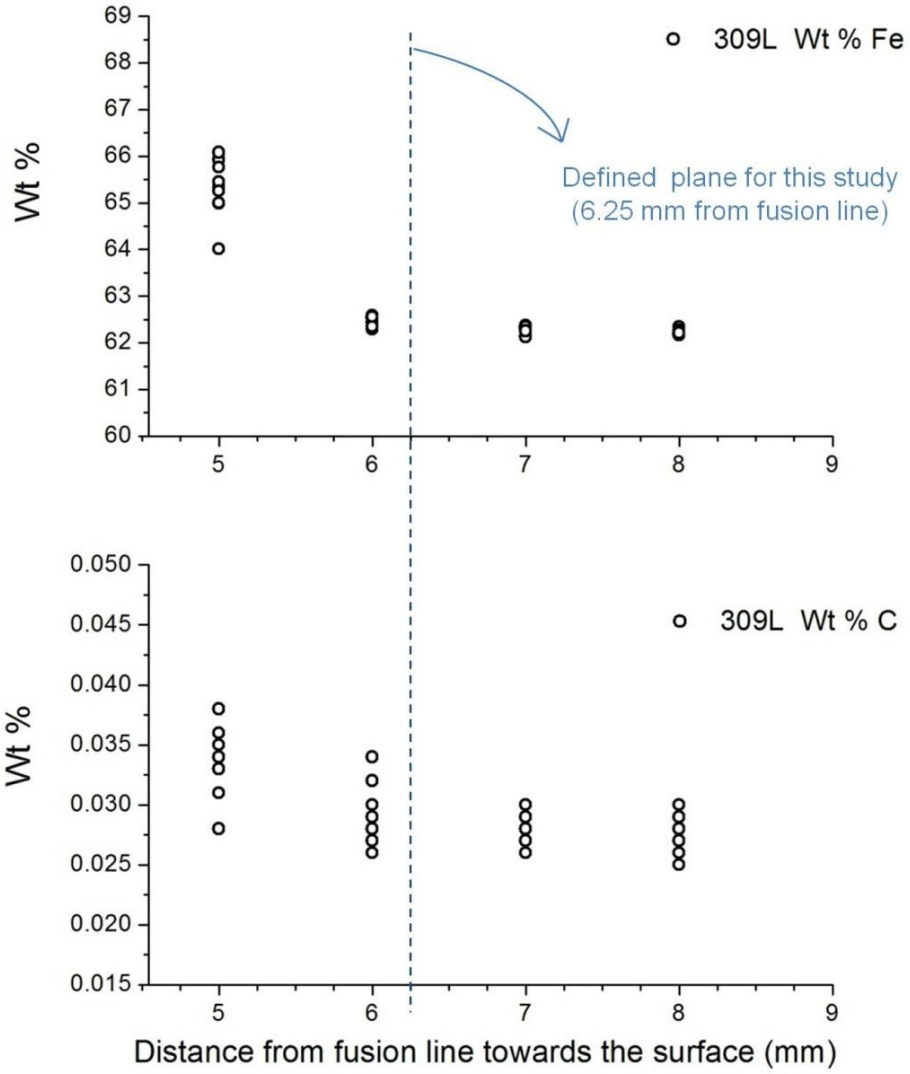

Figure 4-14: Compositional profiles of Fe and C obtained for 309L SS

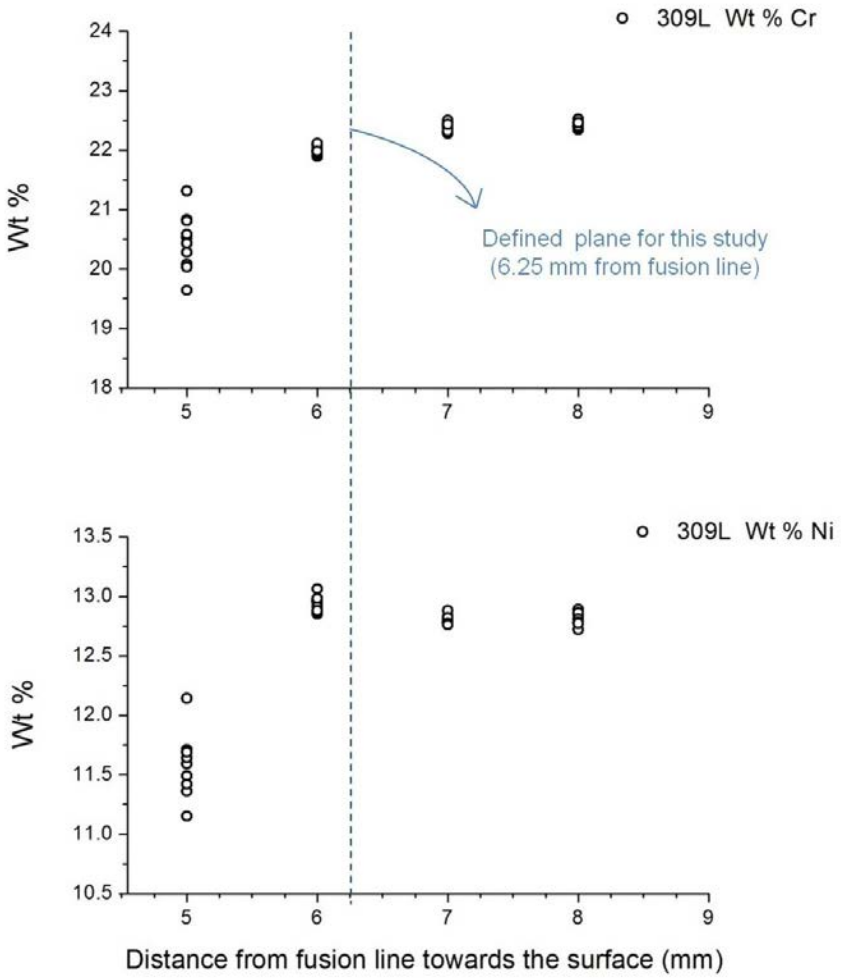

Figure 4-15: Compositional profiles of main alloying elements obtained for 309L SS

A comparison of the complete composition of Plane B and Plane C in Figure 4-13 is shown in Table 4-3. Each reported value corresponds to the mean of the ten tests performed on the plane. A small trend in Cr and Ni composition can be seen in Figure 4-15 across the working plane. However, taking into account the scatter and the small change in the mean values (22.00 Cr, 12.93 Ni in Plane C and 22.37 Cr, 12.80 Ni in Plane B) this variation is considered not relevant for the rest of the study. Finally, the composition of the working plane for 309L samples was obtained as the average of compositions in Plane A and Plane B and is reported in Table 4-4

Table 4-3: OES compositional analysis of Type 309L weld overlay

309L (wt %)	**C**	**Mn**	**P**	**S**	**Si**	**Cr**	**Ni**	**Mo**	**Cu**	**Al**	**Ti**	**Nb**	**V**	**Co**	**N**	**Fe (Bal.)**
	2 mm from surface - Plane B															
Mean	0.028	1.070	0.018	0.002	1.040	22.37	12.80	0.060	0.120	0.005	0.009	0.030	0.100	0.050	0.028	62.28
SD	0.002	0.03	0.0006	0.000	0.02	0.07	0.04	0.000	0.00	0.000	0.000	0.000	0.000	0.000	0.0008	0.08
	3 mm from surface – Plane C															
Mean	0.029	1.070	0.018	0.002	1.040	22.00	12.93	0.060	0.130	0.004	0.010	0.030	0.100	0.050	0.028	62.50
SD	0.003	0.02	0.0005	0.000	0.02	0.07	0.07	0.000	0.00	0.000	0.000	0.000	0.00	0.00	0.001	0.1

Table 4-4: Chemical composition of Type 309L weld overlay at the working plane estimated from measurements of Table 4-3

309L (wt %)	**C**	**Mn**	**P**	**S**	**Si**	**Cr**	**Ni**	**Mo**	**Cu**	**Al**	**Ti**	**Nb**	**V**	**Co**	**N**	**Fe (Bal.)**
	Working Plane – 6.25 mm from fusion line															
	0.029	1.070	0.018	0.002	1.040	22.19	12.87	0.060	0.125	0.005	0.010	0.030	0.100	0.050	0.028	62.39

4.4 Phase prediction using Thermo-Calc and analytical modelling of sensitization during PWHT

4.4.1 Thermo-Calc results using compositions obtained at the working plane

Thermodynamic equilibrium phases were obtained using Thermo-Calc 4.0 with TC-Fe7 database. Given the heterogeneous structure of the multi-pass weld overlay used in cladding fabrication, compositions of the "working planes" determined in Section 4.3. were used in the simulation in order to predict equilibrium phases expected in these planes for both 347L and 309L materials and keep consistency with the study of mechanical and corrosion properties performed along the present work.

Thermo-Calc predicted phases are those that minimize the free energy of the system in the thermodynamic equilibrium state. Although thermodynamic equilibrium is not expected due to the dynamic processes involved in pressure vessel fabrication, results obtained could be used to highlight the phases that are expected to be found in the system.

347L Stainless Steel

Analyzing the predicted phase diagrams obtained for 347L (Figure 4-16 and Figure 4-17), it is possible to see that sigma phase (σ) starts to be stable below 800°C. From the thermodynamic standpoint, apart from sigma and the austenite matrix (γ), all other phases are at a very low level and only the high temperature FCC phases (TiN - NbC) and MnS are likely to be seen below this temperature. A summary of the predicted phases at 1000°C and 600°C is shown in Table 4-5.

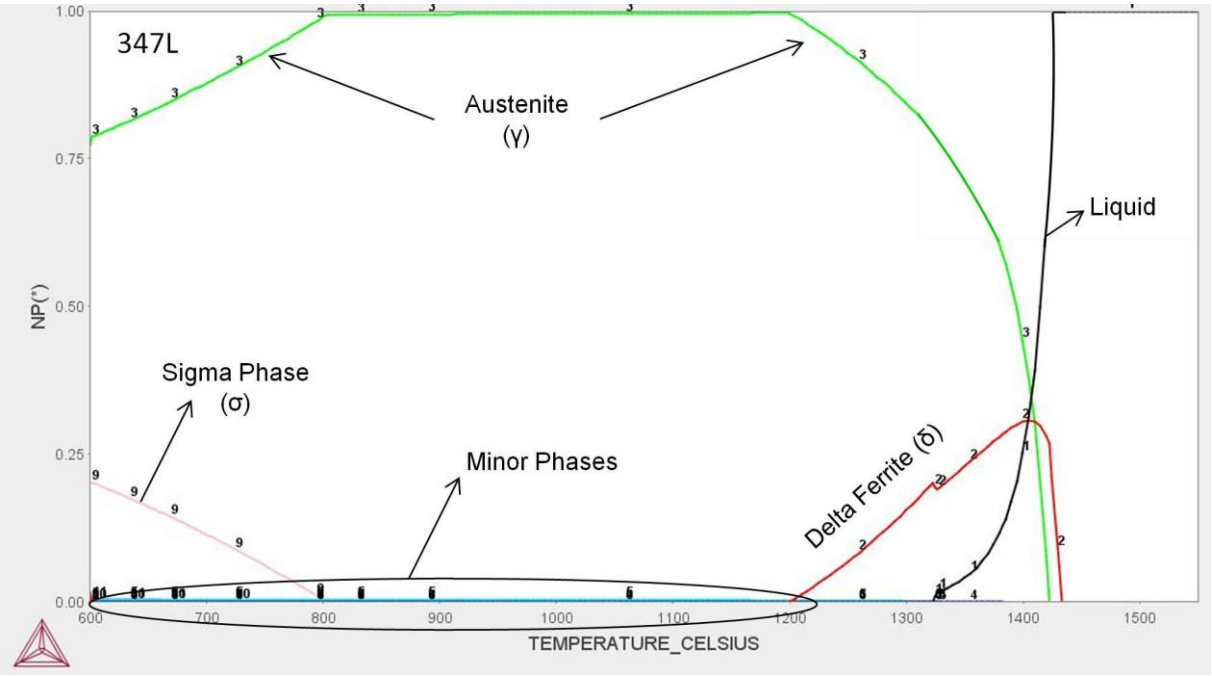

Figure 4-16: Phase diagram of 347L obtained using Thermo-Calc 4.0 with TC-Fe7 database

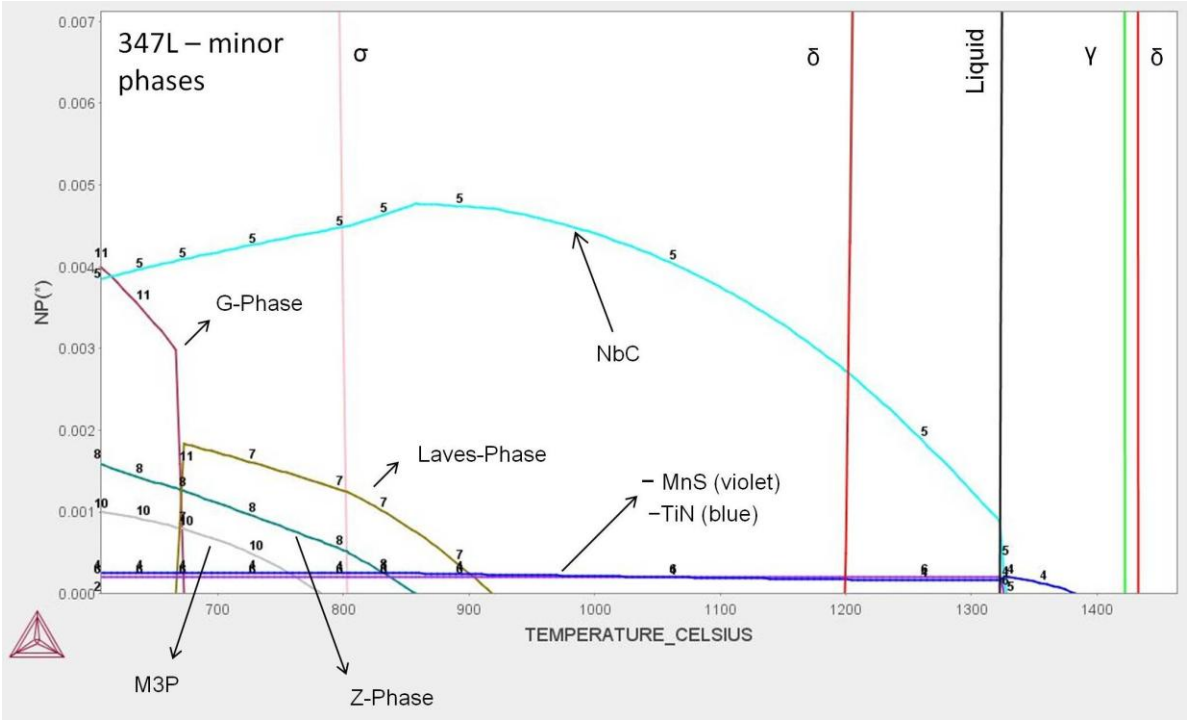

Figure 4-17: Detail of minor phases in 347L obtained using Thermo-Calc 4.0 with TC-Fe7 database

Table 4-5: Phase distribution of Type 347L weld overlay predicted by Thermo-Calc 4.0

347L (Mol %)	***Predicted Phases using Thermo-Calc***						
	Austenite (γ)	Delta Ferrite (δ)	Sigma (σ)	NbC	G-Phase	MnS	TiN
1000 °C	99.49	-	-	0.468	-	0.021	0.023
600 °C	78.16	0.463	20.49	0.547	0.318	0.021	-

309L Stainless Steel

The analysis of the predicted phase diagrams obtained for 309L stainless steel (Figure 4-18, Figure 4-19) showed that sigma phase starts to be stable below 800°C. From the thermodynamic standpoint, apart from sigma and the austenite matrix, all other phases are at a very low level and only $M_{23}C_6$, TiN and MnS are likely to be seen below this temperature. A summary of the predicted phases in 309L at 1000°C and 600°C is shown in Table 4-6.

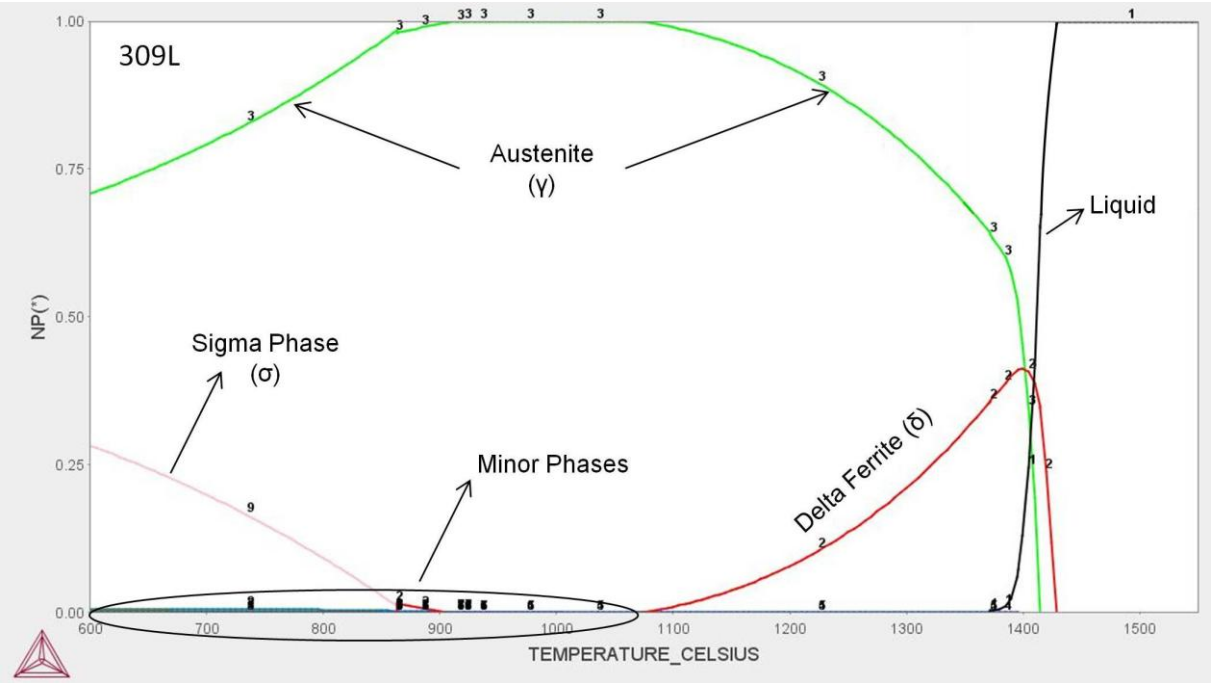

Figure 4-18: Phase diagram of 309L obtained used Thermo-Calc 4.0 with TC-Fe7 database

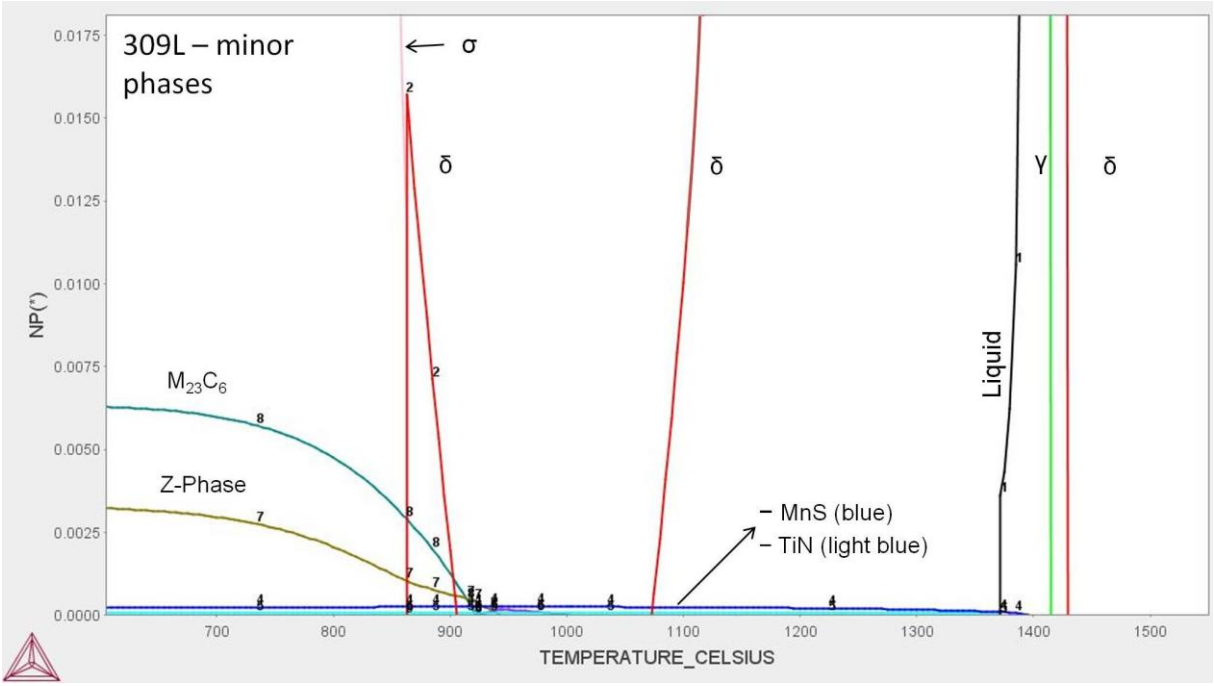

Figure 4-19: Detail of minor phases in 309L obtained using Thermo-Calc 4.0 with TC-Fe7 database

Table 4-6: Predicted phase distribution of Type 309L weld overlay

309L (Mol %)	***Predicted Phases using Thermo-Calc***						
	Austenite (γ)	Sigma phase (σ)	$M_{23}C_6$	Z-phase	MnS	TiN	NbC
1000 °C	99.97				0.068	0.026	0.011
600 °C	70.79	28.23	0.629	0.324	0.068	0.023	-

4.4.2 Analytical modelling of sensitization during PWHT at 600°C

In the following section a theoretical analysis of the sensitization process expected during PWHT at 600°C is performed based on the Strawstrom and Hillert model [63].

Sensitization of stainless steel involves the precipitation of $M_{23}C_6$ carbides and the consequent formation of a chromium-depleted zone (CDZ) around carbides where the local content of Cr is low enough to lose the protective features of the oxide layer, leaving the material prone to suffer localized attack in this area. The associated lower limit of Cr concentration in solid solution is generally accepted to be 13%. According to Strawstrom and Hillert [63], the depleted zone where Cr concentration is less than 13% can be calculated according to Equation 4-1

$$m = 2\sqrt{D_{Cr}^{\gamma} t}\left(\frac{0.13 - \chi_{Cr}^{i}}{\chi_{Cr}^{o} - \chi_{Cr}^{i}}\right)$$

Equation 4-1

Where:

m: = distance from the carbide precipitate towards the matrix where the Cr content is lower than 13% (mole fraction lower than 0.13). There is not agreement on the value of m required for sensitization. Values reported range from 20 to 300 nm [163]

χ_{Cr}^{o} = mole fraction of Cr in the bulk alloy

χ_{Cr}^{i} = mole fraction of Cr at the interface austenite – carbide (temperature and composition dependent)

D_{Cr}^{γ} = diffusion coefficient of Cr in austenite.

Following Tedmon's approach [68], chromium concentration in the interface (χ_{Cr}^{i}) can be estimated considering the following assumptions:

a) The carbide being formed is $Cr_{23}C_6$ and the effects of partial substitution of Cr by Fe and or Ni are disregarded.
b) Thermodynamic equilibrium exists at the matrix-carbide interphase
c) Due to its high mobility, the gradient of carbon activity is zero and its content at the matrix-carbide Interphase does not differ from that of the bulk.

The precipitation reaction can be expressed as:

$$23\,Cr + 6\,C \;<\equiv>\; Cr_{23}C_6$$

Equation 4-2

The equilibrium constant K for this reaction is given by:

$$K = \frac{1}{(\gamma_{Cr}\,\chi_{Cr})^{23}\,(\gamma_C\,\chi_C)^6}$$

Equation 4-3

Where:

γ_{Cr}: Activity coefficient of Cr

χ_{Cr}: Molar fraction of Cr

γ_C: Activity coefficient of C

χ_C: Molar fraction of C

Considering the previously described assumption for carbon, a single activity of C (a_C) can be defined as a function of alloy carbon content:

$$a_C = (\gamma_C \chi_C)$$

Equation 4-4

Then, Equation 4-5 can be derived from Equation 4-3 and Equation 4-4.

$$\chi_{Cr}^{i} = \frac{1}{K^{1/23} \gamma_{Cr} (a_C)^{6/23}}$$

Equation 4-5

Devine [69] used for this analysis the equilibrium constant K taken from Richardson [164] K(600°C) = 5.24 x 10^{26} however, there is a big spread of values and calculation methodologies for $\gamma_{Cr,}\gamma_C$ and a_C reported in the open literature. No specific values were found either for 347L or for 309L SS. Table 4-7 summarizes χ_{Cr}^{i} values reported by Devine [69] for a 308 SS with Cr and Ni contents similar to the materials of the present work (20.95 % Cr and 9.82 % Ni) using different formulations when the carbon of the matrix is 0.032 %.

Table 4-7:Reported values in literature for a_C, γ_{Cr}, and χ^i_{Cr} [69]

	According to Tedmon et al.	a_C: according to Natesan and Kassner γ_{Cr}: calculated by Fullman according to Kaufman and Nesor	a_C: according to Natesan and Kassner γ_{Cr}: calculated by Fullman according to Hasebe and Nishizawa
a_C	0.00076	0.00194	0.00194
γ_{Cr}	3.77	4.85	4.09
$\boldsymbol{\chi^i_{Cr}}$	0.109	0.073	0.086

Once χ^{i}_{Cr} is estimated, Equation 4-6 can be obtained from Equation 4-1 and used to calculate the time at 600°C required to reach a Cr-depleted zone around carbides of 20 nm for 347L and 309L, considering the initial molar fraction of Cr in each alloy.

$$t = \frac{m^2}{4\, D^{\gamma}_{Cr}} \left(\frac{\chi^{o}_{Cr} - \chi^{i}_{Cr}}{0.13 - \chi^{i}_{Cr}} \right)^2$$

Equation 4-6

Where:

D^{γ}_{Cr} = 0.08 exp (-244.764 kJ mol^{-1} / RT) cm^2 S^{-1} [69]

m = 20 nm

These calculated times will be the expected time to sensitization according to Strawstrom and Hillert [63]. Resulting values using chemical compositions obtained in Section 4.3 are reported in Table 4-8.

Table 4-8: Calculated time at 600°C to reach a 20 nm CDZ around carbides for 347L and 309L according to Strawstrom & Hillert model [63] using data from different calculation methodologies [69]

Time to sensitization	According to Tedmon et al.	a_C: according to Natesan and Kassner γ_{Cr}: calculated by Fullman according to Kaufman and Nesor	a_C: according to Natesan and Kassner γ_{Cr}: calculated by Fullman according to Hasebe and Nishizawa
347L	30.01 h	7.85 h	10.64 h
309L	53.65 h	12.11 h	17.18 h

4.5 Measurement of delta ferrite using ferritescope

In the following section the evolution of the δ ferrite content in 347L and 309L samples subjected to the different thermal treatment conditions of the present study is followed using a ferritescope. As described in Chapter 3, this instrument provides a direct measurement of the ferrite content in duplex stainless steels based on the different magnetic behaviour of the γ and δ phases.

4.5.1 Type 347L Stainless Steel

Simulated Service Ageing at 425°C without PWHT

Figure 4-20 shows the evolution of the δ ferrite content in 347L during ageing at 425°C. The average content of ferrite in the as-welded condition was 6.6 % and appears to show a slight increase after 142.2 h and then a slight decrease after 284.4 h, but the scatter observed suggests that there are no significant variations of δ ferrite content with ageing time at 425°C.

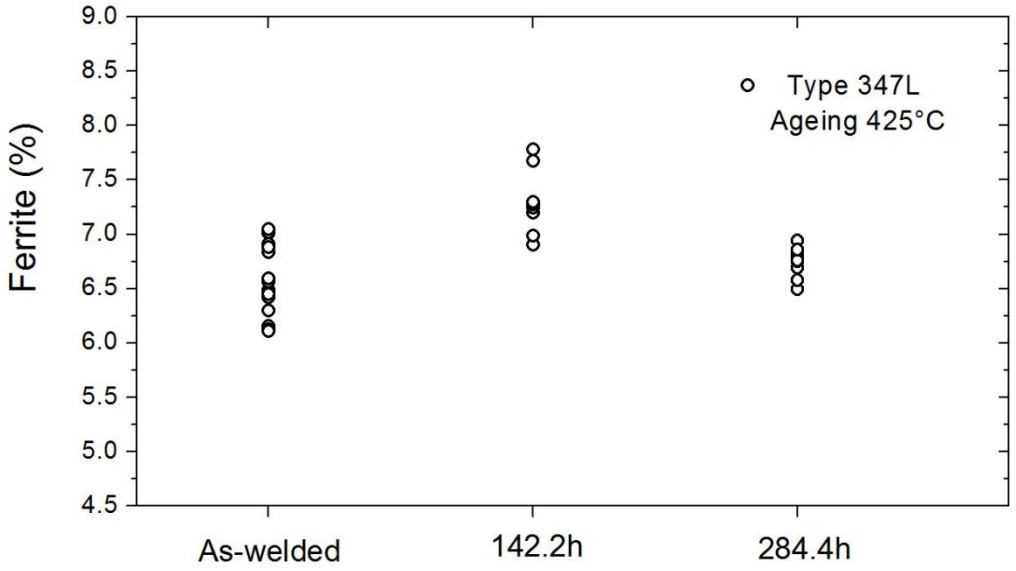

Figure 4-20: Content of δ ferrite in 347L samples in the as-welded condition and after accelerated laboratory ageing at 425°C

PWHT – Ageing 600°C up to 100 h

A clear reduction of δ ferrite content as a function of treatment time was observed when 347L samples were subjected to PWHT at 600°C for up to 100 h (Figure 4-21). The reduction was found to be more pronounced at the beginning of the treatment, tending to reach a plateau for the later stages. However, equilibrium at 600°C is not expected after only 100 h of treatment and longer ageing times are considered for future work.

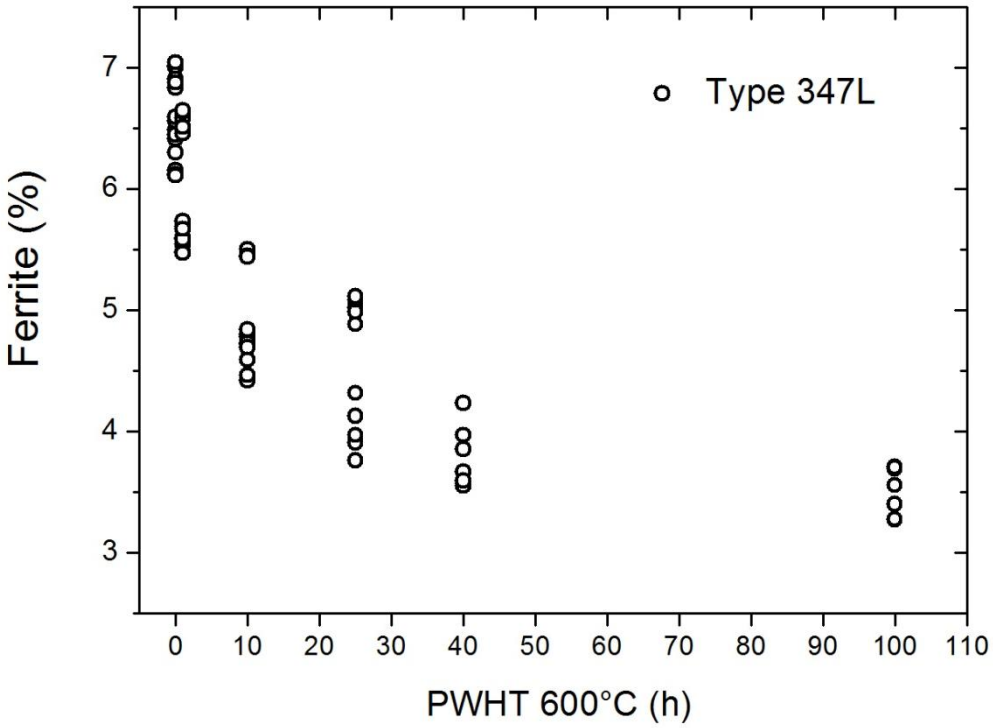

Figure 4-21: Content of δ ferrite in 347L samples given PWHT at 600°C for 1 h, 10 h, 25 h, 40 h, and 100 h

Effect of accelerated laboratory ageing following PWHT

Figure 4-22 shows a comparison of the δ ferrite content measured in as-welded samples, after PWHT at 600°C for 40 h, and after subjecting to ageing at 425°C samples that had been given the PWHT at 600°C for 40 h. No changes were observed when PWHT samples were further aged at 425°C.

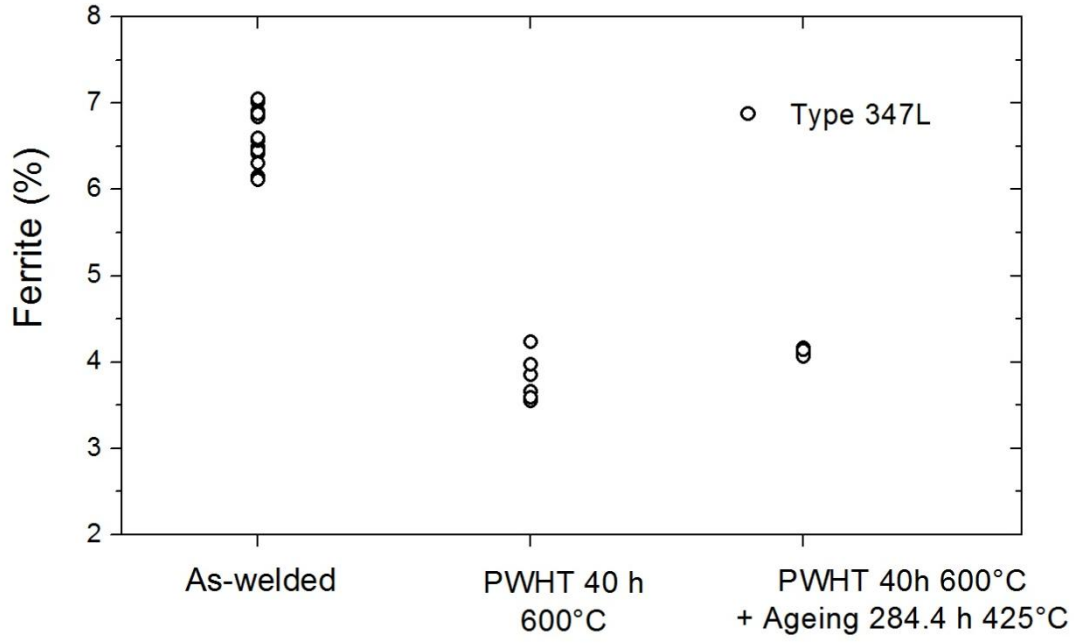

Figure 4-22: Content of δ ferrite in 347L in the as-welded condition, after PWHT at 600°C for 40 h, and after the same PWHT followed by accelerated laboratory ageing at 425°C for 284.4 h

4.5.2 Type 309L Stainless Steel

Simulated Service Ageing at 425°C without PWHT

Figure 4-23 shows the evolution of the δ ferrite content in 309L samples during ageing at 425°C. The average content of ferrite in the as-welded condition was 9.6% and appears to show a slight decrease with ageing time. However, taking into account the scatter of the measurements the average reduction of 1% ferrite after 284.4 h cannot be considered significant. This would suggest a lack of a clear variation of δ ferrite content with ageing time at 425°C for this material.

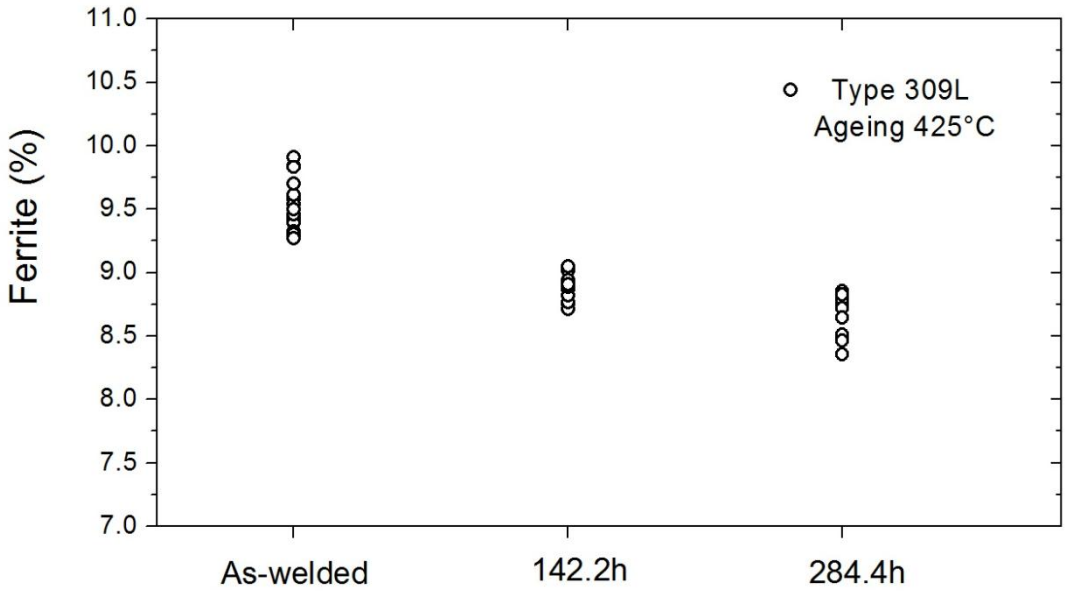

Figure 4-23: Content of δ ferrite in 309L samples in the as-welded condition and after accelerated laboratory ageing at 425°C

PWHT – Ageing 600°C up to 100 h

Similarly to what was observed for 347L, a clear reduction of δ ferrite content as a function of treatment time was observed when 309L samples were subjected to a PWHT at 600°C for up to 100 h. Once again, a more noticeable reduction was observed in the first stages of the treatment and it appears to not have reached equilibrium after 100 h. Longer treatments are considered for future work.

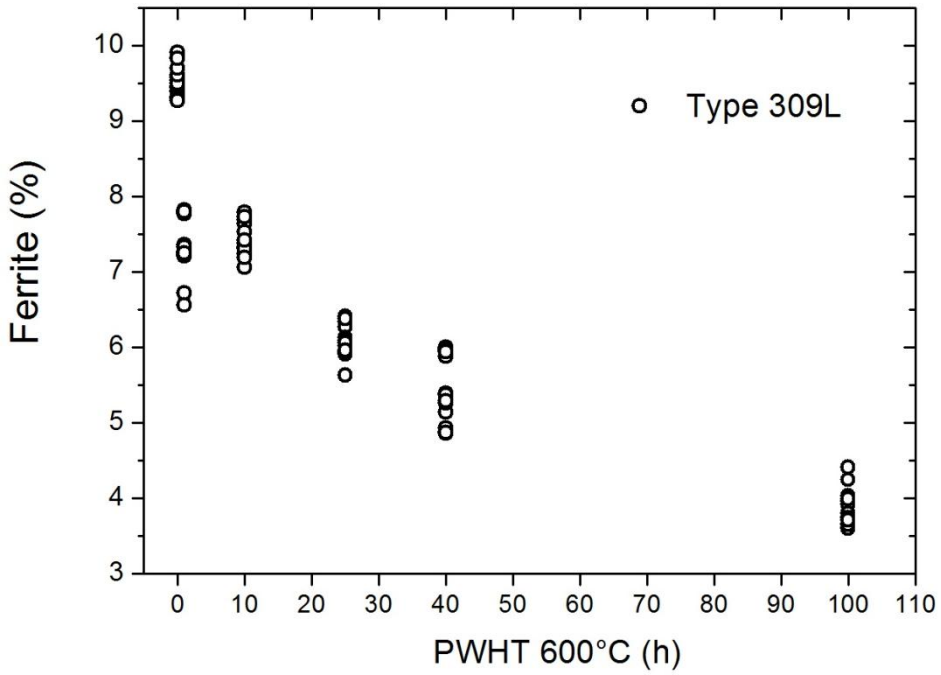

Figure 4-24: Content of δ ferrite in 309L samples given PWHT at 600°C for 1 h, 10 h, 25 h, 40 h, and 100 h

Effect of accelerated laboratory ageing following PWHT

Similar behaviour to that shown by 347L SS (Figure 4-22) was observed for 309L samples when the δ ferrite content of the material in the as-welded condition was compared to that of the PWHT samples after 40 h of treatment at 600 °C and after further ageing these samples at 425°C for 284.4 h. No changes were observed when PWHT samples were further aged at 425°C.

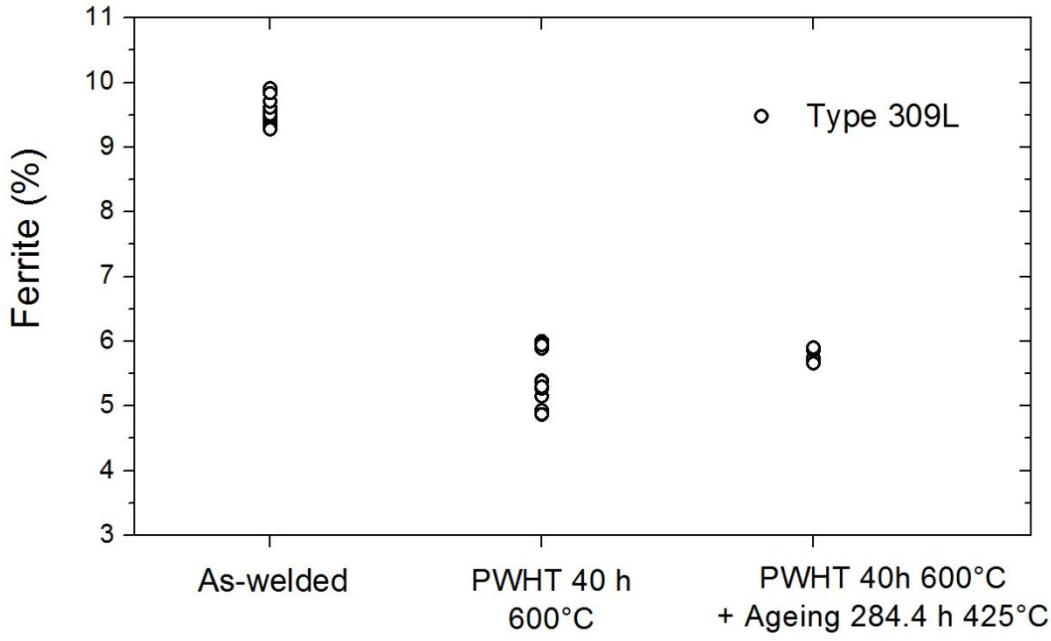

Figure 4-25: Content of δ ferrite in 309L in the as-welded condition after PWHT at 600°C for 40 h, and after the same PWHT followed by accelerated laboratory ageing at 425°C for 284.4 h

4.6 Microstructural analysis

In the following sections, the microstructure of the weld deposits is studied by means of optical and electron microscopy. Murakami´s reagent was used for identifying δ ferrite derived phases observed in the different thermal treatment conditions. In addition, SEM in electron backscatter mode was used to identify phases based on the different atomic number of their constitutive elements.

4.6.1 Type 347L SS

As-welded

Figure 4-26 shows the microstructure of 347L samples in the as-welded condition. A duplex microstructure formed by delta ferrite on an austenitic matrix was observed. This microstructure can be interpreted as a cross section at 5.55 mm from the fusion line (plane defined for 347L in Section 4.2) of the ferrite dendrites observed in Figure 4-3.

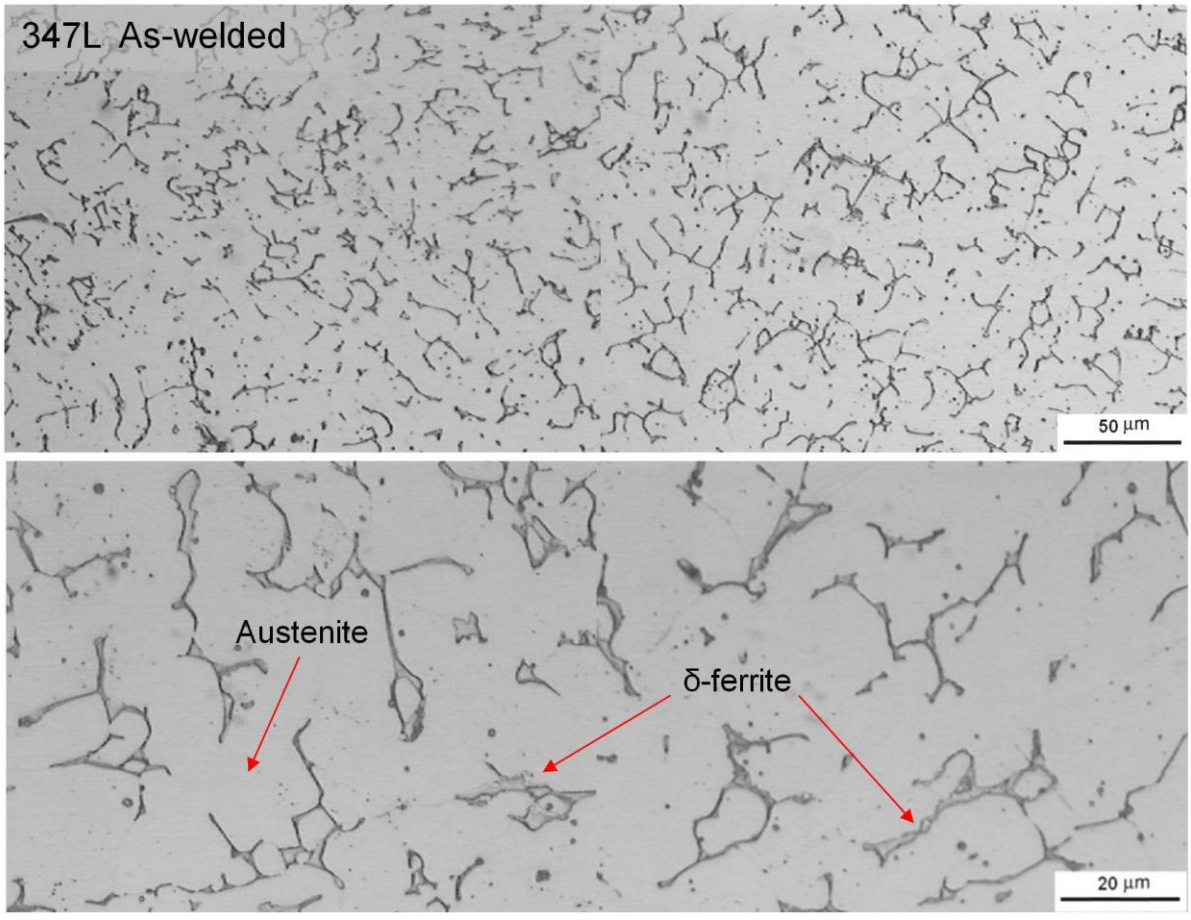

Figure 4-26: Duplex microstructure of 347L in the as-welded condition

In addition to the main phases (γ and δ), niobium-containing precipitates and spherical particles from welding process were identified using EDS and SEM in backscatter mode (Figure 4-27) analysis was performed using non-etched samples in order to avoid removal of particles or precipitates during etching.

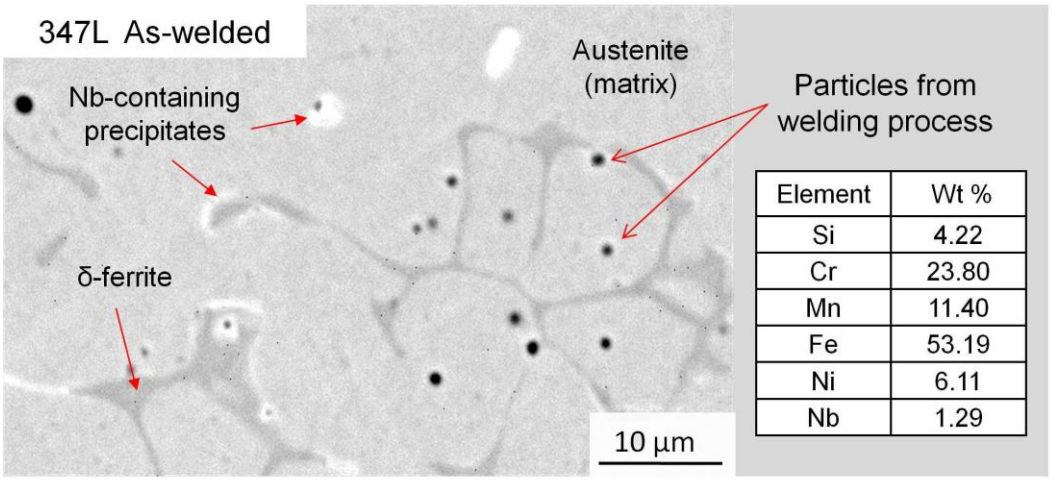

Element	Wt %
Si	4.22
Cr	23.80
Mn	11.40
Fe	53.19
Ni	6.11
Nb	1.29

Element	Austenitic Matrix	Delta ferrite Islands	Nb-containing precipitates
Si	1.08	1.24	1.23
Nb	0.64	0.58	14.81
Cr	18.92	23.13	19.02
Fe	67.54	66.2	54.91
Ni	11.82	8.85	10.03
Cr/Ni	1.60	2.61	

Figure 4-27: EDS analysis and backscattered electron SEM of 347L samples in as-welded condition

As further described in Section 4.7, the particles from welding process were generically identified as manganese silicates whereas Nb-rich precipitates were associated to typical Nb carbides of Nb-stabilized stainless steels.

Simulated Service Ageing at 425°C without PWHT

Figure 4-28 shows optical micrographs of 347L samples in the as-welded condition and after accelerated ageing at 425°C following etching with Murakami´s reagent. As previously described, this etchant is used to reveal $M_{23}C_6$ carbides and sigma phase. Neither of these phases was identified either in the as-welded condition or after ageing.

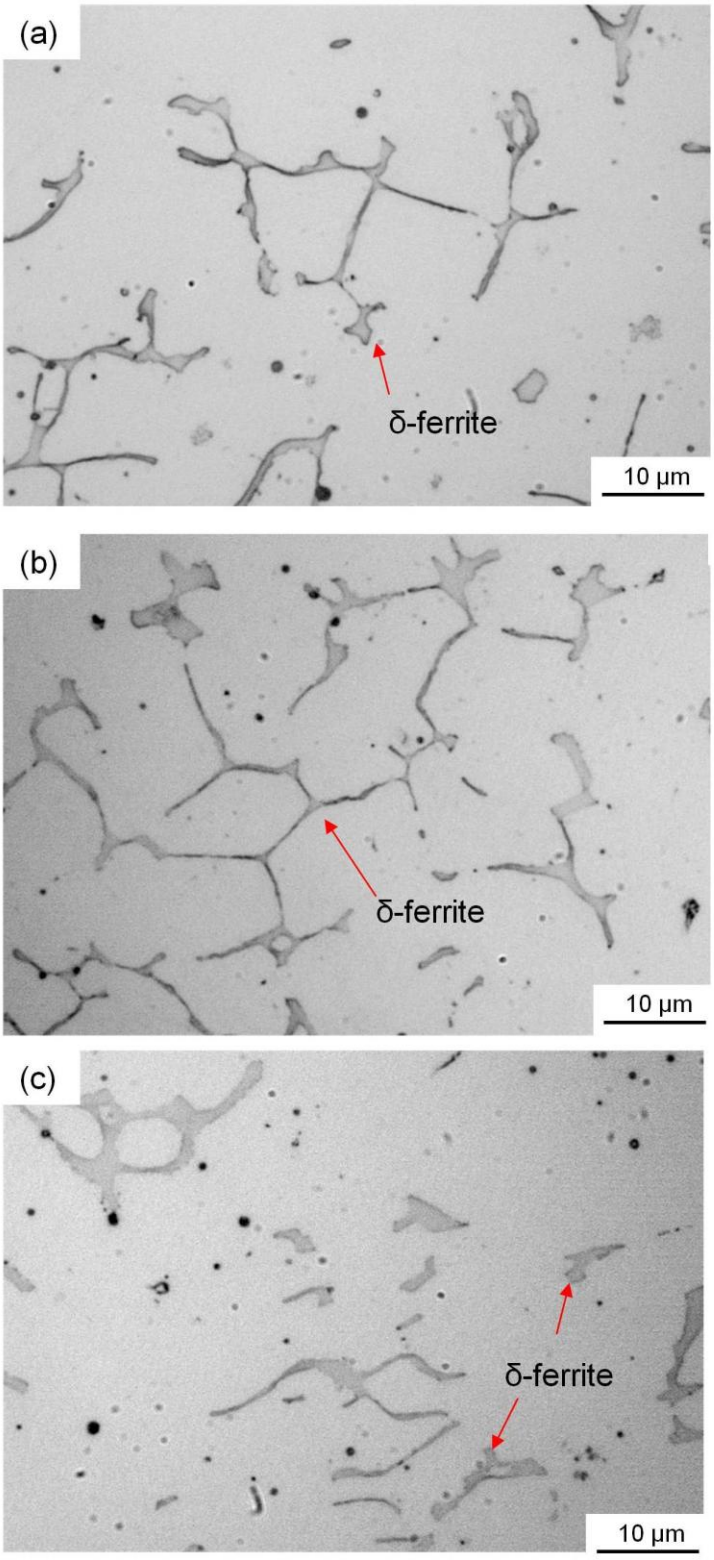

Figure 4-28: Optical micrographs following Murakami´s reagent etching of 347L in the as-welded condition (a) and after accelerated laboratory ageing at 425°C for 142.2 h (b) and 284.4 h (c)

PWHT – Ageing 600°C up to 100 h

Figure 4-29 shows micrographs of 347L samples in the as-welded condition and after PWHT at 600°C for 1h, 10h, 25 h, 40 h, and 100 h following etching with Murakami´s reagent.

In the as-welded condition and after 1 h of treatment no other phases than γ and δ were observed along with the spherical manganese silicates from welding process. It should be noted that NbC remains unchanged because it dissolves above 1000°C, but Murakami ´s reagent is not able to reveal it. After 10 h and 25 h of treatment, $M_{23}C_6$ carbides were observed in the δ-γ interphase and no significant precipitation of carbides was observed after 40 h of treatment at 600°C

A different transformation was observed after 100 h at 600°C as shown in Figure 4-29. Some arms of the δ-ferrite dendrites were observed to transform into σ phase.

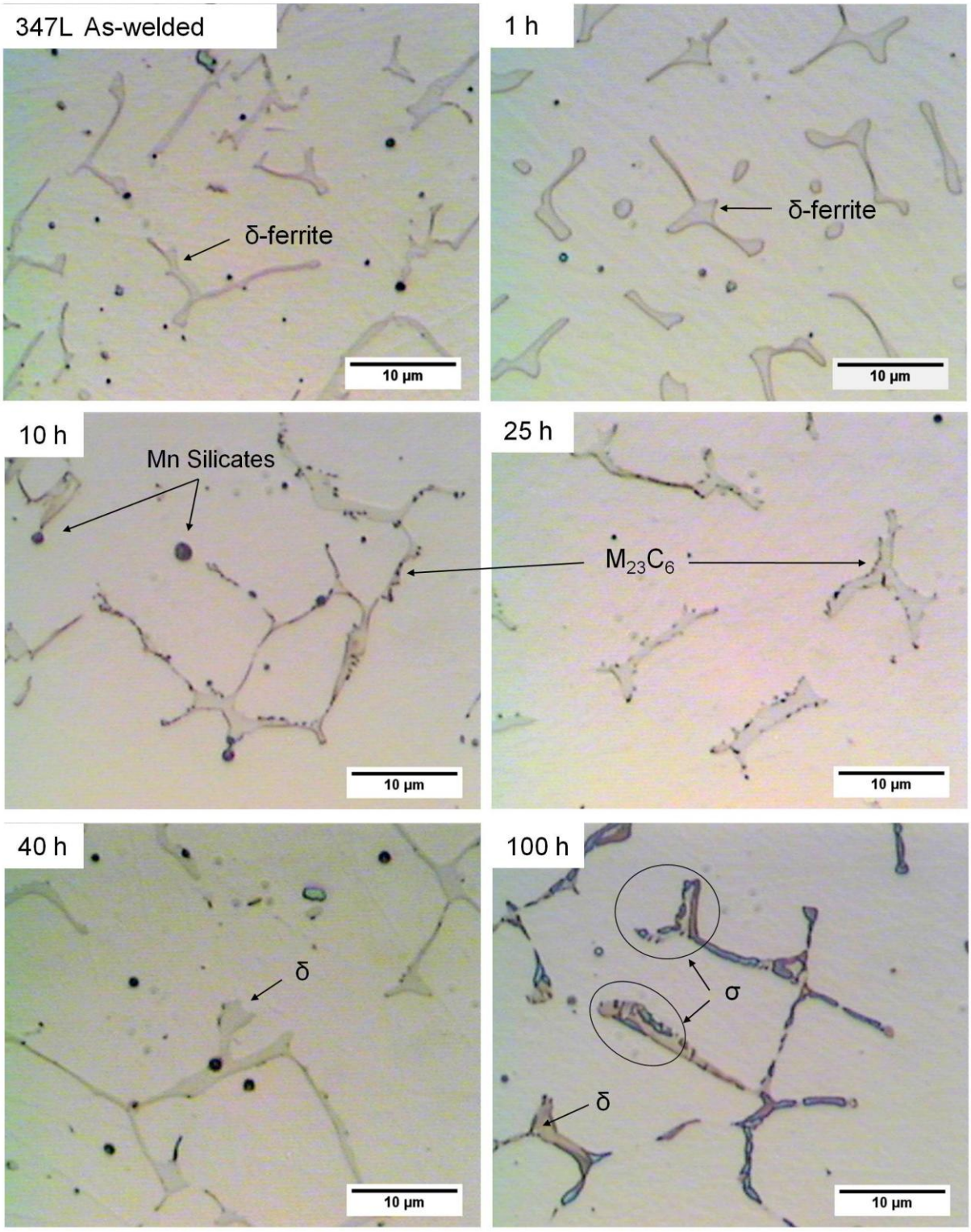

Figure 4-29: Optical micrographs following Murakami´s reagent etching of 347L samples in the as-welded condition and given PWHT at 600°C for 1 h, 10 h, 25 h, 40 h, and 100 h.

Effect of accelerated laboratory ageing following PWHT

Figure 4-30 shows that further ageing at 425°C 347L material that was PWHT at 600°C for 40 h did not produce a significant change in the microstructure. Neither carbide precipitation nor transformation of δ ferrite into σ phase was observed.

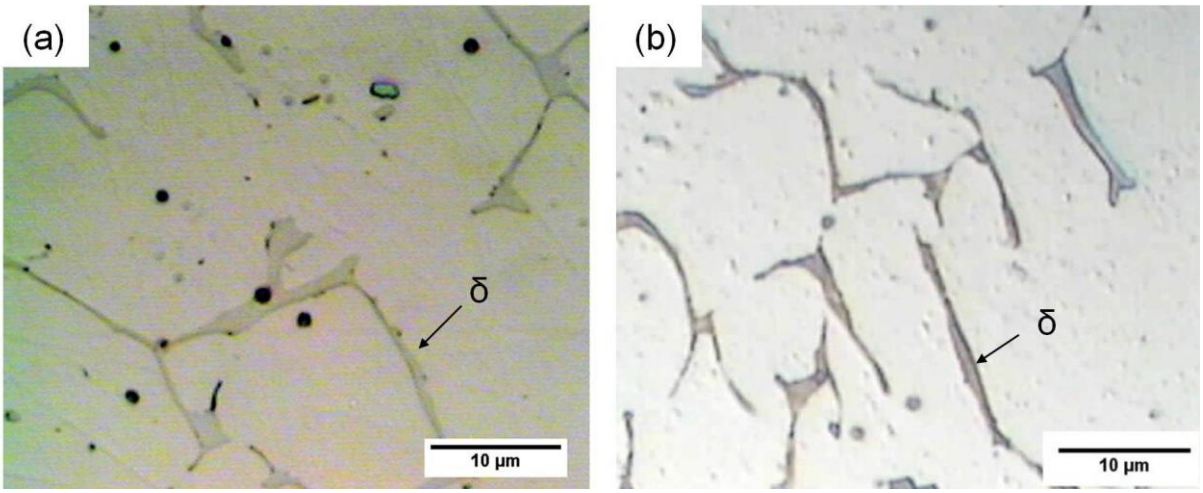

Figure 4-30: Optical micrographs following Murakami´s reagent etching of 347L samples after PWHT at 600°C for 40 h, and after the same PWHT followed by accelerated laboratory ageing at 425°C for 284.4 h

4.6.2 Type 309L SS

As-welded

Figure 4-31 shows the duplex microstructure found in 309L material at the working plane defined in Section 4.2 (6.25 mm from the fusion line towards the surface).

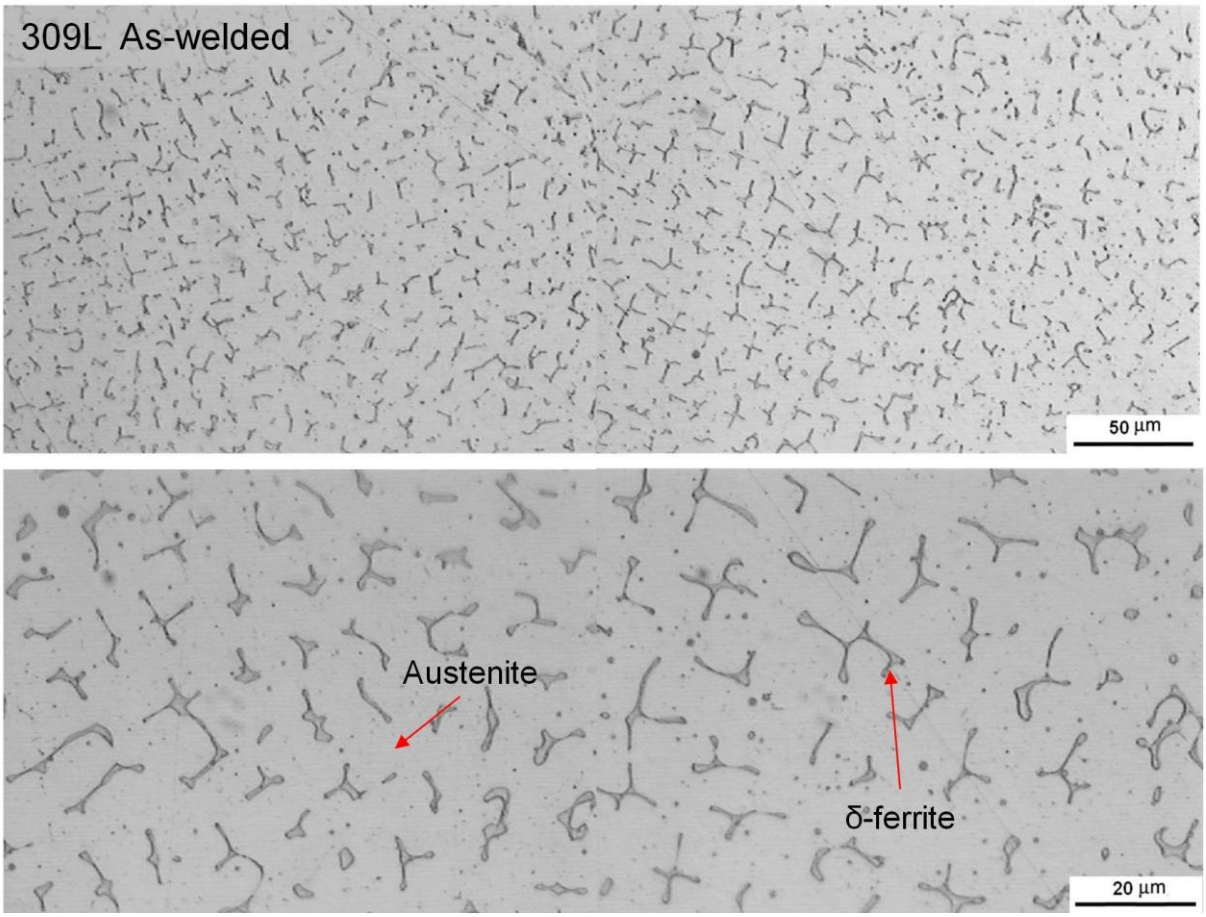

Figure 4-31: Duplex microstructure of 309L in the as-welded condition

EDS and SEM in electron backscattered mode on 309L in the as-welded condition (Figure 4-32) showed asutenite, delta ferrite and the particles from welding process as the phases present in 309L in this condition.

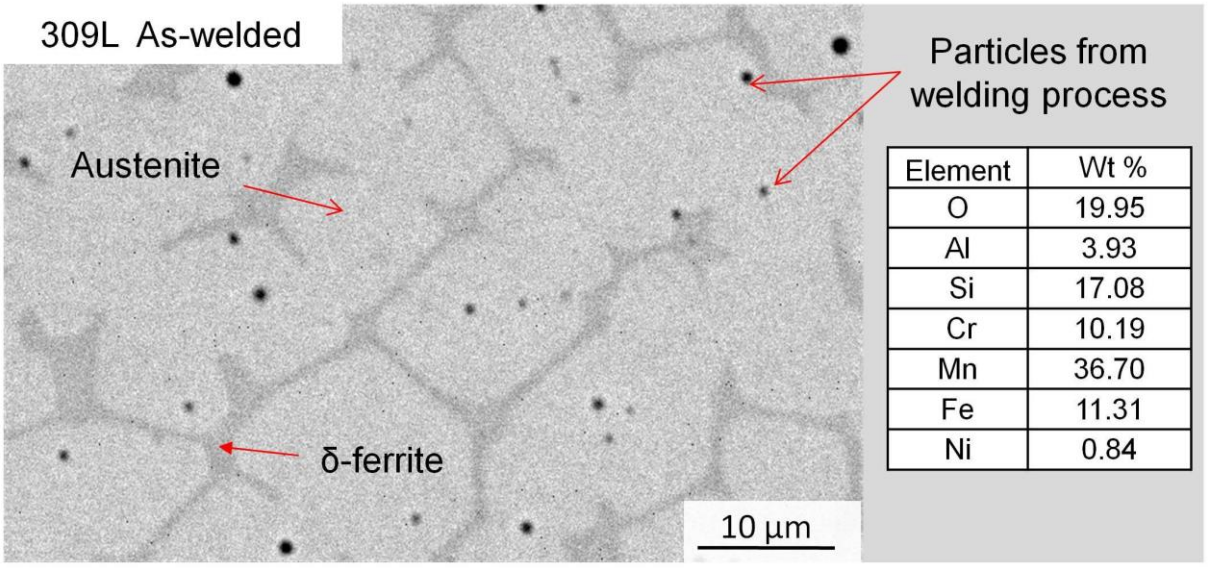

Element	Wt %
O	19.95
Al	3.93
Si	17.08
Cr	10.19
Mn	36.70
Fe	11.31
Ni	0.84

Element (Wt %)	Austenitic Matrix	Delta ferrite Islands
SiK	1.21	1.07
CrK	21.41	25.88
FeK	63.12	63.28
NiK	14.26	9.77
Cr/Ni	1.71	2.65

Figure 4-32: EDS analysis and backscattered electron SEM of 309L samples in as-welded condition

Simulated Service Ageing at 425°C without PWHT

Figure 4-33 shows optical micrographs of 309L samples in the as-welded condition and after accelerated ageing at 425°C following etching with Murakami´s reagent. Similarly to what was found for 347L, neither carbides nor σ phase were identified for these samples.

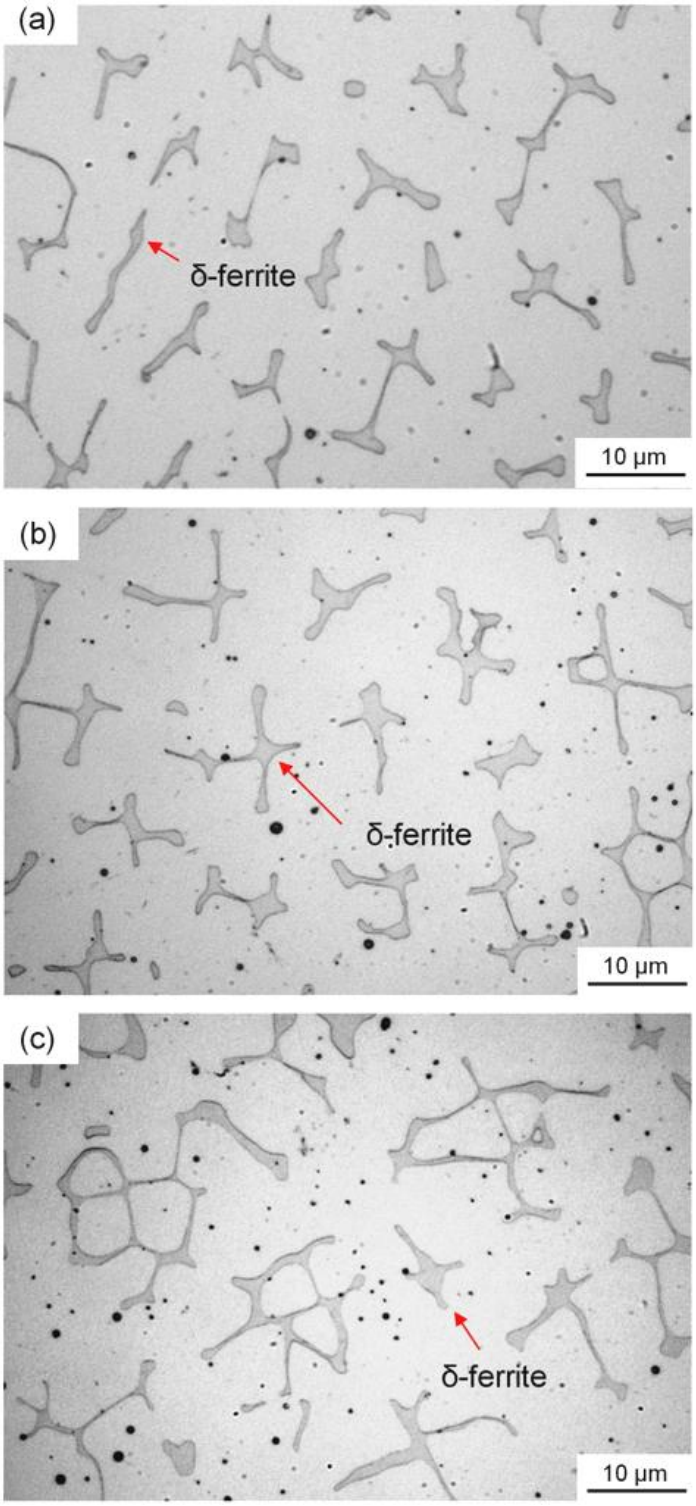

Figure 4-33: Optical micrographs following Murakami´s reagent etching of 309L in the as-welded condition (a) and after accelerated laboratory ageing at 425°C for 142.2 h (b) and 284.4 h (c)

PWHT – Ageing 600°C up to 100 h

Figure 4-34 shows micrographs of 309L samples in the as-welded condition and after PWHT at 600°C for 1h, 10h, 25h, 40h, and 100h following etching with Murakami´s reagent. It can be seen that precipitation of carbides started to be visible after 1 hour of treatment, showed higher resolution after 10 h, and no significant precipitation was detected after 40 h at 600°C. Transformation of δ-ferrite into σ phase started to be detected after 25 h and continued for 40 h and 100 h.

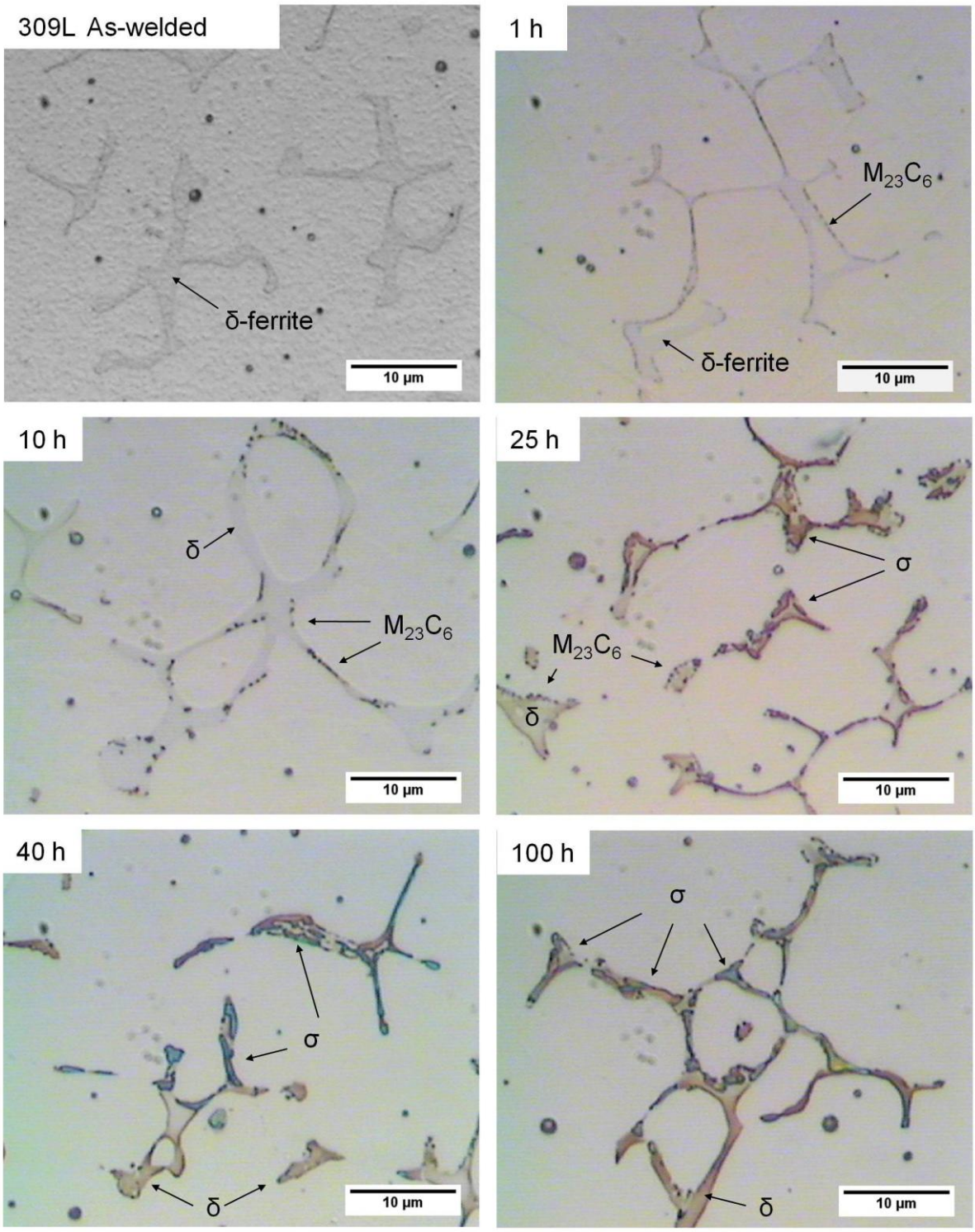

Figure 4-34: Optical micrographs following Murakami´s reagent etching of 309L samples in the as-welded condition and given PWHT at 600°C for 1 h, 10 h, 25 h, 40 h, and 100 h

Effect of accelerated laboratory ageing following PWHT

Figure 4-35 shows a comparison of the microstructures found in 309L after PWHT at 600°C for 40 h and after the combined treatment of PWHT for 40 h followed by the accelerated ageing at 425°C for 284.4 hours. Unlike 347L, where no differences were observed, a significant amount of carbide precipitation at the δ-γ interphase was observed in 309L after the accelerated ageing at 425°- (Figure 4-35 b). The difference in the behaviour of both materials is discussed in Section 4.8 and further linked to corrosion properties in Chapter 6.

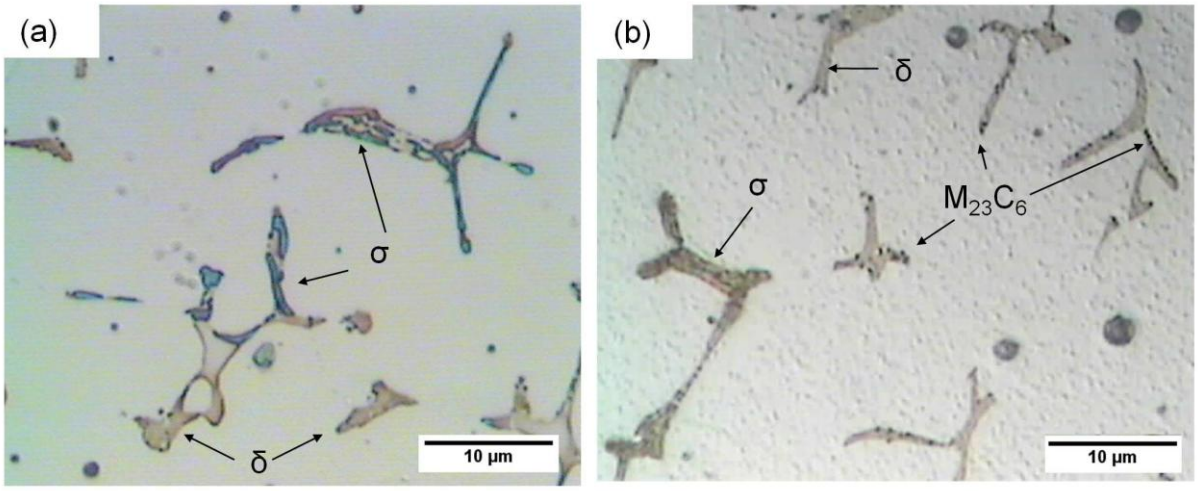

Figure 4-35: Optical micrographs following Murakami´s reagent etching of 309L samples after PWHT at 600°C for 40 h, and after the same PWHT followed by accelerated laboratory ageing at 425°C for 284.4 h

4.7 Analysis of phases by means of electron backscatter diffraction (EBSD) and energy dispersive X-ray spectroscopy (EDS) mapping

EBSD and EDS mapping were applied in order to study the phases present in the as-welded condition and follow their evolution during PWHT at 600°C. Results for 347L in the as-welded condition and after 100 h of treatment were obtained whereas samples of 309L in the as-welded and after PWHT for 10 h, 40 h, and 100 h were analyzed. The study of the remaining intermediate treatment times is considered for future work. In addition to the phase identification, EBSD allowed to see a high level of strain in both alloys (seen as dark lines in the figures), which is expected for welded materials.

The following paragraphs describe the strategy used to index minor phases.

σ phase

As proposed by Bordin et al. [165] crystallographic data from Yakel [79] were used to identify σ. This phase is represented as a Fe-Cr intermetallic with a body-centred tetragonal (BCT) structure.

$M_{23}C_6$

Two different strategies were used to identify carbides. In the first set of studies performed on 347L the software used for indexing was not able to distinguish them from the matrix. Therefore, a reassessment of the data obtained was performed considering the orientation of the FCC regions and the distribution of alloying

elements. Qualitative analysis of the orientation within each phase was studied by means of the inverse pole figure (IPF) in which similar colours represent similar orientations. On the other hand, EDS mapping was used to study element distribution. Then if an FCC region in the δ-γ interphase showed a different orientation than the matrix in the IPF and was coincident with a higher Cr and lower Fe region, it was identified as a chromium carbide.

In the second set of studies performed for 309L with a different equipment, crystallographic data from Bowman et al. [166] could be successfully used for indexing the carbides.

NbC

In addition to the identification using backscattered electron images described in Section 4.6, the combination of FCC regions detected by EBSD with high Nb counts in EDS maps was used to index this phase. Kikuchi diffraction patterns were obtained for one relatively large carbide and this finding was used to confirm the indexing approach.

Manganese Silicates

These particles were generically identified as manganese silicates in the present study based on morphology and the high contents of Si, Mn, and O found in EDS maps (see Figure 4-37) since no Kikuchi patterns were obtained for these particles in any of the EBSD analyzed. Despite the limitations of EDS for quantifying light

elements like oxygen [167], the comparative nature of the maps make them valid to point out the higher concentration of this element in the particles. As shown in Figure 4-36, particles were found to have a very complex composition and are not composed only of silicon, manganese and oxygen. A deeper study of these particles is considered out of the scope of the present work.

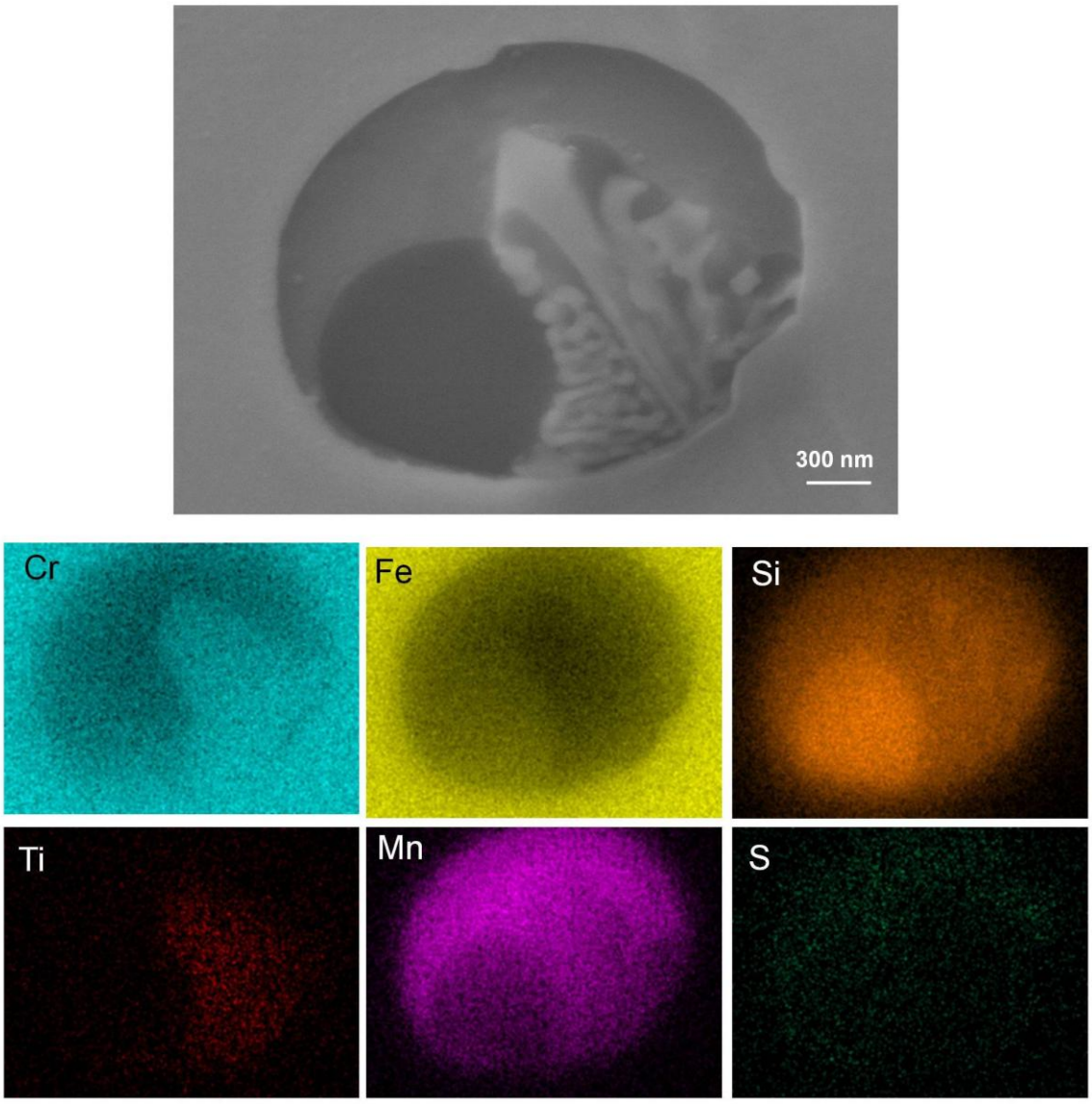

Figure 4-36: EDS mapping of a deoxidizing particle trapped during welding process in 347L SS

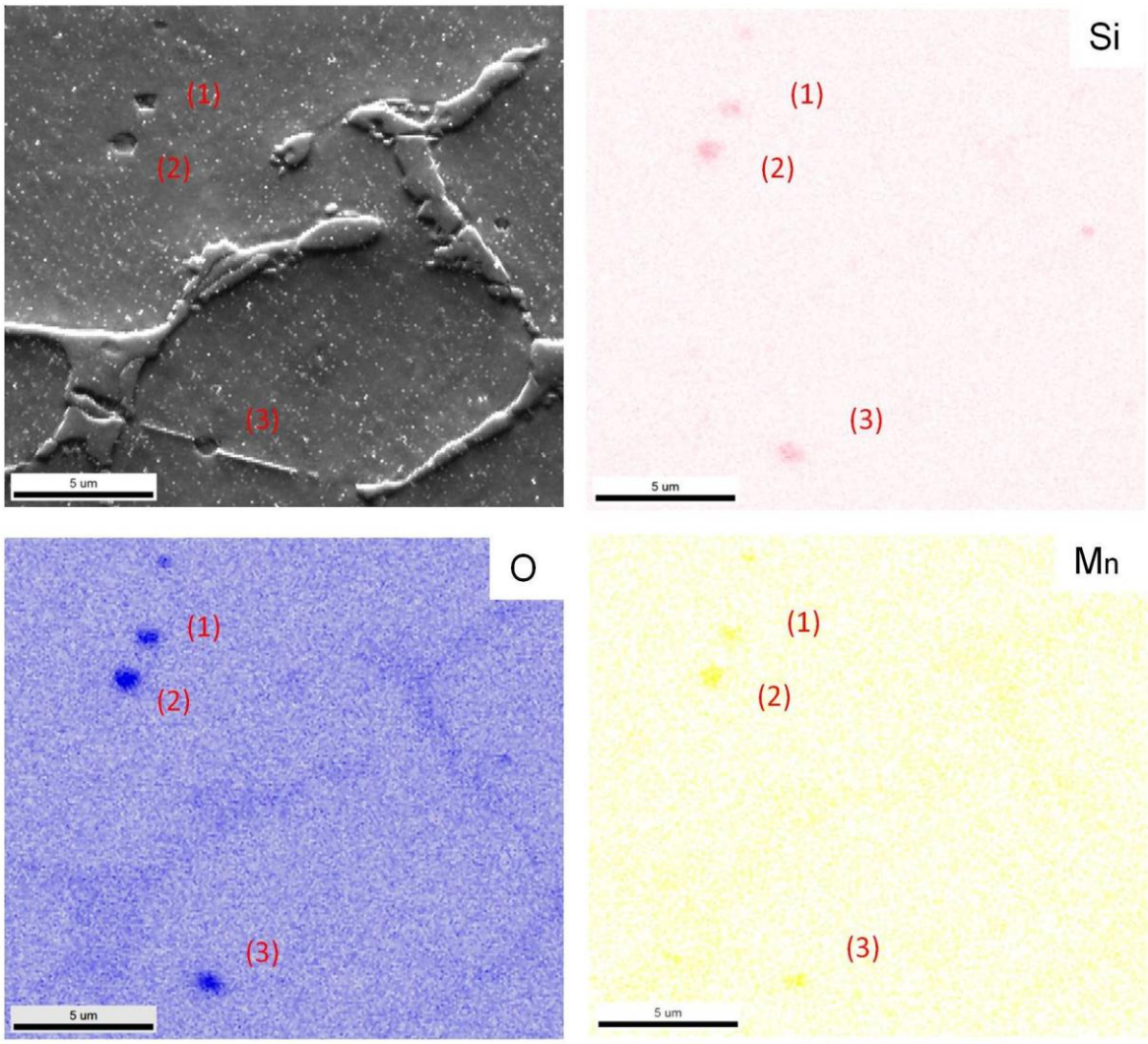

Figure 4-37: Example of silicate indexing in 309L SS. Secondary electron image (upper left) and corresponding EDS maps.

4.7.1 EBSD of Type 347L SS

Figure 4-38 shows a typical EBSD map obtained for 347L in the as-welded condition. Apart from the austenitic matrix (shown in blue in the figure), delta ferrite dendrites (light blue) were identified as the second main phase of the sample. In addition, niobium carbides (orange) were found both adjacent to delta ferrite dendrites and

precipitated in an isolate manner within the austenitic matrix. Manganese silicate particles (magenta) from the welding process were also identified.

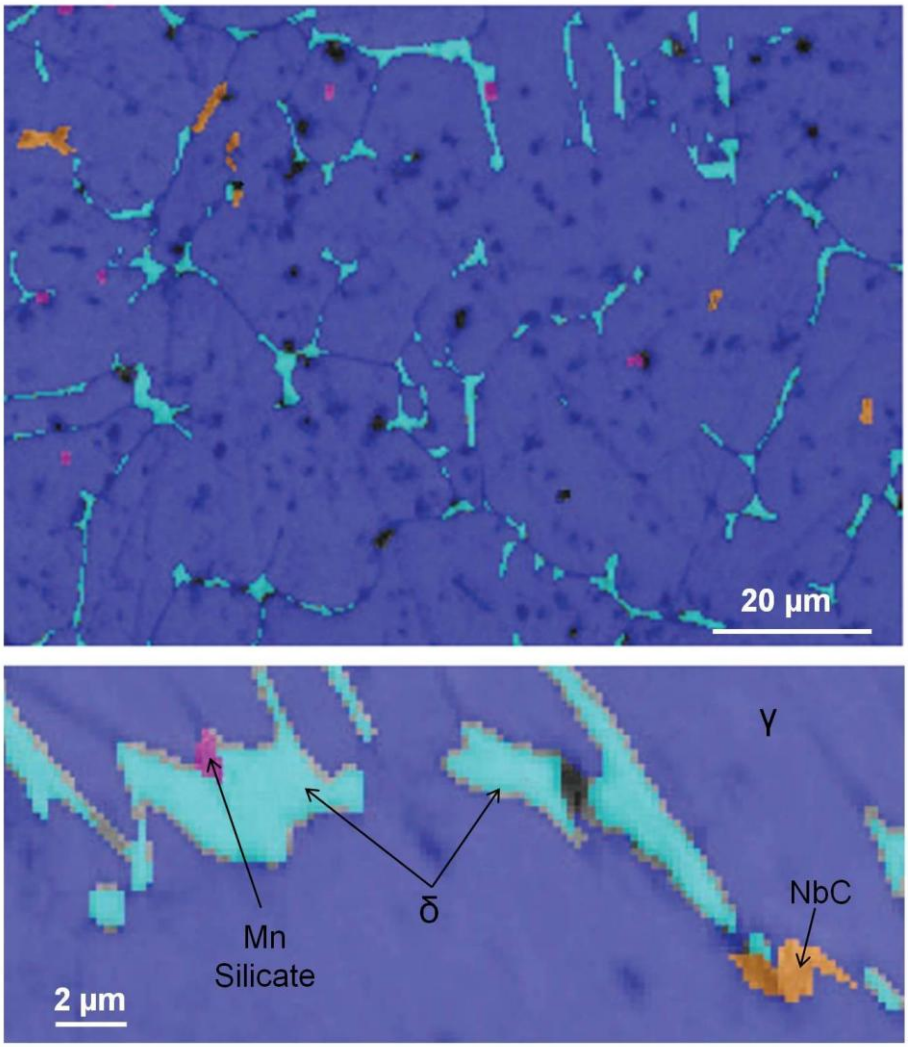

Figure 4-38: EBSD phase map of 347L samples in the as-welded condition. Blue = austenite, Light blue = delta ferrite, Magenta = manganese silicate, Orange = niobium carbide.

After 100 h at 600°C, some δ ferrite dendrites were found to have transformed into σ phase and $M_{23}C_6$ (Figure 4-39). It is worth noting that the dark areas shown within transformed delta ferrite dendrites correspond to regions which could not be properly

indexed. Further research is required to unequivocally identify these regions and better understand the transformation path from δ into σ phase.

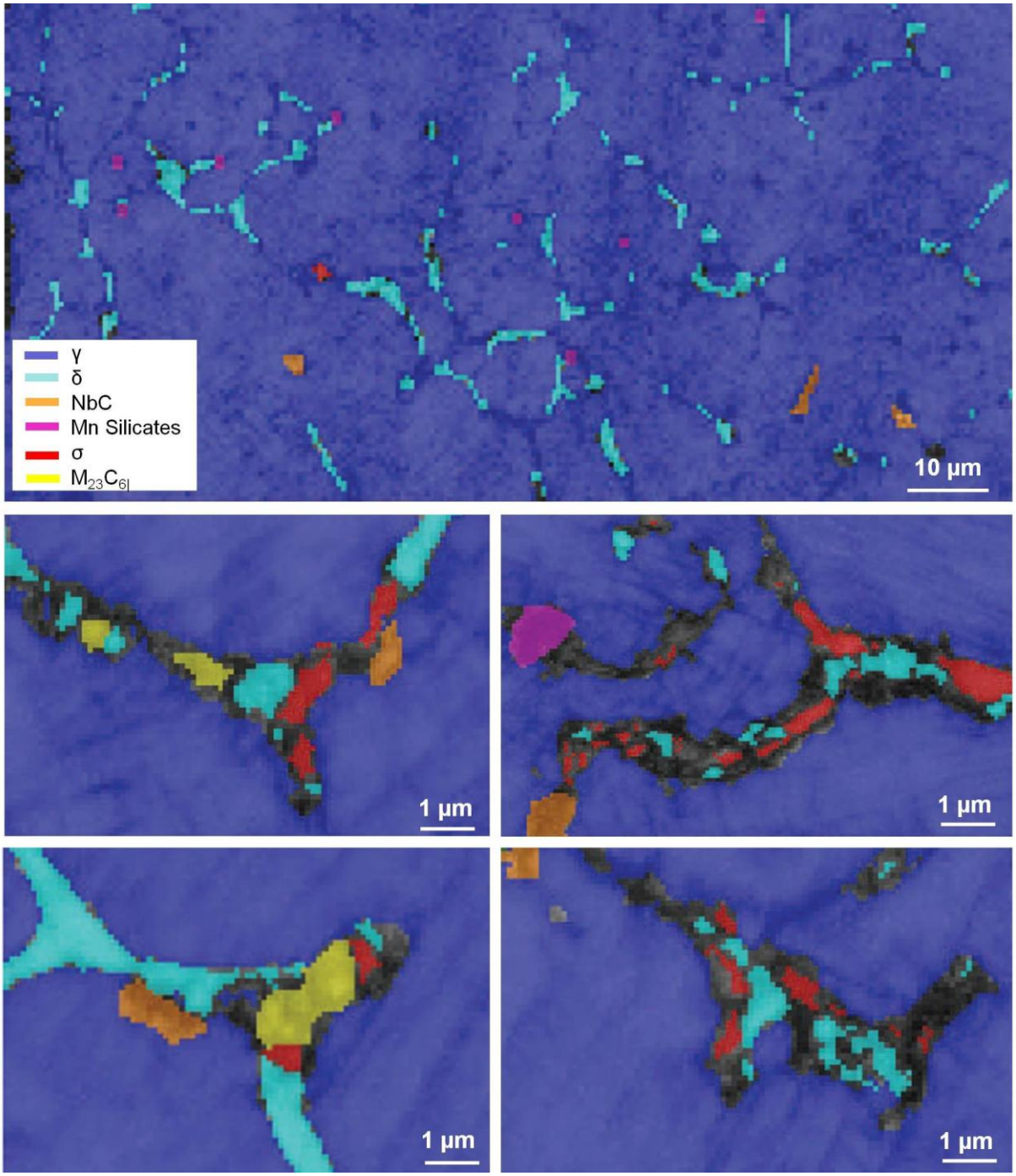

Figure 4-39: EBSD phase map of 347L samples after PWHT at 600°C for 100 h. Blue = austenite, Light blue = delta ferrite, Magenta = manganese silicate, Orange = niobium carbide, Yellow = $M_{23}C_6$, Red = sigma phase

4.7.2 EBSD of Type 309L SS

Figure 4-40 shows an EBSD phase map obtained for 309L samples in the as-welded condition. Austenite, delta ferrite and particles from the welding process were identified

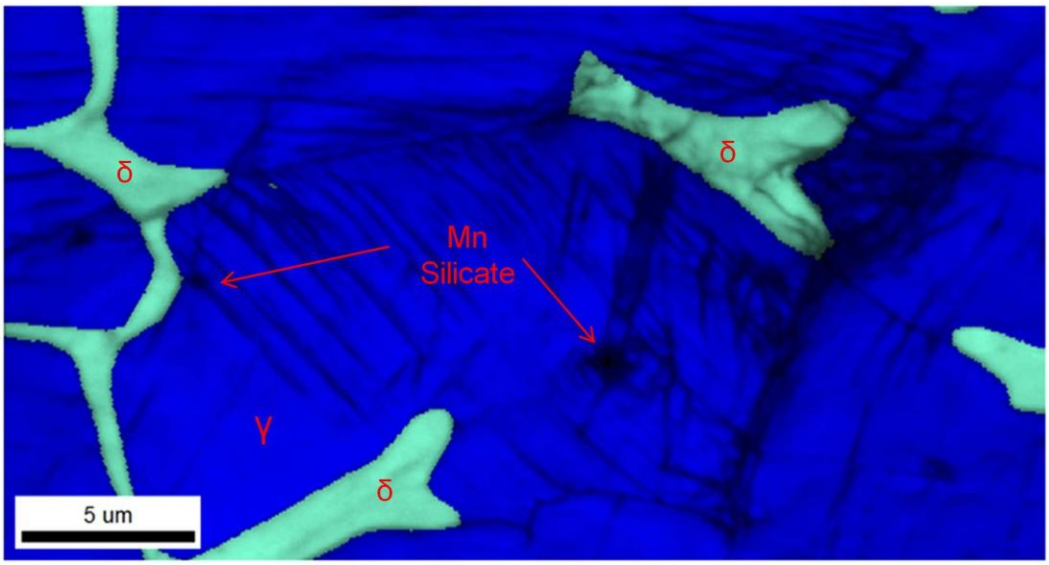

Figure 4-40: EBSD phase map of 309L samples in the as-welded condition

After 10 h at 600°C (Figure 4-41) chromium carbides were also identified in addition to δ and particles from the welding process.

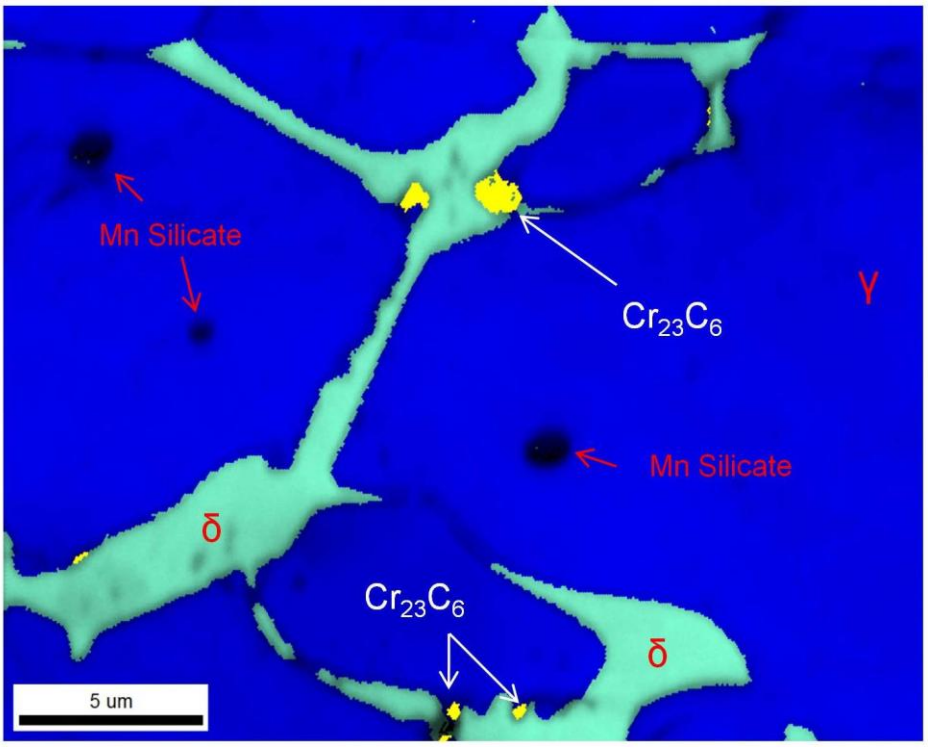

Figure 4-41: EBSD phase map of 309L samples after PWHT at 600°C for 10 h

After 40 h of treatment sigma phase was detected in addition to the austenite, δ-ferrite, Cr carbides and manganese silicates identified for 10 h of treatment. As seen in Figure 4-42, σ was found in some δ ferrite dendrites with the corresponding increase in Cr concentration in comparison to non-transformed δ, which in turn has a higher Cr than γ matrix as observed in Section 4.6. EDS maps of Figure 4-43 point out the higher content of Cr and lower content of Fe in Cr carbides.

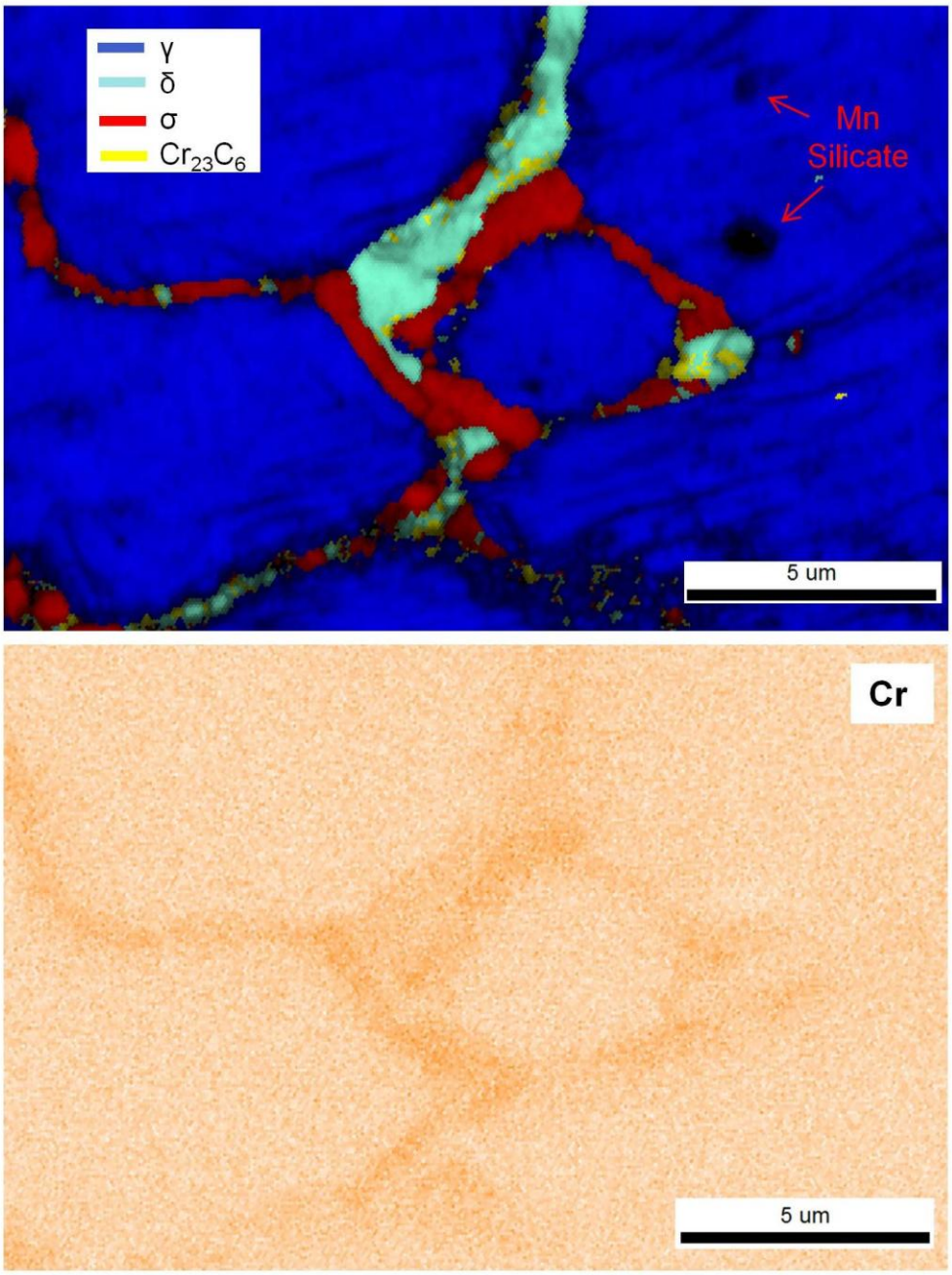

Figure 4-42: EBSD phase map (top) of 309L samples after PWHT at 600°C for 40 h and a EDS map showing Cr levels elevated in σ and δ phases.

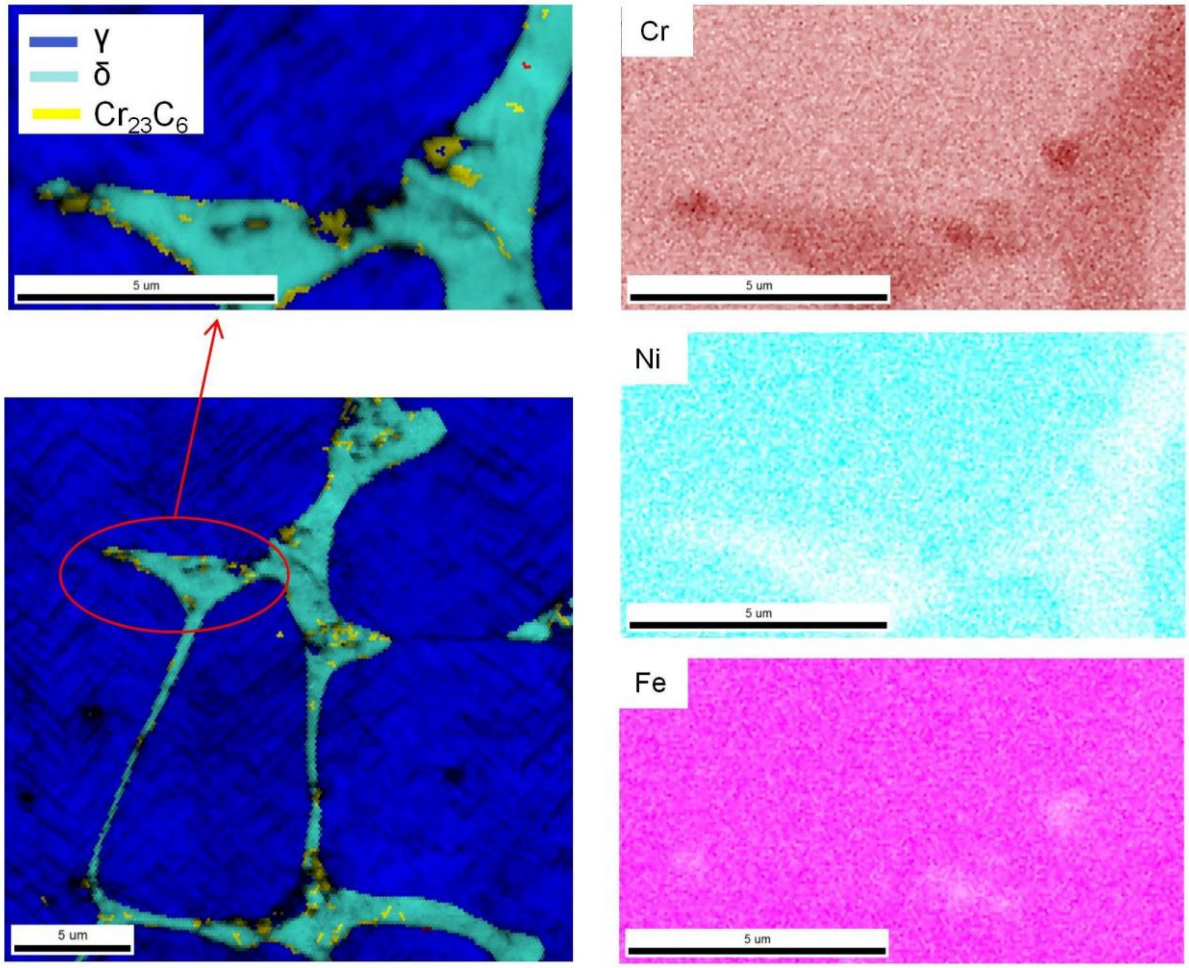

Figure 4-43: EBSD phase map of 309L samples after PWHT at 600°C for 40 h and EDS mapping of a region with precipitated carbides.

After 100 h of treatment at 600°C (Figure 4-44) the same phases than after 40 h were identified. Despite a lack of objective evidence in this study, it could be said that after 100 h it was easier to find transformed regions of δ into σ phase than after 40 h of treatment. This qualitative observation should be confirmed by a quantitative analysis of transformed regions for different treatment times.

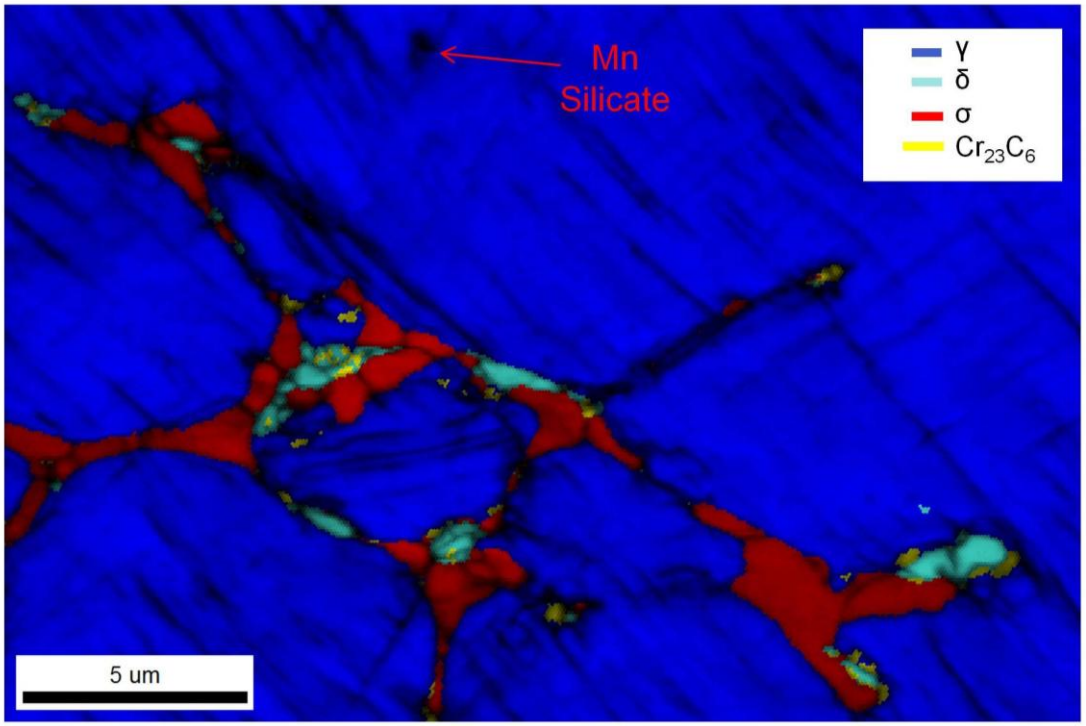

Figure 4-44: EBSD phase map of 309L samples after PWHT at 600°C for 100 h.

4.8 Discussion on microstructure evolution

4.8.1 Graphical Summary

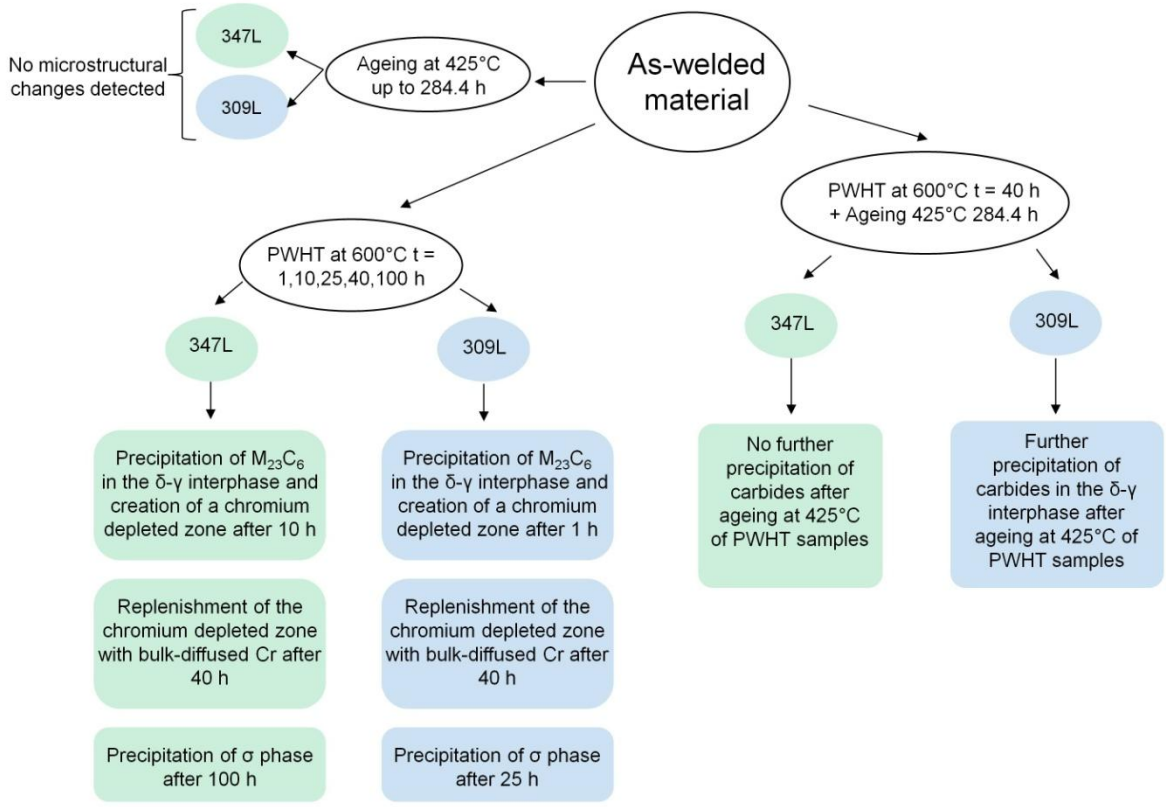

4.8.2 Test sample location, microstructural characterization and composition profiles in the as-welded condition

The use of an industrial-scale process for sample fabrication has the advantage of an increased relevance of the study but entails the need for dealing with a higher degree of variability. In this context it was necessary to study the microstructural regions of the cross-section of the welding coupons obtained from the factory (Figure 4-3 and Figure 4-4) in order to define a suitable sample fabrication method that could allow microstructural, mechanical and corrosion tests to be performed in a consistent way. Milling out 1 mm from the surface would have been a natural way to define the region

for testing. However in the present study it was necessary to accommodate sub-size Charpy samples as per ASTM E-23 [162]. Therefore, the plane defined by the middle of the second weld layer (5.55 mm from fusion line in 347L and 6.25 mm in 309L) was made coincident to the notch tip of the Charpy samples (Figure 4-8 and Figure 4-9) and selected for all the tests in the study. The relatively small variations on microstructure, chemical composition, and hardness (see Chapter 5) found in the vicinity of these planes support the idea of using them as a suitable testing location.

Composition profiles obtained are in agreement with the observed cross-section microstructures of 347L (Figure 4-3) and 309L (Figure 4-4). For both materials, in the region close to the fusion line, the influence of the mixing with the carbon steel base material could be seen as a higher content of Fe and C (Figure 4-11 and Figure 4-14) and a lower content of the alloying elements (Cr, Ni, Nb) characteristic of the stainless steel (Figure 4-12 and Figure 4-15). These compositional variations were seen to be reduced closer to the surface, which allowed definition of an average composition for the “working planes” set at the middle of the second weld layer.

4.8.3 Phase prediction

Simulated phase diagrams from liquid temperature down to 600°C were obtained for 347L and 309L using Thermo-Calc software with the chemical compositions obtained in Section 4.3 for the working planes. The objective of this work was to predict which would be the expected phases during PWHT at 600°C.

It is important to point out that thermodynamic predictions cannot be considered alone to determine the expected phases of a system and the kinetic aspects involved should also be considered. This is particularly important in a very dynamic system such as a welded overlay where melting and solidification occur in a very short period of time.

Major phases predicted for 347L at 600°C were found to be austenite (γ) and sigma phase accounting for more than 98% of the total volume with only 0.46% of stable δ ferrite (see Table 4-5). The stable carbide predicted at 600°C was NbC with no expected $M_{23}C_6$ carbides. Differences with observed structures at 600°C (i.e. higher amounts of δ and precipitation of $M_{23}C_6$ - Figure 4-29) can be explained in terms of kinetics aspects. Given the high cooling rates involved in welding (the base material acts as an important heat sink), in the case of 347L, the time at high temperature might not have been enough for full stabilization (complete precipitation of NbC) and some C might remain in solution. Later, when the material is subjected to PWHT at 600°C, this C could precipitate as $M_{23}C_6$. Similarly, δ ferrite can be retained from high temperature due to the fast cooling experienced after welding. In this condition, δ ferrite is a metastable phase and is able to transform if the material is reheated.

In the case of 309L major phases predicted were γ and σ (with no stable δ ferrite) and $M_{23}C_6$ as the stable carbide (see Table 4-6). Considering the kinetic aspects, $M_{23}C_6$ precipitation could be avoided due to fast cooling rates and these carbides may not be detectable in the as-welded condition (Figure 4-33). $M_{23}C_6$ can precipitate later if the material is reheated. Similarly, δ ferrite can be retained from

high temperature due to the fast cooling experienced after welding and is able to transform if the material is reheated.

It is worth noting that for both materials a significant amount of σ phase is predicted for the thermodynamic equilibrium at 600°C (20.49 % for 347L -Table 4-5 and 28.23% for 309L - Table 4-6). On the other hand, in section 4.6 only a fraction of the δ ferrite was observe to have transformed into σ phase. This difference could be explained based on the fact that thermodynamic equilibrium is not reached after 100 h at 600°C and predicted σ includes transformation from δ and from γ which is known to occur for very long ageing times [82]. Longer ageing times are considered for future work.

As previously described precipitation of $M_{23}C_6$ would be expected during treatment at 600°C of both materials, either because it is a stable phase (309L) or because full stabilization could not be reached in the short cooling times involved in welding process (347L). Kinetics of precipitation has been the subject of discussion in literature sensitization [63, 68, 69] and several models have been proposed to predict times involved in this process, and how they relate to sensitization (i.e. loss of resistance to intergranular corrosion due to the formation of a Cr-depleted zone around precipitated carbides). As described in detail in Section 4.4.2, Strawstrom's model establishes a correlation between sensitization and the time required to form a Cr-depleted zone of ~20 nm around carbides. Following calculations proposed by Devine, a relatively good correlation was found for both materials between model results and the 10 hours required to reach sensitization in Chapter 6 when the activity

of carbon is calculated according to Natesan and Kassner; and the chromium activity coefficient used is that calculated by Fullman according to either the Kaufman and Nesor formulation or Hasebe and Nishizawa´s. On the other hand, no agreement was found when parameters from Tedmon et al. were used. To improve these calculations, more realistic activities of C and Cr could be obtained using multi-component thermodynamics (e.g. Thermo-Calc) in order to consider the influence of the other alloying elements. This is considered for future work.

It is worth noting that in any case, predicted time to sensitization was shorter for 347L than for 309L (see Table 4-8). This result contradicts observations in Section 4.6 where carbides were revealed with Murakami`s reagent after 10 h in 347L and after only one hour in 309L. A possible explanation could be based on the fact that Strawstrom's model considers the initial content of carbon in the alloy to be fully available for carbide precipitation. Under this condition and considering the higher content of C, and the lower content of Cr in 347L, a shorter time to sensitization is estimated for this material. However, calculations should be reformulated considering only the free carbon in 347L without considering the carbon "trapped" as NbC during solidification.

4.8.4 As-welded microstructure

347L

The microstructure of 347L in the as-welded condition was found to be formed of austenite, δ ferrite, NbC and Mn silicates from the welding process, as shown by micrographs in Section 4.6.1 (Figure 4-26 and Figure 4-27) and confirmed by EBSD

(Figure 4-38). Average content of δ ferrite in this condition was found to be 6.6% showing a vermicular morphology, similar to that reported by David [44] for ASSWs with δ ferrite in the range of 5% - 15%.

Niobium carbides were identified first by means of backscattered electron images (Figure 4-27). This tool allows identification of phases based on the different atomic number of the elements that compose the phases. Heavier elements produce a higher flux of backscattered electrons which are translated into brighter images [167]. For this reason niobium carbides are shown white in Figure 4-27 considering that atomic number of Nb=41 whereas atomic number of Fe=26. The presence of this phase was also confirmed by EBSD in Section 4.7.

Spherical particles found for both 347L (Figure 4-27) and 309L (Figure 4-32) are the result of the deoxidation process occurring during welding. Deoxidizing elements such as manganese, silicon, aluminium or titanium are added in the shielding flux in order to control the amount of oxygen that is incorporated during welding process [8]. Unlike casting processes, where deoxidizing times can be properly managed and most of the resulting products are taken out during slag removal, the very fast cooling rates involved in welding lead to a high number of particles trapped in the weld pool.

These particles were found to be enriched in silicon and manganese and oxygen was also found in EDS of Figure 4-32. This result, which would be consistent with the composition of manganese silicates, cannot be taken as definitive due to the limitations of EDS for quantifying light elements (Z<11) like oxygen [167].

The exact composition and structure of the particles could not be determined in the present study and they were generically identified as manganese silicates. However, EDS mapping in Section 4.7 showed a complex element distribution within the silicates identifying also regions rich in Ti and S. A deeper study of these particles is considered out of the scope of the present work.

309L

Microstructure of 309L in the as-welded condition was found to be formed by austenite, δ ferrite and the same particles from the welding process described for 347L (Figure 4-32). Average content of δ ferrite was found to be 9.6% (Section 4.5) and the same vermicular morphology was observed (Figure 4-5) . Higher contents of Ni in the austenitic matrix and of Cr in δ-ferrite dendrites were found in EDS analysis (Figure 4-32) in comparison to 347L due to the higher contents of these alloying elements in 309L. This observation is in accordance with the chemical analysis performed in Section 4.3 .

4.8.5 Microstructural evolution during PWHT at 600°C

347L

A clear reduction of δ ferrite was observed during PWHT at 600°C for 347L (Figure 4-21) indicating the transformation of this phase. Carbides in 347L were visible following etching in Murakami´s reagent after 10 h of treatment and no significant precipitation was detected for times longer than 40 h (Figure 4-29). This result is

worthy of attention since $M_{23}C_6$ carbides cannot be re-dissolved in stainless steel at 600°C (typical solution treatments are performed above 1000°C). Therefore, since Murakami´s reagent shows the carbides by attacking the CDZ around them, the lack of dark spots in the δ-γ interphase in the micrographs after 40 h of treatment at 600°C may imply that the CDZ has been replenished with bulk-diffused Cr. Presence of carbides in 347L after 100 h of treatment at 600°C was confirmed by EBSD (Figure 4-39) although they were not detected in optical micrographs (Figure 4-29) supporting the idea of the creation and replenishment of the CDZ around carbides, as reported in literature for different stainless steels [60, 64-67].

After 100 h of treatment some regions of δ ferrite dendrites were found to have transformed into σ phase. Precipitation of σ phase in ASSWs is possible in relatively short ageing times due to the presence of δ ferrite and was reported by other authors [14, 16-19]. This phase creates faster diffusion paths for Cr [82] which allow precipitation of σ from δ to be ~100 times faster than directly from γ [8].

309L

Precipitation in 309L during PWHT at 600°C followed a similar pattern to that of 347L showing also a marked reduction of δ ferrite (Figure 4-24). Following Murakami´s etching, carbides started to be observed after 1 h of treatment and were clearly visible after 10 h, whereas no significant precipitation was observed after 40 h. EBSD analysis of 309L samples confirmed the presence of carbides after 10 h (Figure 4-41), 40 h (Figure 4-42), and 100 h (Figure 4-44) of treatment at 600°C

supporting also the idea of the creation and replenishment of a CDZ around carbides for this material.

Sigma phase was first detected after 25 h of PWHT following etching in Murakami´s reagent and confirmed by EBSD after 40 h in comparison to the 100 h required for 347L. Despite no objective evidence was found in this study, a higher amount of σ after 100 h of treatment in comparison to 40 h of treatment was qualitatively observed and is proposed be quantitatively confirmed in future research. The higher tendency of 309L to form σ can be explained by the higher content of Cr (Section 4.3) and δ ferrite (Section 4.5) in this material, given that both factors are known to promote σ precipitation in duplex stainless steels and ASSWs [82, 85]. In addition, 309L has a higher equilibrium content of sigma as shown in the thermodynamic predictions of Section 4.4.1,

4.8.6 Microstructural evolution during simulated service conditions

When accelerated ageing at 425°C was applied to the as-welded condition (i.e. without PWHT at 600°C) no significant changes in microstructure could be detected either for 347L (Figure 4-28) or for 309L (Figure 4-34). Both materials showed the same phases than in the as-welded condition without precipitation of either carbides or σ phase. In addition, no clear variations of δ ferrite were observed in Section 4.5.

The processes expected for these materials in the referred temperature range are low temperature sensitization (LTS) [12, 71, 72] and spinodal decomposition of δ ferrite [10, 11]. LTS requires the presence of previously deposited chromium carbides

that will continue growing during low temperature ageing. Therefore, this process is unlikely to occur during ageing at 425°C of as-welded samples due to the lack of precipitated carbides in the as-welded condition (Figure 4-28 and Figure 4-34). On the other hand, spinodal decomposition of the ferritic phase is likely to occur but can only be detected by TEM. This technique was not applied in the present study and is considered for future work.

When accelerated ageing at 425°C was applied to samples that have been given a PWHT for 40 h, different behaviour was observed for 347L and 309L

In the case of 347L, the low temperature ageing was applied on PWHT samples that contain γ, δ and Cr carbides which have the CDZ replenished with bulk-diffused Cr, according to the results of the present work. As seen in Figure 4-30, no significant amount of carbides were found following Murakami´s etching after the combined treatment indicating that the accelerated ageing did not produce an increase in the CDZ.

In the case of 309L, the low temperature ageing was applied on PWHT samples that contain γ, δ, σ, and Cr carbides which have the CDZ replenished with bulk-diffused Cr, according to the results of the present work. As seen in Figure 4-35 a significant amount of carbides were found following Murakami´s etching after the combined treatment. Considering that carbides were already present in PWHT samples, this finding indicates that ageing at 425°C of 309L produced the creation of a new CDZ around carbides precipitated during PWHT.

The difference in the behaviour of both materials could be explained in terms of the stabilizing effect of Nb, which traps C in the form of NbC during solidification of 347L (see Figure 4-27 and Figure 4-38), leaving very little free carbon to continue growing at 425°C the carbides deposited during PWHT avoiding the creation of a new CDZ.

4.9 Conclusions

Several characterization techniques such as OES, optical microscopy, SEM, EDS, EBSD and δ ferrite measurements with ferritescope, were used to study the evolution of the microstructure of austenitic stainless steel welds during fabrication and service conditions of reactor vessel claddings. Stainless steel cladding materials 347L and 309L were subjected to three different sets of thermal treatments, corresponding to the different fabrication and service stages of the component.

The following conclusions can be drawn from the present study:

1) Microstructure of 347L in the as-welded condition was found to be composed by an austenitic matrix, vermicular delta ferrite (6.6% average), precipitates of NbC resulting from the stabilization process, and amorphous particles derived from the deoxidizing process with a complex structure containing Mn, Si, Ti, and S, generally identified as manganese silicates for this study.

2) Microstructure of 309L in the as-welded condition was found to be composed by an austenitic matrix, vermicular delta ferrite (9.6% average), and amorphous particles derived from the deoxidizing process with the same features than those found in 347L.

3) PWHT at 600ºC leads to the transformation of δ ferrite in 347L according to the following sequence:
    a) Precipitation of $M_{23}C_6$ in the δ-γ interphase after 10 h of treatment with the creation of the consequent Cr-depleted zone (CDZ) around the precipitated carbides
    b) Replenishment of the CDZ with bulk-diffused Cr after 40 h of treatment
    c) Precipitation of σ phase observed after 100 h of treatment

4) PWHT at 600ºC lead to the transformation of δ ferrite in 309L according to the following sequence:
    a) Precipitation of $M_{23}C_6$ in the δ-γ interphase after 1 h of treatment with the creation of the consequent Cr-depleted zone (CDZ) around the carbides
    b) Replenishment of the CDZ with bulk-diffused Cr after 40 h of treatment
    c) Precipitation of σ phase after 25 h of treatment

5) 309L SS showed a higher tendency to precipitate σ phase and $M_{23}C_6$ from δ ferrite in comparison to 347L.

6) Ageing of 309L samples that had been given a PWHT at 600ºC for 40 h at 425ºC produced a new CDZ around carbides in the δ-γ interphase. This finding is thought to be linked to the growing at 425°C of carbides previously precipitated during PWHT at 600°C (low temperature sensitization – LTS)

7) Ageing of 347L of samples that had been given a PWHT at 600ºC for 40 h at 425ºC produced no changes in the microstructure indicating a higher resistance of 347L to LTS.

8) Higher resistance of 347L to LTS could be associated to the presence of Nb in the material as a stabilizing element. This element may prevent the occurrence of LTS by trapping free C as NbC during material solidification in the fabrication stage.

9) Microstructural changes could not be detected either in 347L or in 309L, during ageing at 425ºC of samples in the as-welded condition (i.e. without PWHT at 600°C).

5 Mechanical Properties of Stainless Steel Cladding Materials following Accelerated Ageing

5.1 Introduction

The objective of the present chapter is to follow the evolution of mechanical properties of reactor pressure vessel cladding materials during ageing at 425°C simulating service conditions of 30 and 60 years at 300°C according to the Arrhenius calculations described in Chapter 3.

Samples were aged directly from the as-welded condition and subjected to Vickers micro-hardness and Charpy impact tests. Fracture surfaces were also analyzed using SEM and EDS. A correlation between the observed changes in mechanical properties and microstructural modifications due to ageing is discussed. The study of the evolution of mechanical properties during PWHT at 600°C and in the combined treatment of PWHT followed by ageing at 425°C is left for future work.

5.2 Determination of Vickers micro-hardness profiles through the weld overlay

In the following section results of micro-hardness profiles carried out as described in Chapter 3 are shown. These profiles were obtained by measuring hardness from the fusion line towards the surface in as-welded samples and in samples subjected to accelerated ageing at 425 °C for 142.2 h and 284.4 h.

5.2.1 Type 347L Stainless Steel

As-welded

Despite the high scatter found, it was possible to identify three regions in the hardness profile of 347L samples in the as-welded condition (Figure 4-12). The first region, showing hardness in the range of 240-270 Hv, goes from the fusion line itself up to approximately 3 mm from this line. The following region shows a marked reduction of hardness up to approximately 5 mm from fusion line, where the hardness reaches a lower plateau in the range of 200-220 Hv until the end of the sample (i.e. the surface). It is worth mentioning that this last region, where the hardness profile is quite flat, contains the "working plane" defined for the present study in Chapter 4, indicating a relative uniformity in hardness above and below this plane.

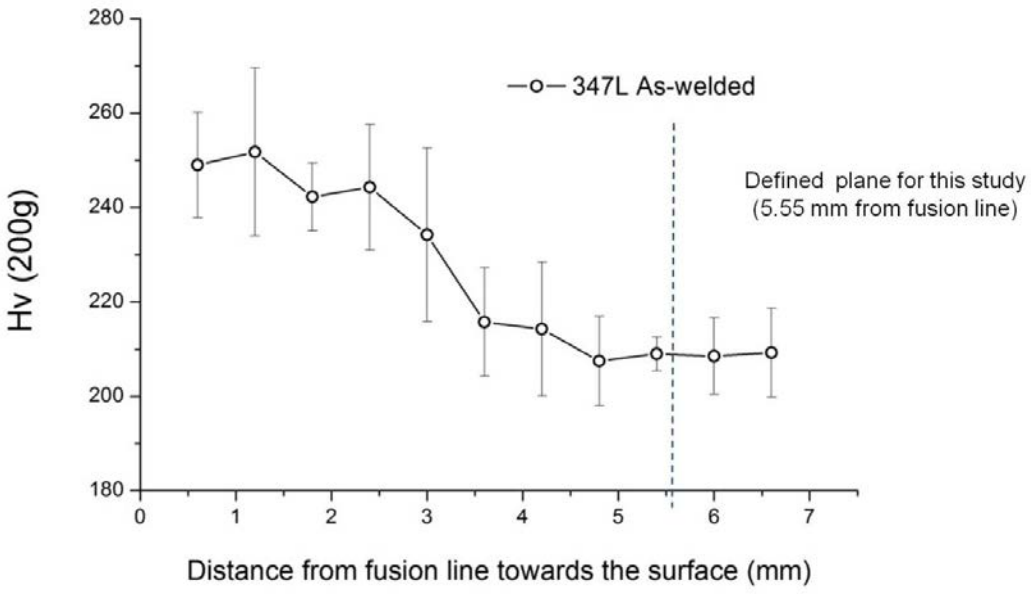

Figure 5-1: Vickers micro-hardness profile of 347L samples in the as-welded condition. Dotted line indicates the position of the "working plane" used for microstructural and corrosion tests.

Simulated Service Ageing at 425°C without PWHT

Figure 5-2 shows the profiles obtained for 347L SS after accelerated ageing at 425ºC for 142.2 h and 284.4 h.

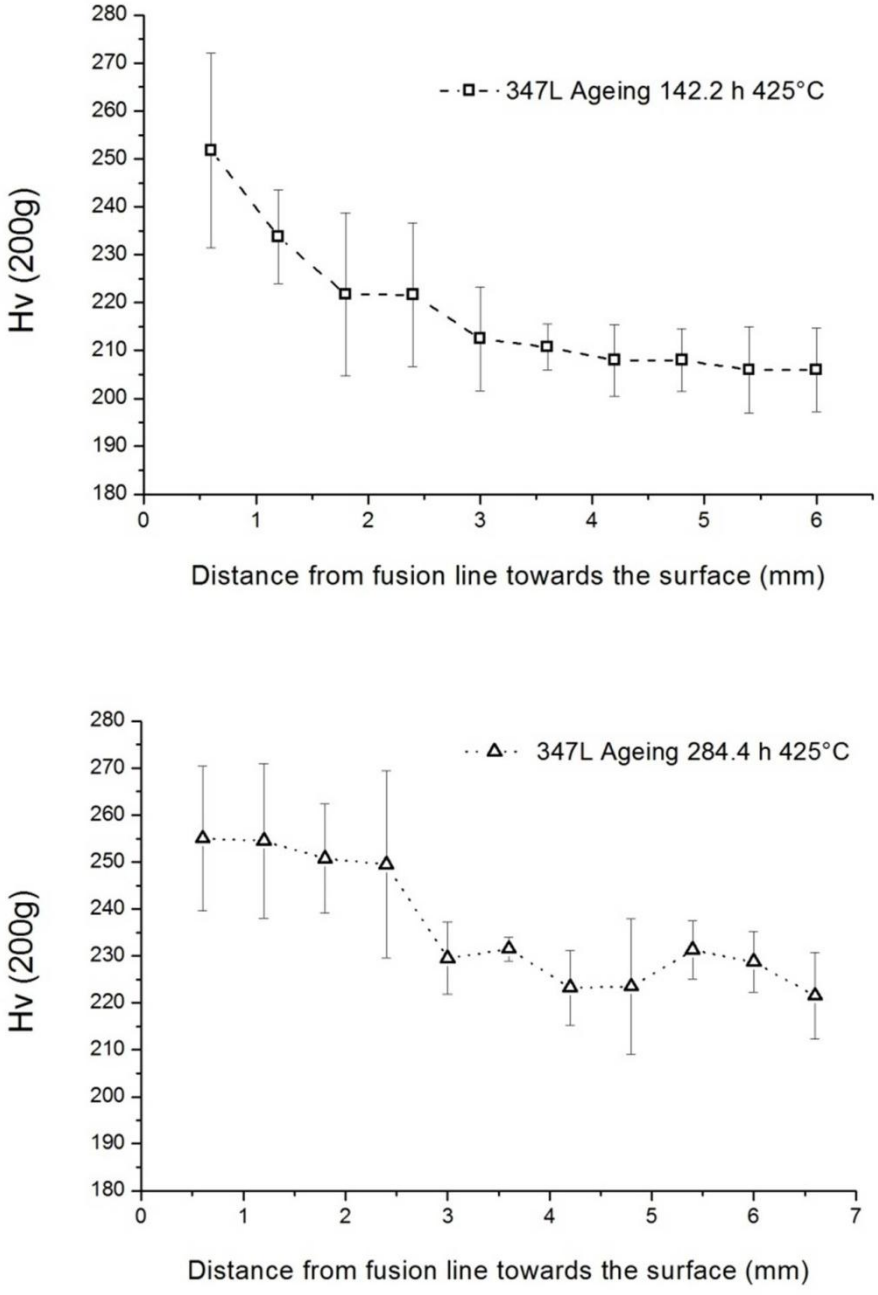

Figure 5-2: Vickers micro-hardness profile of 347L samples after accelerated ageing at 425 ºC

Some differences could be found between these profiles and that obtained for the as-welded condition (Figure 4-12). For both ageing times, reduction in hardness seems to be almost complete at 3 mm from the fusion line in comparison to the 5 mm observed in the as-welded condition. After 142.2 h a general softening appears in the region closer to the fusion line, whereas values nearer to the surface do not show major changes remaining around 210 HV. This would be consistent with a stress relief effect which has a higher influence on the most stressed region of the sample (i.e. closer to the fusion line). After 284.4 h two plateaus could be observed. The first one going from the fusion line up to 2 mm, and the second one for distances longer than 3 mm. Both of them showed an increase in hardness. The reasons behind this hardening are further discussed in Section 5.5.

Figure 5-3 shows a comparison of the three profiles obtained without the confidence intervals for clarity reasons. The high scatter found in the region closer to the fusion line did not allow for a proper comparison of the hardness values in this area. However, values could be compared in the lower plateau region (Figure 5-4) observing that after 142.2 h no significant variations were observed whereas a significant increase in hardness was observed after 284.4 h of treatment at 425°C.

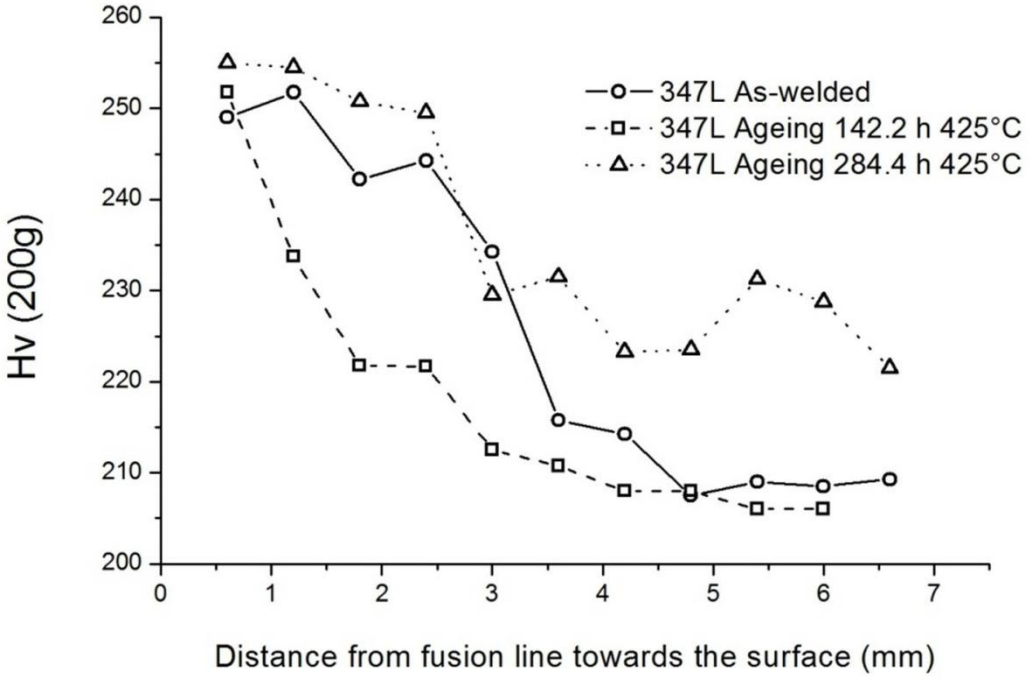

Figure 5-3: Vickers micro-hardness profiles of 347L samples in the as-welded condition and after accelerated ageing at 425 ºC.

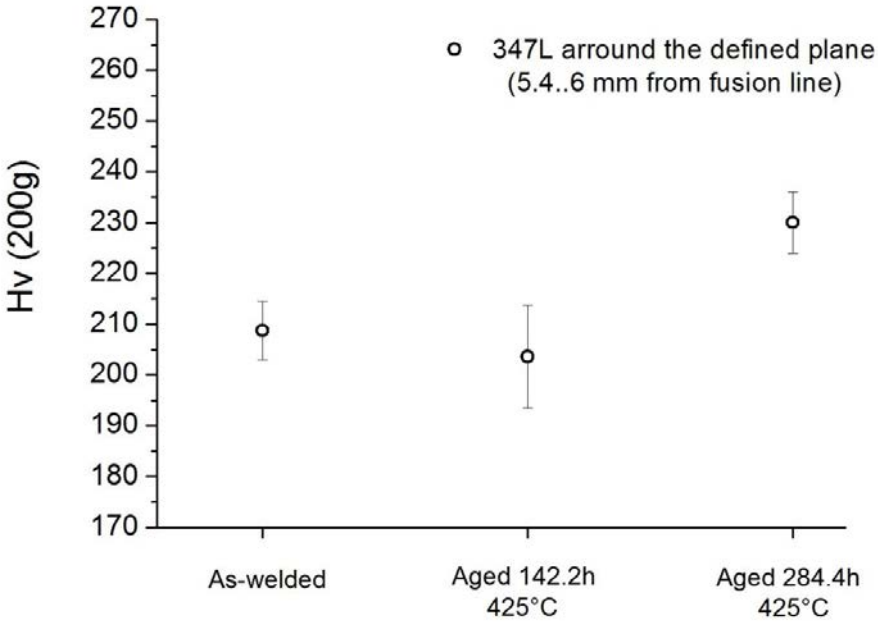

Figure 5-4: Vickers micro-hardness of 347L samples in the lower plateau region of the profile in the as-welded condition and after accelerated ageing at 425 ºC

5.2.2 Type 309L Stainless Steel

As-welded

Figure 5-5 shows the hardness profile obtained for Type 309L stainless steel samples in the as-welded condition from the fusion line towards the surface. Similarly to what was observed for Type 347L samples, higher hardness values with bigger scatter were obtained for the first two millimetres of the cladding. The most noticeable trend was a gradual reduction in hardness until around 3.5 mm from the fusion boundary after which there was a slight increase in hardness towards the sample surface. The 309L weldment was generally softer than the 347L one with the fusion boundary showing an average hardness of 217 Hv whilst the surface gave an average hardness of 195 Hv. As shown in Figure 5-5, the working plane defined for microstructural and corrosion tests is contained in this last region of relatively uniform hardness values.

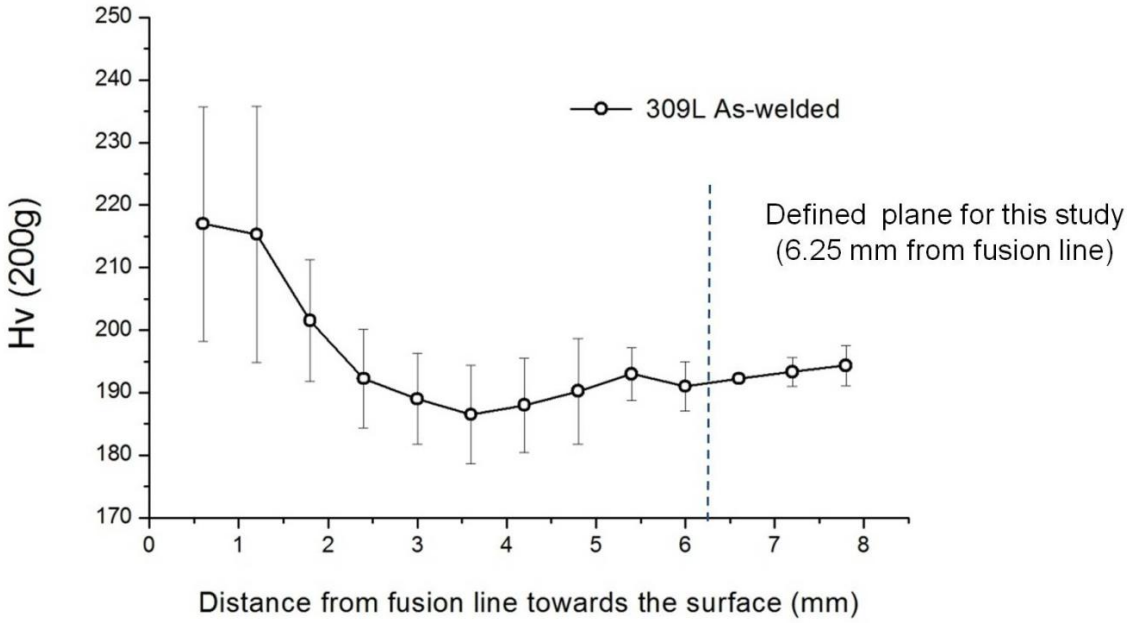

Figure 5-5: Vickers micro-hardness profile of 309L samples in the as-welded condition. Dotted line indicates the position of the plane of interest within the profile (6.25 mm from fusion line towards the surface)

Simulated Service Ageing at 425°C without PWHT

Figure 5-6 shows the hardness profiles obtained for 309L SS after an accelerated ageing at 425ºC for 142.2 h and 284.4 h.

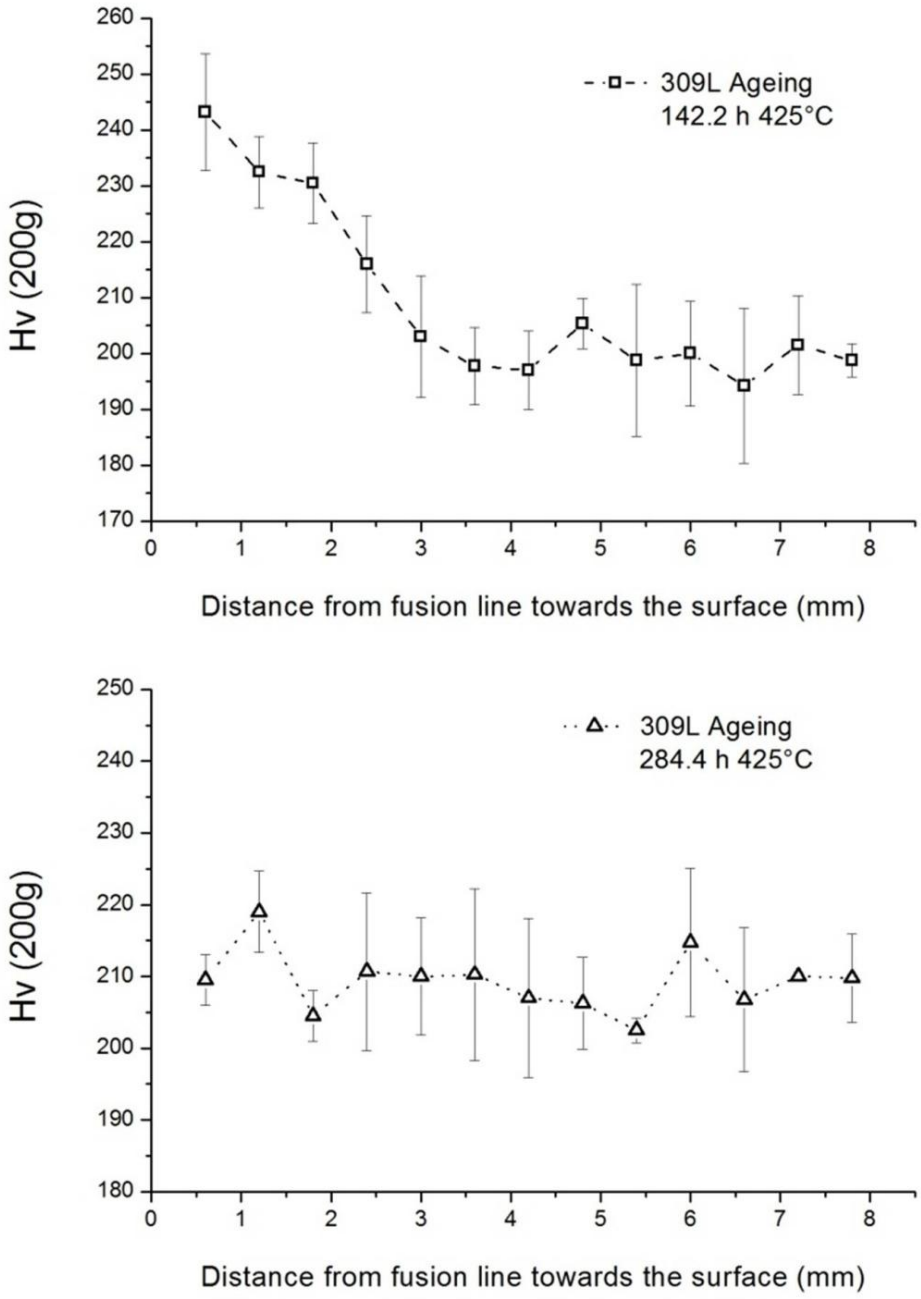

Figure 5-6: Vickers micro-hardness profile of 309L samples after accelerated ageing at 425°C

As shown in Figure 5-6 and Figure 5-7 the effects of ageing at 425°C seem to be more complex for 309L than for 347L. After 142.2 h, there appears to be no stress relief effect as all areas of the sample showed an increase in hardness. However, for

longer ageing time, the region closer to the fusion line seems to soften whereas the region nearer to the surface continues to harden, giving as a result the flatter profile observed for 284.4 h in Figure 5-7. This behaviour is unexpected and further research is required to clarify this issue.

Despite the unexpected behaviour of the region closer to the fusion line, it was possible to observe a significant increase of hardness with ageing time in the lower plateau of the profile, as shown in Figure 5-8.

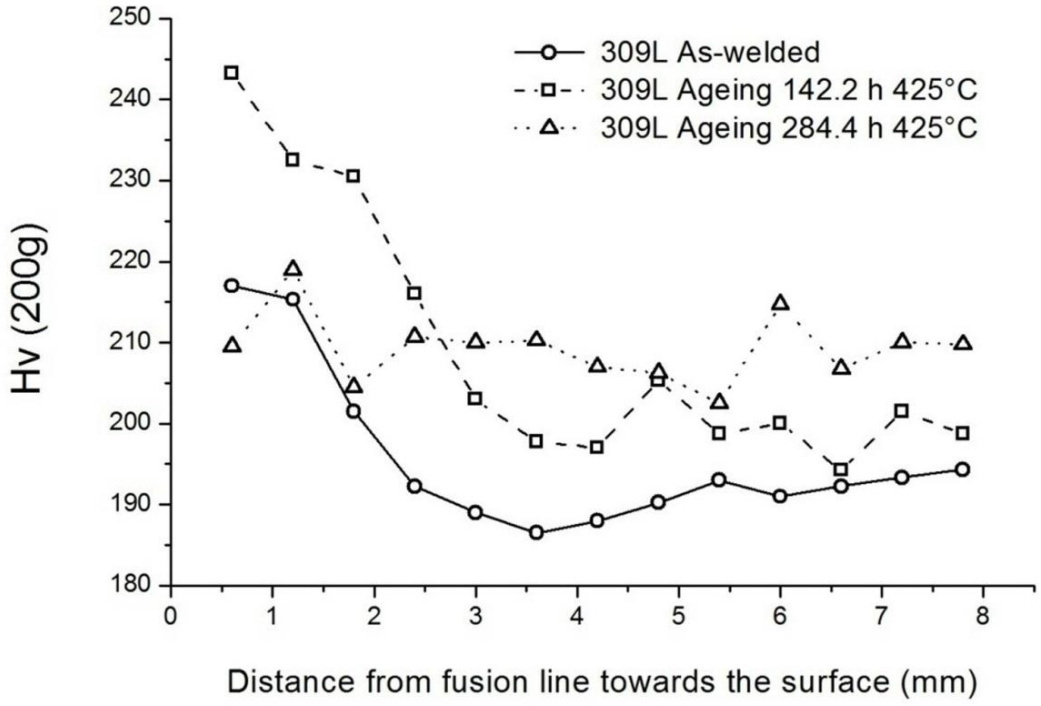

Figure 5-7: Vickers micro-hardness profile of 309L samples in the as-welded condition and after accelerated ageing at 425 ºC.

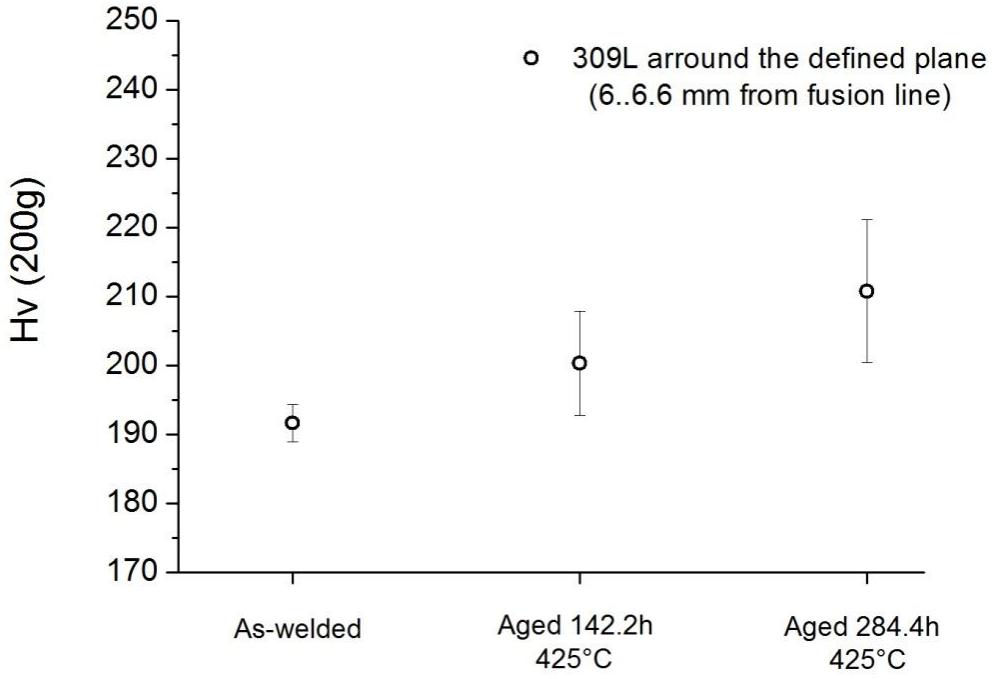

Figure 5-8: Vickers micro-hardness profile of 309L in the lower plateau region of the profile in the as-welded condition and after accelerated ageing at 425 ºC

5.3 Charpy impact testing of weld overlay

In the following sections results obtained for room temperature (24°C) Charpy impact tests performed in both 347L SS and 309L SS are reported for the as-welded condition and following ageing at 425°C for 142.2 h and 284.4 h. It is worth mentioning that since sub-size samples were used due to the limited size of the cladding (5x5x55 mm as per ASTM-E23 standard [162]), the values of the absorbed energy are reported in Joules / mm^2 in order to avoid confusion in their interpretation.

As discussed in Chapter 4, samples were machined from the weld cladding making the notch tip of the samples coincident with the “working plane” defined for

microstructural and corrosion tests in order to reduce the influence of the variability of the microstructure across the weld profile.

5.3.1 Type 347L Stainless Steel

Table 5-1 and Figure 5-9 show the Charpy impact test absorbed energy values obtained for 347L stainless steel samples in the as-welded condition and after accelerated ageing at 425°C.

Table 5-1: Room temperature Charpy impact energy of 347L stainless steel in the as-welded condition and after accelerated ageing at 425°C

347L Absorbed Energy (Joules / mm^2)	*As-welded*	*Aged 142.2h 425°C*	*Aged 284.4h 425°C*
	0.71	0.66	0.63
	0.75	0.71	0.64
	0.78	0.71	0.64
	0.75		
Mean	0.75	0.69	0.64
SD	0.03	0.03	0.01

The highest impact energy for 347L was obtained in the as-welded condition. Samples that were aged at 425ºC showed a reduction of the impact energy with ageing time, with an average loss of 8.0 % and 14.7% of the as-welded energy after 142.2 h and 284.4 h respectively.

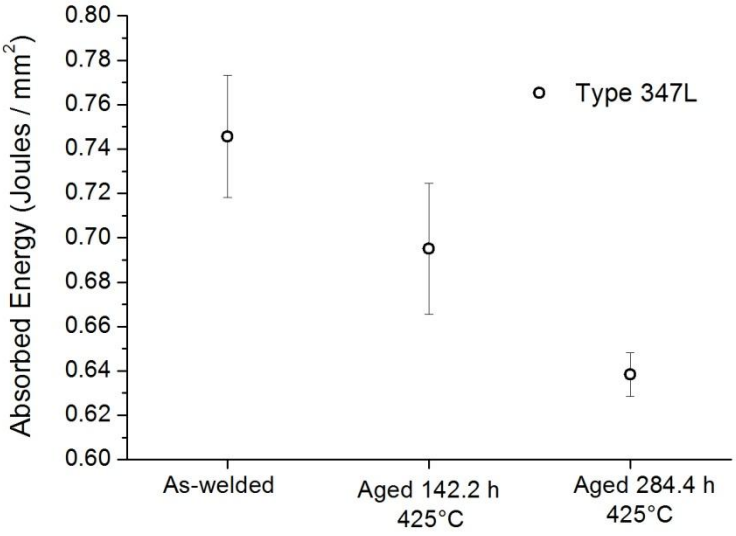

Figure 5-9: Room temperature Charpy impact energy of Type 347L stainless steel specimens aged at 425°C

5.3.2 Type 309L Stainless Steel

Table 5-2 and Figure 5-10 show the Charpy impact test absorbed energy values obtained for 309L samples in the as-welded condition and after accelerated ageing at 425°C for 142.2 h and 284.4 h.

Table 5-2: Room temperature Charpy Impact energy of 309L stainless steel in the as-welded condition and after accelerated ageing at 425°C

309L Absorbed Energy (Joules / mm^2)	*As-welded*	*Aged 142.2h 425°C*	*Aged 284.4h 425°C*
	0.64	0.58	0.53
	0.70	0.54	0.53
	0.71	0.61	0.54
Mean	0.68	0.58	0.53
SD	0.04	0.03	0.01

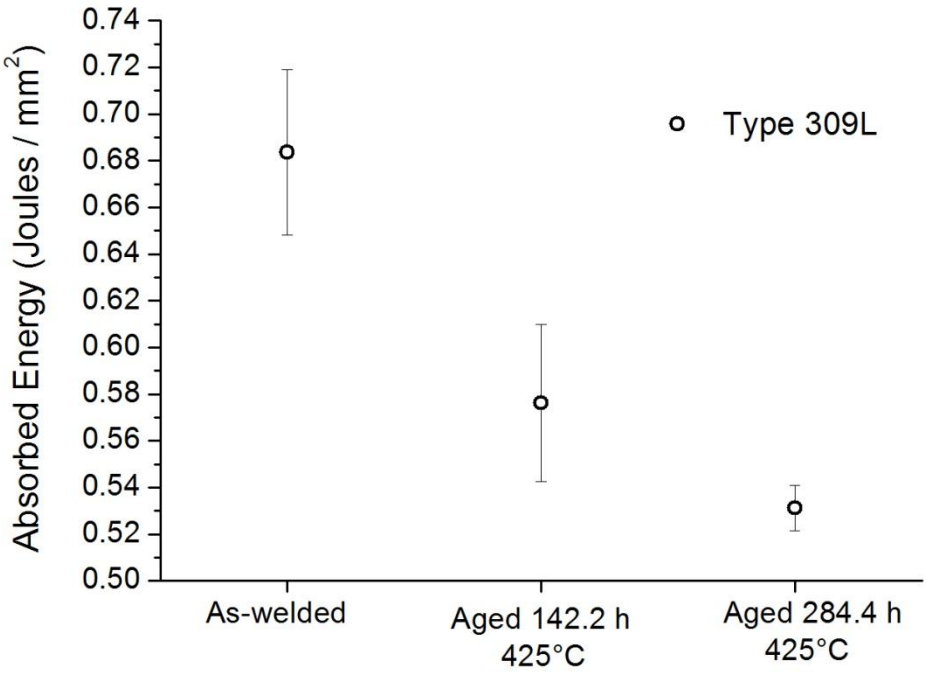

Figure 5-10: Room temperature Charpy impact energy of sub-size Type 309L stainless steel specimens aged at 425°C

Similarly to what was observed in Type 347L stainless steel, the highest impact energy of 309L stainless steel samples was observed in the as-welded condition (Figure 5-10). Ageing at 425ºC of Type 309L stainless steel samples produced an average reduction of the impact energy of 14.7% after 142.2h and 22.1% after 284.4h. As it can be appreciated impact values found for 309L were lower than those of 347L despite the latter showed higher hardness. This finding is unexpected and will be further discussed in Section 5.5.

5.4 Fractographic analysis of Charpy samples

In the following sections, fracture surfaces obtained after Charpy impact tests are analyzed by SEM and EDS in order to establish the fracture mode and characteristics. The evolution of these features is followed during ageing at 425°C.

5.4.1 Type 347L Stainless Steel

As seen in Figure 5-11, frature surface of 347L in the as-welded condition showed an homogeneous morphology consistent with a ductile fracture initiated by spherical inclusions. The compositional analysis of these inclusions performed by EDS showed that they are mainly formed by manganese, oxygen, and silicon, allowing them to be associated to manganese silicates, as observed in Chapter 4. This result cannot be taken as definitive due to the limitations of EDS for quantifying light elements (Z<11) like oxygen [167]. However, the size of the oxygen peak found in all the analyzed particles support the idea that this element is contained in these inclusions. Size and shape of the particles are also coincident with those observed in Chapter 4.

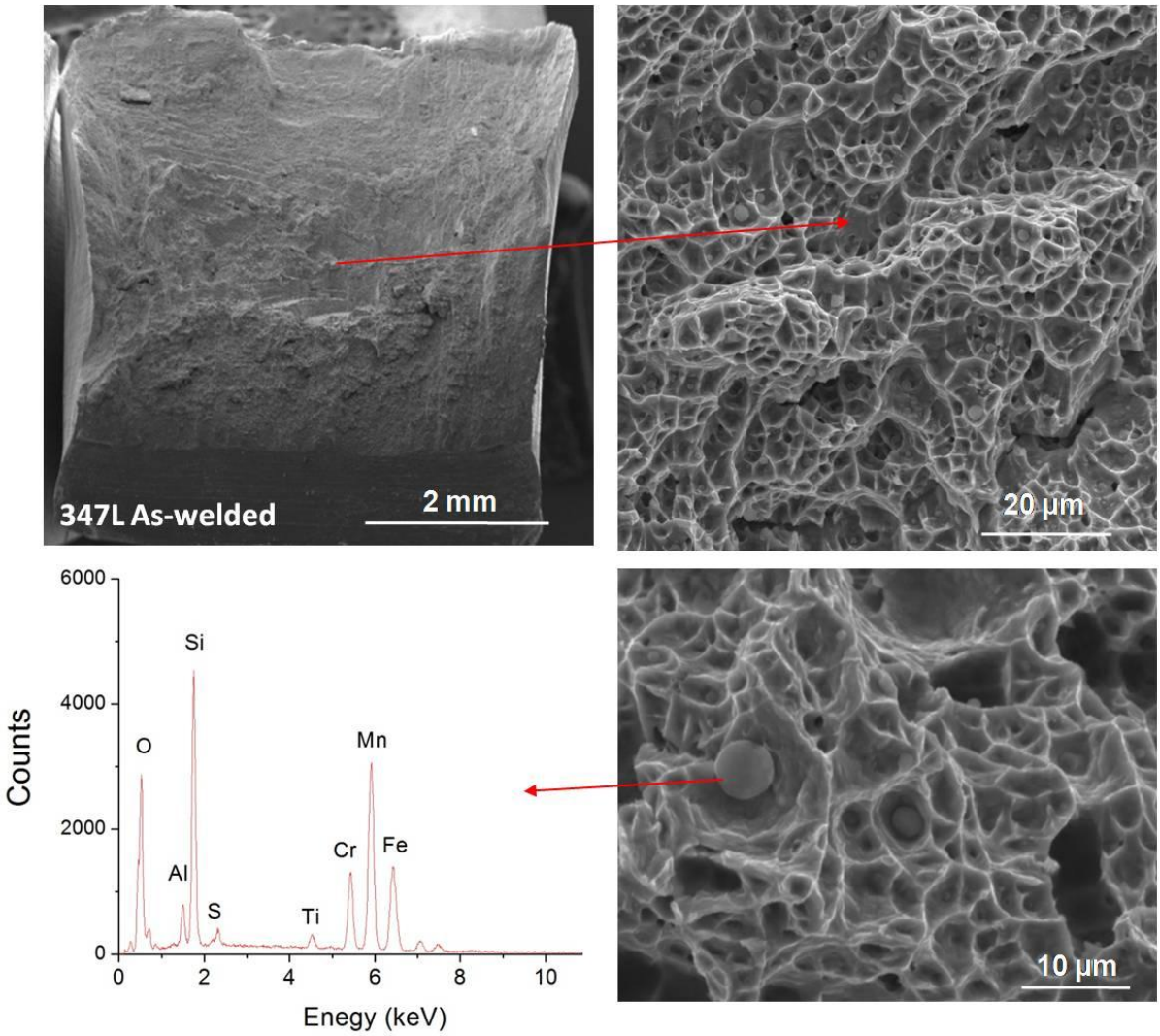

Figure 5-11: Fractography of 347L in the as-welded condition

The evolution of 347L fracture surface during ageing at 425°C is shown in Figure 5-12 for 142.2 h of treatment and in Figure 5-13 for 284.4 h. In both cases the fracture mode was found to be ductile and initiated by the same manganese silicate particles. Fracture surface of aged samples was found to be flatter than that of the as-welded condition suggesting that less plastic strain is involved in the fracture process. As discussed in Section 5.5, this is in agreement with the lower absorbed energy shown by these samples.

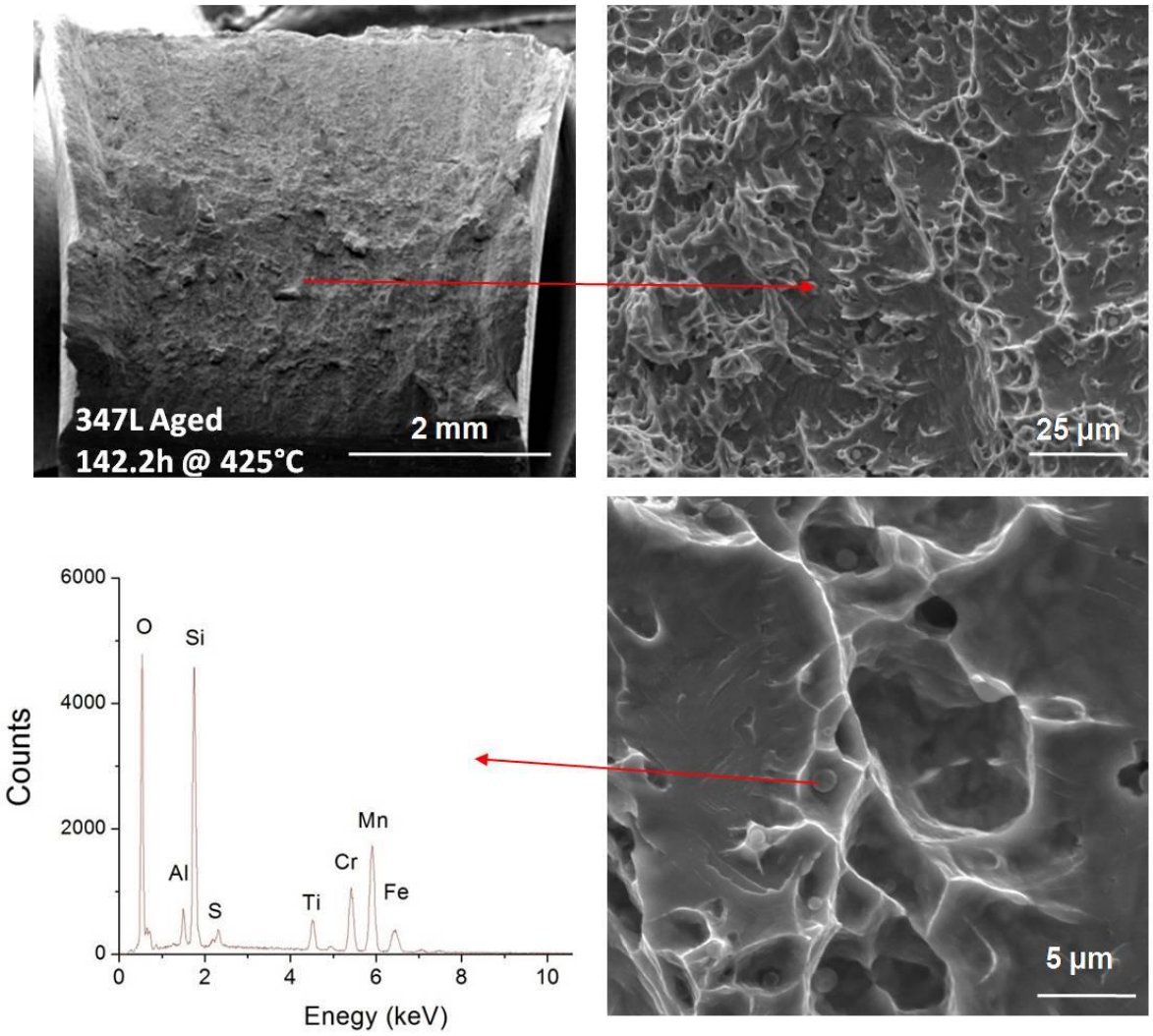

Figure 5-12: Fractography of 347L after accelerated ageing at 425°C for 142.2h

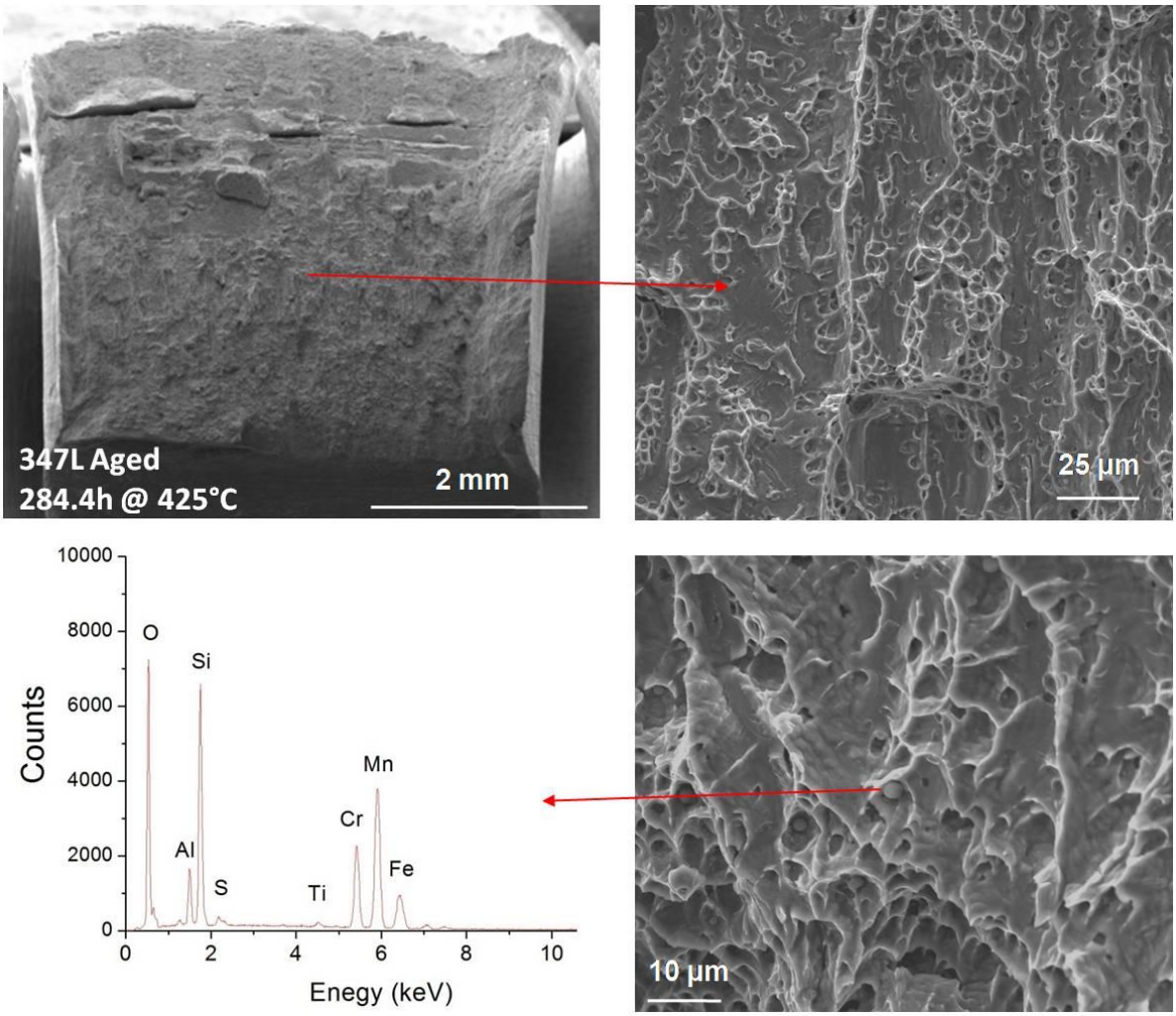

Figure 5-13: Fractography of 347L after accelerated ageing at 425 °C for 284.4 h

As shown in Figure 5-14, a banded morphology parallel to the fracture propagation direction was observed on aged samples in comparison to the isotropic morphology observed in as-welded samples. The width of the observed bands (pointed out in red dotted lines in Figure 5-14) was found to be in the range of 10 µm to 20 µm, comparable to the size of the delta ferrite dendrites observed in Chapter 4, which are also aligned in the same direction. This observation will be further discussed in Section 5.5 of the present chapter.

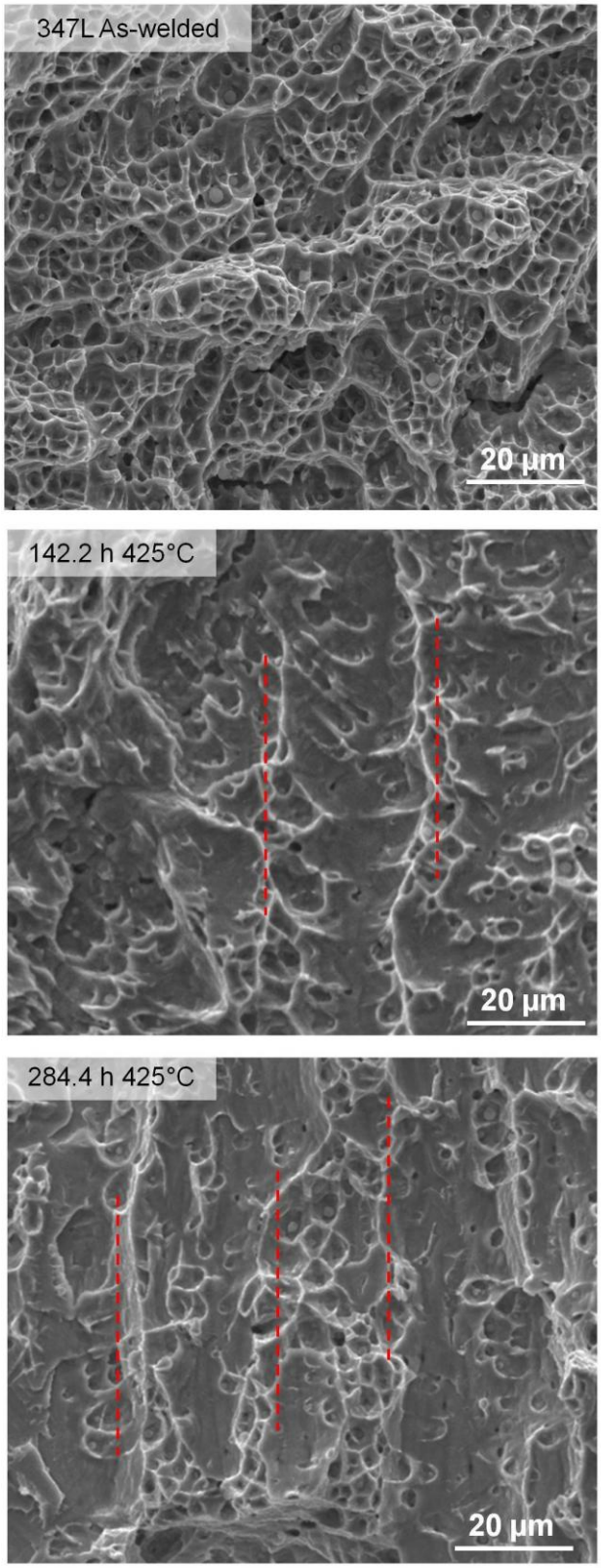

Figure 5-14: Comparison of the fracture morphologies observed in 347L in the as-welded condition and after accelerated ageing at 425°C.

5.4.2 Type 309L Stainless Steel

Figure 5-15 shows the morphology observed in 309L samples in the as-welded condition following Charpy impact test. Similar to what was described for 347L, a ductile fracture originated at Mn silicates was observed.

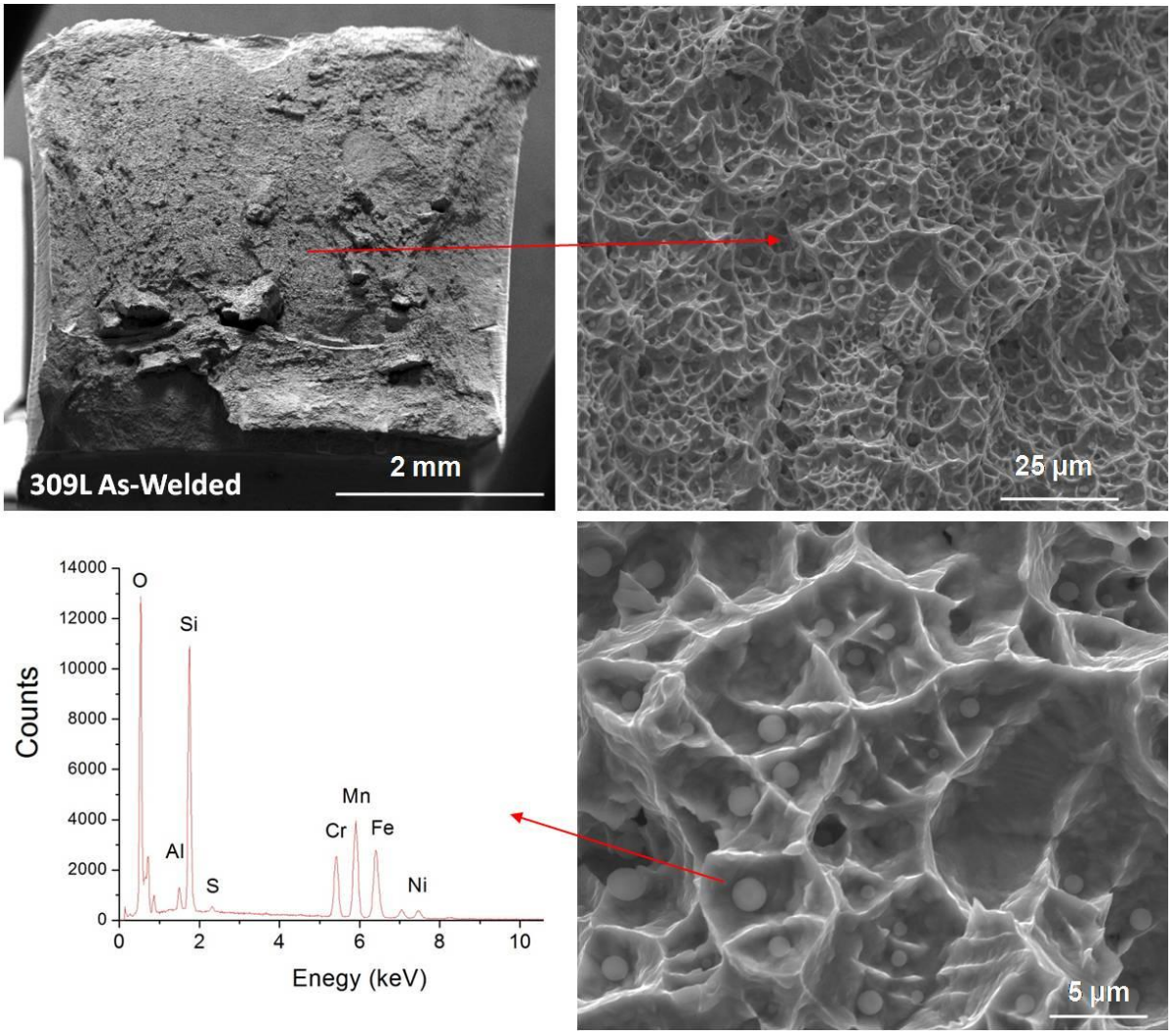

Figure 5-15: Fractography of 309L in the as-welded condition

Figure 5-16 and Figure 5-17 show the fracture morphology observed in 309L samples aged at 425°C for 142.2 h and 284.4 h respectively. A rougher surface was observed after 142.2 h than that of 347L under the same ageing time, which would be consistent with a higher value of absorbed energy unlike what was observed in Section 5.3. After 284.4 h, 309L morphology observed was slightly smoother than that of the same material in shorter ageing time (consistent with lower absorbed energy) but again rougher than 347L for the same treatment time. This finding is unexpected and will be further discussed in Section 5.5.

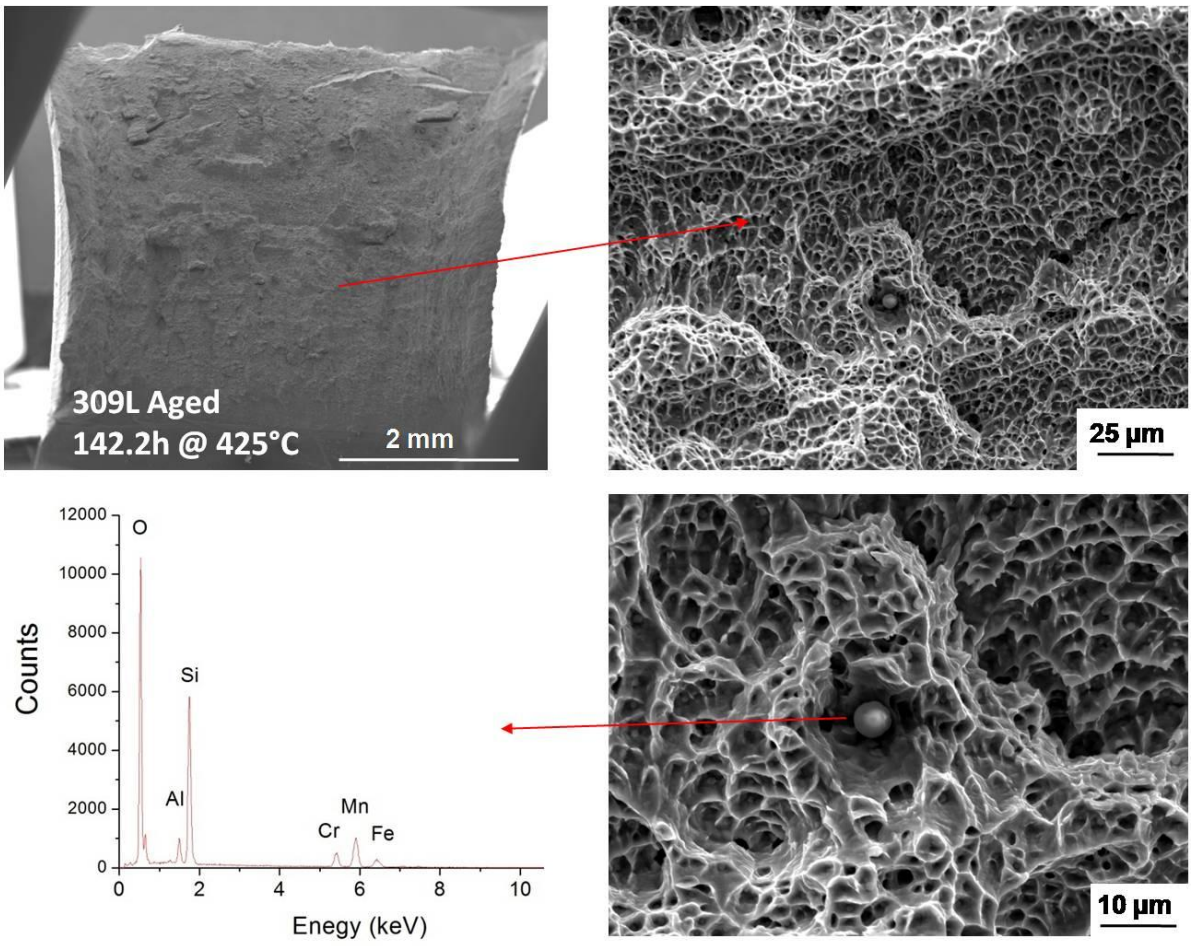

Figure 5-16: Fractography of 309L after accelerated ageing at 425°C for 142.2h

Figure 5-17 shows the fracture surface observed in 309L samples aged at 425°C for 284.4 h.

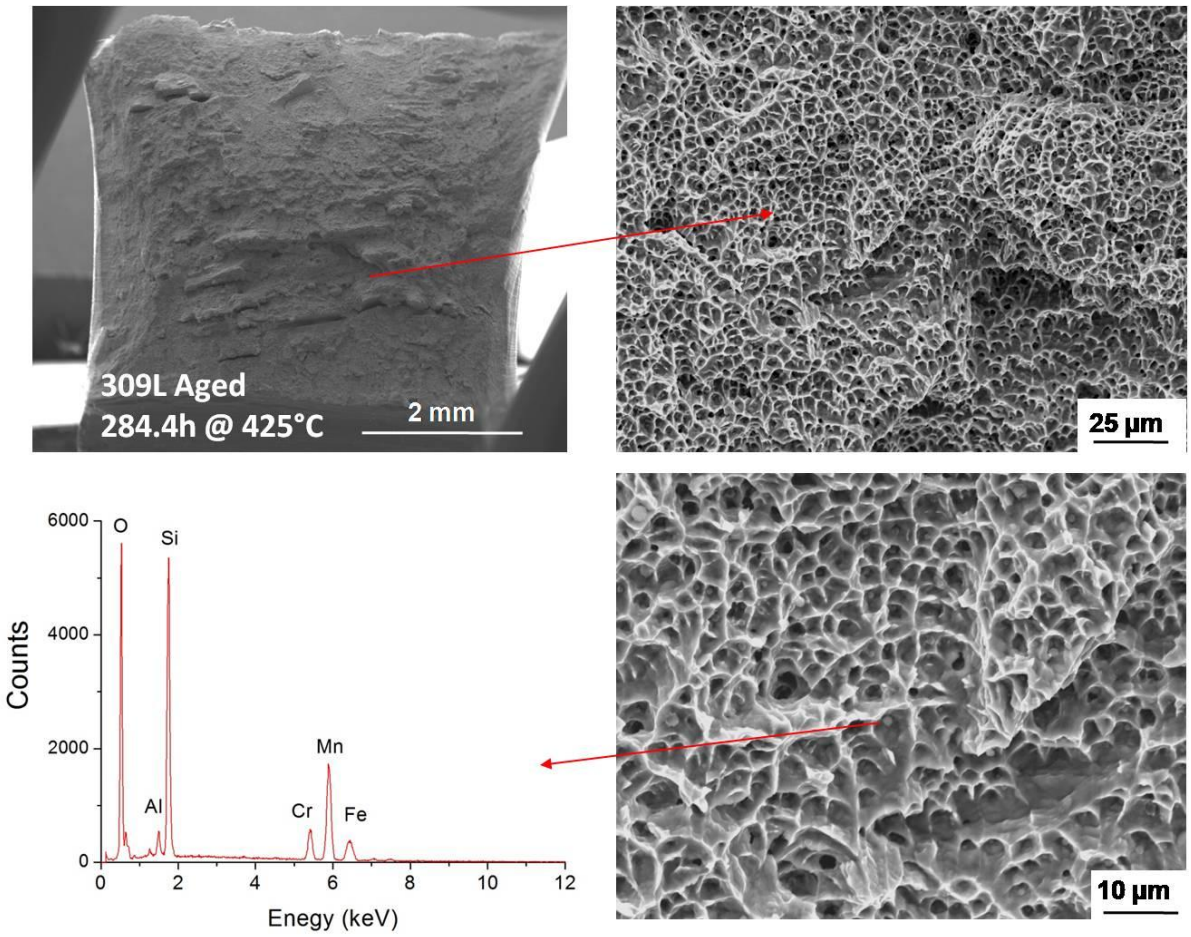

Figure 5-17: Fractography of 309L after accelerated ageing at 425°C for 284.4h

Unlike the banded structure parallel to the crack propagation direction observed in 347L, homogeneous fracture surfaces were observed in 309L in all ageing conditions as shown in Figure 5-18. This unexpected difference will be also discussed in Section 5.5.

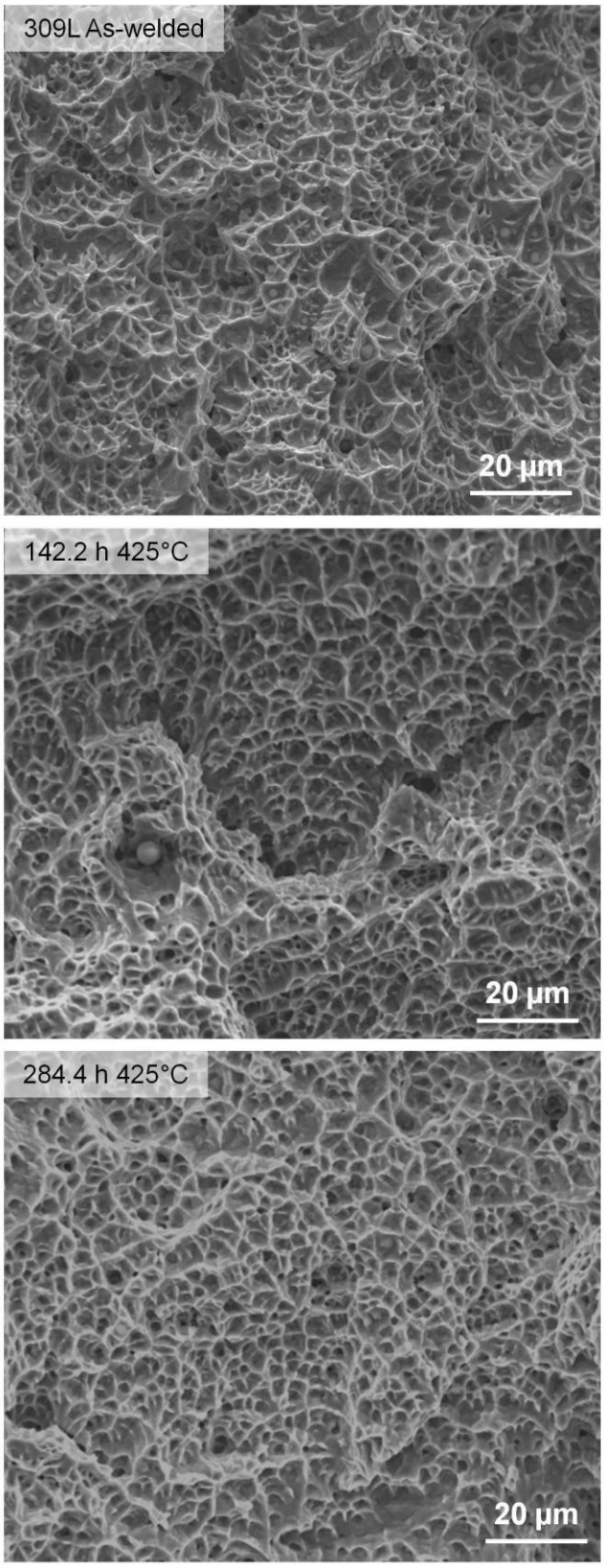

Figure 5-18: Comparison of the fracture morphologies observed in 309L in the as-welded condition and after accelerated ageing at 425°C for 142.2 h and 284.4h

5.5 Discussion on Mechanical Properties Evolution

5.5.1 Graphical summary

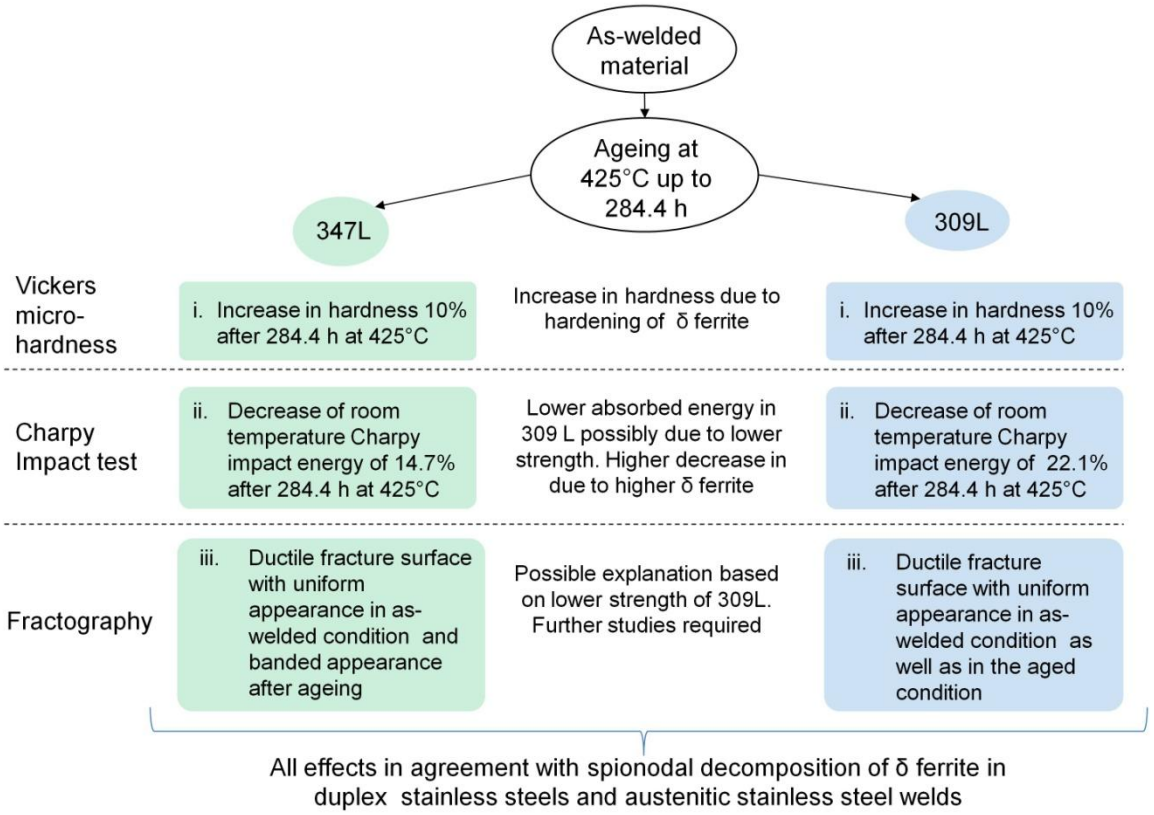

5.5.2 Vickers micro-hardness profiles

Hardness profiles were obtained in order to study the variation of this property from the fusion line towards the surface (i.e. considering the effect of the microstructure variations observed in Chapter 4) and to follow its evolution during ageing at 425ºC in order to simulate service conditions at 300ºC for 30 and 60 years.

Figure 4-12 and Figure 5-5 in Section 5.2 shows the profiles obtained for the as-welded samples of 347L and 309L respectively. A region of higher values and a large scatter in the measurements was observed closer to the fusion line. In this region the

stainless steel is mixed together with the carbon steel base material during deposition of the weld giving as a result a very heterogeneous structure in terms of both chemical composition and constituent phases (see Chapter 4). In the case of 347L an upper plateau with hardness in the range of 240-270 Hv is observed up to 3 mm from the fusion line, where a reduction is observed until a lower plateau is reached at approximately 5 mm from fusion line with values in the range of 200-220 Hv. In 309L, a reduction of hardness is observed up to ~3.5 mm from the fusion line where a slight increase of hardness was observed towards the sample surface.

In the region closer to the surface a flatter behaviour was observed in the microhardness profiles of both materials also showing lower scatter in the measurements. Again this observation can be associated with the higher homogeneity in microstructure and chemical composition detected for this region in Chapter 4, which correspond to the upper part of the second weld layer. The smaller variation found in hardness values, in addition to the higher uniformity in composition and microstructure of this region, support the idea of using the planes defined in Chapter 4 (5.55 mm from the fusion line for 347L and 6.25 mm for 309L) as a suitable location for corrosion tests and to obtain a consistent comparison among microstructure, mechanical properties and corrosion properties.

When 347L was aged for 142.2 h at 425°C a softening of the region closer to the fusion line was observed while no major changes occurred closer to the surface. This observation is consistent with a thermal relief of the most stressed area of the sample. When this ageing was extended to 284.4 h hardening of both regions was

observed. The behaviour of 309L material with ageing time was more complex since in the first stage of ageing no thermal relief was observed showing an increase in hardness for all the regions of the sample. After 284 h the region closer to the fusion line showed a softening while the region closer to the surface continued to harden. The behaviour of the fusion line region of 309L is unexpected and more research is required to clarify this issue.

As shown in Table 5-3 (obtained from Figure 5-4 and Figure 5-8), a small but significant increase in hardness was observed in the surface region of both 347L and 309L materials after ageing 284.4 h at 425ºC.

Table 5-3: Vickers hardness obtained for all ageing conditions and variation compared to the as-welded condition

347L	*As-welded*	*Aged 142.2h 425°C*	*Aged 284.4h 425°C*
Vickers Micro-hardness (Hv_{200g})	209 ± 6	204 ± 10	230 ± 6
Variation (to as-welded condition)	0	- 2.5 %	+ 10.0 %
309L	*As-welded*	*Aged 142.2h 425°C*	*Aged 284.4h 425°C*
Vickers Micro-hardness (Hv_{200g})	192 ± 3	200 ± 8	211 ± 10
Variation (to as-welded condition)	0	+ 4.2 %	+ 9.9 %

These observations are in agreement with the increase in hardness due to spinodal decomposition of the ferritic phase reported by different authors in duplex stainless steels [51, 53, 105, 107, 109, 110] and austenitic stainless steel welds [52, 111] after ageing in the same temperature range. Using nano-hardness measurements Vitek et al.[52] showed that the general increase in hardness in 308 stainless steel weld metal can be attributed to the increase in hardness of the ferritic phase, while the hardness of austenite remains constant even after 10,000 h of ageing at 475°C. This behaviour is explained by the authors based on the fact that spinodal decomposition takes place in δ ferrite during low temperature ageing, whereas no transformations occur in the austenitic phase. Similar conclusions were reached by Yamada et al. [109] who also indicated a two stage process in the hardening of the ferritic phase in a series of molybdenum-containing duplex stainless steels. First stage (up to 3000 h at 400ºC) was associated to spinodal decomposition and produced the higher increase in hardness (up to 150%), whereas precipitation of G phase was indicated to be responsible for a further hardening in the later stages of ageing. Hardening observed in the present study could be associated to spinodal decomposition of the ferritic phase since no G-phase is expected due to the relatively short ageing times applied.

5.5.3 Charpy impact tests

Embrittlement of duplex stainless steels and cast austenitic stainless steels is reported in literature as the other major effect of ageing in the lower temperature range (300°C-450°C) due to spinodal decomposition [52, 110-112]. A permanent decrease in the impact energy absorbed during room temperature Charpy tests was

observed for both 347L and 309L as a function of ageing time at 425°C (see Table 5-4).

Table 5-4: Charpy impact energy obtained for all ageing conditions and variation compared to the as-welded condition

347L	*As-welded*	*Aged 142.2h 425°C*	*Aged 284.4h 425°C*
Absorbed Energy in Charpy test (Joules / mm2)	0.75 ± 0.03	0.69 ± 0.03	0.64 ± 0.01
Variation (to as-welded condition)	0	- 8.0 %	-14.7 %
309L	*As-welded*	*Aged 142.2h 425°C*	*Aged 284.4h 425°C*
Absorbed Energy in Charpy test (Joules / mm2)	0.68 ± 0.04	0.58 ± 0.03	0.53 ± 0.01
Variation (to as-welded condition)	0	- 14.7 %	-22.1 %

The fact that 309L showed lower absorbed energy in comparison to 347L for any ageing time despite 347L were found to have higher hardness is unexpected and should then be analyzed.

As seen in Figure 5-16 and Figure 5-17 fracture surfaces of 309L after ageing for 142.2 and 284.4 h were found to be rougher than those of 347L in an equivalent ageing condition (Figure 5-12 and Figure 5-13) indicating a higher plastic strain involved in the fracture process what would correspond to higher absorbed energy, unlike what was observed in Section 5.3

A possible explanation to these observations could be based on a difference in the strength levels of both alloys. If 309L had a significantly lower strength than 347L, it could show a lower hardness and a rougher fracture surface, since less amount of energy would be required to reach equivalent levels of plastic strain. No tensile tests have been performed in the present work and are considered for future research.

Nominal values in the as-welded condition [8, 168] show a difference in the ultimate tensile strength (UTS) of both materials (637 MPa for 347L and 572 MPa for 309L). However, this difference might not be enough to support the above described explanation. An additional contribution to lower strength in 309L could be provided by the higher heat input during fabrication of this material in comparison to 347L. A higher deposit thickness was obtained for 309L coupon as shown in Chapter 4. This higher thickness implies a higher heat input, which is in turn associated to lower cooling rates that could have led to a softer material with bigger austenitic grains, which also absorb less energy. It is generally accepted that grain growing during welding leads to materials with lower toughness and strength [169]. However, the proposed explanation should be confirmed by both tensile tests and a comparative study of austenitic grain size.

In the present work, reduction of impact energy was found to be more severe in 309L than in 347L. Considering the higher content of δ ferrite found for 309L in Chapter 4, these observations are in agreement with previous work [105, 109, 170] where the content of ferrite was indicated to be in direct relation with the reduction of impact energy during ageing due to the hardening of this phase in contrast to the lack of microstructural changes occurring in the austenite.

The effect of a hardened network of delta ferrite as a result of ageing in the fracture behavior of duplex and cast austenitic stainless steels is worthy of analysis. It has been reported in literature that the increase in hardness of δ ferrite produces an increase in the transition temperature and a decrease in the upper shelf energy of these materials [51, 105, 170, 171]. According to Strangwood and Druce [51] and Alexander and Nanstad [170] the increase in the transition temperature is explained by the ease of fracture and the promotion of cleavage in the δ ferrite phase, which is embrittled as a result of spinodal decomposition. However, this explanation does not apply for the reduction of the upper shelf energy where the fracture mode is ductile and should be therefore controlled by the austenitic matrix [51, 57, 170]. In this case, the authors indicated that the higher hardness of δ ferrite gives a higher constraint to the austenite, reducing then the energy absorbed in the fracture process. In addition, this process can lead to the formation of strain-induced martensite ahead of the crack tip providing a low energy propagation path. Reduction of absorbed energy due to the hardened network of delta ferrite could be understood in a similar way than the reduction of toughness in ductile materials due to an increase on the level of stress triaxiality [172, 173].

Fracture surfaces obtained in the present work for both materials in all ageing conditions showed a ductile behavior, with voids initiated at manganese silicate particles and propagated by void coalescence (see Section 5.4). This indicates that room temperature is above the transition temperature in all ageing conditions. Therefore, the reduction of the impact energy observed in aged samples could be explained in the same way as the previously described reduction of the upper shelf energy, i.e. by an increase in the constraint imposed by the hardened δ ferrite.

The banded structure found in 347L after ageing (Figure 5-14) could support this idea. Although the data obtained in this study are not enough to establish the crack propagation path in this material, it could be inferred from Figure 5-14 that in the aged condition the fracture propagated mainly through the austenitic matrix in a ductile way but absorbing less energy leaving the smoother surfaces observed between the parallel bands indicated in Figure 5-14 which can be associated to the δ ferrite strings, having a similar size and the same orientation than the vermicular ferrite shown in Chapter 4 for this material. On the other hand, in the as-welded condition, the delta ferrite is not hardened, providing no additional constraint to ductile propagation and leading to the uniform fracture surface shown in Figure 5-14 for the as-welded sample.

Fracture surface of 309L showed a uniform appearance both in the as-welded and aged condition. The possible explanation to this behaviour based on the lower strength of this material was already discussed in this section. Further studies are

required to confirm the fracture mechanism and unequivocally identify the crack propagation path of the studied samples

5.6 Conclusions

Vickers micro hardness and Charpy impact tests were used to follow the evolution of mechanical properties of 347L and 309L austenitic stainless steel welds (ASSWs) during accelerated ageing at 425°C simulating service conditions for 30 and 60 years at 300°C of non-post welded heat treated material.

The following conclusions can be drawn from the present study:

1) An increase in hardness and a decrease of absorbed energy during impact test as a function of ageing time at 425°C was observed for both 347L and 309L. This finding is in agreement with the variations reported due to spinodal decomposition and precipitation and growth of α and α´ in the ferritic phase of duplex stainless steel and ASSWs, which are the expected transformations for these materials in the referred temperature range.

2) A high scatter in hardness measurements was observed in the region closer to the fusion line of both materials. This scatter was associated to the microstructural inhomogenity of the mixed zone between carbon steel and the first weld layer of stainless steel. Lower scatter was observed in the vicinity of the plane defined for microstructural and corrosion tests (i.e. 5.55 mm from fusion line towards the surface in 347L and 6.25 mm in 309L).

3) The increase in hardness observed (10% average after 284.4 h at 425°C) was similar for both 347L and 309L

4) Despite the reduction in absorbed energy observed after ageing at 425ºC, fractures were found to be ductile in both the as-welded and aged condition for 347L and 309L materials. All fractures were initiated at spherical particles of manganese silicate, as identified in Chapter 4

6 Corrosion Properties of Stainless Steel Cladding Materials following Post-Weld Heat Treatment and Accelerated Ageing

6.1 Introduction

The objective of the present work is to follow the evolution of the intergranular corrosion resistance of weld cladding materials used in reactor pressure vessels (RPV) through all stages of fabrication and service conditions they could be exposed to during their operational life.

The standardized fast screening technique "*ASTM 262-practice A"* [150] was used as a first approach and double loop electrochemical potentiokinetic reactivation test (DLEPR) was also used to complement the ASTM technique, with the aim of providing quantitative information on the variations in the corrosion properties for each applied treatment.

Further development of DLEPR was carried out to study its capability to detect δ ferrite-derived phases (mainly $M_{23}C_6$ and σ phase) in austenitic stainless steel welds (Section 6.4). A purpose-designed potentiokinetic electrochemical cycle was applied in order to link specific DLEPR parameters with selective attack of $M_{23}C_6$ and σ phase.

In order to study the microstructural changes and the effect on corrosion properties produced by the complex combination of fabrication and service conditions, samples of 347L and 309L stainless steel claddings were prepared as described in Chapter 3 and subjected to three different thermal treatments:

4) *Simulated service Ageing at 425°C without PWHT*

This treatment simulates 60 years of service at 300°C in an accelerated way by ageing as-received samples for 284.4 h at 425°C, according to the Arrhenius equation described in Chapter 3. In addition, a set of samples aged for 142.2 h at the same temperature was also tested to provide more information about the evolution of the process.

5) *PWHT – ageing 600°C up to 100 h*

This treatment is the same as that applied to the whole pressure vessel after welding the forged rings, which are clad individually. In most RPV specifications, PWHT time at 600°C is around 40 h. In the present study PWHT time was extended up to 100 h in order to have a better understanding of the microstructural changes and modifications to the corrosion properties produced by the treatment.

6) *Further ageing for 284.4 h at 425°C of samples that had been given a PWHT for 40 h at 600°*

This treatment represents the real conditions to which RPV clad surfaces are subjected during fabrication and service. As a first step, samples were PWHT at 600°C for 40 h representing the fabrication conditions as previously described. Later, these treated samples were subjected to accelerated ageing at 425°C for 284.4 h in order to simulate 60 years of service at 300°C.

6.2 Determination of susceptibility to intergranular corrosion through ASTM 262-practice A method

The ASTM 262-practice A [150] method is a fast screening test used to detect materials that are resistant to intergranular corrosion and therefore can be excluded from further examination. This qualitative test, also called “Oxalic Acid Test” is always used prior to applying one of the other practices contained in this standard (from Practice B to Practice F) which are more complicated and time consuming, in order to save effort. In the present work, ASTM 262-practice A is applied to 347L and 309L samples subjected to all thermal treatments described in Section 6.1.

6.2.1 Type 347L SS

As-welded

Figure 6-2 shows results of the oxalic acid test applied to 347L in the as-welded condition. It can be noticed that in this condition the austenitic phase (γ – light grey matrix in the image) was more attacked than the δ ferrite dendrites (dark grey), leaving this last phase standing up from the surface. This finding is further discussed in Section 6.5 in terms of the relative Pitting Resistance Equivalent with Nitrogen (PRE_N) of each phase. In addition to γ and δ, a few shallow etch pits were also identified. According to ASTM A262 standard, the resulting microstructure can be classified as isolated ferrite islands and considered “acceptable” since no inter-phase ditches were found.

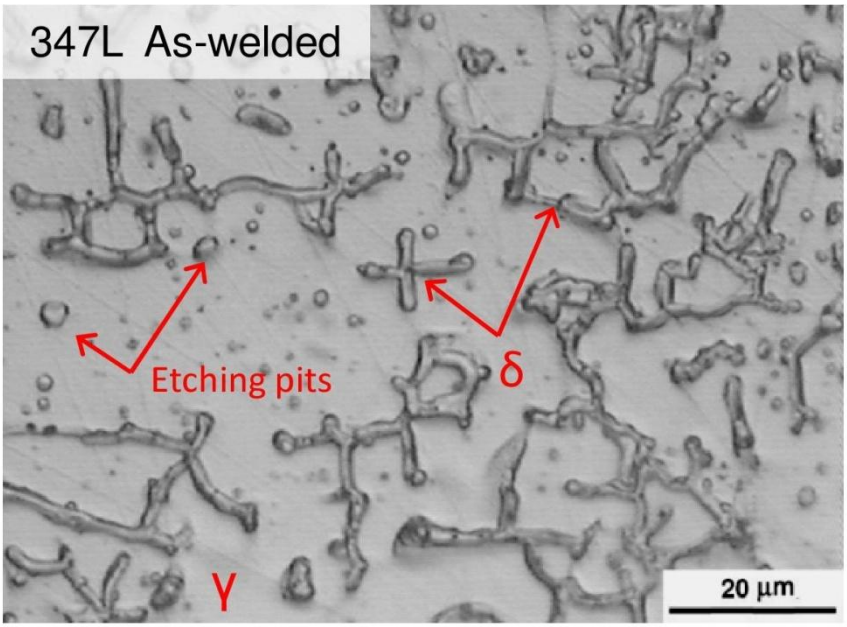

Figure 6-1: Optical micrograph following oxalic acid testing [150] applied to 347L in the as- welded condition.

Simulated service ageing at 425°C without PWHT

Figure 6-2 shows the resulting microstructures following oxalic acid test applied to 347L after ageing for 142.2 h and 284.4 h at 425°C. No inter-phase ditches were found for both ageing times. Therefore, all microstructures found can be classified as “isolated ferrite islands” according to [150]; which means the material is not sensitized in terms of this practice.

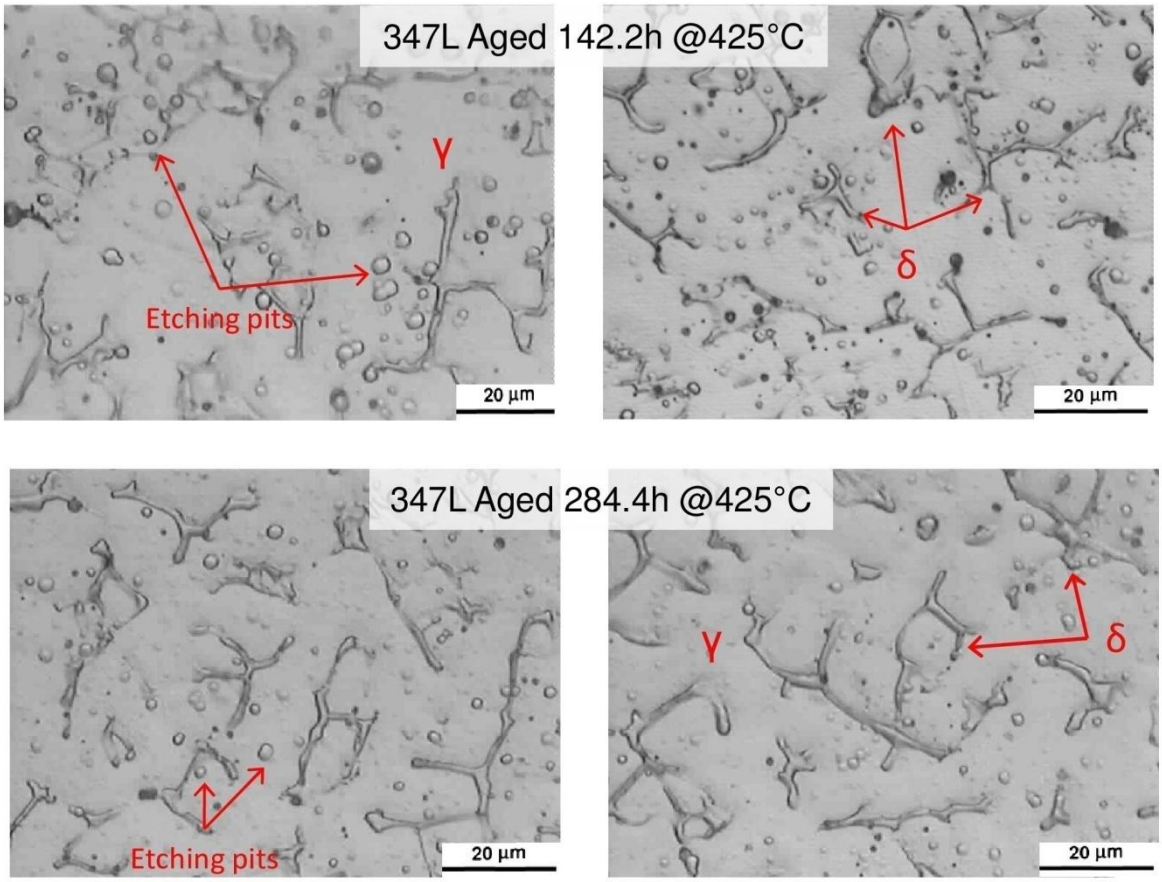

Figure 6-2: Optical micrograph following oxalic acid testing [150] applied to 347L samples after ageing at 425°C. Two characteristic micrographs are shown for each ageing time.

PWHT – Ageing 600°C up to 100 h

Figure 6-3 shows results of ASTM 262 –practice A applied to 347L after PWHT at 600°C for different periods of time. In the as-welded condition (0 h of treatment) the microstructure corresponds to “isolated ferrite islands” (shown as δ in the figure) with δ ferrite standing above the surface, as previously described. As the ageing treatment is carried out for increasing times, interphase ditches were observed for 1 h, 10 h and 25 h. After 40 h of treatment a “dual” microstructure was observed,

showing both isolated ferrite islands as well as interphase ditches. This dual microstructure changed again to only interphase ditches after 100 h of treatment at 600°C.

It can be said that 347L samples are acceptable in the as-welded condition, became “suspect” when they are treated at 600°C for up to 25 h, recover their acceptability at 40 h and turn again to be “suspect” after 100 h of treatment.

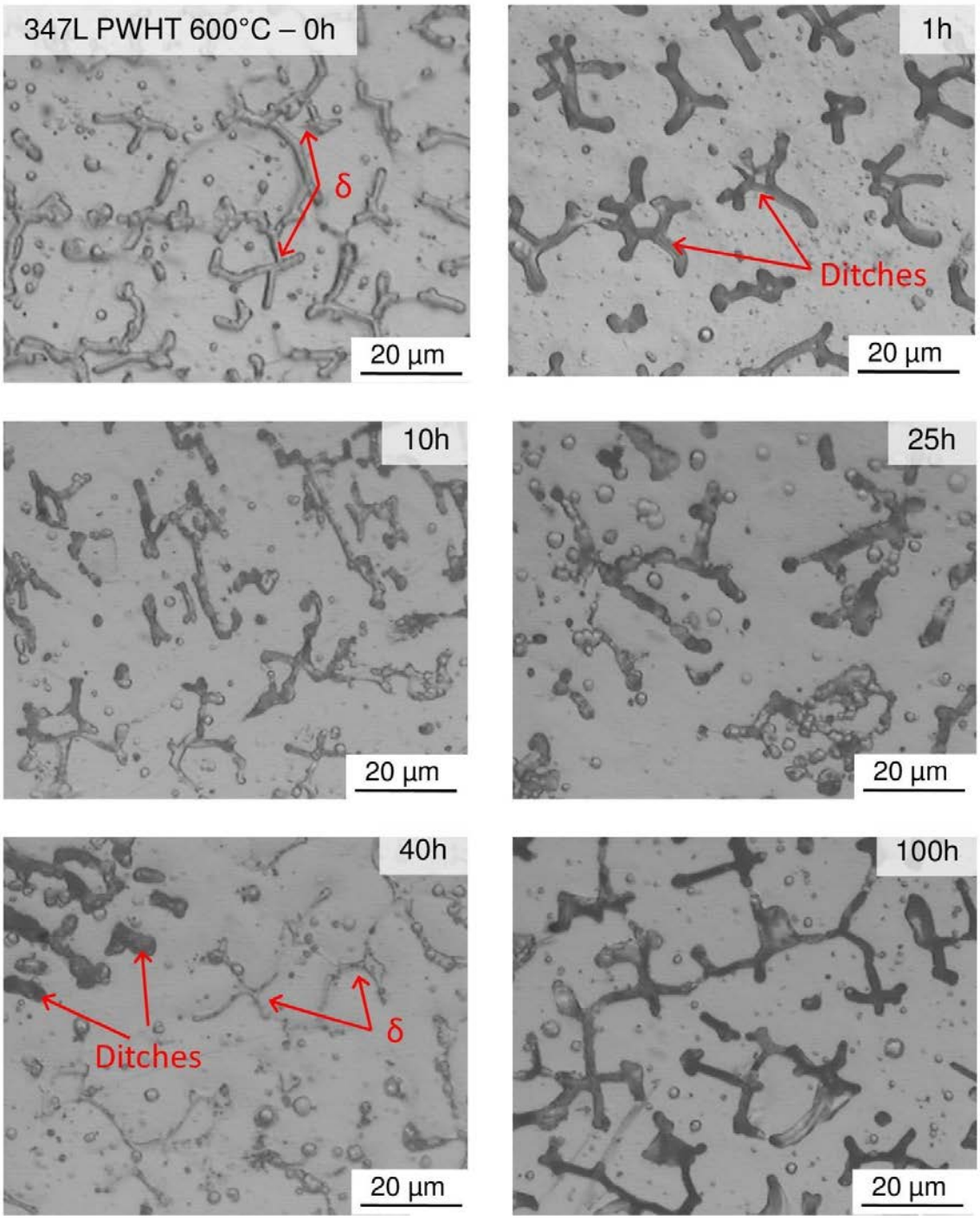

Figure 6-3: Optical micrographs of 347L samples following oxalic acid testing [150] for the as-welded condition (0 h), and after PWHT at 600°C for 1 h, 10 h, 25 h, 40 h and 100 h.

Effect of accelerated laboratory ageing following PWHT

Figure 6-4 shows two representative micrographs of 347L samples following post weld heat treatment at 600°C for 40 hours, and after the same post weld heat treatment time followed by an additional ageing of 284.4 hours at 425°C. As previously described, samples with a PWHT for 40 h at 600°C showed a dual microstructure with both isolated ferrite islands and interphase ditches. When these samples were further subjected to an accelerated laboratory ageing for 284.4 h at 425°C (simulating 60 years of service at 300°C) the number of ditches was increased leading the microstructure to be classified as “interphase ditches” instead of “dual”.

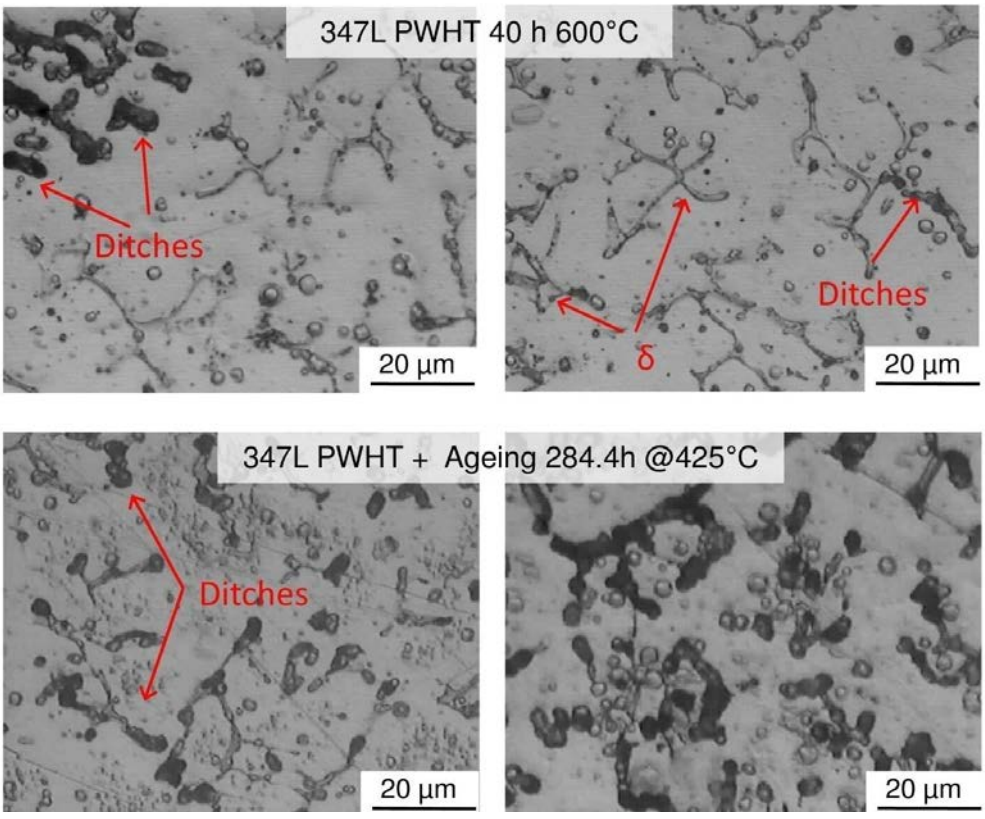

Figure 6-4: Optical micrographs of 347L following oxalic acid testing [150] of samples after PWHT at 600°C for 40 h, and after the same PWHT followed by accelerated laboratory ageing at 425°C for 284.4h. Two characteristic micrographs are presented for each thermal treatment.

6.2.2 Type 309L SS

The following section describes the results obtained after applying the oxalic acid test to 309L austenitic stainless steel welds in all the thermal treatment conditions described in Section 6.1.

As-welded

Figure 6-5 shows a micrograph of 309L in the as-welded condition after the test. Similarly to what was observed for 347L, the austenitic phase (shown as γ) was more attacked than the ferritic phase (δ) leaving this phase standing up from the surface.

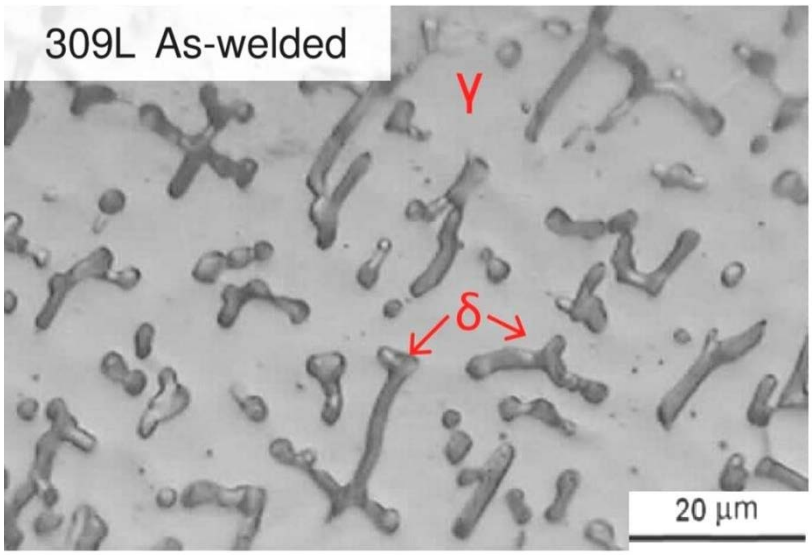

Figure 6-5: Optical micrograph of oxalic acid test applied to 309L in the as- welded condition according to ASTM-262 practice A [150].

Simulated Service Ageing at 425°C without PWHT

Figure 6-6 shows the microstructures following the oxalic acid test applied to 309L after ageing for 142.2 h and 284.4 h at 425°C. No interphase ditches were found for both ageing times. Therefore, all microstructures found can be classified as “isolated ferrite islands” according to [150]; which means the material is not sensitized in terms of this practice.

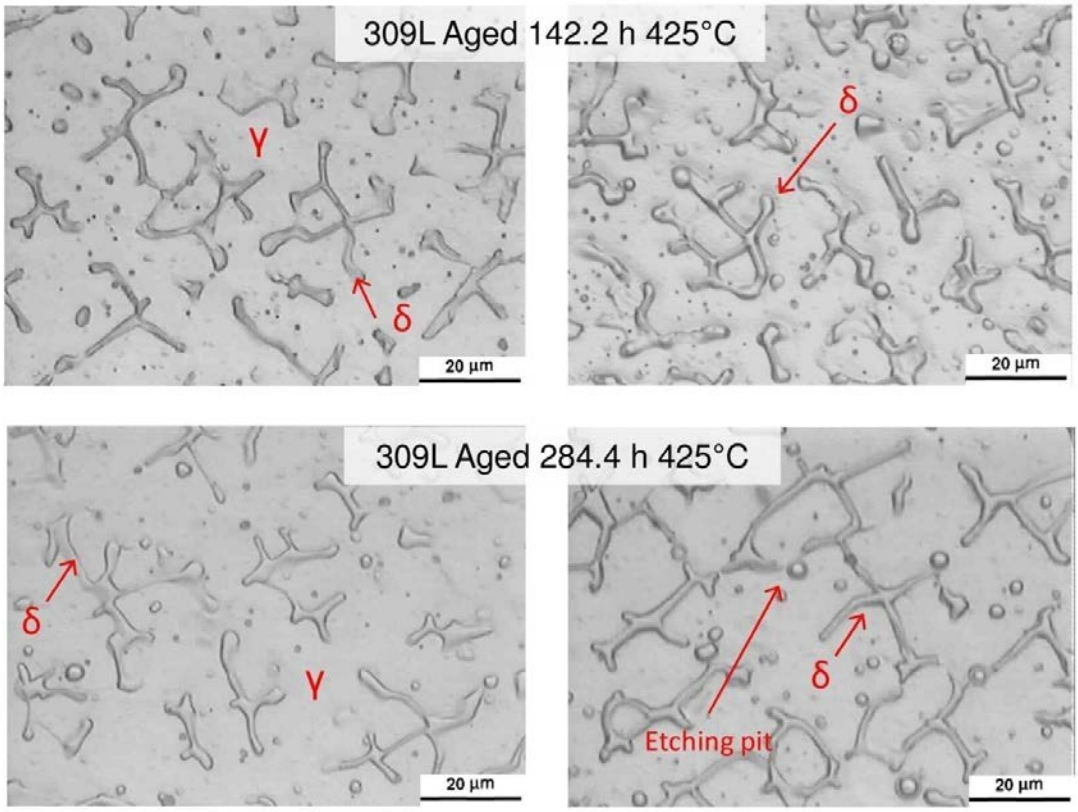

Figure 6-6: Optical micrographs of 309L samples after ageing at 425°C following the oxalic acid test [150]. Two characteristic micrographs are shown for of each thermal treatment.

PWHT – Ageing 600°C up to 100 h

Figure 6-7 shows results following oxalic acid testing of 309L after PWHT at 600°C for different periods of time, reproducing the conditions that clad layers are subjected to during RPV fabrication. In the as-welded condition (0 h of treatment) the microstructure corresponds to “isolated ferrite islands” (shown as δ in the figure) with δ ferrite standing up of the surface as previously described. As the treatment is carried out for increasing times, interphase ditches were observed for every treatment time up to 100 h. According to the standard, all samples subjected to PWHT at 600°C were classified as “suspect”, which means that they cannot be considered acceptable for this test and should further tested by another practice.

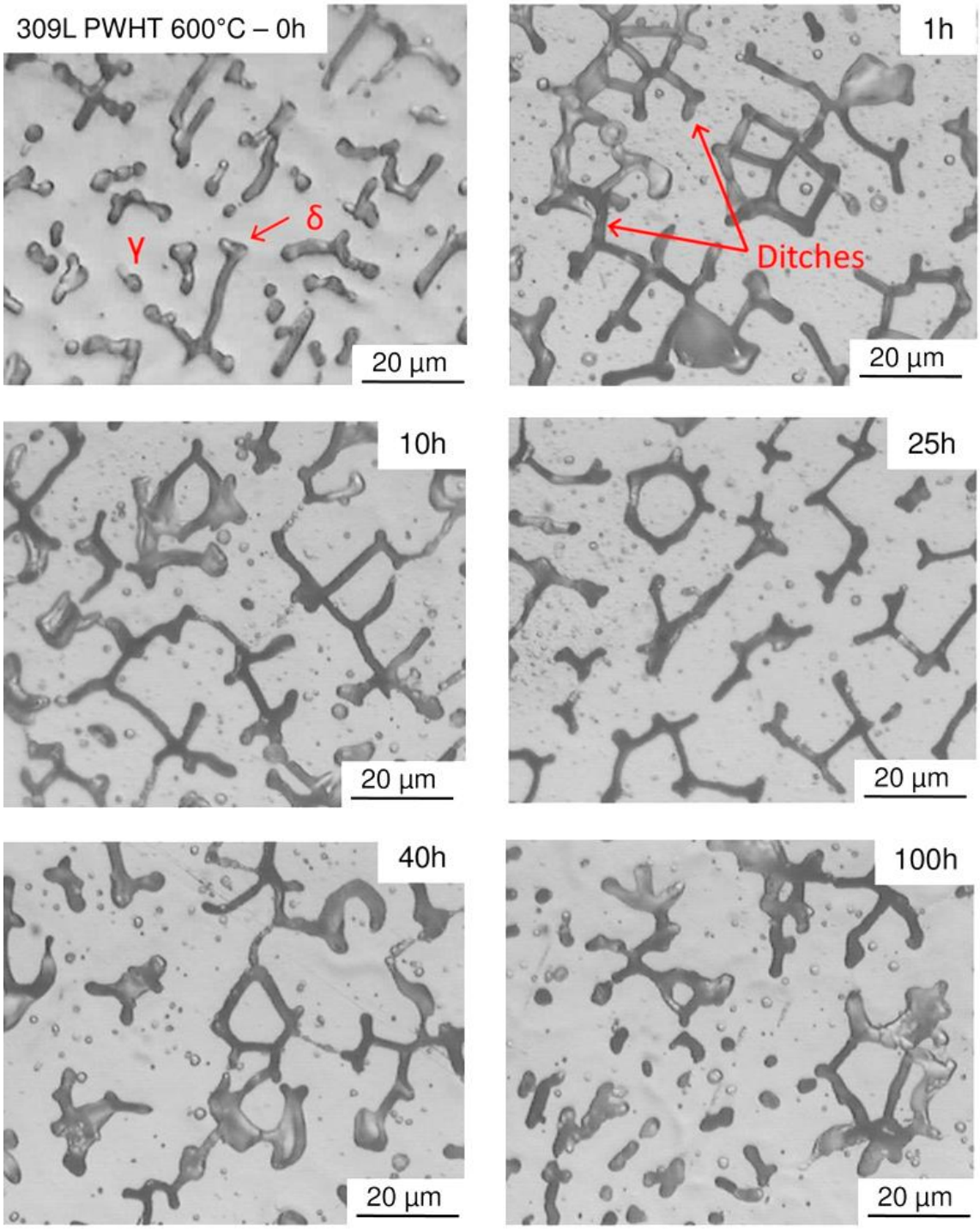

Figure 6-7: Optical micrographs of 309L samples in the as-welded condition (0 h), and after PWHT at 600°C for 1 h, 10 h, 25 h, 40 h and 100 h following oxalic acid testing [150].

Effect of accelerated laboratory ageing following PWHT

Figure 6-8 shows the results obtained for 309L samples following PWHT at 600°C for 40 hours, and after PWHT followed by accelerated laboratory ageing at 425°C. No differences were observed before and after ageing at 425°. Both microstructures showed interphase ditches leading the samples to be classified as “suspect”.

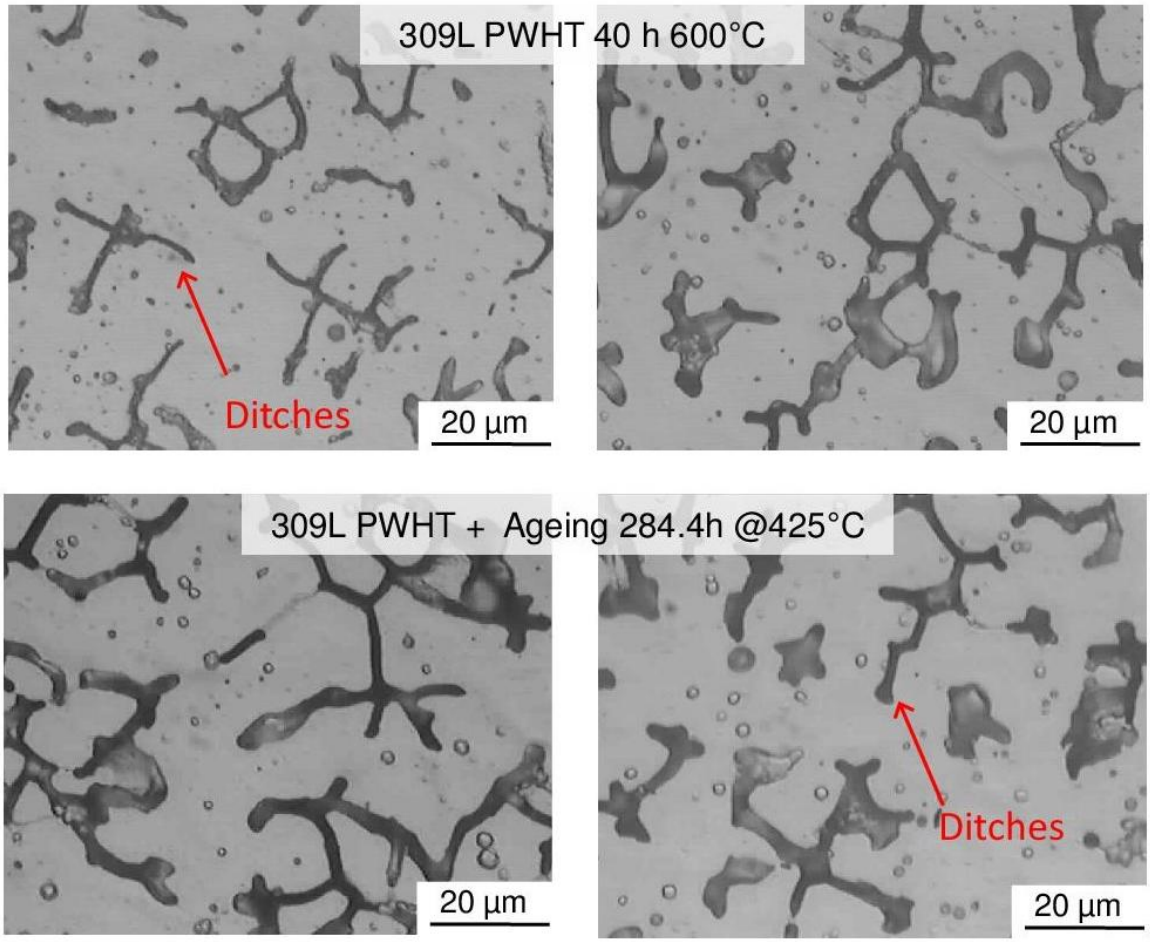

Figure 6-8: Optical micrographs of 309L samples after PWHT at 600°C for 40 h, and after the same PWHT followed by accelerated laboratory ageing at 425°C for 284.4h. Oxalic acid etching according to [150]. Two characteristic micrographs are presented for each thermal treatment.

6.3 Determination of the Degree of Sensitization (DoS) using Double Loop Electrochemical Potentiokinetic Reactivation test (DLEPR)

DLEPR was performed on 347L and 309L samples for all thermal treatment conditions described in Section 6.1. Due to its quantitative nature, this technique, complements and enlarges the analysis provided by qualitative and comparative techniques such as ASTM 262 Practice A applied in sections 6.2.1 and 6.2.2.

The DLEPR technique consists of a sequence of two consecutive electrochemical potentiodynamic sweeps where the potential is increased first from the open circuit potential (OCP) up to the reverse potential, and then decreased to the OCP.

During the forward sweep, which starts at the OCP and goes towards higher potentials, active dissolution of the material occurs with the current density increasing constantly with increasing potential until a maximum current is reached. After this point, which is referred to as the “active peak” at the “passivation potential”, a passive layer is formed on the surface, producing a sharp reduction in the current density. The corrosion protection features of this passive layer depend on the chemical composition and microstructure of the material. If the material is sensitized, certain regions along grain boundaries will have a chromium-depleted zone (CDZ) that will form a less corrosion-resistant protective layer than the rest of the material.

During the reverse sweep, a small or negligible increment in current is seen for non-sensitized materials due to the presence of a uniform and protective passive film.

However, for sensitized samples, chromium-depleted zones are reactivated in a characteristic range of potentials giving a “reactivation peak”. The more sensitized the material, the higher the reactivation peak. Figure 6-9 shows the characteristic potentiokinetic cycles and the more relevant parameters of (a) non-sensitized stainless steel and (b) sensitized stainless steel.

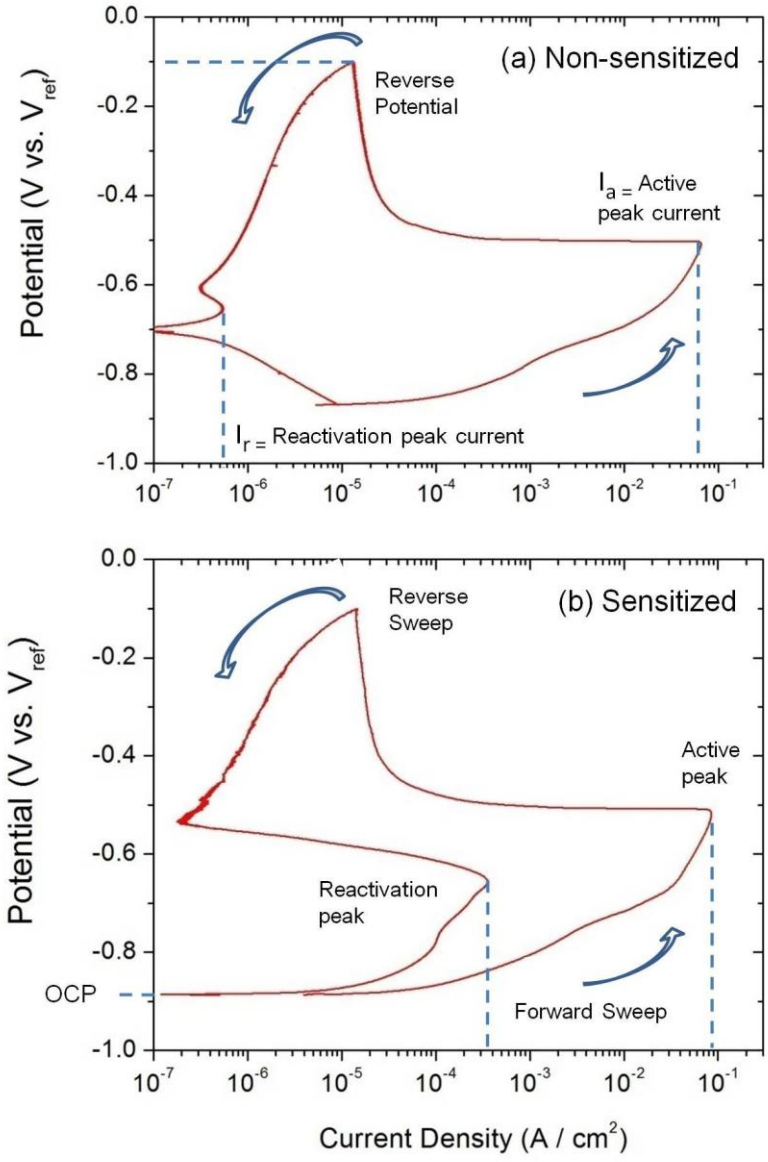

Figure 6-9: Electrochemical cycles and relevant parameters identified during a Double Loop Electrochemical Potentiokinetic Reactivation (DLEPR) test of (a) non-sensitized stainless steel and (b) sensitized stainless steel.

The main value to be reported in the test is the Degree of Sensitization (DoS) which is calculated according to Equation 6-1.

$$DoS\ (\%) = \frac{\mathrm{Ir}}{\mathrm{I}a} \text{ x } 100$$

Equation 6-1

Where:

Ir = Reactivation peak current

Ia = Active peak current

Active and reactivation current densities can also be used in Equation 6-1 given that areas of the sample are cancelled in the DoS calculation.

Due to the wide range of applications of austenitic stainless steels, acceptance limits of the tests are generally defined on a case by case basis. Nevertheless, the British Standard BS EN ISO 12732:2008 [155] gives the following values as a general guide for interpretation of DLEPR results:

Table 6-1: Correlation of Ir/Ia with the degree of sensitization[155]

Ir/Ia (%)	General Interpretation of the degree of sensitization
< 1	Unsensitized
1 to 5	Slightly sensitized (might pass Streicher, Strauss and Huey test)
> 5	Sensitized (Could fail Streicher, Strauss and Huey test)

In the following sections, the degree of sensitization is determined for 347L and 309L samples subjected to all thermal treatments described in Section 6.1

6.3.1 Type 347L SS

As-welded

Figure 6-10 shows curves obtained for 347L samples in the as-welded condition. In the forward sweep peak current density observed was ~0.1 A/cm^2 at the passivation potential of ~-0.5 V. Above this potential, a passive current of ~1.5 x 10^{-5} A/cm^2 was measured until the reverse potential of -0.1 V. The reactivation peak was formed at ~-0.64 V. The black, red and blue lines correspond to different samples tested in identical conditions, showing a good reproducibility of the test.

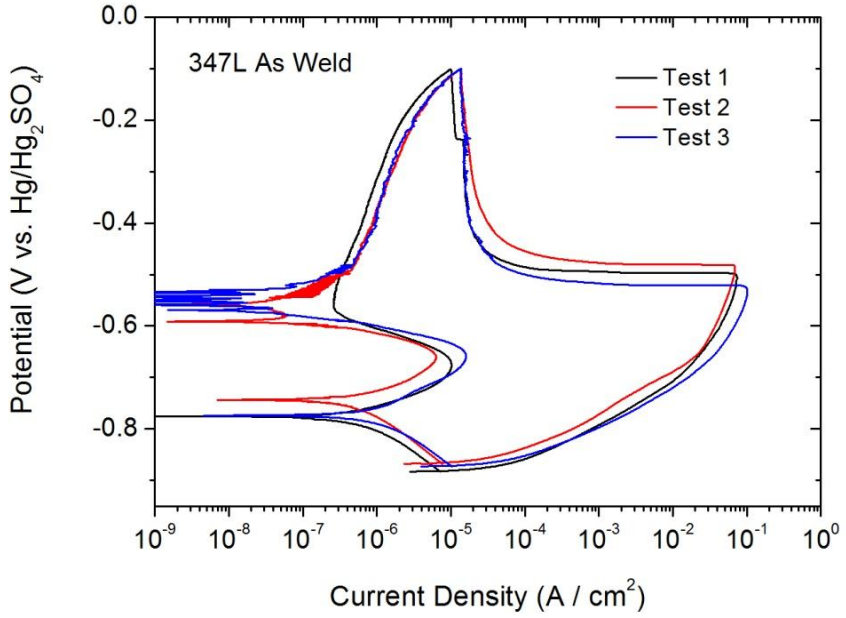

Figure 6-10: Results of DLEPR of 347L samples in the as-welded condition. Black, red, and blue lines correspond to three identical tests on different samples

The average DoS of 347L in the as-welded condition was found to be 0.012% indicating the material is not sensitized in this condition according to [155].

Simulated Service Ageing at 425°C without PWHT

DLEPR test was applied to samples aged at 425°C for 142.2 h and 284.4 h. As observed in Figure 6-11, no significant differences were found for both ageing times, compared with the as-welded condition.

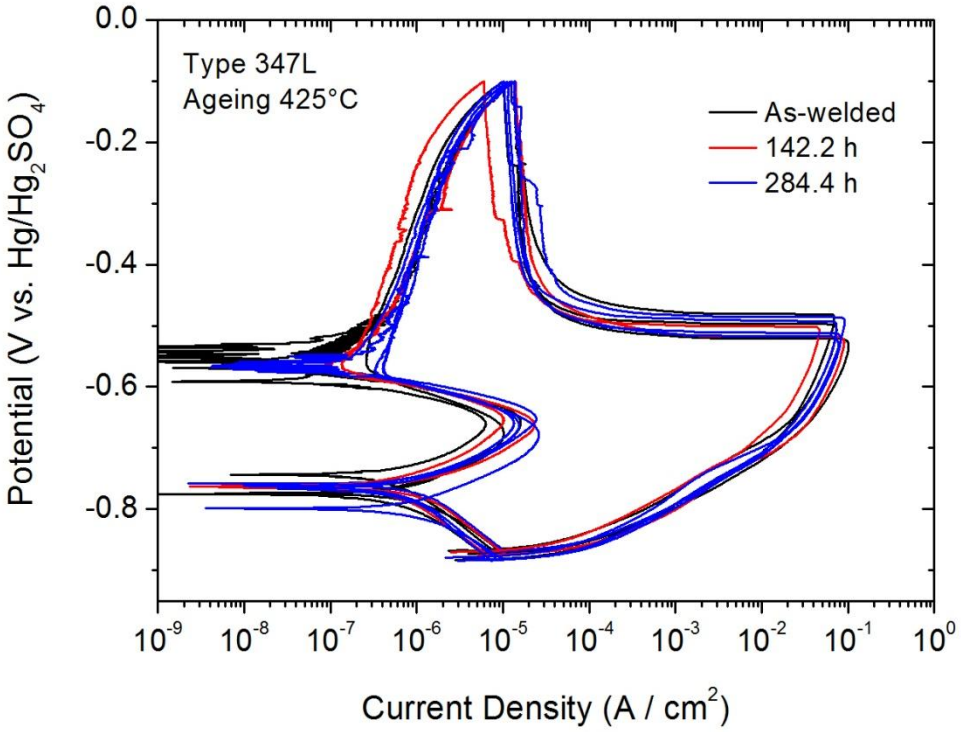

Figure 6-11: DLEPR of 347L samples in the as-welded condition and after accelerated laboratory ageing at 425°C

Figure 6-12 shows that only a minor increase in the DoS could be observed for both ageing times compared with the as-welded condition and without a significant difference between the ageing times.

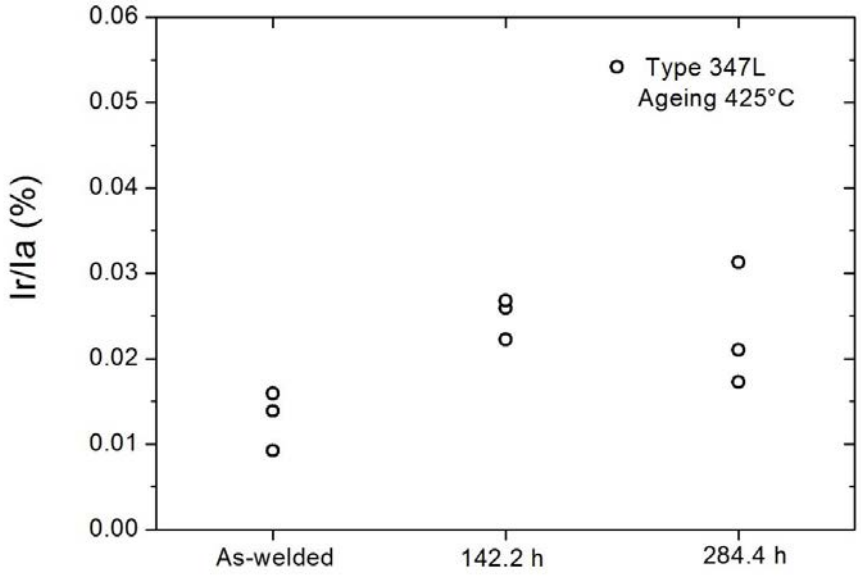

Figure 6-12: DoS of 347L samples in the as–welded condition and after accelerated laboratory ageing at 425°C

PWHT – Ageing 600°C up to 100 h

Figure 6-13 (A) shows results of DLEPR tests applied to 347L samples subjected to PWHT at 600°C for 1h, 10h, 25h, 40h, and 100h. Each curve represents the typical of a minimum of three tests.

For every treatment time, the active parts of the forward curves show a similar behaviour to the as-welded material. However, during the reverse sweep, reactivation peaks showed increasing current densities for 1 h and 10 h, when the

maximum reactivation current density was achieved and then started to decrease for longer treatment times up to 100 h. Additionally, as shown in Figure 6-13 (B), a second reactivation peak at around -0.74 V in addition to the main one at -0.64 V can be observed with different current densities depending on treatment time. This second peak could sometimes be clearly visible as a peak or otherwise as a shoulder in the resulting curve.

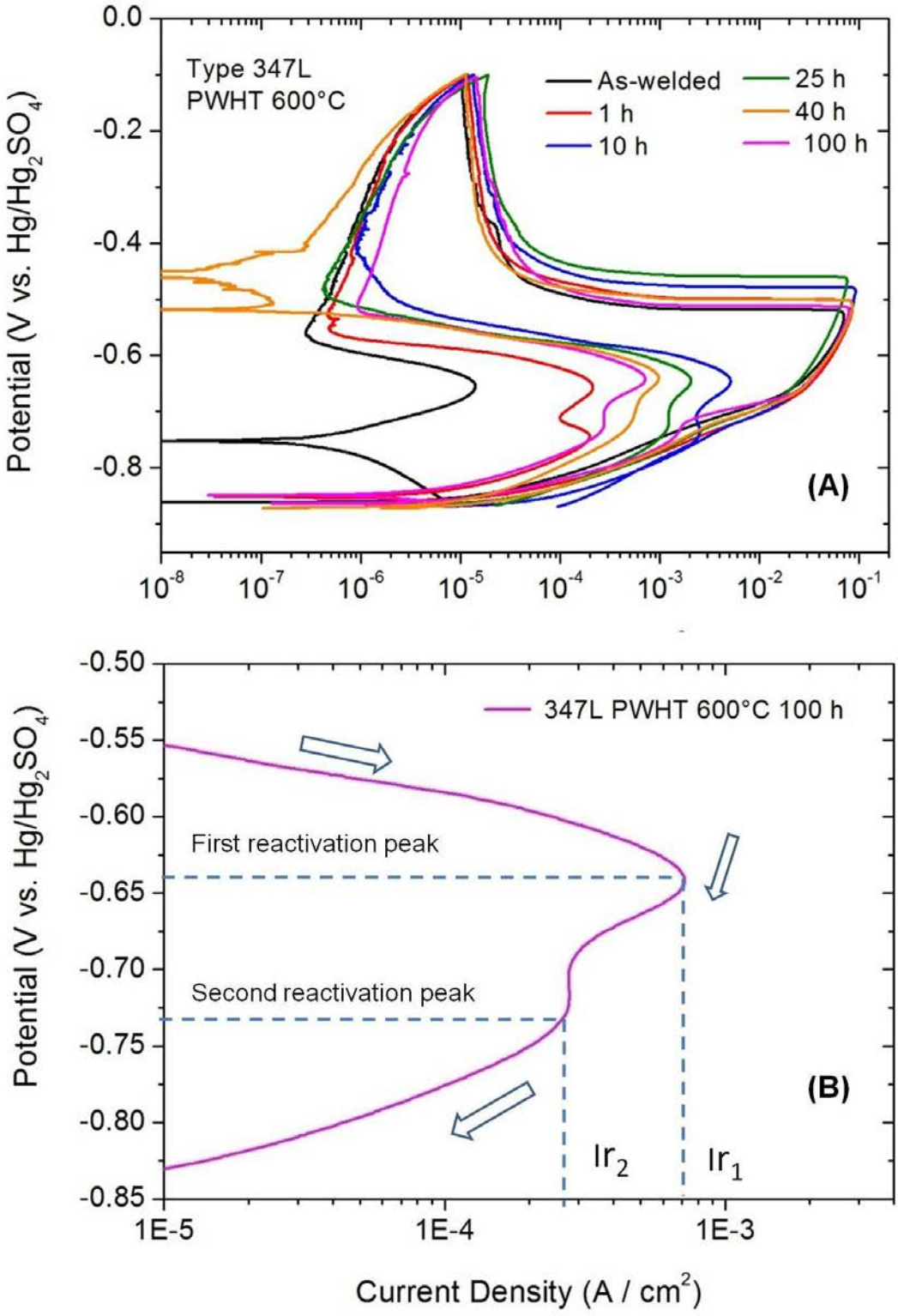

Figure 6-13: DLEPR of 347L samples given PWHT at 600°C for 1 h, 10 h, 25 h, 40 h, and 100 h (A) and detail of the reactivation peak splitting for the sample treated for 100 h (B).

Due to the presence of the second peak, it was necessary to split the analysis of the DoS into two separated parameters DoS_1 and DoS_2. Considering Equation 6-1, DoS_1 and DoS_2 were calculated for each treatment time as described in Equation 6-2 and Equation 6-3. DoS_1 corresponds to the first reactivation peak found at ~-0.64 V, whereas DoS_2 corresponds to the second reactivation peak found at ~-0.74 V.

$$DoS_1\ (\%) = \frac{\mathrm{Ir}_1}{\mathrm{I}a}\ \mathrm{x}\ 100$$

Equation 6-2

$$DoS_2\ (\%) = \frac{\mathrm{Ir}_2}{\mathrm{I}a}\ \mathrm{x}\ 100$$

Equation 6-3

Where:

Ir_1 = Reactivation current associated to the first reactivation peak;

Ir_2 = Reactivation current associated to the second reactivation peak;

Ia = Active current on the forward sweep

The reactivation current associated to the first reactivation peak (Ir_1) was defined as the maximum value of current found during the reverse sweep between -0.6 V and -0.7 V and was obtained directly from the electrochemical measurements. However, since the second peak was not always clearly defined as a standalone peak, it was necessary to define a fitting process to calculate its intensity (Ir_2).

The fitting process is based on the assumption that the whole reactivation peak is formed by the sum of two Gaussian curves corresponding to the first and second reactivation peak respectively. This model [174] was developed in collaboration with Dr. Diego Passarella (Universidad de Quilmes, Argentina).

Figure 6-14 (A) shows the evolution of DoS_1 with PWHT time in 347L. DoS_1 increased from almost nil in the as-welded condition reaching a maximum at 10 h of treatment. After this time, a sharp decrease of DoS_1 was found up to 40 h of treatment, where an average value of around 1% was reached and kept until the end of treatment at 100h.

The evolution of DoS_2 with PWHT time in 347L (Figure 6-14 B) showed a similar behaviour to DoS_1, but with significantly lower values for same treatment times. DoS_2 increased from 0 in the as-welded condition (no such second peak was found in the as-welded samples) reaching a maximum at 10 h of treatment. After this time a sharp decrease was found up to 40 h of treatment, where an average value of 0.47% was reached. A further and smoother reduction in DoS_2 was observed after 100h of treatment reaching an average value of 0.24%.

Figure 6-14 C shows the ratio of DoS_2 to DoS_1 as a function of PWHT time. As seen in the figure, after the first hour and for the rest of the treatment, DoS_2 is approximately half of DoS_1

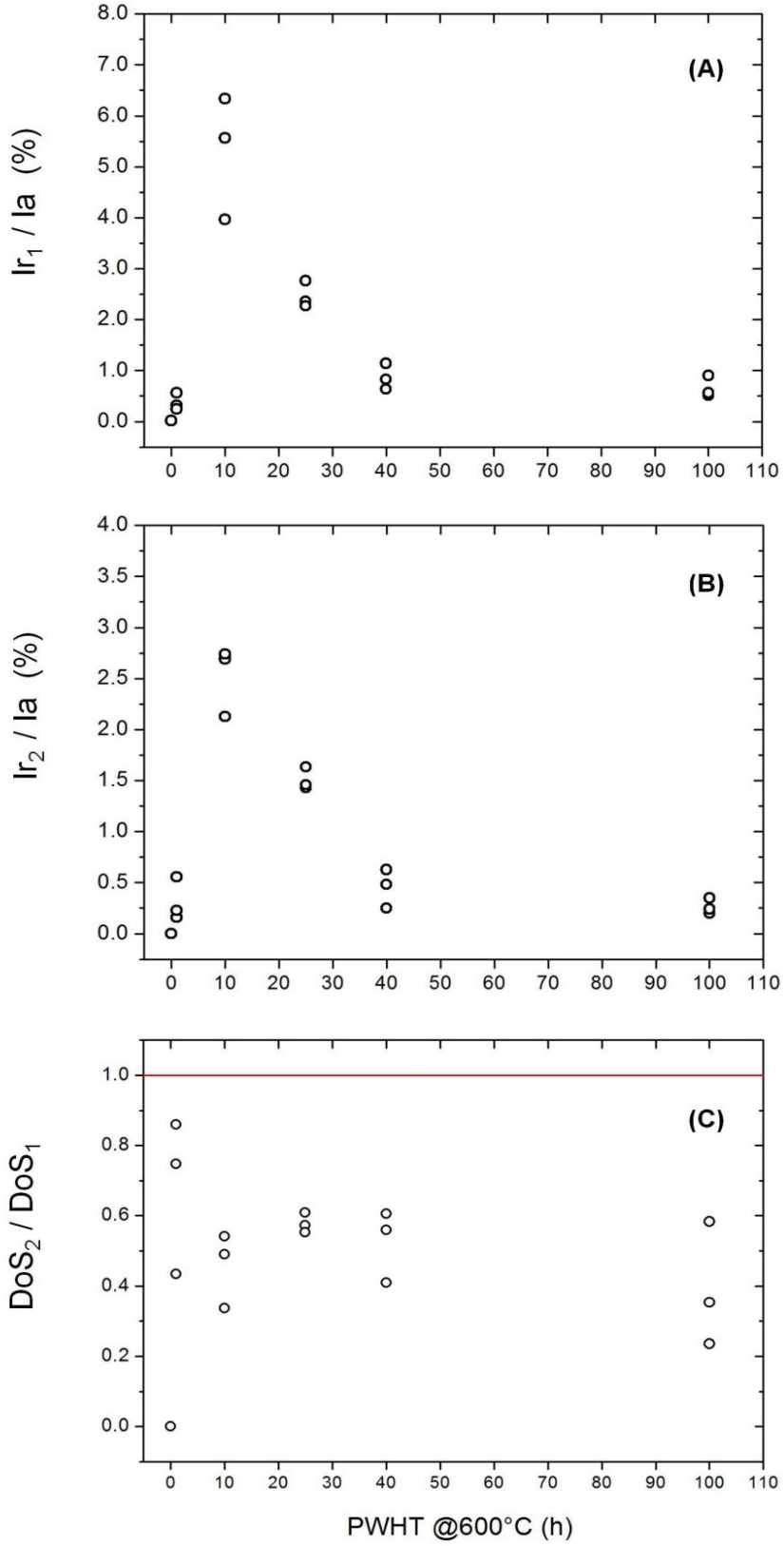

Figure 6-14: DoS_1 (A), DoS_2 (B) and of DoS_2 to DoS_1 ratio (C) for 347L samples given PWHT at 600°C for 1 h, 10 h, 25 h, 40 h, and 100 h.

Effect of accelereted laboratory ageing following PWHT

When PWHT samples were further aged at 425 °C, no appreciable differences compared to the as-welded condition could be noticed in either the first or the second reactivation peak, which fell into the scatter of the curves. This suggests the lack of a clear effect of the accelerated ageing at 425°C on the degree of sensitization of 347L samples PWHT at 600 °C for 40 h.

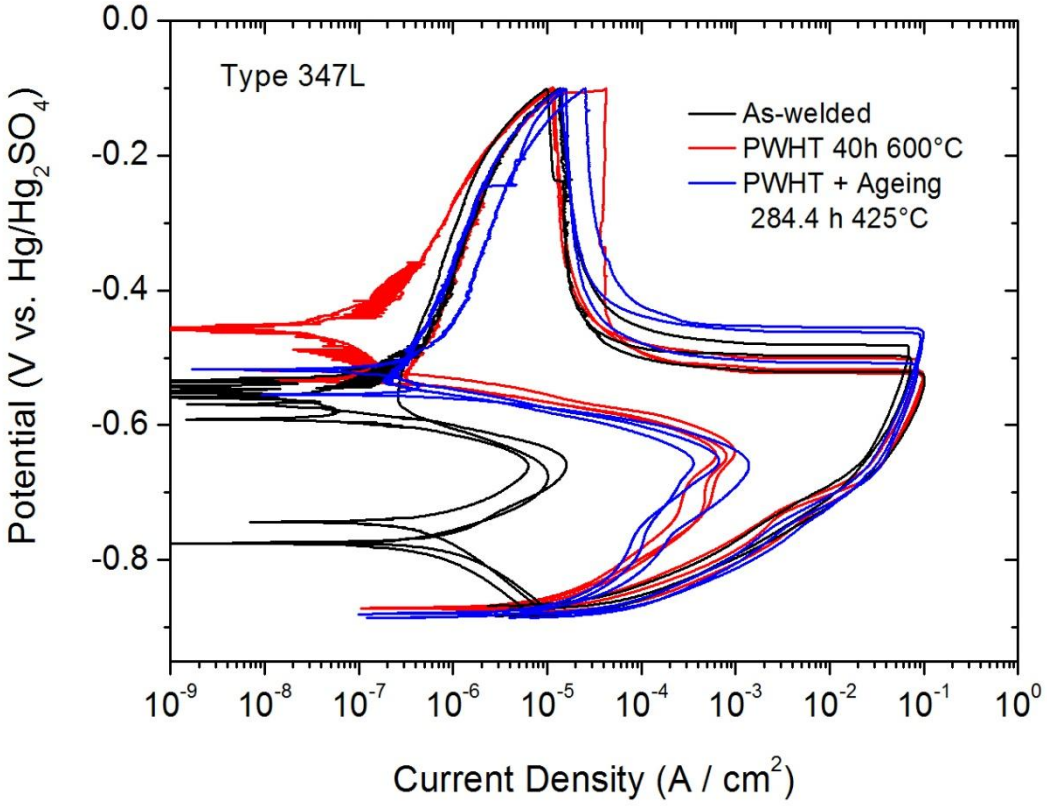

Figure 6-15: DLEPR of 347L samples in the as-welded condition, after PWHT of 40 h at 600°C, and after accelerated laboratory ageing at 425°C of PWHT samples

Figure 6-16 (A) shows that DoS_1 is increased after PWHT at 600°C and no further increase is reported after the additional ageing at 425°C. After PWHT at 600°C for

40 h DoS_2 reached an average of 0.47% and an average of 0.17% was found when samples with the additional ageing treatment were tested (Figure 6-16 B).

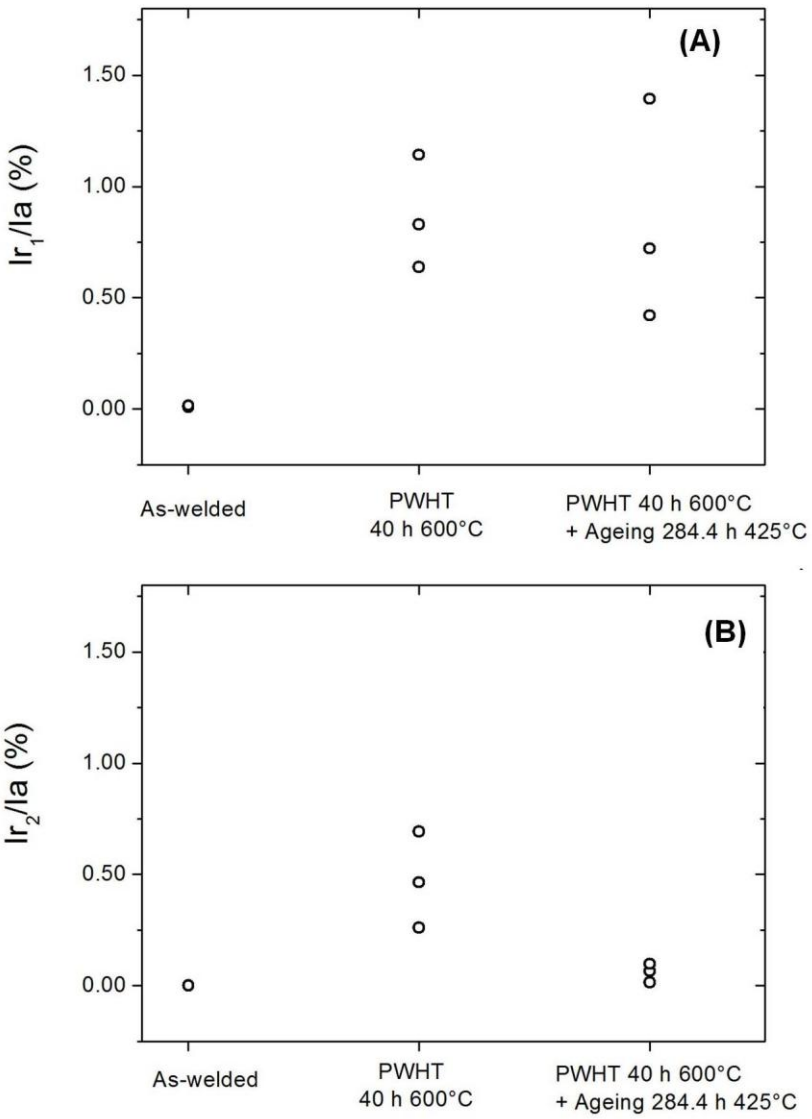

Figure 6-16: DoS_1 (A) and DoS_2 (B) of 347L samples in the as-welded condition, after PWHT of 40 h at 600°C, and after accelerated laboratory ageing at 425°C of PWHT samples

6.3.2 Type 309L SS

As-welded

Results of DLEPR test for 309L samples in the as-welded condition are shown in Figure 6-17. During the forward sweep, the active peak was found in the range between -0.46 V and -0.56 V. The current density at the active peak was ~0.06 A/cm^2. Similarly to what was found for 347L, passive current density measured for 309L in the as-welded condition was ~1.5 x 10^{-5} A/cm^2. It can be noticed that after reaching the reversion potential of -0.1 V; the reverse sweep showed a quite noisy response in the range of the lowest currents, showing multiple peaks in the reactivation region. This fact can be explained by the low current densities found in this zone.

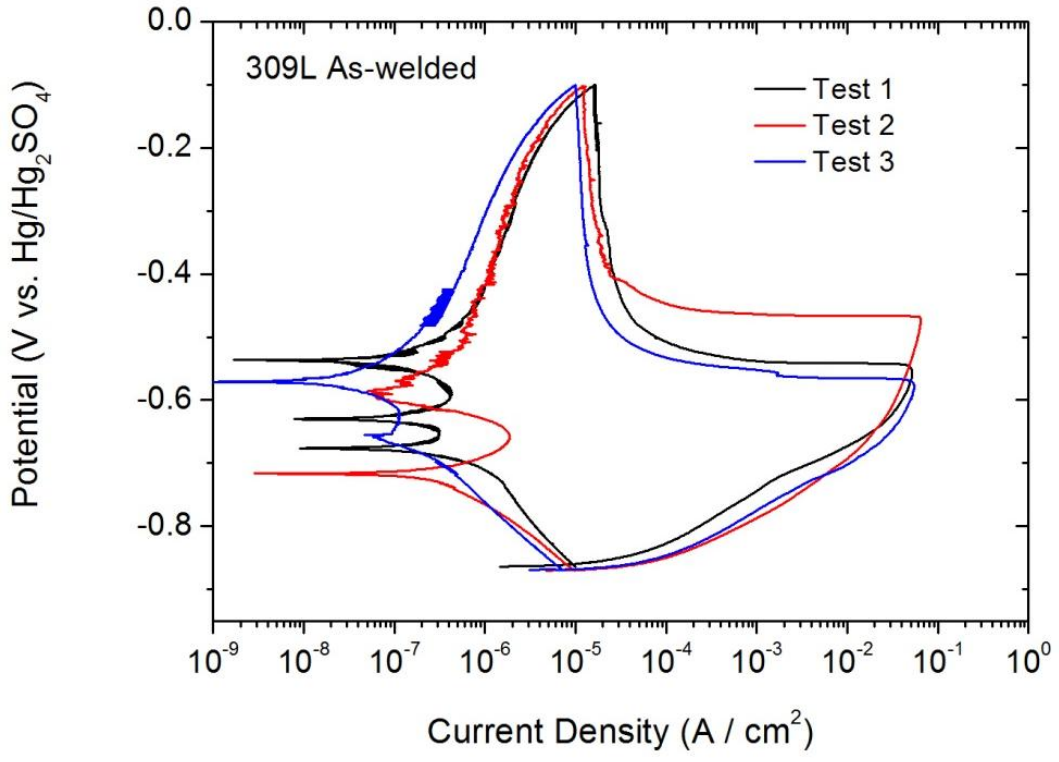

Figure 6-17: Results of DLEPR in the as-welded condition. Black, red, and blue lines correspond to three identical tests on different samples

Average DoS of 309L in the as-welded condition was found to be 0.0014% indicating the material is not sensitized in this condition [155].

Simulated Service Ageing at 425°C without PWHT

DLEPR test was applied to samples aged at 425°C for 142.2 h and 284.4 h. Figure 6-18 shows that the noisy response found for lower current densities in the as-welded condition is repeated after 142.2 h of ageing at 425°C, and then evolves into a small reactivation peak for 284.4 h. This evolution is reflected into the degree of sensitization found for both ageing times. A small but noticeable increase in the DoS could be observed for samples aged 284.4h, as shown in Figure 6-19. Nevertheless, the average DoS found for 284.4 h (0.0089 %) is very small and the material remained not sensitized for this condition [155].

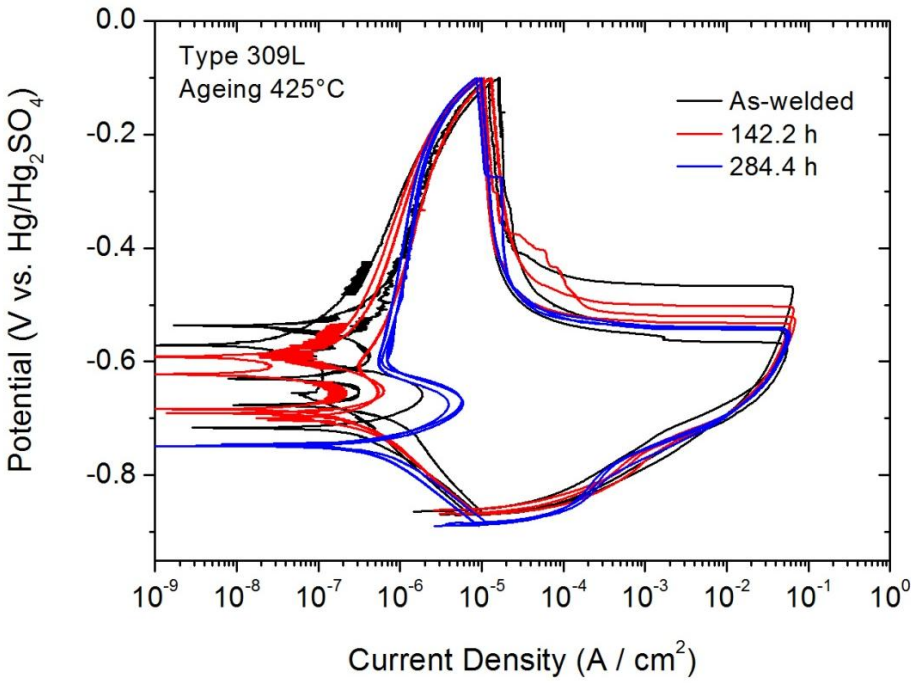

Figure 6-18: DLEPR of 309L samples in the as-welded condition and after accelerated laboratory ageing at 425°C

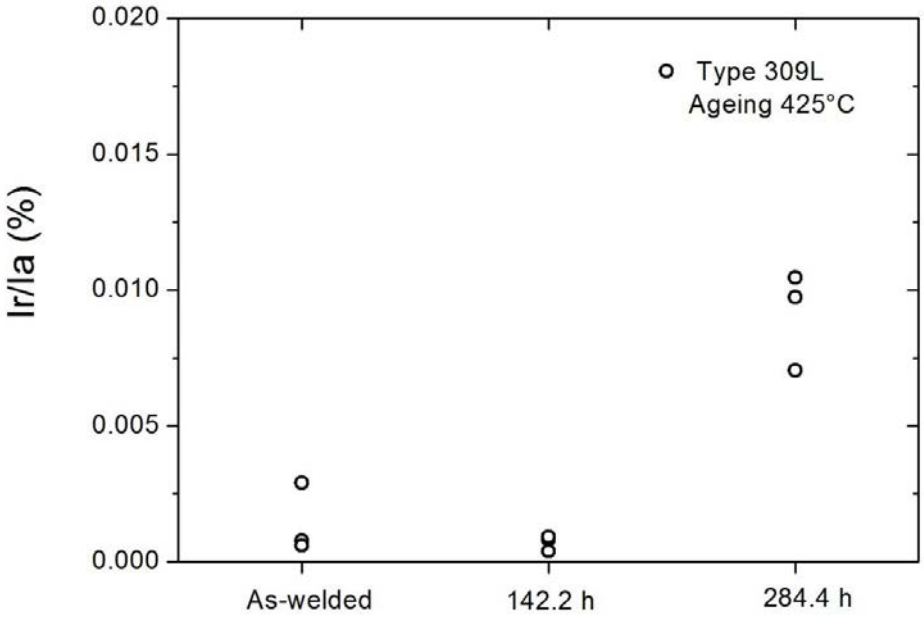

Figure 6-19: Degree of Sensitization (DoS) of 309L samples in the as–welded condition and after accelerated laboratory ageing at 425°C

PWHT – Ageing 600°C up to 100 h

Figure 6-20 (A) shows DLEPR results of 309L samples after PWHT at 600°C for 1 h, 10 h, 25 h, 40 h, and 100 h. Each curve represents the typical of a minimum of three tests, except for the samples treated for 100 h, when only two valid curves were obtained.

Similarly to what was observed for 347L samples, the active part of the curves showed the same behaviour shown by as-welded material. In the reverse sweep, two reactivation peaks were clearly formed for each treatment time. The position of these peaks was similar to that found for 347L, with the first peak around -0.64 V and the

second around -0.74 V. However, a different behaviour was observed for the second reactivation peak which showed increasing values with PWHT time (Figure 6-20 B).

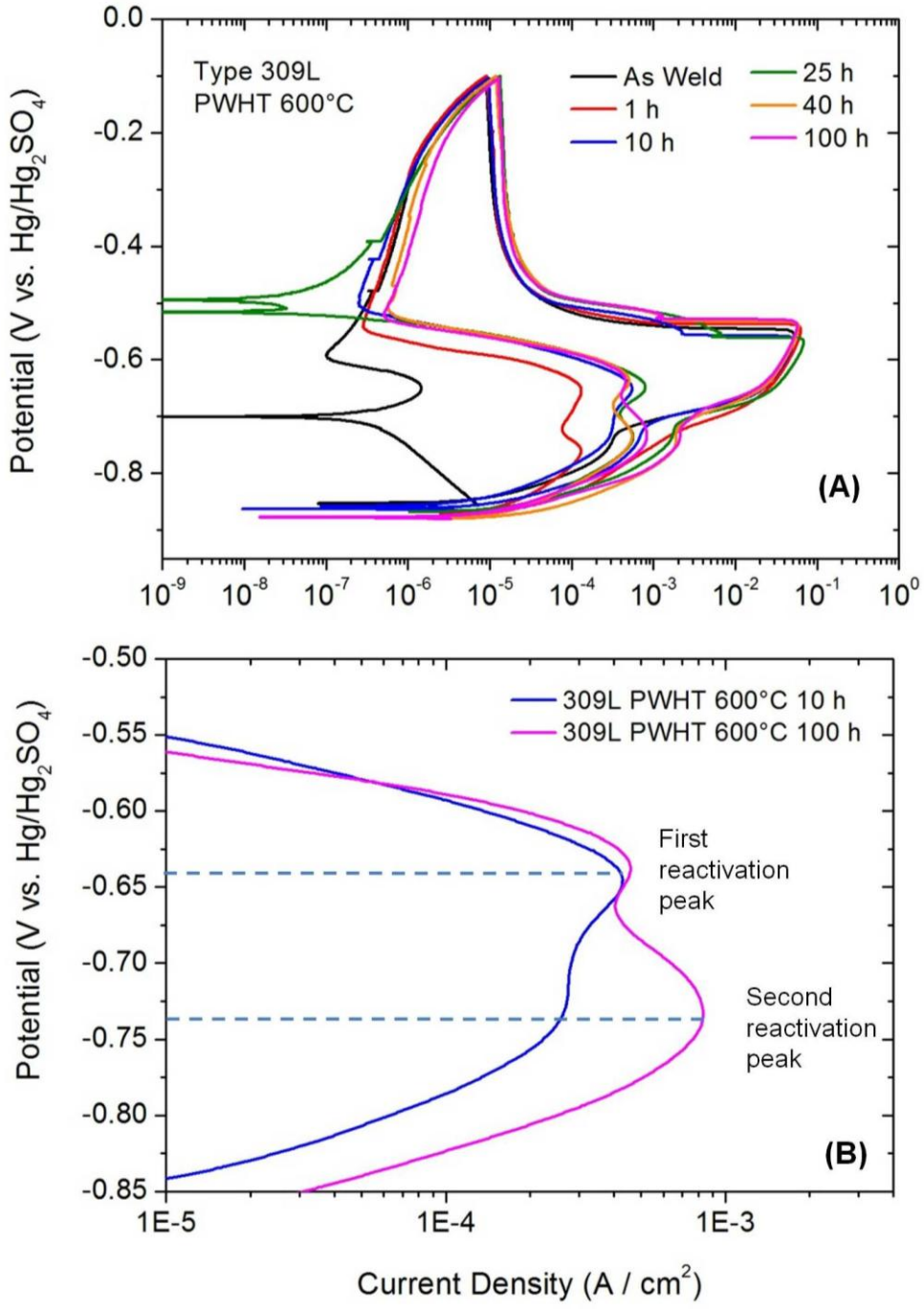

Figure 6-20: DLEPR of 309L samples given PWHT at 600°C for 1 h, 10 h, 25 h, 40 h, and 100 h (A). Detail of the evolution of reactivation peaks for 10 h and 100 h of treatment (B)

DoS_1 and DoS_2 were calculated according to Equation 6-2 and Equation 6-3. As shown in Figure 6-21 (A), DoS_1 of 309L increased from almost zero in the as-welded condition and reached a maximum of approximately 1% in the range of 10 h to 25 h of treatment. This value, which is considerably lower than the maximum of 5% (average) reached by DoS_1 of 347L, was reduced to an average of 0.74% at 40h, and only slightly increased to an average of 0.89% after 100h of treatment. This behaviour seems to be similar to that observed for 347L material but considerably flatter and with lower values, especially for the 10 h-25 h interval, where maximum DoS_1 values were observed.

DoS_2 of 309L samples (Figure 6-21 B) showed completely different behaviour with PWHT time when compared with DoS_1 of the same material and with both, DoS_1 and DoS_2 of 347L material. Instead of the sensitization – healing behaviour observed in the other cases, a permanent increase of DoS_2 with PWHT time at 600°C was observed in 309L material.

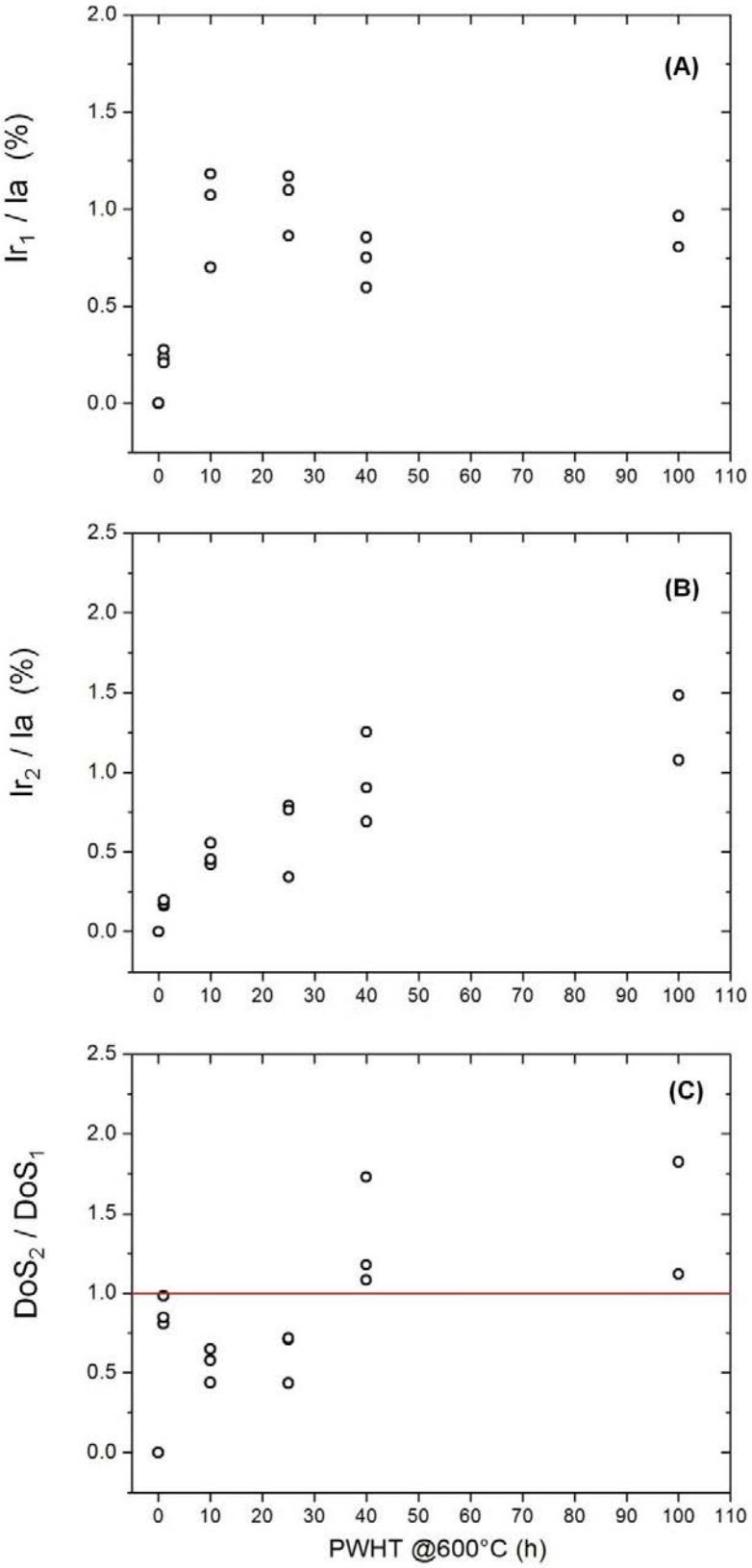

Figure 6-21: DoS_1 (A), DoS_2 (B) and of DoS_2 to DoS_1 ratio (C) for 309L samples given PWHT at 600°C for 1 h, 10 h, 25 h, 40 h, and 100 h.

Figure 6-21 (C) shows the ratio of DoS_2 to DoS_1 as a function of PWHT time. It can be seen that up to 40 h of treatment DoS_2 / DoS_1 follows the same behaviour than that observed in 347L material, reaching a value of approximately 0.5 after the first hour of treatment. However, after 40 h at 600°C it is seen that DoS_2 becomes higher than DoS_1 with a DoS_2 / DoS_1 average value of 1.33 for 40 h and 1.48 for 100 h.

Effect of accelereted laboratory ageing following PWHT

Figure 6-22 shows a comparison of the DLEPR curves obtained for 309L samples in the as-welded condition, after 40 hours of PWHT at 600°C and for those PWHT samples for 40 h that were subjected to an accelerated laboratory ageing at 425°C. When PWHT samples were further aged at 425° for 284.4 h a marked increase in the first reactivation peak was observed.

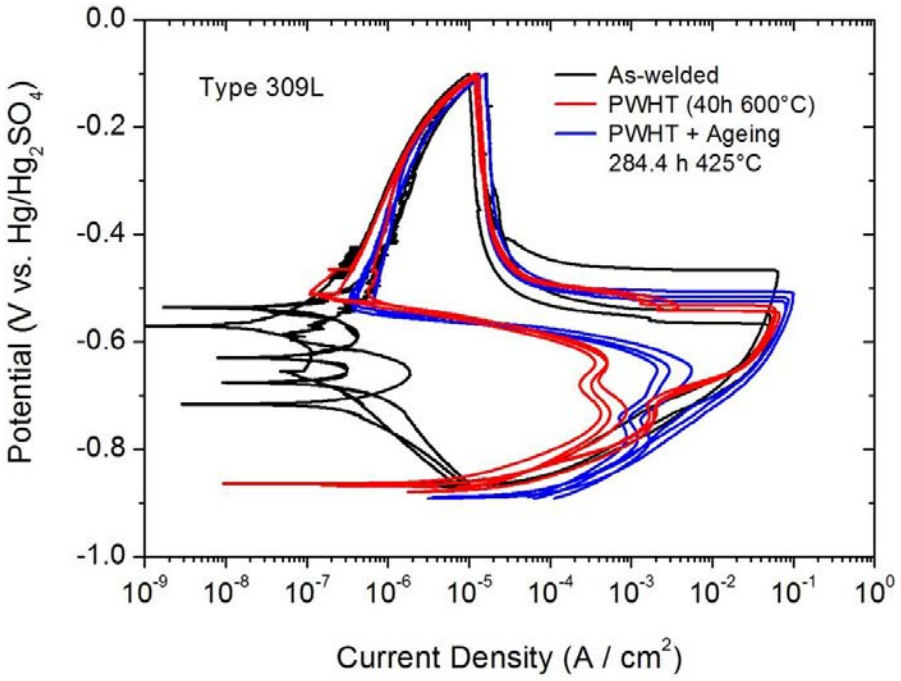

Figure 6-22: DLEPR of 309L samples in the as-welded condition, after PWHT of 40 h at 600°C, and after accelerated laboratory ageing at 425°C of PWHT samples

Figure 6-23 shows DoS_1 and DoS_2 obtained from tests on Figure 6-22. When PWHT samples were further aged at 425°, different behaviour was observed for these parameters. A marked increase in DoS_1 was observed, as shown in Figure 6-23 (A); whereas no increase was detected for DoS_2 (Figure 6-23 B).

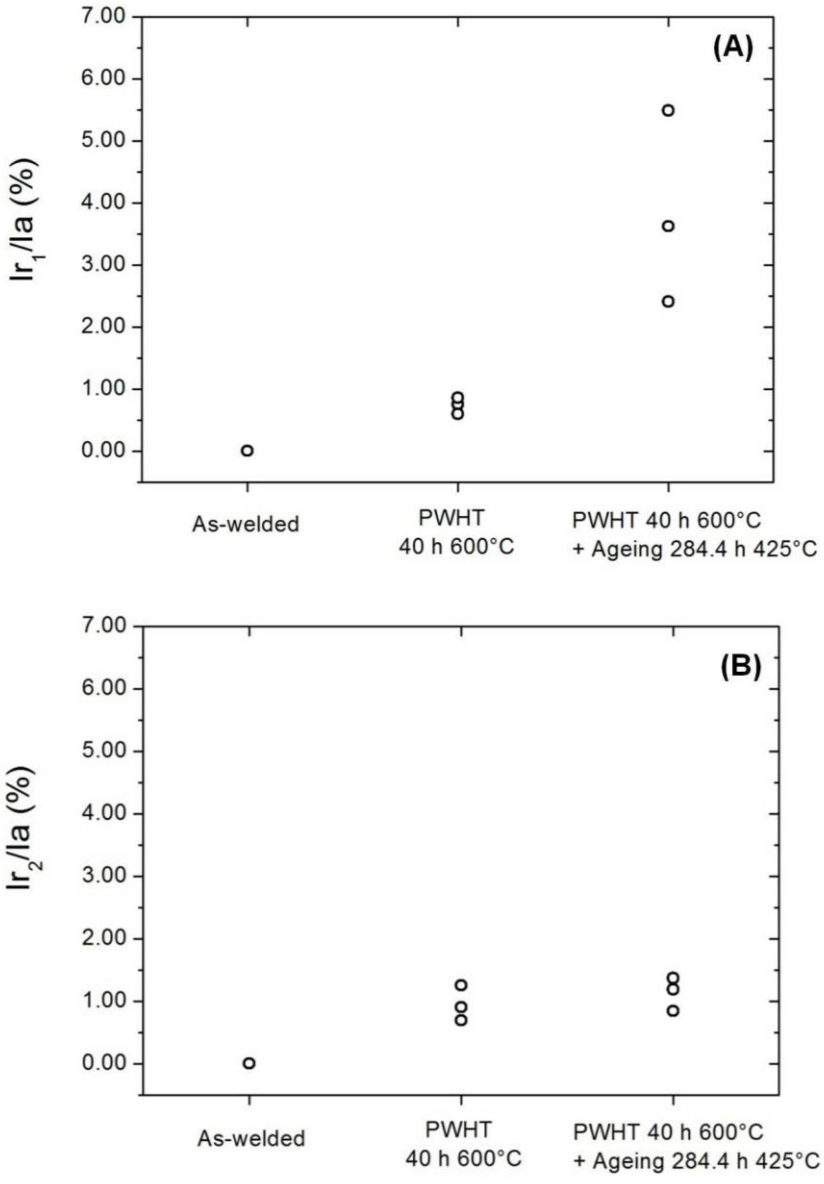

Figure 6-23: DoS_1 (A) and DoS_2 (B) of 309L samples in the as-welded condition, after PWHT of 40 h at 600°C, and after accelerated laboratory ageing at 425°C of PWHT samples

6.4 Potential of DLEPR test for phase identification

Given that two peaks were observed at characteristic potentials and no agreement is found in literature about the physical meaning of these peaks [21, 25-29]; a set of studies were carried out in order to correlate reactivation peaks of DLEPR experiments with microstructural modifications observed, aiming to explore the potential of the DLEPR technique to identify deleterious phases derived from δ ferrite decomposition.

6.4.1 Reactivation peak splitting in 309L

Description

Based on DLEPR cycles obtained for each PWHT time of 309L material (Figure 6-20); specific potentiokinetic cycles were designed and applied in an attempt to isolate the effects of the attack produced in the potential ranges corresponding to each reactivation peak. Type 309L material was selected to this study due to the marked second peak shown in Section 4.6.1. The study of 347L material is left out of the scope of the present work and will be considered for future research.

Taking into account the variability of the reactivation peak potentials among the DLEPR tests performed; first and second reactivation peaks were respectively defined at -0.64 V and -0.74 V. Electrochemical cycles designed for peak study, included cathodic cleaning and open circuit potential determination exactly as used for standard DLEPR (see Chapter 3). After these two steps, potentiokinetic cycles were applied as follows:

Cycle to study first reactivation peak (-0.64 V)

Forward Sweep: OCP to -0.1 V

Reverse Sweep: -0.1 V to -0.69 V

Cycle to study second reactivation peak (-0.74 V)

Forward Sweep: OCP to -0.1 V

Reverse Sweep 1: -0.1 V to -0.55 V

Potential step from -0.55 V to -69 V skipping the first reactivation peak

Reverse Sweep 2: -0.69 V to -0.77 V

In the cycle designed for studying the first reactivation peak, the DLEPR cycle is interrupted after the formation of the first peak; whereas a “split” reverse sweep was used for studying the second peak, skipping the formation of the first reactivation peak. It is worth noticing that, in addition to the DLEPR sample preparation procedure described in Chapter 3; all samples used in Section 6.4 were polished up to 1 μm diamond paste, and then finished with colloidal silica (OPS) in order to allow metallographic observation after performing the different electrochemical tests.

Since different behaviour of each peak with PWHT time at 600°C was observed for 309L material; samples subjected to 10 h and 100 h of PWHT have been analyzed. These samples showed the maximum DoS values for the first and second reactivation peak respectively, according to Figure 6-21. In addition, as-welded samples were tested performing the whole DLEPR cycle as in Sections 6.3.1 and

4.6.1 in order to have a reference of the morphology of the attack in 309L samples that were free of reactivation peaks.

As-welded

Figure 6-24 shows DLEPR test and resulting attack morphology of 309L material in the as-welded condition. As observed in Section 4.6.1, no reactivation peaks were observed for this condition. It is worth mentioning that the active peak of the curve showed a split into two peaks. This behaviour was also visible for the samples PWHT at 600°C for 10 h and 100 h (Figure 6-25, Figure 6-26, Figure 6-27, and Figure 6-28). The separation of the active peak can be associated to an interim passivation that could be related to the different passivation potentials of γ and δ [21, 25-29]. However, the study of the active peak is considered out of the scope of the present work and will be considered for future research.

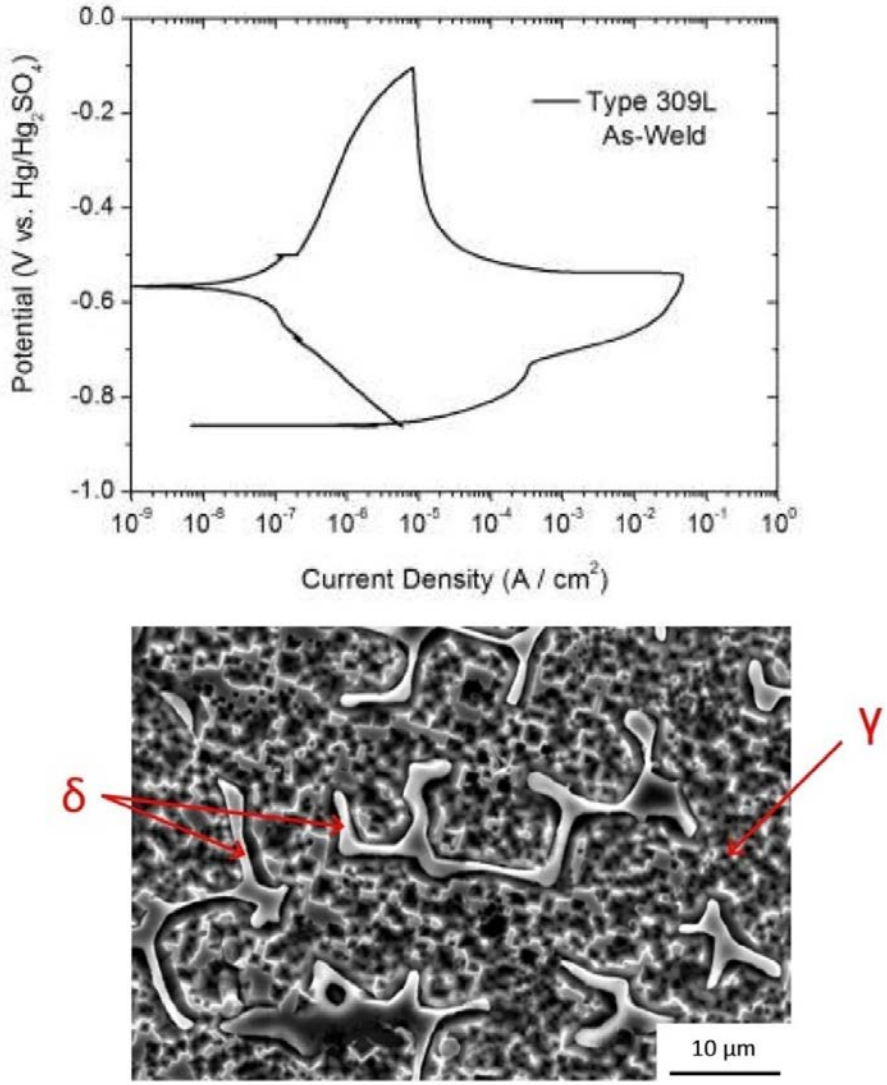

Figure 6-24: Standard DLEPR cycle including and resulting attack morphology of 309L sample in the as-welded condition.

After completing the test in the as-welded condition, the attack was found to be evenly distributed in the austenitic matrix without attacking the ferritic phase (shown as δ in the figure). This attack is due to the combination of that produced in the active peak and the corrosion produced during the determination of the OCP. Although it is not possible in principle to separate each contribution; the resulting morphology can be considered as the baseline for the following experiments in this

section, given that all of them were subjected to OCP determination and active dissolution in the forward sweep. The finding that austenitic matrix is preferably attacked over δ ferrite dendrites is further discussed in Section 6.5.

PWHT at 600°C for 10 h

Figure 6-25 shows the results of the potentiokinetic test used for studying the attack in the first reactivation peak of 309L material PWHT for 10 h at 600°C. It can be seen that, in addition to the attack on the austenitic matrix (γ), a strong removal of the γ-δ interface was produced without damaging the ferritic phase (δ).

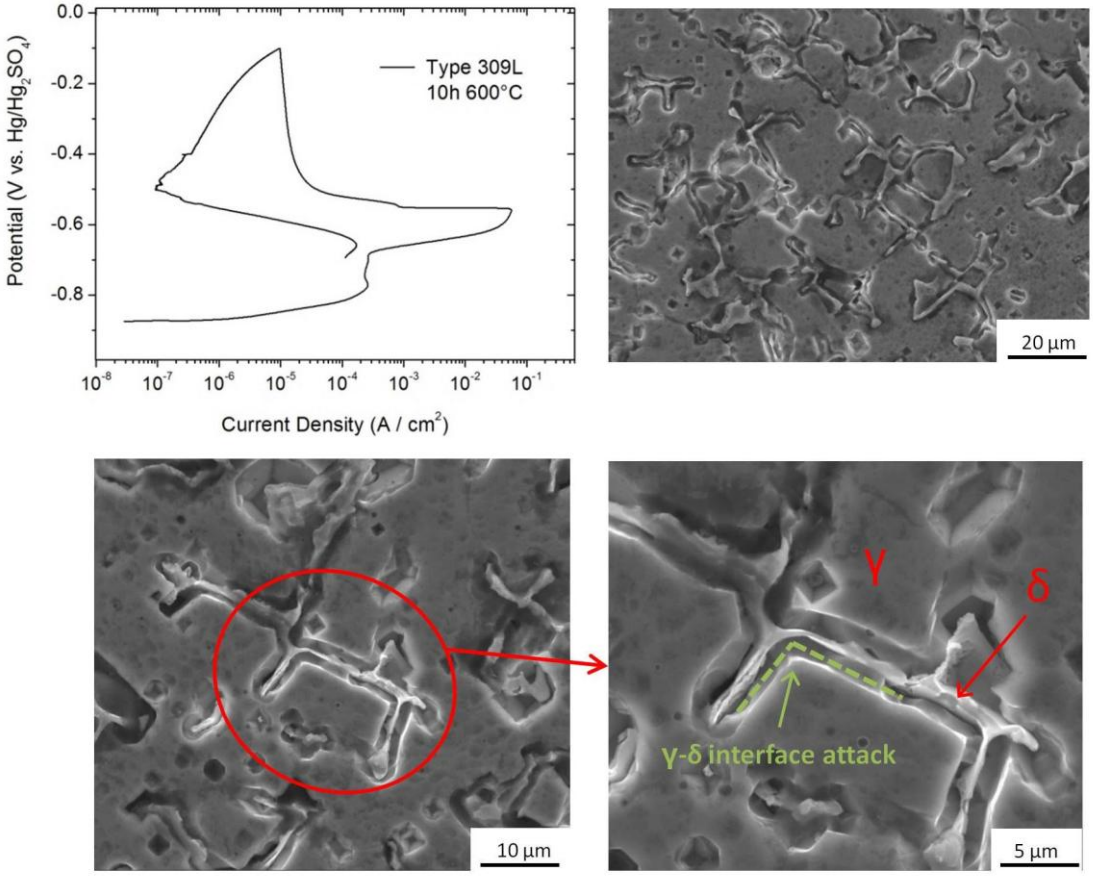

Figure 6-25: Potentiokinetic cycle corresponding to the first reactivation peak and resulting attack morphology of 309L PWHT for 10 h at 600°C.

The results of the potentiokinetic test used for studying the attack in the second reactivation peak of 309L material PWHT at 600°C for 10 h are shown in Figure 6-26. Although the γ-δ interface was visible, a deep localized attack was not found. Again an even attack of the austenitic matrix was observed and δ ferrite was not attacked.

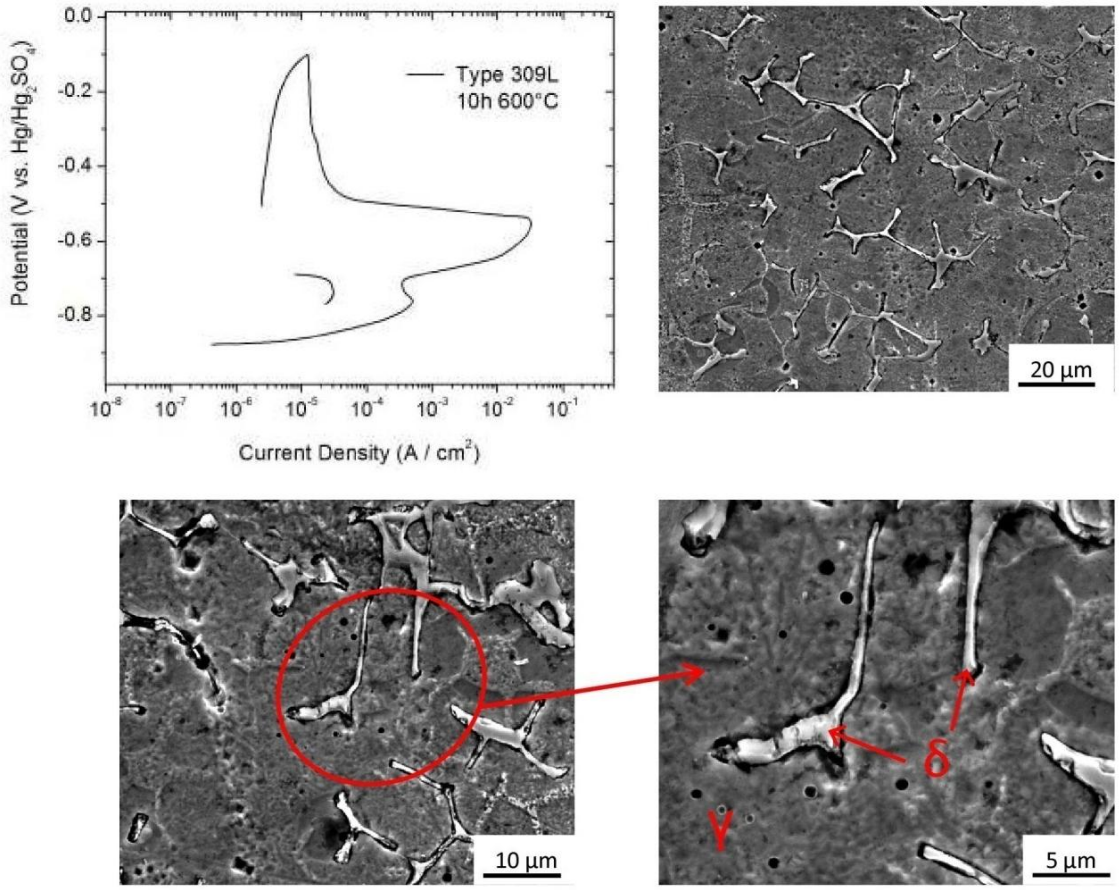

Figure 6-26: Potentiokinetic cycle corresponding to the second reactivation peak and resulting attack morphology of 309L PWHT for 10 h at 600°C.

PWHT at 600°C for 100 h

Figure 6-27 shows the results for the first reactivation peak of 309L samples PWHT for 100 h. Similarly to what was observed for the first reactivation peak of the

samples PWHT for 10 h, a deep removal of γ-δ interface is seen without attack to the δ ferrite dendrites

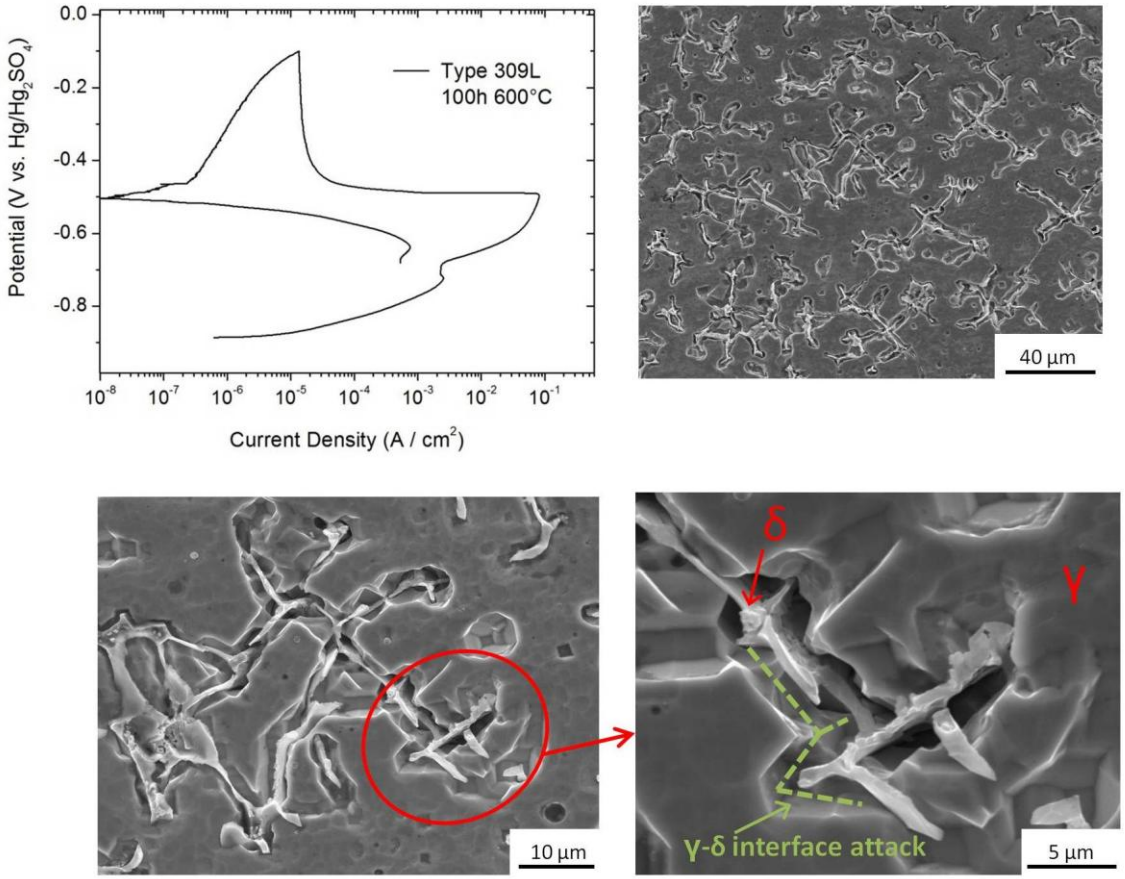

Figure 6-27: Potentiokinetic cycle and resulting morphology of the first reactivation peak of 309L sample PWHT for 100 h.

Figure 6-28 shows the results for the second reactivation peak of the 309L samples PWHT at 600°C for 100 h. Similarly to what was observed for the second peak of 309L samples PWHT for 10 h, the γ-δ interface was revealed without massive attack. However, a distinctive attack was observed in some regions of the dendrites of samples treated for 100 h. This attack could be associated to phase transformations

carried out in δ ferrite for long PWHT times, as further discussed in section 6.5 of the present chapter.

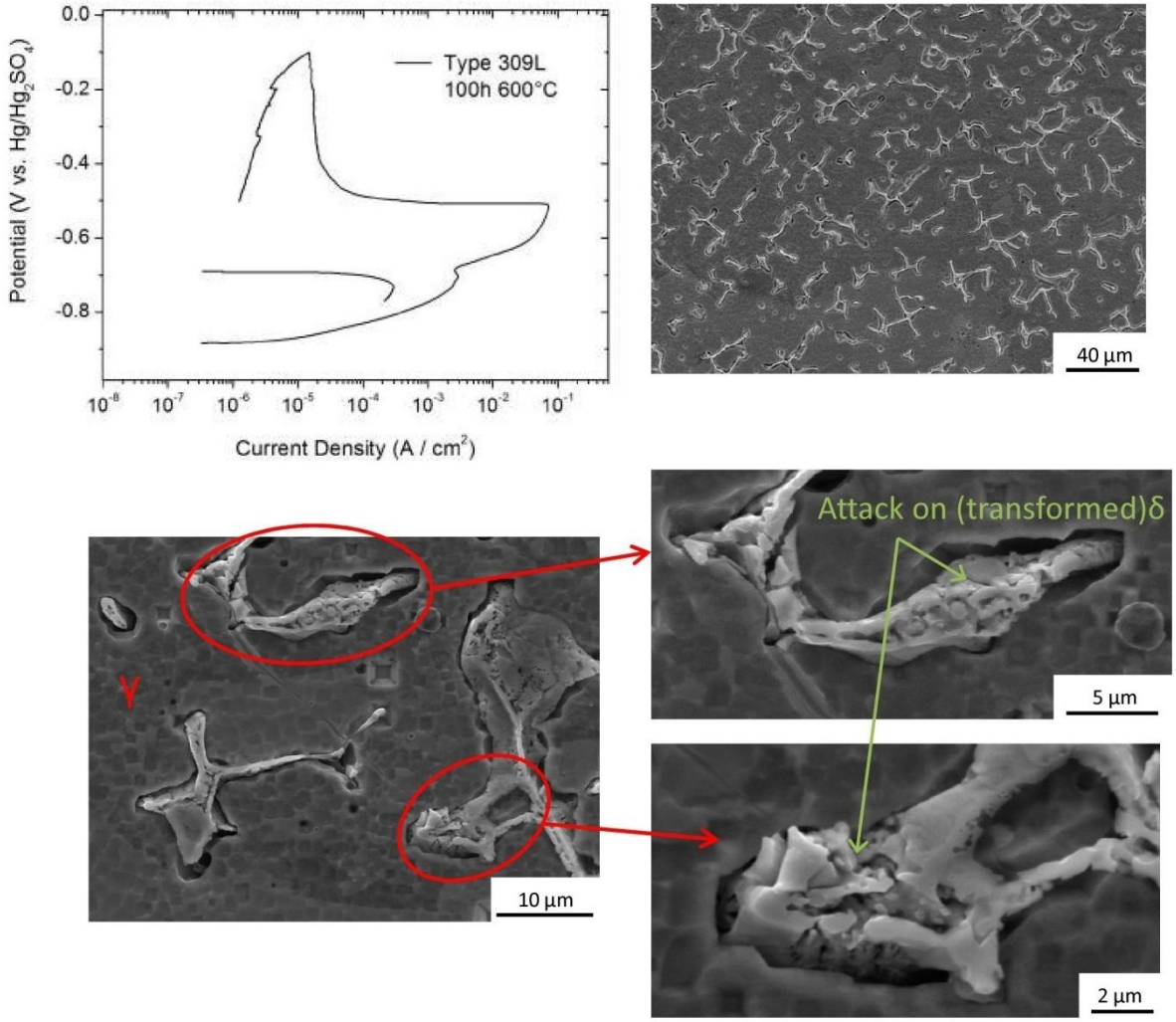

Figure 6-28: Potentiokinetic cycle and resulting morphology of the second reactivation peak of 309L samples PWHT for 100 h

Table 6-2 summarizes the morphologies found for the different peaks and specific potentiokinetic cycles.

Table 6-2: Summary of the morphologies found after potentiokinetic cycles

Type 309L	As-Welded	10 h – 600°C	100 h – 600°C
Whole DLEPR cycle	Baseline morphology		
First reactivation peak		Baseline morphology + interface attack	Baseline morphology + interface attack
Second reactivation peak		Baseline morphology	Baseline morphology + distinctive attack on transformed δ ferrite

6.5 Discussion on corrosion properties evolution

6.5.1 Graphical Summary

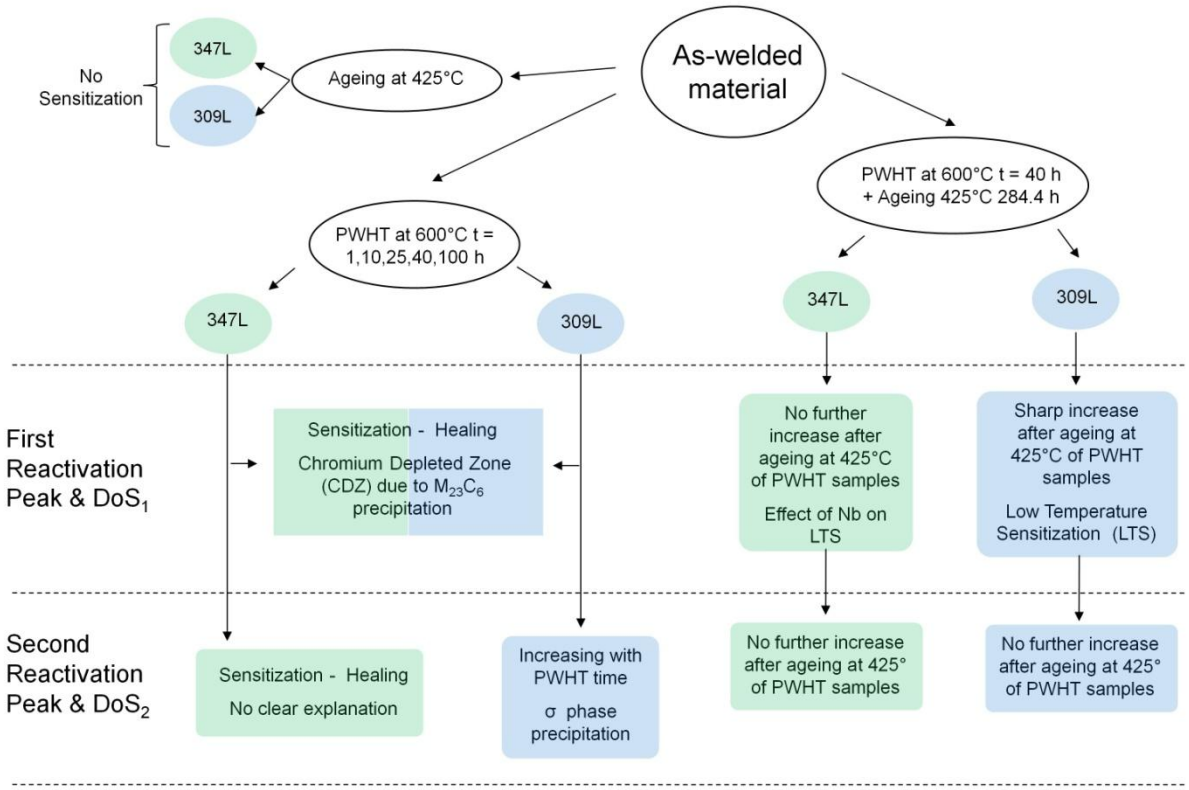

6.5.2 Reactivation peaks

Two reactivation peaks were observed for both 347L and 309L materials during PWHT at 600°C (Figure 6-13 and Figure 6-20). The first reactivation peak to appear in the reverse sweep (-0.64 V) was always formed as a clear peak, whereas the second peak (-0.74 V) could be clearly visible as a peak or as a shoulder in the resulting curve. It is worth noting that both peaks appear approximately at the same potential for both 347L and 309L materials and for any post welding treatment time, whereas the intensity of the peak (and the associated degree of sensitization) showed different behaviour depending on material and PWHT time.

The presence of more than one reactivation peak in the reverse sweep was reported in literature for single loop and double loop EPR tests of different materials such as nickel-based Alloy 600, iron-based Alloy 800, duplex stainless steel and Type 316L stainless steel [21-25]. deAssis et al. [25] were able to link the first reactivation peak they found to sigma phase whereas the second peak was attributed to austenite attack. Unfortunately, it is not possible to compare numerically the potentials found by these authors with those of the present work due to the different electrolytes and experimental conditions used. This observation applies to other studies found in the open literature [23, 30]. The lack of a clear agreement about the process behind each peak motivated the present study.

An analysis of both reactivation peaks in terms of microstructural modifications observed in this study is performed in the following paragraphs

Significance of first reactivation peak

DoS_1 in 347L and 309L could be linked to the creation of a Cr-depleted zone (CDZ) around precipitated $M_{23}C_6$ according to the following considerations:

1. *Reactivation peak splitting technique*

The procedure described in Section 6.4 allowed studying separately the morphology of the attack corresponding to each reactivation peak found during PWHT at 600°C. In addition to the as-welded condition, two ageing times (10 h, and 100 h) were tested and the morphology of the attack produced by the first and second reactivation peak was studied. In the case of the first reactivation peak, a very selective attack was found to be located in the γ-δ interface for 10 h (Figure 6-25) and 100 h (Figure 6-27) of treatment. In both cases δ ferrite dendrites and γ matrix remained unattacked and only precipitates in the interphase seemed to have been removed. Taking into account that carbides (but no sigma phase) were observed after 10 h of PWHT as described in Chapter 4, and that after 100 h σ was observed within the δ ferrite dendrites and not only in the interphase; the morphology observed is consistent with the idea that the first reactivation peak could be linked to the creation of a chromium depleted zone due to precipitation of $M_{23}C_6$ in the δ/γ interphase.

2. *Evolution of DoS_1 as a function of PWHT time*

The study of the evolution of the DoS_1 as a function of time at 600°C showed for both 347L (Figure 6-14) and 309L (Figure 6-21) an increase in this parameter up to 10 h of treatment followed by a decrease up to 40 h, where a plateau is reached until the end of treatment at 100 h. This behaviour can be associated with the sensitization-

healing process reported for carbide precipitation in stainless steels in the range of 500 ºC – 800 ºC [41]. According to this process, Cr-rich carbides precipitate creating a Cr-depleted zone around them. Simultaneously, and given that the relatively high temperature allows diffusion of bulk-contained Cr, the depleted zone is replenished with this element for longer treatment times. These two processes (Cr depletion around precipitates and replenishment with bulk-diffused Cr) occur at the same time but with different kinetics. Depletion of Cr around precipitates occurs faster, simultaneously with $M_{23}C_6$ precipitation, and prevails during the first stages of treatment; whereas replenishment of Cr involves slow diffusion of bulk Cr through longer diffusion paths [63] [64] and can compensate depletion of Cr only for longer treatment times.

The peak value of DoS_1 as a function of time at 600°C was found after 10 h of treatment for both 347L and 309L (Figs. 6-15 and 6-22 respectively). As analyzed in Chapter 4, this time is consistent with the time required to create a depleted zone of 20 nm around carbides with Cr concentration lower than 13%; which is the condition to reach sensitization according to the model of sensitization proposed by Strawstrom and Hillert [63].

The sharper increase and decrease and the higher peak values of DoS_1 found in 347L (Figure 6-14) in comparison to the flatter behaviour of 309L (Figure 6-21) could also be explained in terms of the evolution of the Cr-depleted zone around $M_{23}C_6$. The stabilizing element contained in 347L (niobium) and the higher content of Cr of 309L could play important roles to explain this difference.

During cooling of 347L after solidification, a significant part of the free carbon in the alloy is trapped as niobium carbide (NbC) as seen in Chapter 4. When the material is later subjected to PWHT at 600°C, the remaining carbon precipitates as $M_{23}C_6$ and forms the CDZ in the first stage of treatment. After 10 h most of the free C is supposed to be trapped either as NbC or $M_{23}C_6$. In this situation, where very little carbon is free to continue precipitating, the balance between creation and replenishment of the CDZ is strongly inclined to replenishment of the CDZ, which is seen as a sharp decrease of DoS_1 in Figure 6-14. On the other hand, the higher chromium content of 309L gives a higher sensitization resistance to this alloy (seen as lower DoS_1 values). However, given that no C can be trapped during solidification due to the lack of stabilizing elements, a higher proportion of the C contained in the alloy is available for $M_{23}C_6$ precipitation. In these conditions, contributions to sensitization and healing processes could be more compensated all along the treatment leading to the "flatter" behaviour of the DoS_1 as a function of PWHT time observed in 309L.

A quantitative analysis can be performed to confirm this explanation. The study could be based on a comparison between total carbon content in the alloy and a metallographic count of (NbC + $M_{23}C_6$) at each treatment time in order to determine the real amount of free carbon in the as-welded condition and its evolution during PWHT at 600°C.

3. Metallographic observations

Both 347L and 309L were found to be free of carbides in the γ-δ interphase in the as-welded condition (see Chapter 4). These precipitates were clearly visible in metallographic observations with Murakami´s reagent after 10 h of treatment at 600°C. Carbides were also detected for 25 h of treatment and were not longer visible after 40 h of treatment in both materials. This is consistent with the increase and decrease of DoS_1 in Figure 6-14 and Figure 6-21 and with the above described sensitization-healing process. The fact that carbides were not visible in etched samples after 40 h of treatment does not imply that these precipitates were not present; it might rather imply that the CDZ had been replenished. Murakami etchant works attacking the Cr-depleted zone leaving it visible as a dark spot. Therefore, if the Cr-depleted zone is replenished with bulk-diffused Cr, carbides will not be revealed by the etchant but will still be present in the alloy, since they cannot be dissolved at 600°C (solution treatments above 1000°C are required to dissolve carbides in stainless steel). In fact, $M_{23}C_6$ were detected in Chapter 4 using EBSD in non-etched samples of both materials after 100 h of treatment at 600°C which showed no dark spots in the interface after Murakami etching.

Significance of second reactivation peak

DoS_2 showed different behaviour for 347L and 309L. As shown in Figure 6-14, DoS_2 of 347L followed the same sensitization-healing cycle than DoS_1, whereas DoS_2 of 309L (Figure 6-21) showed an increase with PWHT time at 600°C tending to reach a plateau for the last stage of treatment. The discussion about the relationship between DoS_2 and microstructure evolution should then be split for each material.

Second reactivation peak of 309L SS

DoS_2 of 309L could be linked to the precipitation of sigma phase according to the following considerations:

1. *Reactivation peak splitting technique in 309L*

A selective attack was obtained in the cycle designed to study the second reactivation peak in 309L after 10 h (Figure 6-26) and 100 h (Figure 6-28) of post welding treatment at 600°C.

After 10 h of treatment Figure 6-26 shows that neither δ ferrite dendrites nor δ-γ interface were affected by the second reactivation peak, and the only attack found was that uniformly produced in γ matrix. The fact that δ-γ interface was not attacked is worthy of special attention. After 10 h at 600°C 309L samples were found to be sensitized in Chapter 4, showing precipitation of $M_{23}C_6$ but not σ phase. In addition they showed the highest values of DoS_1 in Figure 6-21, and were selectively attacked at the δ-γ interface when the first reactivation peak was applied - (Figure 6-25). The lack of δ-γ interface attack found after applying the second reactivation peak in an isolate manner could imply that this peak is not related to the CDZ created due to $M_{23}C_6$ precipitation in 309L.

After 100 h at 600°C (Figure 6-28) 309L samples subjected only to the second reactivation peak, showed a distinctive attack on δ ferrite dendrites in addition to the uniform attack of the austenitic matrix found in the as-welded condition. It should be

noted that δ ferrite dendrites were found to be partially transformed into σ phase in Chapter 4.

Considering that the morphology of the attack left by the second reactivation peak on δ ferrite dendrites (Figure 6-28) was similar to that produced by Murakami etchant to reveal σ phase in Chapter 4, and similar to the coral-like morphology reported in literature for σ precipitation [65, 91, 93]; it could be possible to link the second reactivation peak to precipitation of σ phase in 309L SS.

It was not possible to distinguish precisely which part of the transformed dendrite is attacked in the second reactivation peak. Sigma phase is reported to precipitate according to the following process [8, 86-88]:

$$\delta \rightarrow \sigma + \gamma_2$$

Therefore dissolution of either secondary austenite or the σ itself can be responsible for the formation of the second reactivation peak. Creation of a CDZ within δ as a consequence of σ precipitation is also discussed in literature [65, 78, 146, 147]. Further studies are required to clarify this issue.

2. Metallographic observations

As described in Chapter 4, sigma phase in 309L started to be observed after 25 h of PWHT and was clearly seen after 40 and 100 h confirmed by EBSD. This last stage of the treatment is in coincidence with the period where DoS_2 is increased not only in

its absolute value but also in comparison to DoS_1. This can be observed as the increase of DoS_2 to DoS_1 ratio shown in Figure 6-21 after 40 h of treatment.

Second reactivation peak of 347L SS

In the case of 347L, DoS_2 followed a sensitization-healing behaviour with a very similar shape and approximately half of the value of DoS_1 (Figure 6-14) of the same material for each PWHT time. It was not possible to formulate a clear explanation for this behaviour in the present study. As seen in Chapter 4, 347L has a lower tendency to precipitate σ phase which was only observed after 100 h of treatment at 600°C in comparison to the 25 h required in 309L. If DoS_2 were linked to precipitation of σ phase in 347L, this observation would be in agreement with the lower DoS_2 values found for 347L than for 309L. However, it could not explain the sensitization-healing behaviour showed by this parameter.

Treatments longer than 100 h could be used to see if the amount of σ in 347L is further increased and whether or not the behaviour of DoS_2 is consequently changed. A thorough analysis should be performed since DoS_2 of 347L could be initially expected to be linked to the same process than DoS_2 of 309L, given that precipitation of σ occurred in both materials and the same characteristic potential associated to DoS_2 was found (-0.74 V).

Considerations about the evolution of DoS_2 as a funtion of PWHT time in 309L

With the data obtained in the present study it is not possible to establish a quantitative relationship between DoS_2 in 309L and the amount of δ ferrite transformed into σ during PWHT. Longer treatment times would be required in order to obtain the "saturation" DoS_2 associated with the total transformation of δ ferrite. This is considered for future work.

Recent studies in the open literature indicate a qualitative relationship between DoS and the amount of σ phase in duplex and ASSWs as a result of δ ferrite decomposition [25, 175]. However, neither numerical formulations nor distinctive interpretation of the double peak can be found. Moreover, different electrolytes and scan rates are used by different authors, which make it impossible to incorporate data of longer ageing times into that obtained in this study.

6.5.3 Evolution during simulated service conditions

As-welded condition

After the oxalic acid test and the DLEPR, a preferential attack on the austenitic phase was observed for both materials. The individual electrochemical behaviour of phases present in duplex SS has been studied by means of micro-electrochemical techniques [87, 140, 141]. Perren et al. [141] found a good correlation between the corrosion resistance of each phase with their pitting resistant equivalent with nitrogen (PRE_N), which can be calculated from the chemical composition of each phase according to the following formulation

$$PRE_N = wt.\% Cr + 3.3\ wt.\% Mo + 20\ wt.\% N$$

Equation 6-4

Using chemical compositions and ferrite content obtained in Chapter 4 PRE_N of each phase was calculated showing a higher value for δ (21.61 in 347L and 27.58 in 309L) than for γ (18.08 in 347L and 22.01 in 309L) in both materials. This observation is in agreement with the preferential attack of γ observed in the as-welded condition.

Simulated service conditions without PWHT

When the accelerated ageing at 425°C was applied to 347L and 309L samples in the as-welded condition (i.e. without PWHT at 600°C) no significant changes in corrosion properties were observed. All samples passed the oxalic acid test (Figure 6-2 and Figure 6-6) and a single reactivation peak with very low DoS values was observed in DLEPR tests (Figure 6-12 and Figure 6-19). The lack of degradation of corrosion properties observed due to ageing at 425°C of non-PWHT samples is in agreement with what is reported in literature for ASSWs in the 300°C – 500°C temperature range. Spinodal decomposition and precipitation and growth of α and α´ in the ferritic phase are pointed out as the main transformations taking place, and for these processes the degradation of corrosion properties takes place for longer treatment times (several thousand hours). The increase in hardness and decrease in the Charpy impact energy observed in Chapter 5 for these samples are also consistent with these mechanisms since degradation of mechanical properties is reported to occur

before reduction of corrosion resistance as a result of spinodal decomposition [53, 110].

The other mechanism reported for ASSWs aged at 425°C is Low Temperature Sensitization (LTS), which is the growth by short-range diffusion of already precipitated $M_{23}C_6$ carbides and the consequent creation of a chromium depleted zone- around them sensitization [71, 72]. However, microstructural characterization of both 347L and 309L (see Chapter 4) showed that there is not a significant amount of $M_{23}C_6$ in the as-welded condition which would be able to grow during ageing at 425°C, explaining the lack of influence of this mechanism.

Simulated service conditions following PWHT

Different results were obtained when the accelerated ageing at 425°C was applied to samples that had been given a PWHT at 600°C for 40 h. No significant increase was found either in DoS_1 or in DoS_2 of 347L when the combined treatment was compared with the PWHT only (Figure 6-16) whereas a sharp increase in DoS_1 was observed for 309L with no changes in DoS_2 (Figure 6-23).

After 40 h of PWHT at 600°C, δ ferrite in 347L and 309L was found to be partially transformed into $M_{23}C_6$ (see Chapter 4) and the CDZ created in this process replenished with bulk-diffused Cr (Section 6.3). When these PWHT samples were further aged at 425°C, LTS can take place in the material growing the existing carbides due to short–range diffusion and creating a new CDZ that cannot be

replenished, due to the low temperature of the treatment that makes bulk diffusion of chromium extremely slow [71, 72]

The sharp increase in DoS_1 of 309L in Figure 6-23 can be associated to this process considering that DoS_1 was linked to the creation of a CDZ in the present study (Section 6.5.2). The fact that DoS_2 of 309L was not modified after ageing at 425°C samples that had been PWHT for 40 h at 600 °C is also in agreement with the results of this study. DoS_2 was linked to σ phase precipitation in 309L during PWHT and 425°C is a too low temperature for this phase to continue growing.

In the case of 347L, the lack of variation in DoS_1 shown in Figure 6-16 could be explained by the stabilizing effect of Nb which would leave very little free carbon available to continue growing during ageing at 425°C the $M_{23}C_6$ carbides precipitated during PWHT, avoiding thus the creation of a new CDZ. A quantitative analysis of the amount of NbC + $M_{23}C_6$ compared with the total carbon of the alloy needs to be performed in order to confirm this explanation. In addition, the higher resistance of 347L to create a new CDZ during ageing at 425 °C of PWHT samples was shown in Chapter 4. The comparison of micrographs before and after the treatment at 425 °C showed a significant amount of dark spots appearing in the γ-δ interface of 309L after the treatment indicating sensitization, whereas 347L kept the same microstructure before and after the accelerated ageing.

The evolution of DoS_2 in 347L samples cannot be fully explained with the results of the present study since there is not enough evidence to link DoS_2 to a microstructural

transformation in this material. The scatter found in DLEPR curves (Figure 6-15) suggests that further ageing at 425°C does not have an influence in the process and that the apparent reduction on DoS_2 shown in Figure 6-16 could be attributed to experimental variations. These observations should be taken into account to continue studying the relationship between DoS_2 and microstructural transformations in 347L.

6.5.4 Industrial relevance of the studied parameters

The kinetics of the sensitization-healing behaviour of DoS_1 has an important correlation with the industrial fabrication of reactor pressure vessels (RPV). According to the results of the present study, precipitation of $M_{23}C_6$ will occur in RPV claddings during the first stage of the stress-relief PWHT at 600°C and sensitization will take place due to the creation of the corresponding CDZ around carbides. However, after 40 h at 600°C, healing will be observed in both 347L and 309L with a reduction of DoS_1 to an acceptable value according to ISO 12.732 standard [155] (0.74% average for 309L and 1% average for 347L) and will remain like this until the end of the 100h treatment. Reference values provided by this standard (DoS < 1% = not sensitized, 1% < DoS < 5% = slightly sensitized, DoS > 5% = sensitized) should not be taken as prescriptive due to the wide range of applications of the method, but can be considered as an acceptable framework. In this context, it is possible to say that the 40 hours generally specified for stress-relief PWHT at 600°C during RPV fabrication is a safe time bound from sensitization standpoint due to replenishment of the CDZ; and special care should be taken if shorter periods of time are to be specified.

Considering that DoS_2 was linked to σ precipitation in 309L, it can be said that care should be taken when long treatments at 600°C are applied to 309L given that DoS_2 in 309L showed a constant increase with PWHT time.

The study of simulated service conditions showed that no variations are expected for DoS_2 in both 347L and 309L when put in service after fabrication. However, 309L showed a sharp increase in DoS_1 whereas no variations were observed for this parameter in 347L. Considering the results of the present study, this difference would indicate that RPV claddings made of 347L would have a higher resistance to sensitization due to LTS during long term service than those made of 309L.

6.6 Conclusions

DELPR and microstructural characterization were used to study the processes behind loss of intergranular corrosion resistance of austenitic stainless steel welds during fabrication and service conditions of reactor vessel claddings. Stainless steel cladding materials 347L and 309L were subjected to three different sets of thermal treatments, corresponding to the different fabrication and service stages of the component.

The following conclusions can be drawn from the present study:

1) Two characteristic reactivation peaks at -0.64 V and -0.74 V were identified for both 347L and 309L ASSWs when exposed to PWHT at 600°C for up to 100 h.

The DLEPR control parameter (Degree of Sensitization - DoS) can be further expanded into two parameters, DoS_1 (-0.64 V) and DoS_2 (-0.74 V) associated with each reactivation peak, to better explain sensitization in these materials.

2) It was possible to correlate DoS_1 with the creation of a chromium-depleted zone in both 347L and 309L, associated to precipitation of $M_{23}C_6$ during first stages of PWHT at 600°C.

3) DoS_2 could be linked to the precipitation of σ phase in the ferritic phase in 309L confirmed by EBSD, showing a promising new application of DLEPR to identify deleterious phases in ASSWs.

4) A direct relationship between DoS_2 and microstructural modifications in 347L could not be established in the present study.

5) During PWHT at 600°C a sensitization-healing process was observed for both 347L and 309L. This process implies the loss of intergranular corrosion resistance due to creation of a Cr-depleted zone around precipitated carbides during first stages of treatment at 600°C; followed by a restoration of properties due to replenishment of the depleted zone with bulk-diffused Cr. Maximum sensitization was shown after 10 h of treatment and healing to an acceptable value according to BS EN ISO 12.732:2008 standard [155] was reached after 40 h in both materials. This time is consistent with the PWHT time specified for reactor vessel fabrication, indicating that, although $M_{23}C_6$ are

present, they do not represent a risk for PWHT longer than 40 h due to the replenishment of the CDZ.

6) DoS_2 of 309L stainless steel, associated to precipitation of σ phase in this material, increased with PWHT time up to 100 h of treatment at 600°C.

7) Modification of microstructure and corrosion properties of RPV cladding materials during fabrication and service conditions can be described as a three step process:
   a. Formation of a -Cr depleted zone due to precipitation of $M_{23}C_6$ carbides during first stages of PWHT at 600°C producing an increase of sensitization, shown by a rise of DoS_1 value
   b. Restoration of resistance to intergranular corrosion due to Cr replenishment (healing) during last stage of PWHT at 600°C (25 h - 40 h) shown by a decrease of DoS_1
   c. Eventual growth during simulated service ageing at 425°C of carbides previously precipitated during PWHT at 600°C and creation of a new CDZ (low temperature sensitization - LTS).

8) 347L showed a higher resistance to intergranular corrosion due to low temperature sensitization than 309L when samples PWHT for 40 h at 600°C were subjected to reactor simulated service conditions at 425°C. The presence of Nb as a stabilizing element in 347L may prevent the occurrence

of LTS by trapping free C as NbC during material solidification in the fabrication stage.

9) 347L and 309L showed no sensitization when exposed in the as-welded condition (i.e. without PWHT at 600°C) to reactor simulated service conditions at 425°C. No transformation of δ ferrite either into $M_{23}C_6$ or into σ phase was observed for these samples.

7 Summary and conclusions

7.1 Summary

7.1.1 Relevance of the work

Interior of RPVs are clad with a relatively thin (6 – 10 mm) layer of austenitic stainless steel which provides corrosion protection to the load-bearer base material. As a final stage of fabrication RPVs are subjected to a PWHT at 600°C for ~40 h in order to relieve stresses built in the base material during welding [2]. Once in service, RPV claddings are expected to operate at ~300 °C with neutron fluxes in the range of 1 x 10^{10} to 1 x 10^{11} $\frac{n}{cm^2\,S}$ for at least 30 to 40 years according to original design specifications [1]. However, care must be taken to avoid phase changes produced by combination of fabrication PWHT and service exposure that could lead to sensitization of the cladding increasing its susceptibility to intergranular corrosion and IGSCC.

Despite there are not significant damages reported in reactor vessel claddings to date, nuclear power plant life extension processes taking place around the world add an increased importance to the study of low-kinetics degradation processes such as low-temperature sensitization (LTS) in order to avoid problems in reactors that will be expected to operate for up to 80 years [4]. In addition, relatively little work is available in the open literature about the effects of combined treatments during fabrication and service [14, 15] and the whole precipitation sequence has not yet been studied in detail.

The present study investigated the relationship between metallurgical transformations of RPV cladding materials with the resulting modifications on corrosion and mechanical properties. Special care has been taken in trying to reproduce in a realistic manner the processes occurring during fabrication and service of these materials.

Samples of 347L and 309L austenitic stainless steel welds have been obtained using an industrial-scale process (submerged arc welding with strip electrodes) and commercially available materials. Industry specifications and procedures [160] have also been followed. Given the practical impossibility of reproducing in-service ageing at 300°C for 60 years and considering that ageing is a thermally activated process [10, 11]; an Arrhenius model was used to simulate in-service ageing with a laboratory ageing at higher temperature in a shorter time (see Chapter 3). The accelerated ageing temperature was limited to 425°C in order to ensure the same ageing mechanism than that occurring at 300°C [57] . Neutron irradiation is known to affect SS microstructure [33-37]. However, the present work was focused on the study of modifications due to high temperature exposure and the influence of irradiation is considered for future research.

The use of an industrial-scale process for sample fabrication entails the need for dealing with a higher degree of variability. For this reason it was necessary to define a suitable sample fabrication method that could allow microstructural, mechanical, and corrosion tests to be performed in a consistent way (see Chapter 4).

7.1.2 Performance of RPV cladding materials analyzed in the present study

The knowledge of the precipitation sequence (Chapter 4) and corrosion properties (Chapter 6) during weld deposit, PWHT at 600°C, and simulated service ageing of RPV cladding materials lead to the view that although the cladding can be free from sensitization after fabrication, sensitization could develop later during long term service by LTS (growing of previously deposited carbides and creation of a new CDZ). This mechanism has been largely studied for different ASSWs of pipes and nuclear waste containers [13, 66, 67, 72, 73, 176-179] but is scarcely reported in literature for weld claddings of RPVs [14, 15].

After welding, 347L and 309L were not found to be sensitized as shown by oxalic acid test and DLEPR. No carbides were found in this condition presumably due to the high cooling rates involved in the welding process. After PWHT for 40 h at 600 °C it has been shown that $M_{23}C_6$ carbides are present in both 347L and 309L. However, due to the PWHT time and temperature the CDZ could be replenished with bulk-diffused Cr following a sensitization-healing process and showing no risk from the intergranular corrosion stand point. When PWHT material was further subjected to simulated service conditions at 425°C for 284.4 h, 309L showed increased sensitization whereas 347L remained resistant. This difference could be attributed to the role of Nb in reducing free C in 347L by trapping it as NbC during solidification, as observed in Chapter 4. This observation is in agreement with Hamada and Yamauchi [14] who proposed the addition of Nb to make Type 308 SS weld metal resistant to PWHT and LTS for RPV cladding applications. Lippold [76] has also

reported that LTS was observed in low carbon SS but does not seem to be a problem for stabilized grades such as Type 347.

Precipitation of σ phase is known to affect corrosion and mechanical properties of ASSWs [6, 16, 17, 80, 101, 129]. This phase was found in the present study by metallographic observations and further confirmed by EBSD during the last stages of PWHT for both 347L and 309L. Precipitation of σ in ASSWs is possible in relatively short ageing times due to the fast diffusion paths for Cr provided by δ ferrite [8] as has been observed by other authors [14, 16-19]. 309L showed a higher tendency to precipitate σ presumably due to the higher content of Cr and δ ferrite in comparison to 347L, given that both factors are known to promote σ precipitation in ASSWs [82, 85]. The effect on corrosion properties of this higher amount of σ was seen as a particular increase in the second reactivation peak of 309L. The expected reduction of toughness associated to this phase could not be confirmed in the present study since impact tests were not performed on PWHT samples and are proposed for future research.

These results suggest that 347L shows advantages from the intergranular corrosion resistance standpoint in comparison to 309L. However, this conclusion cannot be used alone for the decision-making process of material selection, since many other parameters such as weldability, availability, costs, and even local industry experience at the place of fabrication are to be considered.

Degradation of mechanical properties (increase of hardness and decrease of impact energy) observed in Chapter 5 for as-welded 347L and 309L after ageing at 425°C is in agreement to what is expected for low temperature ageing of duplex and ASSWs due to spinodal decomposition of the δ ferrite [105, 108, 110, 112, 180]. Data of changes during PWHT and PWHT followed by simulated service ageing was not obtained in the present study and is considered for future work. Reduction of δ ferrite fraction observed in Chapter 4 and possible thermal relief during PWHT, would lead to the conclusion that no further concerns are expected. However, more research is required to confirm this observation.

7.1.3 Contribution to the development of DLEPR as a detection tool for deleterious phases in stainless steels.

The presence of more than one reactivation peak was reported in literature for single-loop and double loop EPR tests of different materials. However, there is not a clear agreement about the processes behind each peak [21-25, 30].

Two characteristic DLEPR reactivation peaks have been found in the present study for 347L and 309L after PWHT at 600°C. Therefore the DLEPR control parameter (degree of sensitization – DoS) was proposed to be split into two parameters DoS_1 and DoS_2 associated to the first and second reactivation peak to appear in the reverse sweep (at ~-0.64 V and -0.74 V respectively).

Analyzing the evolution of DoS_1 with PWHT time and comparing it with microstructural changes detected in Chapter 4; the first reactivation peak was linked

to the creation of a CDZ due to precipitation of $M_{23}C_6$ for both 347L and 309L. In a similar way, the second reactivation peak was linked to the precipitation of σ phase in 309L, whereas not enough evidence was collected to extend this observation to 347L. deAssis et al. [25] were able to link the first reactivation peak they found to sigma phase in superduplex SS, whereas the second peak was attributed to austenite attack. Unfortunately it is not possible to compare numerically the potentials of the peaks found by these and other authors [21-24, 30] with those of the present work due to the spread of electrolytes and experimental conditions used.

A specific split-cycle DLEPR test was designed and successfully applied to 309L in order to provide additional evidence of the selectivity of the attack produced by each reactivation peak (see Chapter 6). Extension of this test to 347L would be necessary to identify the process behind the second reactivation peak for this material and is proposed for future work.

7.2 Conclusions

- Austenitic stainless steels Type 347L and Type 309L used as reactor pressure vessel cladding materials have been evaluated under realistic temperature conditions. Microstructural modifications during each stage of fabrication and simulated service heat treatment have been identified and linked to variation of intergranular corrosion resistance quantitatively evaluated by the DoS.

- After weld deposit both materials were found to be free of sensitization. During the first stage of PWHT at 600°C $M_{23}C_6$ carbides precipitated creating a CDZ

which was replenished with bulk-diffused Cr after 40 h of treatment following a sensitization-healing cycle.

- When PWHT material was further subjected to simulated service treatment at 425°C, 309L was found to be re-sensitized whereas 347L was not. The higher resistance of 347L to LTS was attributed to role of Nb in reducing free C in 347L by trapping it as NbC during solidification.

- Sigma phase was found to precipitate during last stages of PWHT at 600”C. The higher tendency of 309L to precipitate σ was attributed to the higher content of Cr and δ ferrite in comparison to 347L.

- Type 347L showed advantages from the intergranular corrosion resistance standpoint in comparison to 309L with a higher resistance to LTS and lower tendency to precipitate σ phase.

- Two characteristic reactivation potentials were identified for both 347L and 309L. A specific split-cycle DLEPR was designed to study the selective attack produced by each reactivation peak showing that DLEPR could be further developed to provide semi-quantitative evaluation of deleterious phases in ASSWs.

8 Future Work

8.1 Consider the effects of neutron irradiation

In the present study RPV cladding service conditions were simulated by an accelerated laboratory ageing without considering the effects of neutron irradiation in ageing kinetics. Optimal experimental conditions would include simultaneous radiation and thermal ageing.

8.2 Study the existence of a quantitative relationship between DoS_1, DoS_2 and precipitated phases

In the present work chromium carbides and σ phase were identified and linked to DLEPR reactivation peaks, but no numeric relationships could be established. A quantitative relationship could be obtained by performing an analysis of precipitated phase's fraction as a function of PWHT time and resulting DoS_1 and DoS_2 from DLEPR. Fraction of phases could be determined by quantitative metallography or by in-situ synchrotron X-ray diffraction as proposed by Elmer et al. [20]. Longer isothermal ageing times could be considered since complete transformation of δ into σ phase was not achieved in the present study. Increasing ageing temperature might be found more convenient to obtain complete transformation in shorter times. As a result of this process DoS_2 would be expected to fit with reasonable agreement a Johnson-Mehl-Avrami curve to confirm its relationship with precipitation of σ phase.

8.3 Perform potentiostatic etching at the characteristic reactivation potentials found

Instead of the split-cycle DLEPR technique applied in the present study, simpler potentiostatic tests in the same experimental set up could be applied at -0.64 V and -0.74 V for a fixed period of time. If the analysis of the surface after the test confirms the selectivity of the attack, a quantitative relationship between the charge circulated during the test at each potential and the amount of material removed could also be explored as a potential detection technique.

9 References

1. IAEA, *Integrity of Reactor Pressure Vessels in Nuclear Power Plants: Assessment of Irradiation Embrittlement Effects in Reactor Pressure Vessel Steels*. 2009, Vienna: International Atomic Energy Agency.
2. Gillemot, F., *Overview of reactor pressure vessel cladding.* Int. J. Nuclear Knowledge Management, 2010. **4**(4).
3. *Requirements for Renewal of Operating Licenses for Nuclear Power Plants.* 10.CFR Part 54 - US NRC.
4. *Standard Review Plan for Review of Subsequent License Renewal Applications for Nuclear Power Plants.* PRE-FINAL NUREG-2192 - US NRC
5. Nowacki, J. and A. Łukojc, *Microstructural transformations of heat affected zones in duplex steel welded joints.* Materials Characterization, 2006. **56**(4–5): p. 436-441.
6. Smith, J.J. and R.A. Farrar, *Influence of microstructure and composition on mechanical properties of some AISI 300 series weld metals.* International Materials Reviews, 1993. **38**(1): p. 25-51.
7. Farrar, R.A. and R.G. Thomas, *The microstructure and phase transformations in duplex 316L submerged arc weld metals.* Journal of Materials Science, 1983. **18**(11): p. 3461-3474.
8. Folkhard, E., et al., *Welding Metallurgy of Stainless Steels*. 1988: Springer Vienna.
9. Parvathavarthini, N., et al., *Sensitization behaviour of modified 316N and 316L stainless steel weld metals after complex annealing and stress relieving cycles.* Journal of Nuclear Materials, 2006. **355**(1–3): p. 68-82.
10. Chung, H.M., *Aging and Life Prediction of Cast Duplex Stainless Steel Components.* Int. J. Pres. Ves. & Piping, 1992. **50**: p. 179 - 213.
11. Gonzalez, J.J., et al., Journal of Testing and Evaluation, 1997. **25**(2): p. 154-162.
12. Nishimoto, K., M. Hiroaki, and N. Yoshikuni, *Low Temperature Sensitization in the Weld Metal of Type 308 Stainles-steel and its Improvement by Laser Surface Melting Treatment.* ISIJ International, 1995. **35**(10): p. 1265-1271.
13. Singh, R., et al., *Low-Temperature Sensitization Behavior of Base, Heat-Affected Zone, and Weld Pool in AISI 304LN.* Metallurgical and Materials Transactions A, 2009. **40**(5): p. 1219-1234.
14. Hamada, I. and K. Yamauchi, *Niobium-Added 308 Stainless Steel Weld Metal Resistant to Sensitization by Postweld Heat treatment and Low -Temperature Aging.* Corrosion 2002. **58**(1): p. 82-93.
15. Hamada, I. and K. Yamauchi, *Intergranular stress corrosion cracking behavior of niobium-added Type 308 stainless steel weld overlay metal in a simulated BWR environment.* Nuclear Engineering and Design, 2002. **214**(3): p. 205-220.
16. Lo, I.-H. and W.-T. Tsai, *Effect of heat treatment on the precipitation and pitting corrosion behavior of 347 SS weld overlay.* Material Science and Engineering, 2003. **A355**: p. 137-143.
17. Pujar, M.G., et al., *Susceptibility of As-Welded and Thermally Aged Type 316LN Weldments Toward Pitting and Intergranular Corrosion.* Corrosion, 1992. **48**(7): p. 579-586.
18. Liu, F., Y.H. Hwang, and S.W. Nam, *Precipitation of Sigma-phase and creep fatigue behavior of 308L steel weldment.* Materials Science and Engineering A, 2008. **483-484**: p. 418-421.
19. David, J.V.a.S., *The solidification and ageing behaviour of Types 308 and 308CRE Stainless Steel Welds.* The Welding Journal, 1984. **63**.
20. Elmer, J.W., T.A. Palmer, and E.D. Specht, *Direct Observations of Sigma Phase Formation in Duplex Stainless Steels Using In-Situ Synchrotron X-Ray Diffraction.* Metallurgical and Materials Transactions A, 2007. **38**(3): p. 464-475.

21. de Assis, K.S., et al., *Practical aspects on the use of on-site Double Loop Electrochemical Potentiodynamic Reactivation Technique (DL-EPR) for Duplex Stainless Steel.* Corrosion Science, 2013. **74**: p. 250-255.
22. Gill, T.P.S., J.B. Gnanamoorthy, and K.A. Padmanabhan, *Influence of Secondary Phases on the Localized Corrosion of Thermally Aged AISI 316L Stainless Steel Weld Metal.* Corrosion, 1987. **43**(4): p. 208-213.
23. Edgemon, G.L., et al., *Sensitization Behavior of Alloy 800H as Characterized by the Electrochemical Potentiokinetic Reactivation (EPR) Technique.* Corrosion, 1994. **50**(12): p. 912-918.
24. Wu, T.-F., T.-P. Cheng, and W.-T. Tsai, *The electrochemical potentiokinetic reactivation behavior of Alloy 600.* Materials Chemistry and Physics, 2001. **70**(2): p. 208-216.
25. de Assis, K.S., et al., *Assessment of electrochemical methods used on corrosion of superduplex stainless steel.* Corrosion Science, 2012. **59**(0): p. 71-80.
26. Cristini, S.I., et al., *Detection of sigma phase in 22% Cr duplex stainless steel by electrochemical methods.* Russian Journal of Electrochemistry, 2010. **46**(10): p. 1094-1100.
27. Tsai, W.-T. and J.-R. Chen, *Galvanic corrosion between the constituent phases in duplex stainless steel.* Corrosion Science, 2007. **49**(9): p. 3659-3668.
28. Lo, I.H., et al., *Effect of electrolyte composition on the active-to-passive transition behavior of 2205 duplex stainless steel in H2SO4/HCl solutions.* Corrosion Science, 2006. **48**(3): p. 696-708.
29. Lo, I.H. and W.-T. Tsai, *Effect of selective dissolution on fatigue crack initiation in 2205 duplex stainless steel.* Corrosion Science, 2007. **49**(4): p. 1847-1861.
30. Leal, P., et al., *Magnetic and Electrochemical Techniques as Tools to Detect Deleterious Phases in Duplex Stainless Steels.* CORROSION, 2015. **71**(7): p. 865-871.
31. Provens, H. *Primary circuit contamination in Nuclear Power Plants: Contribution to occupational exposure* in *Towards harmonisation of radiation protection in Europe: European IRPA Congress 2002*. 2002. Florence, Italy.
32. Davis, W., *Doel-3 in Belgium reports possible pressure vessel flaw.* American Nuclear Society Nuclear Cafe, 2012.
33. Takeuchi, T., et al., *Effect of neutron irradiation on the microstructure of the stainless steel electroslag weld overlay cladding of nuclear reactor pressure vessels.* Journal of Nuclear Materials, 2013. **443**(1–3): p. 266-273.
34. J.S. Lee, I.S.K., R. Kasada, A. Kimura, *Microstructural Characterization and embrittlement phenomena in neutron irradiated 309L stainless steel RPV clad.* Journal of Nuclear Materials, 2004. **326**: p. 38-46.
35. F.M. Haggag, R.K.N., *Effects of Thermal Aging and Neutron irradiation on the Mechanical Properties of Three-Wire Stainless Steel Weld Overlay Cladding*, 1995, Oak Ridge National Laboratory: Oak Ridge.
36. Haggag, F.M., W.R. Corwin, and R.K. Nanstad, *Effects of irradiation on the fracture properties of stainless steel weld overlay cladding.* Nuclear Engineering and Design, 1990. **124**(1): p. 129-141.
37. Corwin, W.R., et al., *Fracture behavior of a neutron-irradiated stainless steel submerged arc weld cladding overlay.* Nuclear Engineering and Design, 1985. **89**(1): p. 199-221.
38. Fontana, M.G., *Corrosion Engineering*. 1987: National Association of Corrosion Engineers.
39. Galvele, J. and G. Duffo, *Degradacion de Materiales I - Corrosión Intergranular*, 2004, Instituto Sabato: Buenos Aires - Argentina.
40. Lippold, J.C. and D.J. Kotecki, *Welding metallurgy and weldability of stainless steel* 2005, New Jersey: John Wiley & Sons, Inc.

41. Brooks, J.A. and J.C. Lippold, *Selection of Wrought Austenitic Stainless Steels* in *ASM Handbook - Volume 6 - Welding, Brazing, and Soldering*1993, ASM.
42. Lundin, C.D., W. Ruprecht, and G. Zhou, *Ferrite Measurement in Austenitic and Duplex Stainless Steel Castings* 1999, Materials Joining Research Group - Department of Materials Science and Enginereeing - The University of Tennessee.
43. Suutala, A., T. Takalo, and T. Moisio, *The relationship between solidification and microstructure in austenitic and austenitic-ferritic stainless steel welds.* Metallurgical Transactions A, 1979. **10A**.
44. David, S.A., *Ferrite morphology and variations in ferrite content in austenitic stainless steel welds.* 1981.
45. Brooks, J.A., A.W. Thomson, and J.C. Williams, *A Fundamental Study of the Beneficial Effects of Delta Ferrite in Reducing Weld Cracking.* Welding Journal, 1984. **63**: p. 71-s to 83-s.
46. *Standard Procedures for Calibrating Magnetic Instruments to Measure the Delta Ferrite Content of Austenitic and Duplex Austenitic-Ferritic Stainless Steel Weld Metal*, in *ANSI/AWS A4.2-91*, A.W. Society, Editor 1991.
47. Lo, K.H., C.H. Shek, and J.K.L. Lai, *Recent developments in stainless steels.* Materials Science and Engineering R, 2009. **65**: p. 39–104.
48. Porter, D. and E. K.E., *Phase transformations in metals and alloys*. 1992: Chapman & Hall.
49. Carter, W.C. *Spinodal decomposition - MIT 3.0 Thermodynamics of Materials*. 2002; Available from: http://pruffle.mit.edu/3.00/Lecture_32_web/node3.html.
50. Chung, H.M. and O.K. Chopra, *KINETICS AND MECHANISM OF THERMAL AGING EMBRITTLEMENT OF DUPLEX STAINLESS STEELS.* Materials and Components Technology Division Argonne National Laboratory, 1987.
51. Strangwood, M. and S.G. Druce, *Aging effects in Welded cast CF3 stainless steel.* Material Science and Technology, 1990. **6**: p. 237 - 247.
52. Vitek, J.M., et al., *Low Temperature Aging Behavior of Type 308 Stainless Steel Weld Metal.* Acta Metallurgica et Materiallia, 1990. **39**(4): p. 503 - 516.
53. Jiang, X.-c., T. Yoshimura, and Y. Ishikawa, *Investigation of Alpha Prime Precipitation in Aged Duplex Stainless Steel.* J. Electrochem. Soc.,, 1992. **139**(4): p. 1001 - 1006.
54. Tsuchiya, S., et al., *Atom Probe Study of the Aging Embrittlement of Cast Duplex Stainless Steel.* JSME International Journal, 1995. **Series A, Vol 38**(3): p. 384 - 392.
55. Iacoviello, F., F. Casari, and S. Gialanella, *Effect of "475 °C embrittlement" on duplex stainless steels localized corrosion resistance.* Corrosion Science, 2005. **47**(4): p. 909-922.
56. Bonnet, S., et al., *Relationship between evolution of Mechanical properties of various cast duplex stainless steels and Metallurgical and aging parameters: outline of current EDF programes.* Material Science and Technology, 1990. **6**: p. 221 - 229.
57. Strangwood, M., *Personal comunication - 2010. Birmingham*
58. Sourmail, T., *Precipitation in creep resistant austenitic stainless steels.* Material Science and Technology 2001. **17**: p. 1-14.
59. Bain, E.C., R.H. Aborn, and J.J. Rutherford, *The Nature and Prevention of Intergranular Corrosion in Austenitic Stainless Steels.* Trans. Am. Soc. Steel Trea., 1933. **21**: p. 481-509.
60. Sahlaoui, H., et al., *Effects of ageing conditions on the precipitates evolution, chromium depletion and intergranular corrosion susceptibility of AISI 316L: experimental and modeling results.* Materials Science and Engineering: A, 2004. **372**(1–2): p. 98-108.
61. Bruemmer, S.M. and L.A. Charlot, *Development of grain boundary chromium depletion in type 304 and 316 stainless steels.* Scripta Metallurgica, 1986. **20**(7): p. 1019-1024.

62. Thorvaldsson, T. and G.L. Dunlop, *Grain boundary Cr-depleted zones in Ti and Nb stabilized austenitic stainless steels.* Journal of Materials Science, 1983. **18**(3): p. 793-803.
63. Strawstrom, C. and M. Hillert, *An Improved Depleted-Zone Theory of Intergranular Corrosion of 18-8 Stainless Steel.* Journal of the Iron and Steel Institute, 1969. **207**: p. 77-85.
64. Devine, T.M., *Kinetics of sensitization and de-sensitization of duplex 308 stainless steel.* Acta Metallurgica, 1988. **36**(6): p. 1491-1501.
65. Bai, G., et al., *Intergranular corrosion behavior associated with delta-ferrite transformation of Ti-modified Super304H austenitic stainless steel.* Corrosion Science, 2015. **90**: p. 347-358.
66. Parvathavarthini, N., et al., *Continuous cooling and low temperature sensitization of AISI Types 316 SS and 304 SS With different degrees of cold work.* Journal of Nuclear Materials, 1989. **168**(1): p. 83-96.
67. Lv, J. and H. Luo, *The Effect of Low Temperature Sensitization on Corrosion Resistance of Ultrafine-Grained Type 321 Stainless Steels.* Journal of Materials Engineering and Performance, 2014. **23**(1): p. 262-267.
68. Tedmon, C.S., D.A. Vermilyea, and J.H. Rosolowski, *Intergranular Corrosion of Austenitic Stainless Steel.* Journal of The Electrochemical Society, 1971. **118**(2): p. 192-202.
69. Devine, T.M., *The mechanism of sensitization of austenitic stainless steel.* Corrosion Science, 1990. **30**(2): p. 135-151.
70. Lima, A.S., et al., *Sensitization evaluation of the austenitic stainless steel AISI 304L, 316L, 321 and 347.* Journal of Materials Science, 2005. **40**(1): p. 139-144.
71. Povich, M.J., *Low Temperature Sensitization of Type 304 Stainless Steel.* CORROSION, 1978. **34**(2): p. 60-65.
72. Povich, M.J. and P. Rao, *Low Temperature Sensitization of Welded Type 304 Stainless Steel.* CORROSION, 1978. **34**(8): p. 269-275.
73. Singh, R., et al., *Low Temperature Sensitization on the Orthogonal Surfaces of Prior Deformed AISI 304LN and Aged at 673 K to 873 K (400 °C to 600 °C).* Metallurgical and Materials Transactions A, 2012. **43**(3): p. 986-1003.
74. Kain, V., et al., *Effect of cold work on low-temperature sensitization behaviour of austenitic stainless steels.* Journal of Nuclear Materials, 2004. **334**(2–3): p. 115-132.
75. Singh, R., et al., *Intergranular Corrosion Behavior of 304LN Stainless Steel Heat Treated at 623 K (350 °C).* Metallurgical and Materials Transactions A, 2013. **44**(1): p. 173-187.
76. Lippold, J.C., *Welding Metallurgy and Weldability*. 2014: Wiley.
77. Dayal, R.K., N. Parvathavarthini, and B. Raj, *Influence of metallurgical variables on sensitization kinetics in austenitic stainless steels.* International Materials Reviews, 2005. **50**(3): p. 129-155.
78. Kwok, C.T., et al., *Effect of laser surface melting on intergranular corrosion behaviour of aged austenitic and duplex stainless steels.* Corrosion Science, 2011. **53**(4): p. 1581-1591.
79. Yakel, H., *Atom distributions in sigma phases. I. Fe and Cr atom distributions in a binary sigma phase equilibrated at 1063, 1013 and 923 K.* Acta Crystallographica Section B, 1983. **39**(1): p. 20-28.
80. Y. Minami, e.a., *Microstructural changes in austenitic stainless steel during long term aging.* Materials Science and Technology, 1986. **2**: p. 795-806.
81. Sahlaoui, H. and H. Sidhom, *Experimental Investigation and Analytical Prediction of σ-Phase Precipitation in AISI 316L Austenitic Stainless Steel.* Metallurgical and Materials Transactions A, 2013. **44**(7): p. 3077-3083.
82. Barcik, J., *Mechanisms of sigma phase precipitation in Cr-Ni austenitic steels.* Materials Science and Technology, 1988. **4**: p. 5-15.

83. Vitek, J.M. and S.A. David, *The aging behavior of homogenized type 308 and 308CRE stainless steel.* Metallurgical Transactions A, 1987. **18**(7): p. 1195-1201.
84. Sato, Y.S. and H. Kokawa, *Preferential precipitation site of sigma phase in duplex stainless steel weld metal.* Scripta Materialia, 1999. **40**(6): p. 659-663.
85. Hull, F.C., *Effects of composition on embrittlement of austenitic stainless steels.* Welding Journal - Reserch Suplement, 1973. **52**: p. 104s-113s.
86. Perricone, M.J., et al., *Effect of Composition on the Formation of Sigma during Single-Pass Welding of Mo-Bearing Stainless Steels.* Metallurgical and Materials Transactions A, 2007. **38**(9): p. 1976-1990.
87. Perren, R.A., et al., *Corrosion resistance of super duplex stainless steels in chloride ion containing environments: investigations by means of a new microelectrochemical method: II. Influence of precipitates.* Corrosion Science, 2001. **43**(4): p. 727-745.
88. Padilha, A.F., et al., *Precipitation in AISI 316L(N) during creep tests at 550 and 600 °C up to 10 years.* Journal of Nuclear Materials, 2007. **362**(1): p. 132-138.
89. Badji, R., et al., *Phase transformation and mechanical behavior in annealed 2205 duplex stainless steel welds.* Materials Characterization, 2008. **59**(4): p. 447-453.
90. Chun, E.J., et al., *Prediction of σ Phase Precipitation in Type 316FR Stainless Steel Weld Metal.* QUARTERLY JOURNAL OF THE JAPAN WELDING SOCIETY, 2013. **31**(4): p. 168s-172s.
91. Villanueva, D.M.E., et al., *Comparative study on sigma phase precipitation of three types of stainless steels: austenitic, superferritic and duplex.* Materials Science and Technology, 2006. **22**(9): p. 1098-1104.
92. Green, G., et al., *Evolution of sigma phase in 321 grade austenitic stainless steel parent and weld metal with duplex microstructure.* Materials Science and Technology, 2014. **30**(12): p. 1392-1398.
93. Ar, et al., *Determination of Susceptibility to Intergranular Corrosion of UNS 31803 Type Duplex Stainless Steel by Electrochemical Reactivation Method: A Comparative Study.* International Journal of Corrosion, 2012. **2012**: p. 14.
94. Pohl, M., O. Storz, and T. Glogowski, *Effect of intermetallic precipitations on the properties of duplex stainless steel.* Materials Characterization, 2007. **58**(1): p. 65-71.
95. Vitek, J.M. and S.A. David, *The sigma phase transformation in austenitic stainless steel.* Welding Journal - Reserch Suplement, 1986.
96. Magnabosco, R., *Kinetics of sigma phase formation in a Duplex Stainless Steel.* Materials Research, 2009. **12**: p. 321-327.
97. Shinohara, K., S. Toshihiro, and K. Kenzaburo, *Recrystallization and sigma phase formationn as concurrent and interacting phenomena in 25%Cr-20%Ni steel.* Materials Transactions, JIM, 1979. **20**(12): p. 713-723.
98. Thomas, R.G. and D. Yapp, *The Effect of Heat Treatment in Type 316 Stainless Steel.* Welding Journal - Welding Research Suplement 1978: p. 361-366.
99. Schwind, M., et al., *SIGMA-PHASE PRECIPITATION IN STABILIZED AUSTENITIC STAINLESS STEELS.* Acta Materialia, 2000. **48**(10): p. 2473-2481.
100. Smith, J.J. and R.A. Farrar, *Effect of composition on the transformation behaviour of duplex 316 weld metal.* Journal of Materials Science, 1991. **26**(18): p. 5025-5036.
101. Calliari, I., M. Zanesco, and E. Ramous, *Influence of isothermal aging on secondary phases precipitation and toughness of a duplex stainless steel SAF 2205.* Journal of Materials Science, 2006. **41**(22): p. 7643-7649.
102. Christian, J.W., *The Theory of Transformations in Metals and Alloys*. 2002, Oxford: Pergamon.
103. Ferro, P. and F. Bonollo, *A Semiempirical Model for Sigma-Phase Precipitation in Duplex and Superduplex Stainless Steels.* Metallurgical and Materials Transactions A, 2012. **43**(4): p. 1109-1116.

104. dos Santos, D.C. and R. Magnabosco, *Kinetic Study to Predict Sigma Phase Formation in Duplex Stainless Steels.* Metallurgical and Materials Transactions A, 2016. **47**(4): p. 1554-1565.
105. Chopra, O.K. and H.M. Chung, *Aging of Cast Duplex Stainless Steel in LWR Systems.* Nuclear Engineering and Design, 1985. **89**: p. 305 - 318.
106. Cortie, M.B. and H. Pollak, *Embrittlement and aging at 475 °C in an experimental ferritic stainless steel containing 38 wt.% chromium.* Materials Science and Engineering A, 1995. **199**(2): p. 153-163.
107. Chung, H.M. and T.R. Leax, *Embrittlement of laboratory and reactor aged CF3, CF8, and CF8M duplex stainless steel.* Material Science and Technology, 1990. **6**: p. 249 - 262.
108. Timofeev, B.T. and Y.K. Nikolaev, *About the prediction of and assessment of thermal embrittlement of Cr-Ni austenitic-ferritic weld metal and casting s at the ageing temperatures 260 - 425 C.* International Journal of Pressure Vessels and Piping, 1999. **76**: p. 849-856.
109. Yamada, T., S. Okano, and H. Kuwano, *Mechanical property and microstructural change by thermal aging of SCS14A cast duplex stainless steel.* Journal of Nuclear Materials, 2006. **350**: p. 47 - 55.
110. Chandra, K., et al., *Low temperature embrittlement of duplex stainless steel: Correlation between mechanical and electrochemical behavior.* Materials Science and Engineering A, 2010. **527**: p. 3904 – 3912.
111. Alexander, K.B., et al., *Microscopical evaluation of low temperature aging of type 308 stainless steel weldments.* Material Science and Technology, 1990. **6**: p. 314 - 320.
112. Chopra, O.K., *Estimation of Fracture Toughness of Cast Stainless Steels During Thermal Aging in LWR Systems*, in *NUREG/CR-4513 - US Nuclear Safety Commision* 1994.
113. Abou-Elazm, A., et al., *Correlation between the degree of sensitization and stress corrosion cracking susceptibility of type 304H stainless steel.* Corrosion Science, 2009. **51**(2): p. 203-208.
114. Gaudett, M.A. and J.R. Scully, *Distributions of Cr Depletion Levels in Sensitized AISI 304 Stainless Steel and Its Implications Concerning Intergranular Corrosion Phenomena.* Journal of The Electrochemical Society, 1993. **140**(12): p. 3425-3435.
115. Mozhi, T.A., W.A.T. Clark, and B.E. Wilde, *The effect of nitrogen and carbon on the stress corrosion cracking performance of sensitized AISI 304 stainless steel in chloride and sulfate solutions at 250°C.* Corrosion Science, 1987. **27**(3): p. 257-273.
116. Solomon, H.D., *Transgranular, Granulated, and Intergranular Stress Corrosion Cracking in AISI 304 SS.* CORROSION, 1984. **40**(9): p. 493-506.
117. Galvele, J. and G. Duffo, *Degradación de Materiales I - Corrosión bajo tensiones*. 2004, Buenos Aires, Argentina.: Instituto Sabato.
118. Revie, R.W., *Uhlig's Corrosion Handbook*. 2011: Wiley.
119. IAEA-PRIS. *Operational and long-term shutdown reactors - Power Reactor Information System*. 2017.
120. Aaltonen, P. and H. Hanninen, *Water chemistry and behavior of materials in PWRs and BWRs (IAEA-TECDOC--965)*. 1997: International Atomic Energy Agency (IAEA).
121. Horn, R.M., et al., *Experience and assessment of stress corrosion cracking in L-grade stainless steel BWR internals.* Nuclear Engineering and Design, 1997. **174**(3): p. 313-325.
122. Wachter, O. and G. Brümmer, *Experiences with austenitic steels in boiling water reactors.* Nuclear Engineering and Design, 1997. **168**(1): p. 35-52.
123. Yamashita, H., et al., *SCC growth behavior of BWR core shroud materials.* International Journal of Pressure Vessels and Piping, 2008. **85**(9): p. 582-592.
124. Raquet, O., et al., *SCC of cold-worked austenitic stainless steel in PWR conditions.* Advances in Materials Science, 2007. **7**(1).

125. IAEA, *Stress Corrosion Cracking in Light Water Reactors: Good Practices and Lessons Learned*. IAEA Nuclear Energy Series. 2011, Vienna: INTERNATIONAL ATOMIC ENERGY AGENCY.
126. Persaud, S.Y., S. Ramamurthy, and R.C. Newman, *The effect of weld chemistry on the oxidation of Alloy 82 dissimilar metal welds.* Corrosion Science, 2015. **91**: p. 58-67.
127. Nakagawa, T., et al., *Influence of Dissolved Hydrogen on Oxide Film and PWSCC of Alloy 600 in PWR Primary Water.* Journal of Nuclear Science and Technology, 2003. **40**(1): p. 39-43.
128. Hwang, S.S., *Review of PWSCC and mitigation management strategies of Alloy 600 materials of PWRs.* Journal of Nuclear Materials, 2013. **443**(1): p. 321-330.
129. Lopez, N., M. Cid, and M. Puiggali, *Influence of o-phase on mechanical properties and corrosion resistance of duplex stainless steels.* Corrosion Science, 1999. **41**(8): p. 1615-1631.
130. Lai, J.K.L. and A. Wickens, *Effect of intergranular particle size and spacing on creep ductility of type 316 stainless steel.* Scripta Metallurgica, 1979. **13**(12): p. 1197-1198.
131. Li, D.J., et al., *Effect of σ-Phase on the creep properties of Cr25Ni20 stainless steel.* Scripta Metallurgica, 1989. **23**(8): p. 1319-1321.
132. Shek, C.H., et al., *Creep properties of aged duplex stainless steels containing σ phase.* Materials Science and Engineering: A, 1999. **266**(1–2): p. 30-36.
133. Galvele, R. and G. Duffo, *Degradación de Materiales I - Corrosion*. 2004, Buenos Aires - Argentina: Instituto Sabato.
134. Sedriks, A.J., *Corrosion of stainless steel*, in *Encyclopedia of materials -Science and Technology*, Elsevier, Editor. 2001.
135. R.G. Kelly, J.R.S., D.W. Shoesmith, R.G. Buchheit, *Electrochemical Techniques in Corrosion Science and Engineering* ed. M. Dekker. 2003.
136. Galvele, R. and G. Duffo, *Degradación de Materiales I - Picado*. 2004, Instituto Sabato: Buenos Aires - Argentina.
137. Frankel, G.S., *Pitting Corrosion of Metals A Review of the Critical Factors.* Journal of the Electrochemical Society,, 1998. **145**(6): p. 2186-2198.
138. Tipping, P.G., *Understanding and Mitigating Ageing in Nuclear Power Plants: Materials and Operational Aspects of Plant Life Management (PLIM)*. 2010: Elsevier Science.
139. Hänninen, H., et al., *Characterization of Austenitic Stainless Steel Pipe Welds After Prolonged Power Plant Exposure.* Corrosion, 1992. **48**(2): p. 114 - 123.
140. Park, C.-J., H.-S. Kwon, and M.M. Lohrengel, *Micro-electrochemical polarization study on 25% Cr duplex stainless steel.* Materials Science and Engineering: A, 2004. **372**(1–2): p. 180-185.
141. Perren, R.A., et al., *Corrosion resistance of super duplex stainless steels in chloride ion containing environments: investigations by means of a new microelectrochemical method: I. Precipitation-free states.* Corrosion Science, 2001. **43**(4): p. 707-726.
142. Lee, J.-S., et al., *Corrosion behaviour of ferrite and austenite phases on super duplex stainless steel in a modified green-death solution.* Corrosion Science, 2014. **89**: p. 111-117.
143. Yi, Y.S. and T. Shoji, *Detection and evaluation of material degradation of thermally aged duplex stainless steels: electrochemical polarization test and AFM surface analysis.* Journal of Nuclear Materials, 1996. **231**: p. 20 - 28.
144. Chan-Jin, P. and K. Hyuk-Sang, *Effects of aging at 475 °C on corrosion properties of tungsten-containing duplex stainless steels.* Corrosion Science, 2002. **44**(12): p. 2817-2830.
145. Kobelco. *Weld Decay: Its Cause and Cure*. 2017 19/06/2017]; Available from: http://www.kobelco-welding.jp/education-center/abc/ABC_1999-04.html.

146. Dos Santos, D.C., R. Magnabosco, and C. de Moura Neto, *Influence of Sigma Phase formation on Pitting Corrosion of an Aged UNS S31803 Duplex Stainless Steel.* Corrosion, 2013. **69**(9): p. 900-911.
147. Park, C.J., V.S. Rao, and H.S. Kwon, *Effects of Sigma Phase on the Initiation and Propagation of Pitting Corrosion of Duplex Stainless Steel.* CORROSION, 2005. **61**(1): p. 76-83.
148. Chandra, K., V. Kain, and R. Tewari, *Microstructural and electrochemical characterisation of heat-treated 347 stainless steel with different phases.* Corrosion Science, 2013. **67**(0): p. 118-129.
149. Saithala, J.R., et al., *Environmental Assisted Cracking Behavior of Sigmatized Super Duplex Stainless Steel in Oilfield Production Brine.* Corrosion, 2013. **69**(3): p. 276-285.
150. ASTM, *ASTM A-262. Standard Practices for Detecting Susceptibility to Intergranular Attack in Austenitic Stainless Steels*, 2015, American Satandard for Testing Materials ASTM A-262-02a.
151. Číhal, V.r. and R. Štefec, *On the development of the electrochemical potentiokinetic method.* Electrochimica Acta, 2001. **46**(24): p. 3867-3877.
152. ASTM, *ASTM G-108. Standard Test Method for Electrochemical Reactivation (EPR) for Detecting Sensitization of AISI Type 304 and 304L Stainless Steels*, 1994: 100 Barr Harbor Drive, West Conshohocken, PA 19428-2959, United States.
153. ASTM, *ASTM E-112. Standard Test Methods for Determining Average Grain Size*, 1996: 100 Barr Harbor Drive, PO Box C700, West Conshohocken, PA 19428-2959, United States.
154. Aydoğdu, G.H. and M.K. Aydinol, *Determination of susceptibility to intergranular corrosion and electrochemical reactivation behaviour of AISI 316L type stainless steel.* Corrosion Science, 2006. **48**(11): p. 3565-3583.
155. BSI-EN-ISO, *12.732 : 2008 - Corrosion of metals and alloys — Electrochemical potentiokinetic reactivation measurement using the double loop method (based on Cihal's method)*, 2008.
156. Carranza, R., *Personal communication*, 2017: Buenos Aires - Argentina.
157. de Lima-Neto, P., et al., *Determination of the sensitized zone extension in welded AISI 304 stainless steel using non-destructive electrochemical techniques.* Corrosion Science, 2008. **50**(4): p. 1149-1155.
158. *ASME SA - 516 Specification for Pressure Vessel Plates, Carbon Steel, for moderate and low temperature service.* ASME Boiler and Pressure Vessel Code, 1998. **II C**.
159. Neff, F. and K. Winter, *Die Unterpulver-bandschweißung.* Bohler Schweissdraht-Kundeninformation, 1981. **24**.
160. Solari, M., *Informe Técnico del Revestimiento del Recipiente de Presión (Carem Reactor RPV cladding specifications)* 1994, Comisión Nacional de Energía Atómica: Buenos Aires.
161. Fisher. *FERITSCOPE® FMP30 Operator Manual*. 2008.
162. ASTM, *ASTM E-23. Standard test methods for notched bar impact testing of metallic materials* 2002, ASTM International
163. Robert, M., *Prediction of Low Temperature Sensitization of Austenitic Stainless Steels.* Division of High Level Waste Management - US Nuclear Regulatory Commission 1988.
164. Richardson, F.D., Journal of Iron and Steel Institute, 1953. **167**(3).
165. Bordín, S.F., et al., *EBSD spatial resolution for detecting sigma phase in steels.* Ultramicroscopy, 2016. **171**: p. 177-185.
166. Bowman, A.L., et al., *The crystal structure of Cr23C6.* Acta Crystallographica Section B, 1972. **28**(10): p. 3102-3103.
167. AMMRF. *Quantitative EDS X-ray microanalysis using SEM*. 2014 [cited 2017; Available from: http://www.ammrf.org.au/myscope/analysis/eds/quantitative/.

168. Boheler, *Welding Consumables for Joint Welding.* 2017.
169. Ogborn, J.S., *ASM Handbook Vol. 6 - Welding, Brazing, and Soldering*. 1993: ASM International.
170. Alexander David, N.R., *The Effects of Aging for 50,000 Hours at 343°C on the Mechanical Properties of Type 308 Stainless Steel Weldments*. 1995: Oak Ridge National Laboratory.
171. Hale, G.E. and S.J. Garwood, *Effect of aging on fracture behaviour of cast stainless steel and weldments.* Materials Science and Technology, 1990. **6**(3): p. 230-236.
172. Gomila, M.J.A., *Fractura de materiales*. 2002: Edicions UPC.
173. Mirza, M.S., D.C. Barton, and P. Church, *The effect of stress triaxiality and strain-rate on the fracture characteristics of ductile metals.* Journal of Materials Science, 1996. **31**(2): p. 453-461.
174. Passarella, D.N., *Desarrollo de modelo en Matlab para el ajuste de Gaussianas solapadas.* Universidad Nacional de Quilmes - Argentina, 2016.
175. Arkan, M.E., R. Arkan, and M. Doruk, *Determination of Susceptibility to Intergranular Corrosion of UNS 31803 Type Duplex Stainless Steel by Electrochemical Reactivation Method.* International Journal of Corrosion, 2012. **2012**: p. 10.
176. Kekkonen, T., P. Aaltonen, and H. Hänninen, *Metallurgical effects on the corrosion resistance of a low temperature sensitized welded aisi type 304 stainless steel.* Corrosion Science, 1985. **25**(8): p. 821-836.
177. Lumsden, J.B. and P.J. Stocker, *Composition of grain boundaries of type 304 stainless steel in low temperature sensitization condition.* Scripta Metallurgica, 1981. **15**(12): p. 1295-1298.
178. Fox, M.J., *An overview of low temperature sensitization*, L.L.N. Laboratory, Editor 1983.
179. Schmidt, C.G., et al., *Low temperature sensitization of type 304 stainless steel pipe weld heat affected zone.* Metallurgical Transactions A, 1987. **18**(8): p. 1483-1493.
180. Brown, J.E., et al., *Quantitative atom probe analysis of spinodal reaction in ferrite phase of duplex stainless steel.* Materials Science and Technology, 1990. **6**(3): p. 293-300.